Magnetoresistance and Doping Effects in Conjugated Polymer-Based Organic Light Emitting Diodes

Hang Gu

School of Physics and Astronomy

Queen Mary University of London

Supervisors: Dr. Theo Kreouzis

Professor William Gillin

Submitted for the doctor degree of Philosophy

Declaration

I declare that all the work contained within this thesis is accomplished by myself during my study in Queen Mary University of London.

Abstract

Magnetoresistance (MR) and doping effects have been investigated in a poly(3-hexylthiophene-2,5-diyl) (P3HT) based organic light emitting diodes. In single device of fixed composition (Au/P3HT/Al as spun and processed in air), the measured MR strongly depends on the drive conditions. The magnetoconductance (MC) varies from negative to positive ($-0.4\% \leq MC \leq 0.4\%$) with increasing current density, depending on which microscopic mechanism dominates. The negative MC is due to bipolaron based interactions and the positive MC to triplet-polaron based interactions (as confirmed by light emission). Oxygen doping is prevalent in P3HT devices processed in air and the effect of de-doping (by annealing above the glass transition temperature) is investigated on the MC of an Au/P3HT/Al diode. De-doping reduces the current through the device under forward bias by ~3 orders of magnitude, but increases the negative (low current) MC from a maximum of -0.5% pre-annealing to -3% post-annealing. This increased negative MC is consistent with bipolaron theory predictions based on Fermi level shifts and density of states (DoS) changes due to de-doping. The decrease in current density is explained by increased injection barriers at both electrodes also resulting from de-doping. Deliberate chemical doping of P3HT is carried out using pentacene as a hole trap centre. The trapping effect of pentacene is confirmed by reproducible and significant hole mobility-pentacene concentration behaviour, as measured by dark injection (DI) transient measurements. The enhanced carrier injection resulting from the pentacene doping also leads to increased electroluminescence (EL). The resultant MC in pentacene doped devices is strongly dependent on carrier injection and can be significantly enhanced by doping, for example from -0.2% to -0.6% depending on device and drive conditions. Throughout this thesis Lorentzian and non-Lorentzian function fitting is carried out on the measured MC, although the underlying microscopic mechanisms cannot always be discerned.

Acknowledgements

First of all, I would like to express my sincere and deep gratitude to my supervisor Dr. Theo Kreouzis. All the time he spent to supervise my work and care my life is deeply appreciated. I acquired my practical laboratory knowledge as well as theoretical background from him.

I would like to special thank and acknowledge my co-supervisor Professor William Gillin for devoting his valuable time for commenting and for helpful discussions on my PhD project.

Special thanks go to Mr. Geoff Gannaway, Dr. Pratick Desai, Mr. George Nevill and Dr. Ken Scott for technological support and research assistance.

I am also really appreciated the support from other friendly and talented scholars in Queen Mary: Professor Wen Wang (Dean for Research), Professor Steve Lloyd (Head of Physics School), Professor Martin Dove (Director of Material Research Institute), Professor Mike Watkinson (Deputy Dean for Research), Professor Yang Hao (Professor in Electrical and Engineering) and Dr. Alvara Mata (Associate Director of Institute of Bioengineering) and so on to the “First Chinese-British Students and Scholars Forum” organized by me as the president of Chinese Students and Scholars Association (CSSA) during my PhD study.

Acknowledgements to all my colleagues and friends in our group: Shankui Chang, Haizhou Lu, David Holford, Tingting Zhang, Huanqing Ye, Hongtao Zhang, Yu Peng, Jianxu Hu, Juan Du and so on.

Acknowledgements to the funding supported to my PhD by the collaboration of China Scholars Council (CSC) and Queen Mary University of London.

Last but not least, I would like to thank my beloved parents who have done so much to bring me up.

Contents

List of Figures

Page

List of Publications

Hang Gu, Shankui Chang, David Halford, Tingting Zhang, Haizhou Lu, Theo Kreouzis*, William Gillin. "Annealing and doping-dependent magnetoresistance in a single layer poly(3-hexyl-thiophene) organic semiconductor device" *Organic electronics*, 17, no.19 (2015):51

Hang Gu, Theo Kreouzis*, William Gillin. "The transition from bipolaron to triplet-polaron magnetoresistance in single layer organic semiconductor devices" *Organic electronics* 4, no. 36 (2014):1711.

Lin Gan, Jian Zhou, Fen Ke, **Hang Gu**, Danna Li, Zonghai Hu, Qiang Sun, and Xuefeng Guo. "Tuning the properties of graphene using a reversible gas-phase reaction." *NPG Asia Materials* 4, no. 11 (2012): e31.

Lin Gan, Song Liu, Danna Li, **Hang Gu**, Yang Cao, Qian Shen, Zhen-Xing Wang, Qing Wang, and Xue-Feng Guo. "Facile fabrication of the crossed nanotube-graphene junctions." *Acta Physico-Chimica Sinica* 26, no. 4 (2010): 1151.

List of Abbreviations

6-TTP-6 ..... ω,ω'-dihexylterthiophene

8-PNP-O12 ..... 2-(4'-octylphenyl)-6-dodecyloxynaphthalene

8-PNP-O4 ..... 2-(4'-octylphenyl)-6-butyloxynaphthalene

Al ..... aluminium

Alq_3..... aluminium tris(8-hydroxyquinoline)

Au ..... gold

BCP 2,9-dimethyl-4, 7-diphenyl-1, 10-phenanthroline

BEDT-TTF ..... 2-(5,6-Dihydro[1,3]dithiolo[4,5-b][1,4]dithiin-2-ylidene)-5,6-dihydro[1,3]dithiolo[4,5-b][1,4]dithiine

BEDT-TTF ..... bis(ethylenedithio)-tetrathiafulvalene

C_{60} ..... fullerene

CIπ-FETs ..... π-conjugated organic semiconductors fabricated into OFETs

$CoCp_2$ ..... bis(cyclopentadienyl)-cobalt(II)

CTC ..... charge transfer complex

DCM ..... 4-(dicyanomethylene)-2-methyl-6-(dimethylaminostyryl)-4H-pyrane

DDQ ..... dicyano-dichloro-quinone

DI ..... dark injection

DoS ..... density of states

EA ..... electron affinity energy

E_F ..... Fermi level

E_g ..... band-gap energy

EL ..... electroluminescence

ETL ..... electron transport layer

E_{vac} ..... vacuum level

F16ZnPc ..... hexadecafluoro-zinc-phthalocyanine

F4-TCNQ 2,3,5,6-tetrafluoro-7,7,8,8-tetracyanoquinodimethane

FM ..... ferromagnetic

GDM ..... Gaussian disorder model

HOMO ..... highest occupied molecule orbital

HTL ..... hole transport layer

IE ..... ionisation energy

ILC ..... injection-limited current

ITO ..... indium tin oxide

I-V-L..... current-voltage-luminescence

LEP ..... light emitting polymer

LiF ..... lithium fluoride

LUMO ..... lowest unoccupied molecule orbital

MC ..... magnetoconductance

MeO-TPD ..... N,N,N',N'-tetrakis (4-methoxy-phenyl) benzidine

MFE ..... magnetic field effect

MIST ..... MR controlled by inter-conversion of singlet and triplet

MR ..... magnetoresistance

ND ..... neutral density

N-DMBI ..... (4-(1,3-dimethyl-2,3-dihydro-1H-benzoimidazol-2-yl) phenyl) dimethylamine

NTCDA ..... naphthalenetetracarboxylic dianhydride

OC_1C_{10}-PPV ..poly[2-(3',7'-dimethyloctyloxy)-5-methoxy-1,4-phenylenevinylene]

OFET ..... organic field effect transistor

OLED ..... organic light emitting diode

OMR ..... organic magnetoresistance

OPV ..... organic photovoltaic

OSV ..... organic spin valve

P3HT ..... poly(3-hexylthiophene-2,5-diyl)

Pc ..... phthalocyanine

PCBM ..... [6,6]-phenyl-C_{61}-butyric acid methylester

PEDOT:PSS ..... poly(3,4-ethylenedioxythiophene) polystyrene

PFO ..... poly(9,9-dioctylfluorene)

PL ..... photoluminescence

PLED ..... polymer light emitting diode

PNV ..... poly(naphthalene vinylene)

PPE 5,8-diethynyl-2,3-diphenylquinoxaline

PPV ..... poly(p-phenylene vinylene)

PSD ..... phase-sensitive detector

PTA ..... dithieno[2,3-*d*:2',3'-*d*'] thieno[3,2-*b*:4,5-*b*'] dithiophene

SCLC ..... space charge limited current

TCNQ ..... tetracyano-quinodimethane

TiO_2 ..... titanium dioxide

TPD ..... N,N'-diphenyl-N,N'-bis(3-methylphenyl)-4,4'-diamine

TTA ..... triplet-triplet annihilation

TTN ..... tetrathianaphthacene

UPS ..... ultraviolet photoelectron spectroscopy

ZnPc ..... zinc phthalocyanine

1. Introduction and theory

1.1 Organic semiconductors and devices

The rapid growth of interest in π-conjugated materials, in general and organic semiconductors in particular, has been fuelled by academia and industry. Organic semiconductors are organic materials with semiconductor properties, and they are usually π-conjugated carbon compounds. The application of organic semiconductors, including the organic light emitting diode (OLED), organic spin valve (OSV), organic photovoltaic (OPV) and organic field effect transistor (OFET), in industry has been investigated for more than 20 years. Organic semiconductors are categorised in two classes: small molecules and polymers.

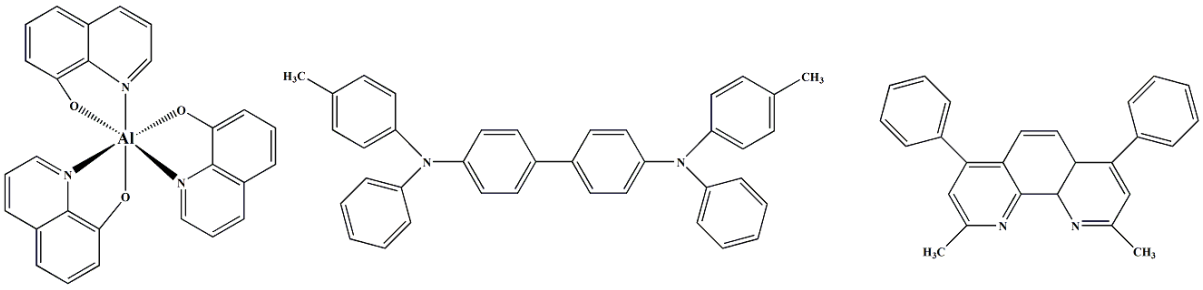

Figure 1: The chemical structure of small molecule organic semiconductors: Alq_3, TPD, and BCP.

Small molecules, such as aluminium tris(8-hydroxyquinoline) (Alq_3), N,N'-diphenyl-N,N'-bis(3-methylphenyl)-4,4'-diamine (TPD), 2,9-dimethyl-4, 7-diphenyl-1, 10-phenanthroline (BCP) are generally fabricated into devices using the vacuum evaporation technique. These molecular structures are shown in figure 1. Polymers, such as poly(3-hexylthiophene-2,5-diyl) (P3HT), poly(phenylene vinylene) (PPV) and poly(9,9-dioctylfluorene) (PFO) dissolved in suitable solvents are generally fabricated into devices using different kinds of techniques such as spin-coating, bench-top coating, spray pyrolysis and so on. The polymer structures are shown in figure 2.

The benzene structure gives an explanation of the semiconductor properties of these π-conjugated materials. As shown in figure 3, each carbon has charge occupancy $1s^2$, $2s^2$, $2p^2$, to form the σ-bonds and π-bonds between the carbon atoms. For a specific carbon atom, 1s level is fully occupied by electrons and three hybridised bonds form three σ-bonds with high excitation

energies. The remaining p-orbitals, which are perpendicular to the molecule, form the weak π-bonds.

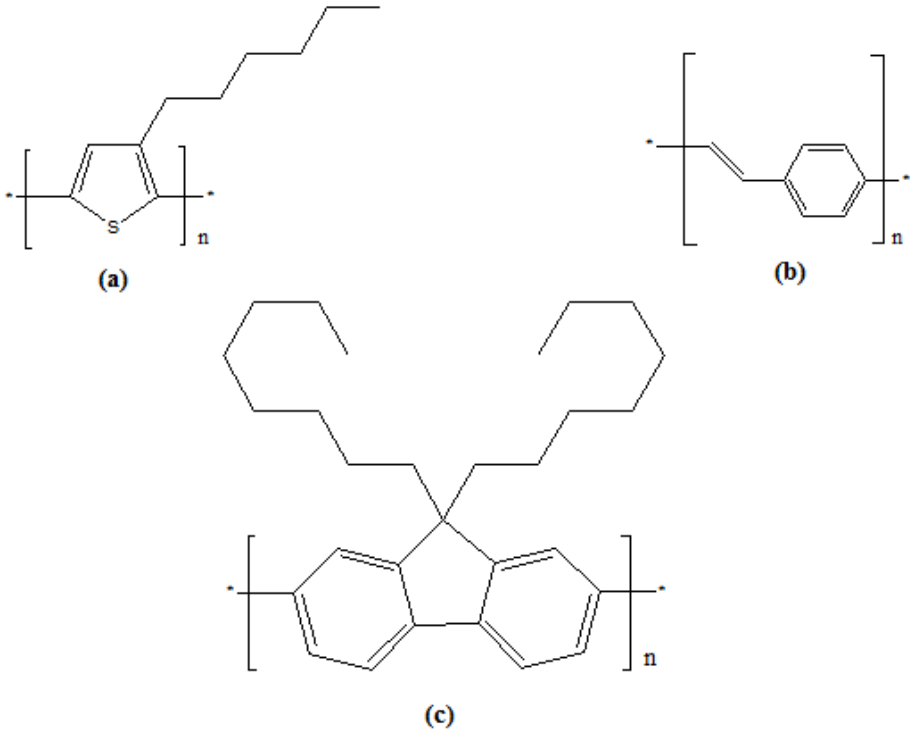

Figure 2: The chemical structure of polymer organic semiconductors: (a) P3HT, (b) PPV, and (c) PFO.

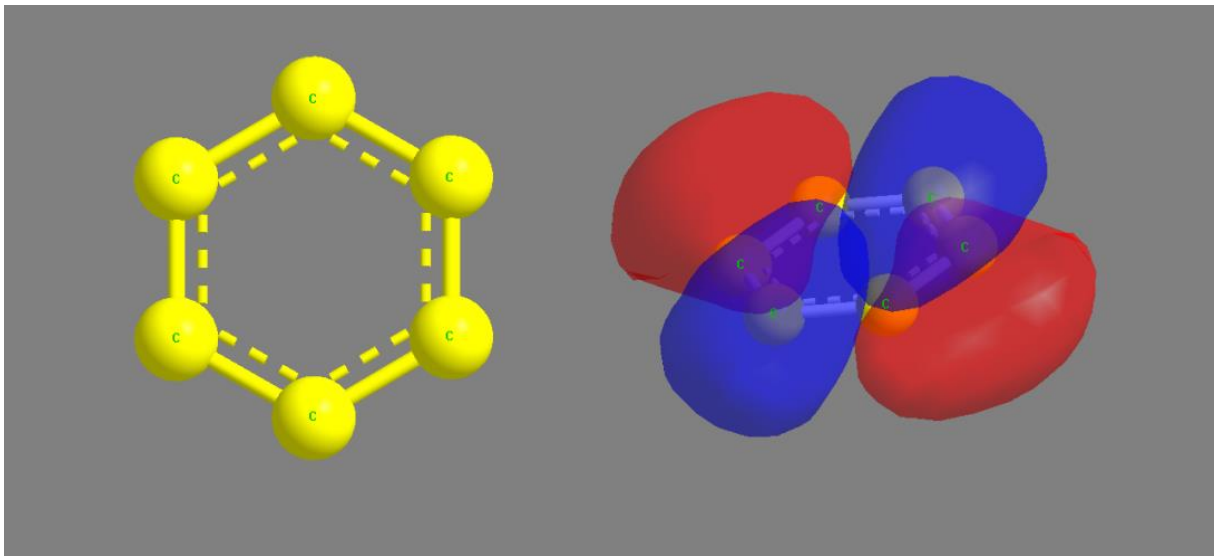

Figure 3: Schematic of π-bonds orbitals in benzene.

Electrons will occupy available states within a molecule according to the Pauli Exclusion Principle. [1] The highest π (bonding) orbital, which is occupied by electrons, is known as the highest occupied molecular orbital (HOMO). The lowest π^* (anti-bonding) orbital, which is unoccupied by electrons, is known as the lowest unoccupied molecular orbital (LUMO). [2]

Compared to inorganic semiconductors, the HOMO and LUMO can be respectively considered to be the valence and conduction band. It is these orbitals that are responsible for the electronic properties of the so called π-conjugated organics. The properties of these organic semiconductors depend on the band-gap, which is the energy gap between HOMO and LUMO in these materials. Typically, the gap ranges from 1.5 eV to 3.5 eV depending upon the chemical structure of the molecule. The band structure in the organic material results in good conducting and emission properties. In this thesis, the work is presented on P3HT which is widely used in OPV and OFET.

1.1.1 Organic light emitting diode (OLED)

Electroluminescence in organic materials such as acridine orange, either deposited on or dissolved in cellulose or cellophane thin films, was first observed in the 1950s. [3-6] W. Helfrich and W. G. Schneider of the National Research Council in Canada produced double injection recombination electroluminescence for the first time in an anthracene single crystal using hole and electron injecting electrodes. [7] The first OLED device was reported at Eastman Kodak by Ching W. Tang and Steven Van Slyke in 1987. [8] This device was based on a novel two-layer structure with separate hole transporting and electron transporting layers whereby recombination and light emission occurred in the middle of the organic layer. This design resulted in a reduction in operating voltage and improvements in efficiency that led to the current OLED research and device production. Research in polymer electroluminescence culminated in the 1990 work by J. H. Burroughes et al. at the Cavendish Laboratory in Cambridge. [9] They reported a high efficiency green light emitting polymer based device using 100 nm thick films of poly(p-phenylene vinylene) (PPV).

The organic light emitting diode is fabricated in a sandwich structure using organic materials as the electroluminescent layer, and metal or doped metal oxides as the electrodes. The organic materials are situated between two electrodes, and typically one of the electrodes should be transparent for light emission. There are also two major families of OLEDs based on small molecules and polymers, as for organic semiconductors.

Here, a small molecule based OLED, ITO/TPD/Alq_3/LiF/Al, as shown in figure 4, is chosen to explain the theory of charge transport and exciton formation mechanism. Indium tin oxide (ITO) is commonly used as the anode material, as it is transparent to visible light and has a high work function, which promotes hole injection into the HOMO level of the hole transport layer TPD. Al is used as the cathode material for electron injection into the LUMO level of the electron transport layer Alq_3. LiF acts as a buffer to improve the electron injection efficiency from the cathode (Al). The voltage applied across the OLED device results in an electrical excitation.

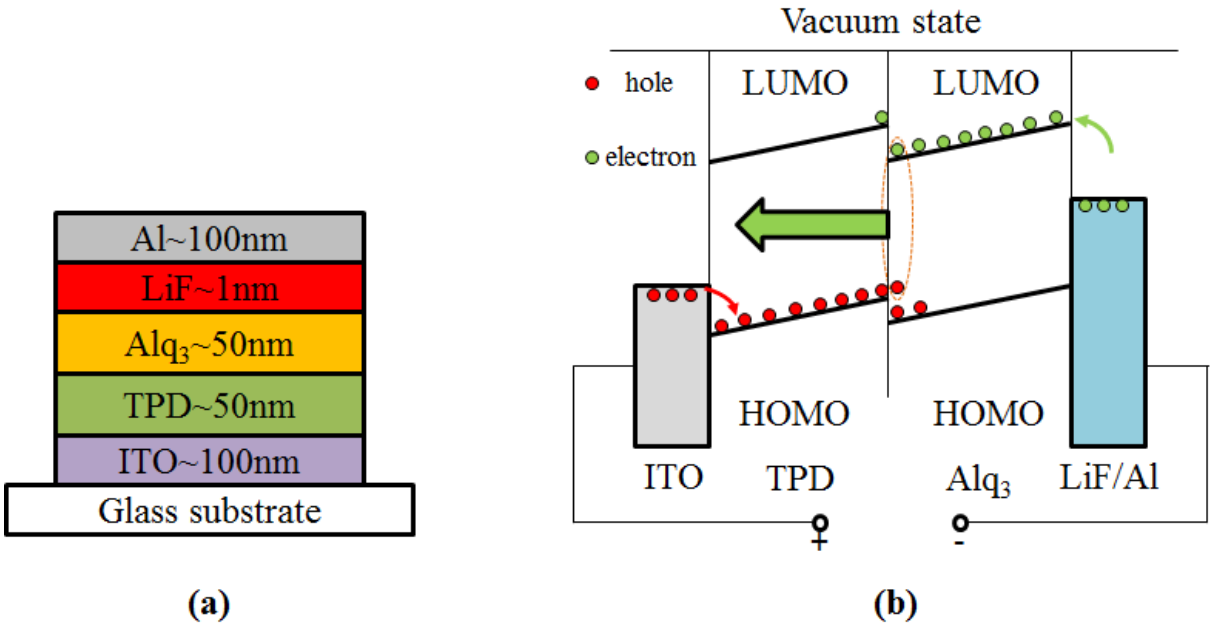

Figure 4: (a) A basic small molecule based OLED device structure ITO(100 nm)/TPD(50 nm)/Alq_3(50 nm)/LiF(1 nm)/Al(100 nm); (b) A typical OLED structure of the injection, transport, recombination and light emission.

The bias voltage should be larger than the built-in potential (the difference between the work function of the anode ITO and cathode LiF/Al) and the effective voltage is equal to the bias voltage minus the built-in potential. As shown in figure 4(b), holes are injected from the anode into the HOMO of the hole transport layer (TPD) and meet the electrons which are injected from the cathode into the LUMO of the electron transport layer (Alq_3). Once both types of charge carriers are present in the emission layer, excitons are generated by the electron-hole pairs with the required spin orientation. In this case, both singlets (short for singlet excited states) and triplets (short for triplet excited states) are formed. Luminescence is achieved in the system due to the singlet decay, known as electroluminescence.

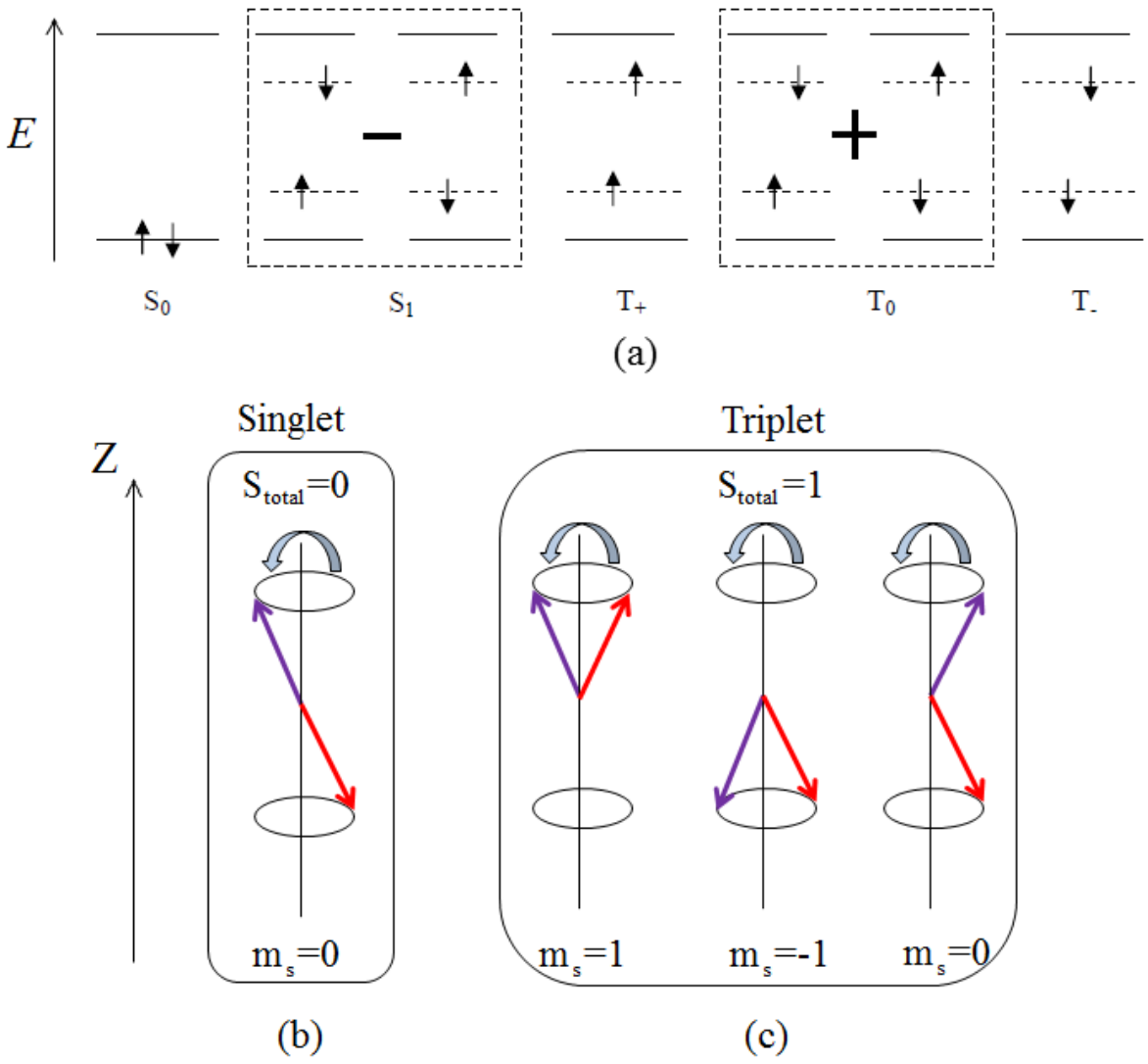

Figure 5: Exciton spin arrangement. (a) Ground states (S_0), singlet states (S_1), and triplet states (T_+, T_-, T_0). The vertical axis in (a) represents the energy. (E) (b) and (c) indicate the spin momentum and angular momentum of singlet and triplet states. The vertical axis in (b) and (c) is Z-factor.

As shown in figure 5, if the spins of the electron and hole are random, the triplet/singlet generation ratio will be 3:1. The electrical excitation leads to 25% of excitons forming singlets, and 75% of excitons forming triplets. The photon is emitted due to the singlet decay, resulting in electroluminescence. Thus making the most of the excitons by transferring the 75% triplets partially into singlets will improve the efficiency of the OLED.

Polymer light emitting diodes (PLED), also known as light emitting polymers (LEP), involve an electroluminescent conductive polymer that emits light under a suitable bias voltage. They are used as thin films for full-spectra colour displays. PLEDs are quite efficient and require a relatively small amount of power for the amount of light produced. Vacuum deposition is not a suitable

method to form thin films of polymers. However, polymers can be processed in solution, and spin-coating is a common method for depositing thin polymer films. This method is more suited to form large-area films than thermal evaporation. No vacuum is required, and the emissive materials can also be applied onto the substrate using a technique derived from commercial inkjet printing. [10] However, as the application of subsequent layers tends to dissolve those already present, the formation of multilayer structures is difficult using these methods. The metal cathode may still need to be deposited by thermal evaporation under vacuum. An alternative method is to deposit a Langmuir-Blodgett film. Typical polymers used in PLED displays include derivatives of PPV and PFO. Substitution of side chains onto the polymer backbone may determine the colour of emitted light or the stability and solubility of the polymer for performance and ease of processing. [11] While unsubstituted PPV is typically insoluble, a number of PPVs and related poly(naphthalene vinylene)s (PNVs) that are soluble in organic solvents or water are prepared via ring opening metathesis polymerisation.

1.1.2 Organic spin valve (OSV)

Organic spin valve (OSV) is another device replacing the anode and cathode of an OLED by ferromagnetic (FM) materials. [12] Figure 6 schematically shows the structure and function of OSV. Two FM materials with different coercivity are separated by a non-magnetic spacer. Spin valve devices function because of a quantum property of electrons called spin. Due to a split in the density of states of electrons at the Fermi energy in ferromagnets, there is a net spin polarisation. An electrical current passing through a ferromagnet therefore carries both charge and a spin component. In comparison, a normal metal has an equal number of electrons with up and down spins so, in equilibrium situations, such materials can sustain a charge current with a zero net spin component. However, by passing a current from a ferromagnet into an organic semiconductor it is possible for spin to be transferred. An organic semiconductor can thus transfer spin between separate ferromagnets, subject to a long enough spin diffusion length. Spin transmission depends on the alignment of magnetic moments in the ferromagnets. If a current is passing into a ferromagnet and the majority spin is spin up, for example, then electrons with spin up will pass through relatively unhindered, while electrons with spin down

will either “reflect” or spin flip scatter to spin up upon encountering the ferromagnet to find an empty energy state in the new material. Thus if both the FM electrodes are polarised in the same direction, the device has relatively low electrical resistance (spin valves open), whereas if the applied magnetic field is reversed and one layer’s polarity reverses, then the device has a higher resistance (spin valves close) due to the extra energy required for spin flip scattering.

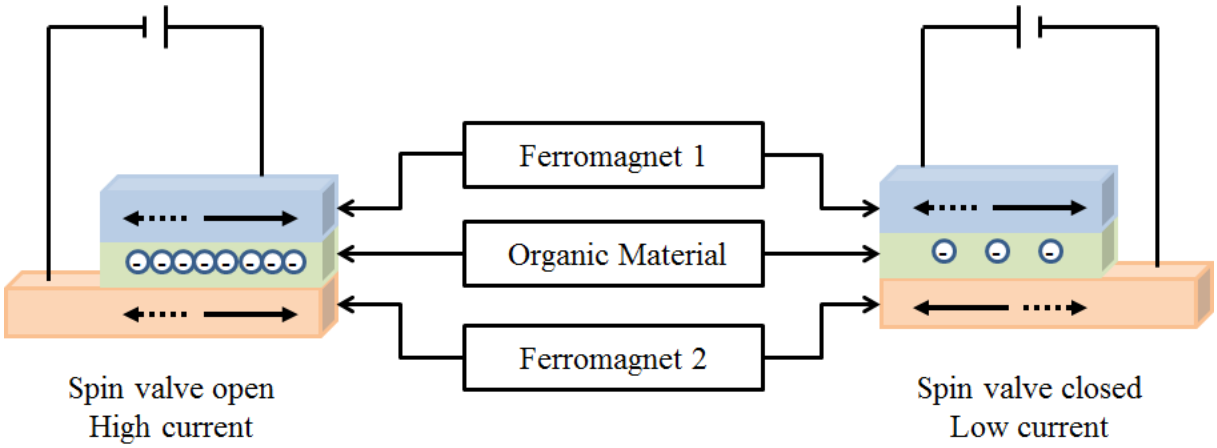

Figure 6: Schematic diagram and function of OSV.

In OSV, charge carriers with certain spin direction are injected from one FM contact and dejected to another. The spin orientation can be changed from parallel (A) to antiparallel (AP) configuration by an external magnetic field. The electronic resistance is higher in AP configuration due to DoS in FM materials dependence on magnetisation and spin.

Due to the spin direction of holes and electrons, excitons can be classified into two groups (figure 5), triplets and singlets, in which triplets have non-zero total angular momentum and singlets that have zero total angular momentum. In electroluminescence only 25% excitons are singlets, which can emit photons as the result of recombination, due to its short life time. The spins of the electron and hole are random. The triplet/singlet generation ratio will be 3:1. The electrical excitation leads to 25% of excitons forming singlets, and 75% of excitons forming triplets. In OSV, controlling spin states of the injected holes and electrons, it is possible to increase the ratio of singlets which will result in electroluminescence enhancement.

1.1.3 Organic solar cell

Organic photovoltaic devices, with the advantages of low cost, light weight, flexibility, and the ease of manufacture, show industrial applications. [13] The photovoltaic effect of organic materials was first observed in 1954. [14] This was followed by the application of organic materials for fabricating solar cells. Initially, organic solar cells were inefficient Schottky diodes that relied on a strong electrical field near the metal electrode-organic interface to separate the photo-generated excitons forming free charge carriers. Excitons could only dissociate around a very small region near the electrodes, leading to a waste of absorbed photons. Afterwards, the heterojunction architecture solar cell was created, leading to a huge revolution in the photovoltaic industry.

The first efficient organic photovoltaic device was reported by Tang in 1986. [15] This cell, as the model for later organic photovoltaic devices, contained a donor that donated electrons and transferred holes, an acceptor that accepted electrons and transferred electrons, a transparent high work function electrode such as ITO (anode), and a low work function electrode such as Al (cathode) as shown in figure 7(a). The anode and cathode would form a nearly Ohmic contact with the organic active layer. The offset between the donor and acceptor should be large enough for exciton dissociation. As the principles developed, the general process of organic solar cells was discovered. Four main procedures are shown in figure 7. [16]

The mechanism works as follows: as the organic material absorbs the photons, it creates excitons which are bound electron-hole pairs with a typical binding energy of 0.3 eV. [17] The electron is optically excited onto the LUMO level of donors. Photon absorption is characterised by an absorption length of $1/\alpha$ where α is the absorption coefficient. [18] For organic materials, the value of α is typically around 10^4~10^5 cm^{-1}, which results in an absorption length of at least 100 nm.

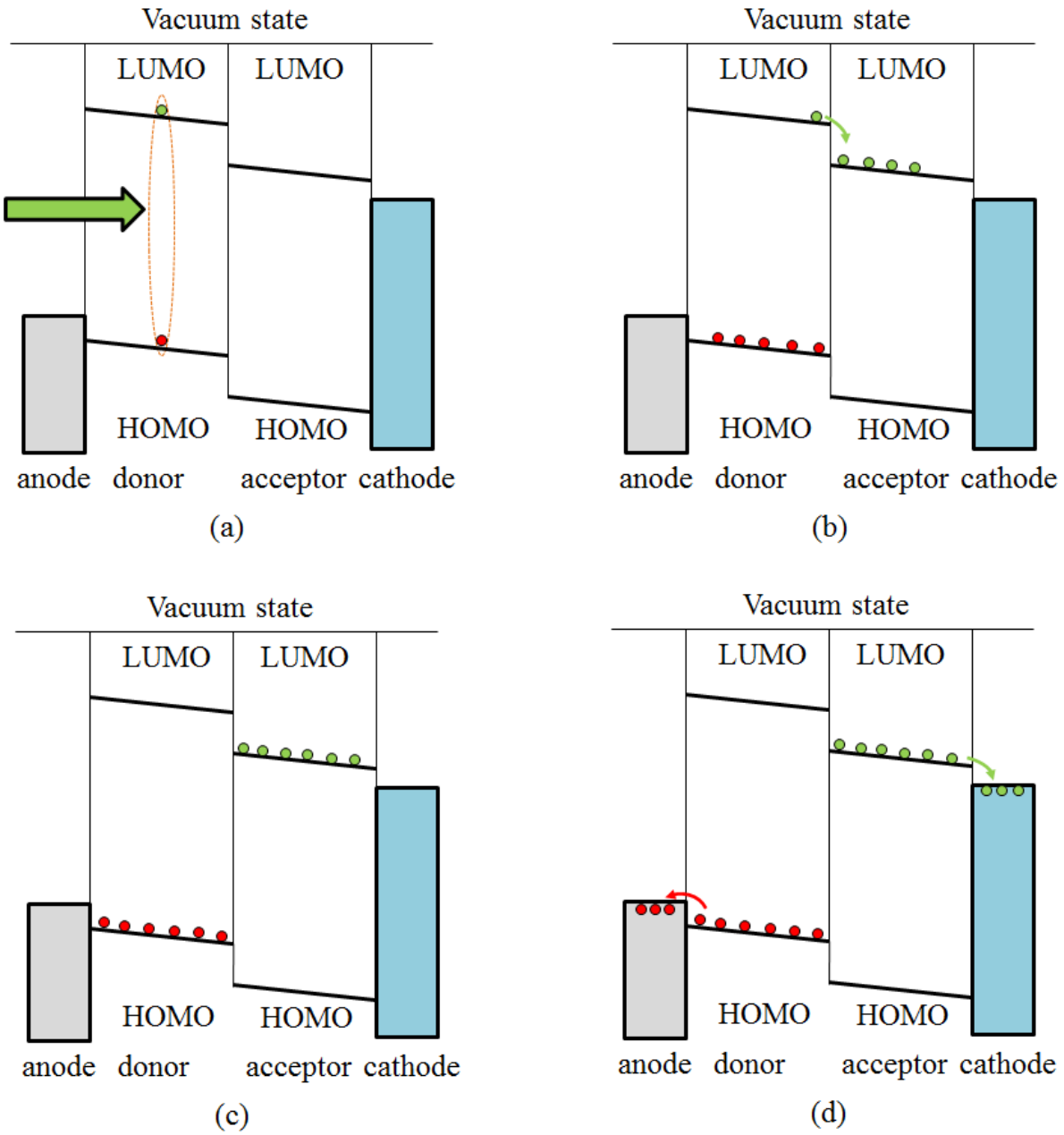

Figure 7: Charge carrier generation process in a bilayer heterojunction solar cell. (a) exciton generation (photon absorption) and diffusion, (b) exciton dissociation, (c) charge transfer and (d) charge collection.

In addition, when illuminated, the thickness of the active layer determines the photon absorption. The efficiency of photon absorption is related to the absorption coefficient and the thickness of the active layer. Excitons are mobile particles that diffuse in organic materials. The diffusion length l_{ex} is characterised by:

$$l_{ex} = \sqrt{D_{ex}\tau} \tag{1}$$

Where D_{ex} is the diffusivity and τ is the exciton lifetime.

For most organic materials, the exciton diffusion length is typically in the order of 10 nm. [19-21] Thus there is a contradiction between photon absorption and exciton diffusion. In order to absorb the incident light, the active layer should be thicker. But on the other hand, the excitons will recombine while diffusing within the materials if the active layer is too thick to exceed their diffusion length.

As reported in the literature, one applicable method was promoted to solve this problem, using bulk heterojunction architecture, which made the different phase domains smaller than the exciton diffusion length. [22-23]

When the excitons diffuse within the active layer, they dissociate into free charge carriers either via the electrical field or the heterojunction interface. Dissociation requires the electric field to be as large as ~10^5 V/m, [24] therefore excitons are primarily dissociated at the heterojunction interface. At the interface, as shown in figure 7, the offset of the LUMO between the donor and acceptor must be sufficient in order to overcome the binding energy of the excitons. [21] Meanwhile the offset should not be so big since the extra energy is then wasted by heat, phonon and vibrational energy, which will reduce the efficiency of the solar cells. After the excitons dissociate into free charge carriers, they transfer to the respective electrodes (electrons to cathode and holes to anode). The charge carrier transport is affected by the trap states (traps) of the composite films. Traps originate from the structural defects and the impurity of the materials. They provide localised energy minima of variable depth for charge carrier transport, which will reduce the charge carrier mobility.

Bimolecular recombination as a general recombination mechanism depends on the production of a number of free charge carriers, electrons and holes. For the bulk heterojunction photovoltaic devices, the electrons and holes have a significant spatial overlap while transferring to their respective electrodes. So the production of electrons and holes is large and the recombination is significant. The last process is the free charge carrier collection and power generation in the external circuit. It is also crucial to the overall efficiency. It requires two conditions for efficient charge carrier collection that the work function of anode is smaller than the ionisation energy (*IE*) of the donor and the work function of cathode is larger than the electron affinity (*EA*) of the acceptor.

In the bulk heterojunction (P3HT:PCBM) solar cells, where PCBM is short for phenyl-C_{61}-butyric acid methyl ester as shown in figure 8, the donor (P3HT) absorbs the incident light and creates excitons. The band-gap between HOMO and LUMO will determine the wavelength that contributes to the creation of the excitons. For P3HT, the band-gap between HOMO and LUMO is ~2.2 eV. [25] So the P3HT can absorb photons with a wavelength smaller than 650 nm, as shown in figure 8.

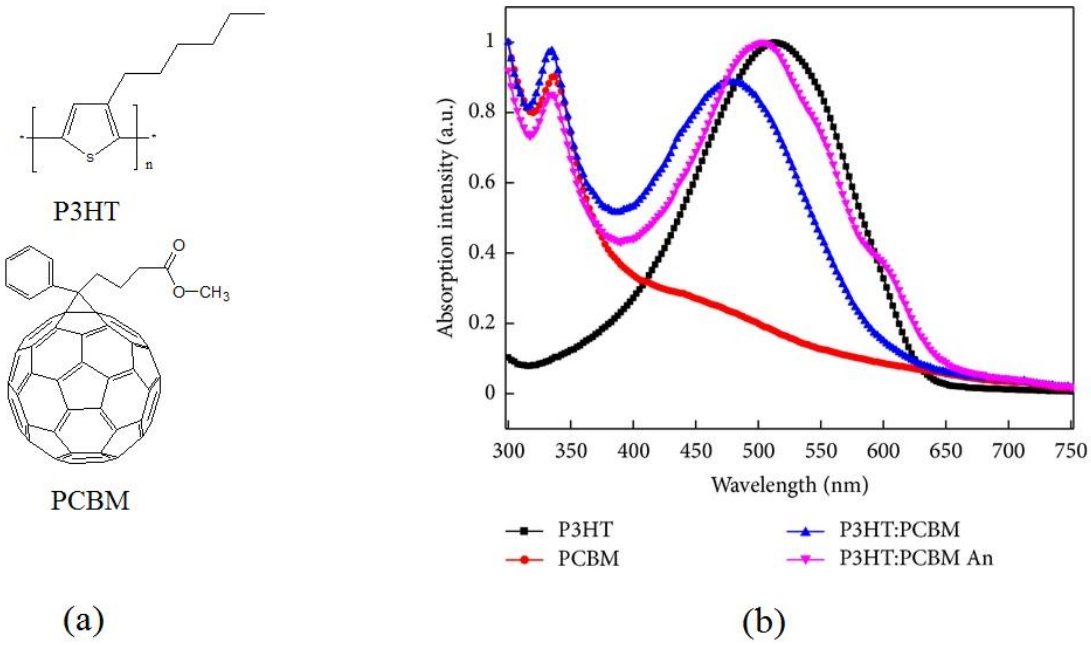

Figure 8: (a) Molecular structure of P3HT and PCBM. (b) Absorption spectra of P3HT film (black squares), PCBM film (red circles), P3HT: PCBM blend (blue up-triangles) and annealed P3HT: PCBM blend (magenta down-triangles). Reproduced from ref. [25]

The key variables of polymer primary structures in P3HT are molecular weight, polydispersity and regioregularity. The efficiency is affected by the molecular weight and regioregularity. Generally, the higher the regioregularity, the higher efficiency the solar cells will be. High regioregular P3HT:PCBM solar cells have a stronger tendency to self-organise within the films, resulting in higher crystallinity and charge carrier mobility. It has also been observed that the increase of P3HT regioregularity leads to a red-shift of absorption and an increase in the absorption coefficient. [26] Some publications concluded that high regioregularity was necessary for achieving highly efficient solar cells. But there were also a few studies that presented different arguments. The high regioregularity was not the crucial reason.

Claire Woo et al. [27] reported that a slightly lower regioregularity could be a better choice for the performance of solar cells. The higher regioregularity

P3HT had a higher degree of crystallinity. It meant a larger extent of phase segregation in the blended films, thus reducing the interfacial area for exciton dissociation and charge carrier transport, leading to lower efficiency. And the slightly lower regioregular P3HT displayed superior thermal stability. Zen et al. [28] also highlighted the effect of polymer molecular weight on the solid-state absorption of light, consistent with the P3HT:PCBM blend films. Samples with molecular weights less than 10,000 g/mol showed weak absorption across the visible spectra and lowered hole mobility, resulting in low efficiency. [29] Blended films with low molecular weight P3HT were proved to have inferior mobility, most likely due to main-chain defects. It was found that the films with low molecular weight fraction could initiate the organisation of crystals, resulting in many smaller crystals. On the other hand, if too high, molecular weights would induce highly entangled polymer networks, leading to no chance for annealing, or requiring a much higher temperature. Claire Woo et al. [27] concluded that the molecular weight for P3HT should be 15000~70000 g/mol.

Another important parameter is the influence of solvent on the efficiency of solar cells. Chlorobenzene is a very good solvent for PCBM based solar cells. First of all, PCBM can be dissolved well in chlorobenzene. [30] The solubility parameter can be described as the attractive strength between the molecules of different materials. The solubility of a polymer increases according to the decrease of the difference between the solubility parameter of the polymer and solvent. The solubility parameters of P3HT and chlorobenzene are comparable, so P3HT will be quite easy to dissolve in chlorobenzene. Good solvents can make a contribution to the morphology of the solar cells in two aspects: it can result in phase segregation length similar to the exciton diffusion length and form more channels to facilitate the charge transport.

The weight ratio of the polymers and fullerene derivatives can also influence the morphology and efficiency. A according to ref. [31-33], 1:1 or 1:0.8 of P3HT to PCBM was found to be optimal. But there were several reports that indicated the ratio to be as low as 1:0.7, [34] or even 1:0.46, [35] which could also show the optimal performance. This is because P3HT and PCBM are both soluble in chlorobenzene or 1,2-dichlorobenzene, as mentioned previously. There is a high degree of interaction between the hexyl side chain of P3HT and the fullerene cages of PCBM, so there is a tendency to get poorly developed morphology that consists of a mixed composite of donor and acceptor, rather than a bicontinuous pathway (P3HT as donor to anode and PCBM as acceptor

to cathode) for charge transport. But initially obtained morphology of P3HT with side chain vibration results in thermodynamically instability. So it is possible to choose some methods to drive the phase segregation of P3HT and PCBM to get good morphology.

Padinger et al. [30] firstly chose thermal annealing to optimise the morphology of the solar cells, and increased the efficiency of the solar cells. Thermal annealing will allow the polymer chains to reorganise and PCBM to diffuse to the composite and reorder. P3HT will crystallise much easier and faster than PCBM. So the fullerene molecules will diffuse into the composite to obtain their aggregation slowly while the thermal annealing is underway. There is a question about the temperature used for thermal annealing. The glass transition temperature (T_g) of polymers is important for deciding the annealing temperature. When the temperature is higher than the T_g, the chains of polymers will move much faster. The reported T_g of P3HT is 110 ^oC. So it is better to choose a temperature higher than T_g such as 130 ^oC or 150 ^oC to anneal P3HT.

Another question which comes up is the length of the annealing process. The time depends on the annealing temperature and devices in different conditions. So the precise details of how the thermal annealing treatment should be applied vary in different results. In general, annealing temperatures between 110 ^oC and 150 ^oC are applied from one minute to two hours. The morphology cannot be optimal with either too short or too long annealing time. If the annealing time is too short, the phase segregation of the active layer is not enough and cannot form an efficient bicontinuous pathway. However, if the time is too long, the phase segregation will be large and will exceed the exciton diffusion length, which results in recombination.

The characteristic of P3HT based devices with OPV structure were investigated and discussed in section 3.

1.1.4 Organic field effect transistors

The field effect transistor (FET) was firstly proposed by J.E. Lilienfeld et al. [36] They proposed that the field effect transistor behaved as a capacitor with a conducting channel between a source and a drain electrode. Applying a

voltage onto the gate electrode would control the amount of charge carriers flowing through the system.

In 1987, Koezuka et al. [37] reported the first organic field effect transistor (OFET) based on polythiophene. Polythiophene, a type of conjugated polymer that was able to conduct charge carriers, eliminated the need to use expensive metal oxide semiconductors. Since then, organic field effect transistors (OFETs) have been of great interest for applications, such as display drivers, identification tags and smart cards, because they have the advantages of low cost, flexibility and light weight. [38-41] Organic semiconductors can be processed at low temperatures compatible with plastic substrates, whereas higher temperatures are required for alternative Si-based FETs. Using solution based methods such as spin-coating, inkjet printing and screen printing, large-area OFET fabrication is successful at low costs. Modification of organic semiconductors can easily tune the transistor characteristics leading to the great perspectives of $OFET_S$ in electronics.

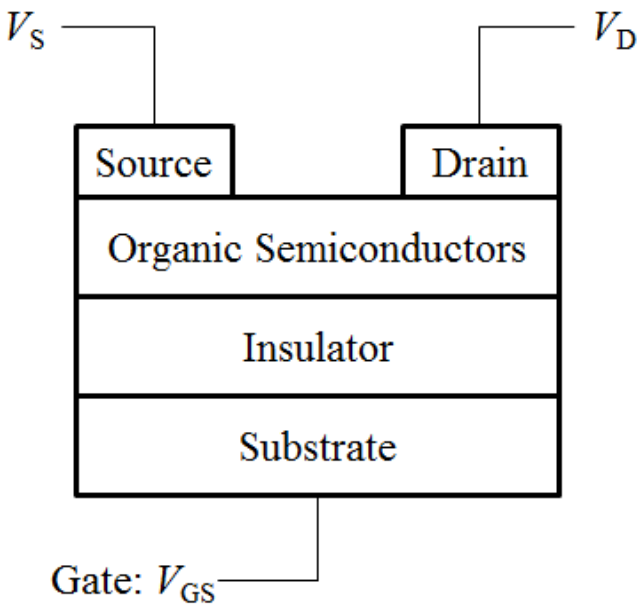

Figure 9: A typical structure of an OFET device.

An OFET usually operates as a capacitor and is composed of two plates. One plate works as a conducting channel between two Ohmic contacts, known as the source and the drain contacts. The other plate works to control the charge induced into the channel called gate. When this capacitor concept is applied to the device design, various devices can be built up based on the difference of the controller. This can be the gate material, the location of the gate with respect to the channel and how the gate is isolated from the channel.

Here a coplanar bottom-gate structure of the organic field transistor (OFET), as shown in figure 9, is taken to explain the mechanism. The charge carriers are injected from the source electrode and drift across the device to the drain electrode. The voltage between source and drain (V_{SD}) can determine the velocity of the carriers. Another voltage, applied between the gate electrode and source electrode, is called the gate voltage (V_{GS}). V_{GS} will tune the Fermi level of the organic semiconductor and determine what type of carrier is induced into the conducting channel (such as electrons in an n-type device, holes in a p-type device, and both electrons and holes in an ambipolar device). There are two ways of characterising the OFET performance. One is to keep the gate voltage fixed and sweep source drain voltage as shown in figure 10(a). Another is to keep the source drain voltage fixed and vary the gate voltage as shown in figure 10(b).

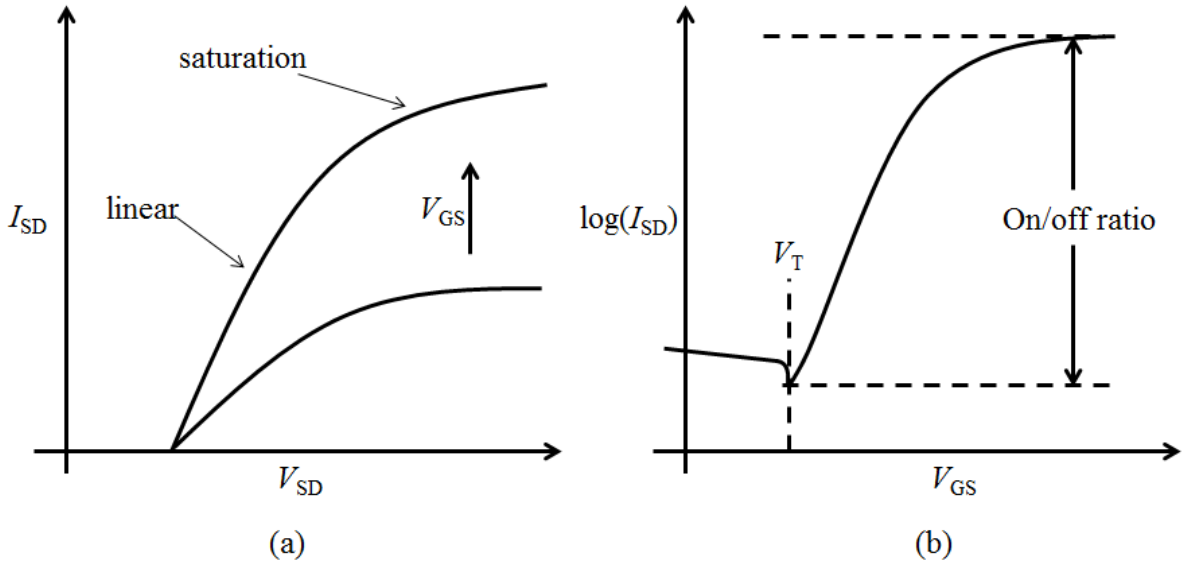

Figure 10: (a) Schematic of an OFET output characteristics for two different values of gate voltage. (b) Schematic of an OFET transfer characteristic.

In figure 10(a), the linear regime is $V_{SD} < (V_{GS}-V_T)$ and the saturation regime is $V_{SD} > (V_{GS}-V_T)$. The threshold voltage (V_T) as shown in figure 10(b) is defined as that at this voltage the current starts to rise and the on/off ratio is defined equal to the saturation current divided by the threshold voltage indicating the ability of the device to shut down.

As reviewed by Horowitz, [42] when the semiconducting film is thinner than the insulating layer, the drain current in the linear and saturation regimes can be given by equations 2 and 3:

$$I_{SD} = \frac{W}{L} \mu C (V_{GS} - V_T) V_{SD} \tag{2}$$

$$I_{SD} = \frac{W}{2L} \mu C (V_{GS} - V_T)^2 \tag{3}$$

Where I_{SD} and V_{SD} are the current and voltage between source and drain, W and L are the width and length of the conducting channel, V_{GS} is the gate voltage perpendicularly applied to the conducting channel, V_T is the threshold voltage at which the current starts to rise, μ is the carrier mobility, and C is the capacitance per unit area of the gate dielectric.

Due to the different electric field distributions, the charge mobility extracted from the OFET I-V curves is generally higher in the saturated regime than that in the linear regime. The mobility can sometimes be gate-voltage dependent, and this observation is often related to the presence of traps due to structural defects. Good transistor performance means high mobility, large on/off ratio and low threshold voltage. In addition, high stability in air is essential for industrial applications. To achieve such performance, the development of new organic semiconductors, as well as the improvement of the device structure, is important.

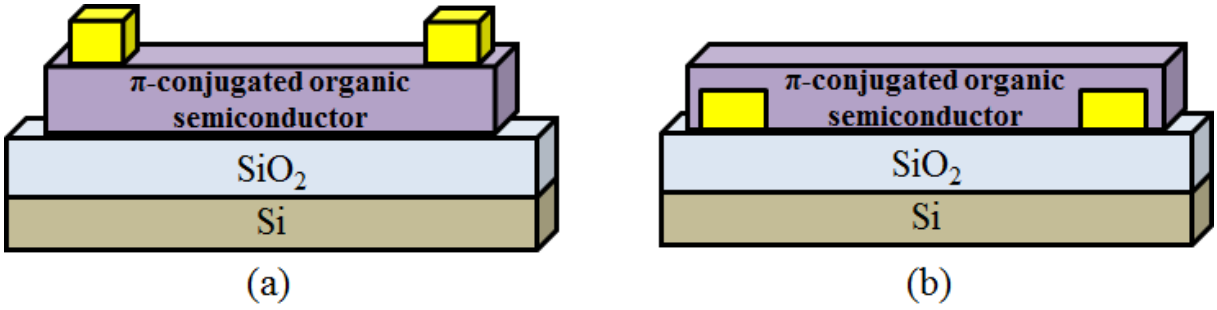

Figure 11: Schematic description of organic transistor based on conductor, insulator and π-conjugated organic material. (a) Top contact configuration and (b) bottom contact configuration.

The π-conjugated organic semiconductors fabricated into OFET are also known as CIπ-FETs [43] and two typical CIπ-FET structures are shown in figure 11. The source/drain electrodes are attached directly to the π-conjugated semiconductor that forms the channel.

In figure 11(a) the source/drain electrodes are on the other side of the π-conjugated material and in figure 11(b) the source/drain electrodes are in direct contact with the insulator (and the channel). These two arrangements are called

bottom contact and top contact configurations respectively.

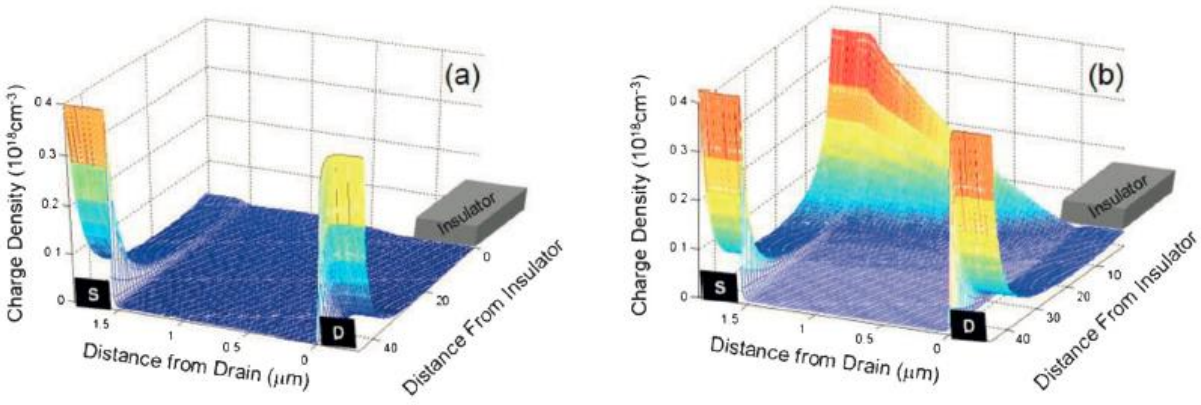

Figure 12: Simulated charge density profile for p-channel top contact OFET V_{DS} = -1. (a) (V_{GS}-V_T) = 0; (b) (V_{GS}-V_T) = -1. Reproduced from ref. [43]

Figure 12 shows the charge density distribution in a top contact OFET for two gate-source bias values. [43] The simulated structure consists of a source-drain distance (L) of 1.5 μm, the π-conjugated layer thickness is ~50 nm, and the insulator is ~100 nm. At zero gate-source bias, figure 12(a), there is no charge density connecting the source and drain, thus the resistance is very high. Once a gate bias exceeding a certain threshold value (V_{GS}) is applied, a high charge density is created next to the insulator interface, as seen in figure 12(b), thus significantly reducing the resistance between the source and drain. As a result, the charges (current) flow through a very thin region called the "channel".

In section 3.3, doping effect of pentacene in P3HT is discussed and both of pentacene and P3HT are popular materials in OFET.

1.2 Charge injection and transport

1.2.1 Charge injection

The basic definition of an interface energy barrier is given as the energy offset between the band-edge (molecular orbital) in the organic semiconductor and the Fermi level of the metal. [44] As shown in figure 13, before contact the two systems are in their original state.

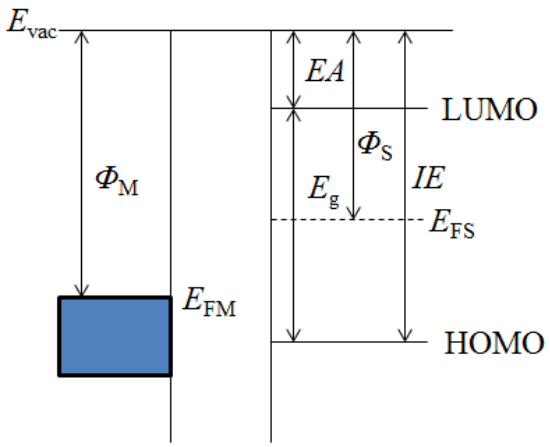

Figure 13: Energy level alignment in a metal/organic semiconductor junction before contact.

The organic semiconductor has a LUMO (conduction band) with electron affinity energy (*EA*) from the vacuum level E_{vac}, and a HOMO (valence band) with ionisation energy (*IE*) from the vacuum level E_{vac}. The Fermi level E_{FS} is located halfway along the band-gap. The work function of the organic semiconductor Φ_S is defined as the distance of the organic semiconductor Fermi level (Φ_{FS}) from the vacuum level, $\Phi_S = (IE + EA)/2$. The energy difference between HOMO and LUMO is the band-gap energy $E_g = IE - EA$. The work function of the metal is Φ_M, which is equal to the distance from the metal Fermi level E_{FM} to the vacuum level, $\Phi_M = E_{FM} - E_{vac}$.

Three different barrier types are shown in figure 14. For an intrinsic organic semiconductor/metal contact in which $\Phi_M = \Phi_S$ as shown in figure 14(a), the Fermi levels of the contact and the organic semiconductor are already lined up, and no charge redistribution is required upon contact. This is called the neutral contact: both the electron and hole contacts have an interfacial concentration of charge equal to their intrinsic free carrier concentration.

For an n-type organic semiconductor/metal contact as shown in figure 14(b) in which the work function of the metal is larger ($\Phi_M > \Phi_S$), electrons are injected from the organic semiconductor into the metal, lowering the organic semiconductor Fermi level (depletion). When the metal and the organic semiconductor are in contact, there is still a space between both surfaces resulting in an electric field in this space due to the exchanged charge. The distance between LUMO is always below the vacuum level E_{vac} with the electron affinity *EA*. The energy barrier Φ_b is required to overcome for electrons injected from the Fermi level of the metal, E_{FM} into the LUMO of the organic semiconductor, and consequently $\Phi_b = \Phi_M - EA$. The distance required for

bending the conduction or valence band towards its original distance from the Fermi level is known as the depletion/accumulation width *W*. Due to the electron depletion, the contact region cannot supply enough charge carriers to the bulk of the organic semiconductor, known as blocking or injection-limited for electrons. At the same time, the contact region contains an excess of holes. As a result, the contact region could supply any charge flow demanded by the bulk of the organic semiconductor, and the contact is called Ohmic or bulk-limited for holes.

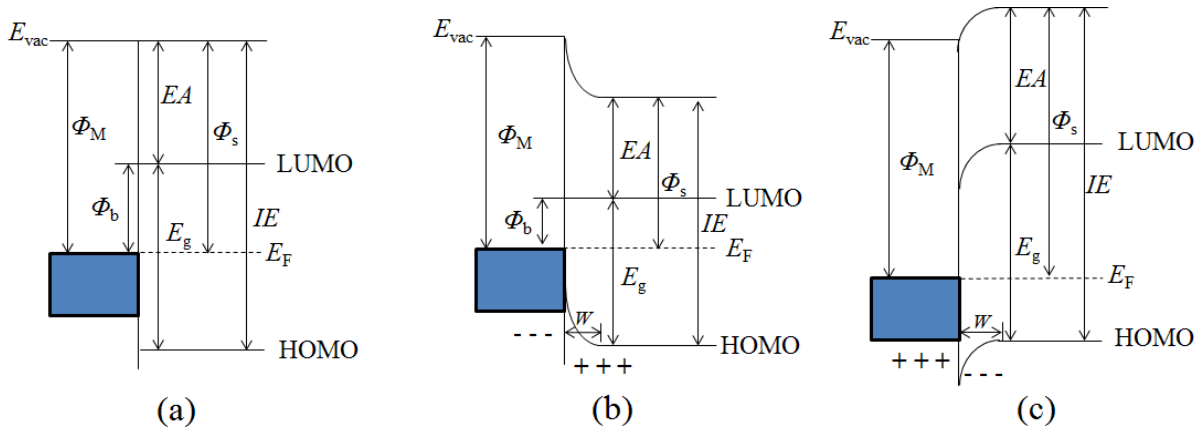

Figure 14: Different barrier types of metal/organic semiconductor contacts. (a) Neutral contact ($\Phi_M = \Phi_S$), (b) n-type organic semiconductor/metal contact ($\Phi_M > \Phi_S$) and (c) p-type organic semiconductor/metal contact ($\Phi_M < \Phi_S$).

For a p-type organic semiconductor/metal contact as shown in figure 14(c) in which the work function of the metal is smaller ($\Phi_M < \Phi_S$), electrons from the metal are injected into the organic semiconductor and lift its Fermi level (accumulation). The situation is reversed: the electrons are accumulated in the organic semiconductor leading to Ohmic contact for electron injection. The hole contact is now injection-limited.

For a contact barrier of Φ_b smaller than 0.3 eV, the current is space charge limited (SCLC) at room temperature, [45] leading to Ohmic contact. When Φ_b is larger than 0.3 eV, the current that the contact can supply is smaller than the SCLC, and at this moment the current is limited by injection. As a result, from the experimental definition, the contact is named as injection-limited. For an injection-limited current (ILC), the amount of injected charge is too small to give a significant bending of the electrostatic potential. Therefore, the electric field in injection-limited devices is constant, and the required voltage *V* for a value of the ILC scaled with the thickness, $J_{ILC} = J\,(V/L)$, which is different from SCLC. For intermediate injection barriers (Φ_b ~0.3 eV at room temperature) there is some build-up of charge in the device, but not enough to

reach the SCLC. The dependence of the current on voltage and thickness are between that of SCLC and ILC. In figure 14(b), an example has been given of the band-bending of an injection-limited device to get some feeling for the relatively small influence of space charge when considerable injection barriers are present.

The band-diagrams in figure 14(a) are sketched for an intrinsic organic semiconductor. However, metal contacts on n-type or p-type organic semiconductors are more common in applications. For such an n-type organic semiconductor as shown in figure 14(b), the depletion width is small compared to the bulk of the organic semiconductor. The depletion width W in that case depends on the doping concentration, and ranges from ~10 nm for heavily doped organic semiconductors ($N_D = 1\times10^{25}$ m^{-3}), to ~100 nm for moderately doped organic semiconductors ($N_D = 1\times10^{23}$ m^{-3}), and wider than 1 μm for lightly doped organic semiconductors ($N_D \leq 1\times10^{21}$ m^{-3}).

In a thermal equilibrium system for a metal/n-type organic semiconductor contact, the quasi-Fermi level E_{Fn} of electrons is constant and the electron (and hole) current is zero:

$$J_n = q\mu_n nF + qD_n \frac{dn}{dx} = 0 \tag{4}$$

Where q is the electron charge, μ_n is the electron mobility, n is the electron concentration, F is the electric field, D_n is diffusion the parameter and x is the distance from the interface to the bulk of organic semiconductor. The electric field F is found from the net charge carrier concentration:

$$\frac{\varepsilon}{e}\frac{dF}{dx} = p - n \tag{5}$$

Where ε is dielectric permeability of the organic semiconductor, e is the electron charge, p is the hole concentration (setting to zero in unipolar device) and n is the electron concentration. The electrostatic potential Φ is given by:

$$\frac{d\Phi}{dx} = F \tag{6}$$

For a thickness of the organic semiconductor (L) larger than the depletion width, $L > W$, and an electron unipolar device (hole concentration is negligible),

the relation between electrostatic potential and distance (and thus the band-bending) can be found analytically in ref. [46].

The boundary condition is the carrier concentration at the contact:

$$n_0 = N_C \exp(-\frac{\Phi_b}{kT}) \tag{7}$$

Where N_C is the carrier effective site density that depends on the site concentration N_{sites}, doping concentration N_D and on their distribution in energy g(E). Φ_b is the contact barrier ($\Phi_b = \Phi_m - EA$), k is the Boltzmann constant and T is the temperature. The zero-field (straight band) at $\Phi = \Phi_S - EA$:

$$\frac{d\Phi}{dx}\Big|_{\Phi_S - EA} = 0 \tag{8}$$

Using the equation 4 to 8 according to ref. [46] results in an expression of distance x as a function of potential Φ:

$$x = \left(\frac{2kT\varepsilon}{e^2 N_C}\right)^{1/2} \exp(\frac{\Phi}{2kT}) \tag{9}$$

The depletion width W can be calculated according to equation 9 using $\Phi = \Phi_s - EA$.

In the experiment of the following section, the hole injection in the p-type organic semiconductor P3HT with oxygen doping (p-type doping) will be introduced and discussed. As shown in figure 15(a), when the doping concentration is higher (larger N_c), according to equation 9, the accumulation width is smaller and at the same time the barrier between metal and HOMO of p-type organic semiconductor is smaller due to the shift of Fermi level. On the other hand (e.g after de-doping), if the doping concentration is low (small N_c) as shown in figure 15(b), the accumulation width will be larger and the barrier will be larger for hole injection.

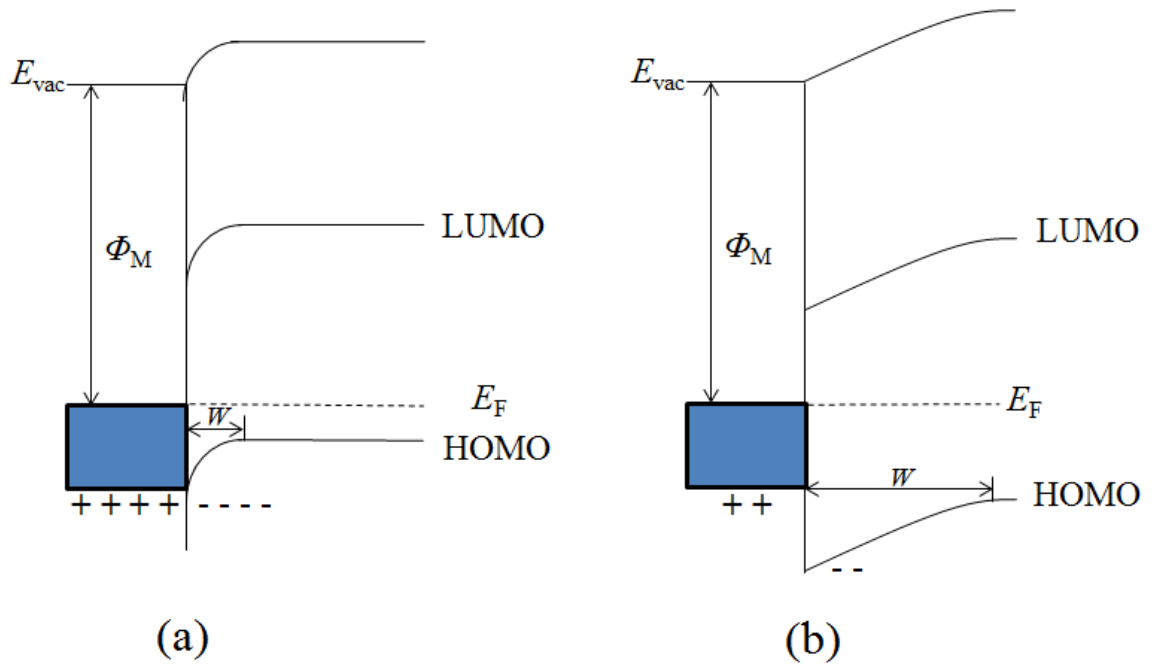

Figure 15: Energy level alignment of a metal/p-type organic semiconductor contact. (a) High doping concentration. (b) Low doping concentration.

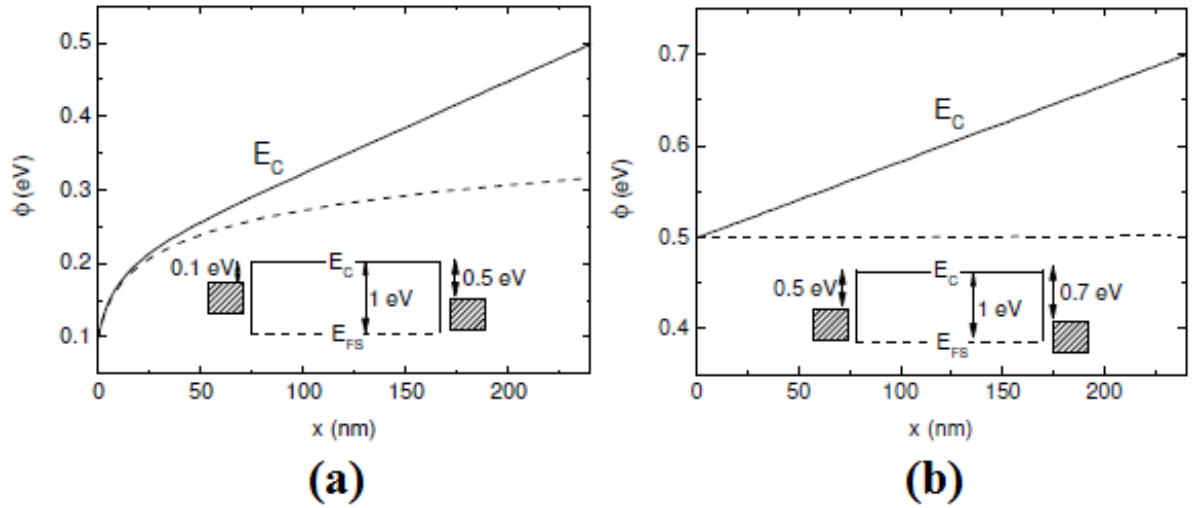

Figure 16: Band diagram of metal/organic semiconductor/metal structure. Φ = 0 eV corresponds to the Fermi level of the system. Two devices are shown: (a) The band offset between metal I and the semiconductor is 0.1 eV, for metal II it is 0.5 eV; (b) The band offset between metal I and the semiconductor is 0.5 eV, for metal II it is 0.7 eV. The solid lines show the numerically calculated band-bending and the dashed lines show the analytically calculated band-bending for (a) a 0.1 eV barrier and (b) a 0.5 eV barrier. Reproduced from ref. [47]

When the device thickness L is smaller than the depletion width W, a numerical program is chosen to calculate the band-bending. [47] The Fermi level of the system, E_F is set to zero. The electrostatic potential is set equal to the LUMO level, $\Phi[0]=E_{FS}[0]-EA$. The electron concentration at the right contact is checked by:

$$n[i_{\max}] = N_C \exp\left(-\frac{\Phi_{b2}}{kT}\right) \qquad (10)$$

Φ_{b2} is the barrier for the right contact. The calculated band-bending is shown in figure 16 for a conjugated polymer with a band-gap E_g = 2 eV and a device thickness of L = 240 nm, at room temperature.

In figure 16, E_c is the conduction band equivalent to the LUMO in an organic semiconductor. Two situations are shown: a device with contact barriers of Φ_{b1} = 0.1 eV and Φ_{b2} = 0.5 eV for the bottom and top metal contact, and a device with contact barriers Φ_{b1} = 0.5 eV and Φ_{b2} = 0.7 eV. In both cases, the metal contacts have a Fermi level above that of the organic semiconductor and will inject charges into the organic semiconductor to shift its Fermi level, resulting in electron accumulation zones at both contacts. The largest effect, the tilting of the band, is caused by the Fermi-alignment between the two metals, which bends the organic semiconductor potential between them uniformly. This is called the built-in field and is an important parameter for devices with a different bottom and top contact, in addition to which, as a rule of a thumb, the built-in potential $V_{bi} = \Phi_{M1} - \Phi_{M2}$. Furthermore, close to the 0.1 eV contact, the band-bending due to excess electrons from the metal is still quite strong. It demonstrates the intention of the organic semiconductor to re-establish the original situation away from the contact, with $E_C - E_F$ = 1.0 eV. However, this situation is nowhere near reached because the device length is too small. The depletion width W for this organic semiconductor amounts to ~1 m. The numerical program is compared with the analytic expression for the limit $L > W$. It is close to the 0.1 eV contact, the band-bending in the device, although $L << W$, is in agreement with the analytic expression according to equation 9.

There is no band-bending in the device with two large contact barriers as shown in figure 16(b). The potential Φ change as a function of x in this device is completely dominated by the contacts. This can be interpreted as follows: the charge concentration in the organic semiconductor is too low to cause any reasonable band-bending. The only organic charge is present at the metal-organic semiconductor interface, and causes a constant electric field inside the organic semiconductor. As a result, for such a device, space charge effects are negligible and it will be observed from experimentation that the device is injection-limited.

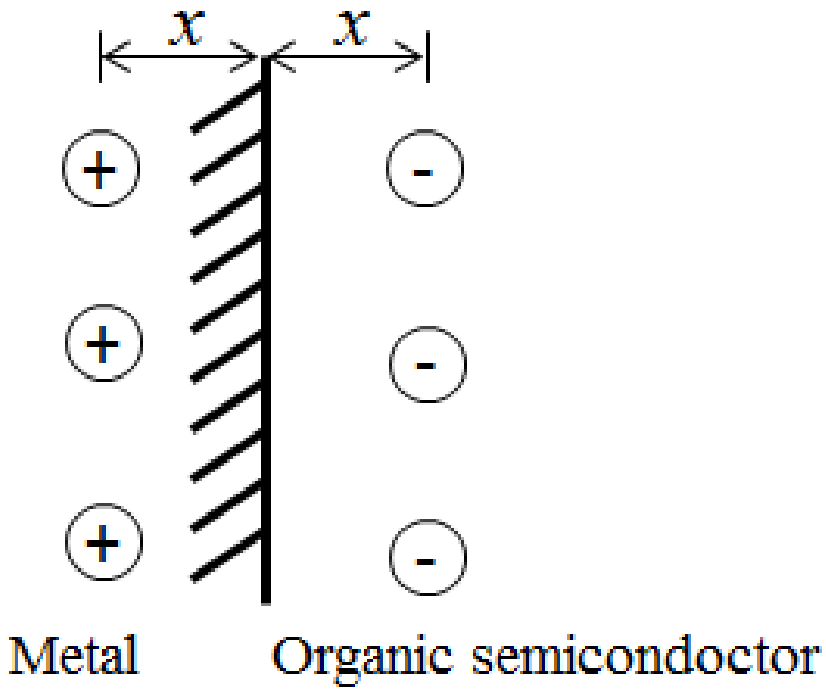

Figure 17: Screening effect at the metal/organic semiconductor interface.

As shown in figure 17 electrons leaving a metal will induce positive charge densities at the metal surface to screen their electrostatic field. This screening effect can be represented by an image charge of the electron at the same distance in the metal. The force f_{screen} between the electron and the image charge is shown in equation 11:

$$f_{screen} = \frac{-e^2}{4\pi(2x)^2\varepsilon} = \frac{-e^2}{16\pi\varepsilon x^2} \tag{11}$$

Where x is the distance of electron-metal interface, and ε is the dielectric permeability of the organic semiconductor, $\varepsilon = \varepsilon_0\varepsilon_r$. As a result, apart from the work done by the electron in the electric field, $U = eFx$, F is the electric field there is an additional amount of work done $U(x) = -\int_x Fdx = e^2/16\pi\varepsilon x$. The resulting potential energy of the electron (or hole for the case of hole injection) as measured from the metal Fermi level is:

$$\frac{U(x)}{e} = \Phi_b - \frac{e}{16\pi\varepsilon x} - xF \tag{12}$$

As shown in figure 18, the interplay between the electrostatic potential xF and the image potential causes a maximum electrostatic potential height given by:

$$\frac{U_{\max}}{e} = \Phi_b - \Delta\Phi = \Phi_b - \sqrt{\frac{eF}{4\pi\varepsilon}} \tag{13}$$

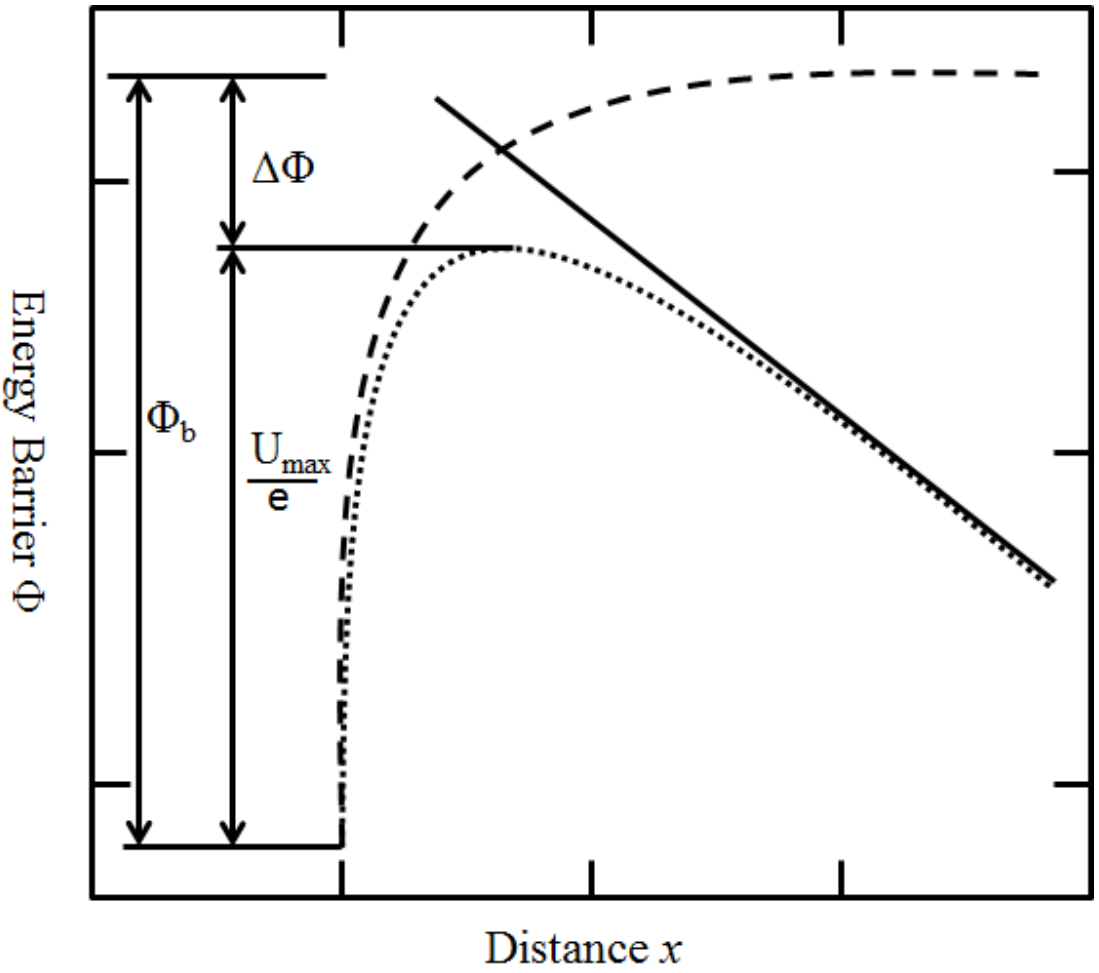

Figure 18: Band diagram at a metal/organic semiconductor contact. The dotted line represents the electrostatic potential including two components: the applied field (solid line) and image force (dashed line).

According to equation 13 at an electric field F, the energy barrier is lower than the original Φ_b. This is called the Schottky effect or image force / barrier lowering. [48-49] Figure 18 shows the two components of the electrostatic potential: the band-tilt by the applied field, and the image force potential. Also shown in figure 18 is the lowering of the barrier.

When an organic semiconductor of large band gap is sandwiched between two electrodes, the charge injection under low field from electrodes is described by thermionic emission: [48]

$$J = A \times T^2 \exp\left[-\frac{(\Phi_b - \Phi)}{kT}\right] \tag{14}$$

Where A is the effective Richardson constant, $A=(1-r_{av})A_0$ in which r_{av} is the factor due to the wave-like nature of electrons, A_0 is the universal constant which equals to 1.2×10^6 $Am^{-2}K^{-2}$, k is the Boltzmann constant, T is the temperature and Φ_b is the effective barrier due to the offset in energy levels at the interface.

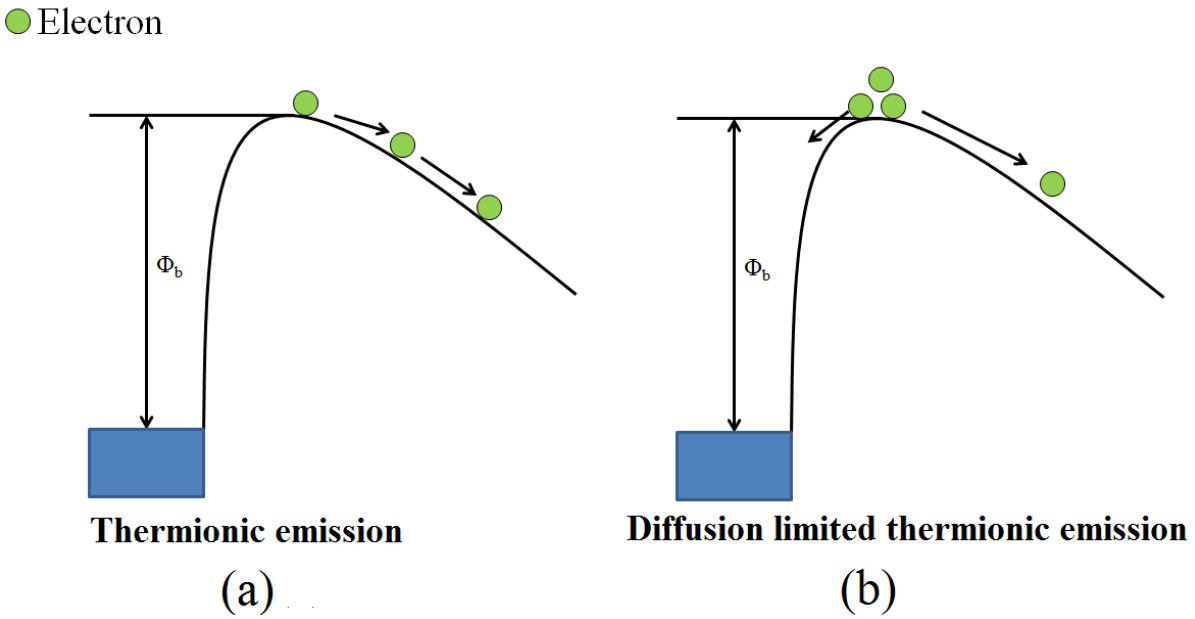

Figure 19: Schematic representation of two important classical injection models: (a) high mobility organic semiconductors; (b) low mobility organic semiconductors.

It has been pointed out that the thermionic emission model is not applicable to low mobility organic semiconductors. [50] For low mobility organic semiconductors, a backflow will occur due to the large concentration of charge carriers that accumulate at the interface. In fact, for low mobility organic semiconductors, the velocity of the charge carriers in the bulk of the organic semiconductor is smaller than that in the interfacial area, [48] which results in a stack of carriers at the interface, as depicted in figure 19. The velocity of charge carriers in the bulk of the material is proportional to the mobility. As a result, the diffusion-limited injection current is predicted by: [50]

$$J = qN_V \mu(T) F \exp\left[-\frac{(\Phi_b - \Delta\Phi)}{kT}\right] \tag{15}$$

Where N_V is the effective density of states in the organic semiconductor, and F is the applied electric field. The same result has also been obtained in the case of insulators at low or moderate fields, where space-charge effects are unimportant. [51] It should be noted that in both thermionic emission (high

mobility) and diffusion limited injection (low mobility), the barrier height Φ_b plays a dominant role in the injection-limited current (ILC).

For conjugated polymers like PPV, the hole mobility was measured to be 5 $\times 10^{-7}$ cm^2/Vs, [52] and the injection process was expected to be completely diffusion limited. For conjugated polymers like P3HT, the hole mobility was measured to be ~10^{-4} cm^2/Vs, [53] the injection process is expected to include thermionic emission because of relatively high mobility.

Under high field, tunnelling will dominate the charge injection. Fowler-Nordheim (FN) model [54] (schematic as shown in figure 20) is used to describe the tunnelling process:

$$J_{FN}(F) = \frac{q^3(\beta F)^2}{16\pi^2 \hbar \times t^2(y)\Phi_b} \exp\left[-4v(y)\frac{\sqrt{2m_{eff}\Phi_b^{\,3}}}{3\hbar e\beta F}\right] \tag{16}$$

Where $J_{FN}(F)$ is the electric field F dependent current density due to FN tunnelling, $\hbar$ is the Plank constant, y is the Nordheim parameter $y = \sqrt{\frac{e^3 F}{4\pi\varepsilon_0 \Phi_b^{\,2}}}$, $t(y)$ is a slowly varying function (special field emission elliptic function) that can be expressed in terms of $v(y)$ and dv/dy, $v(y)$ is a correction function due to image force approximation, Φ_b is the injection barrier, m_{eff} is the effective mass of the carrier inside the dielectric, β is the field enhancement factor and e is the electron charge.

$$t(y) = v(y) - \frac{2}{3} y \frac{dv}{dy} \tag{17}$$

$$v(y) = 1 - y^2 + \frac{1}{3} y^2 \ln y \tag{18}$$

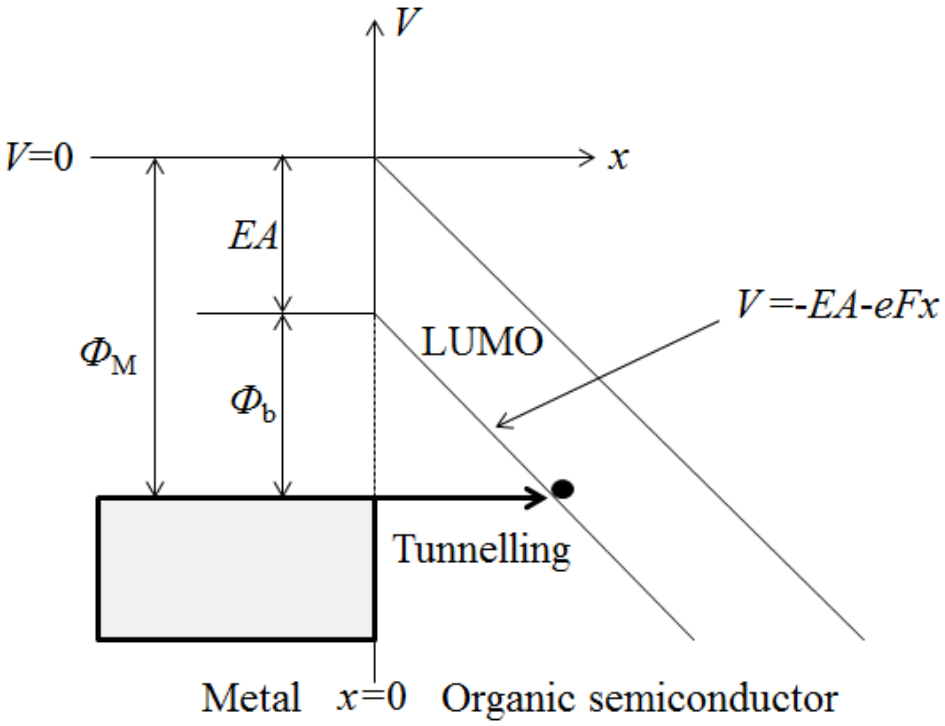

Figure 20: Schematic of tunnelling from metal to organic semiconductor.

Figure 20 describes the potential V as a function of the distance x. The potential for the vacuum level is set to be zero. Electrons can tunnel into the LUMO of organic semiconductor from the metal. The parameter Φ_b is used to describe the effective barrier when the distance x is set to be zero.

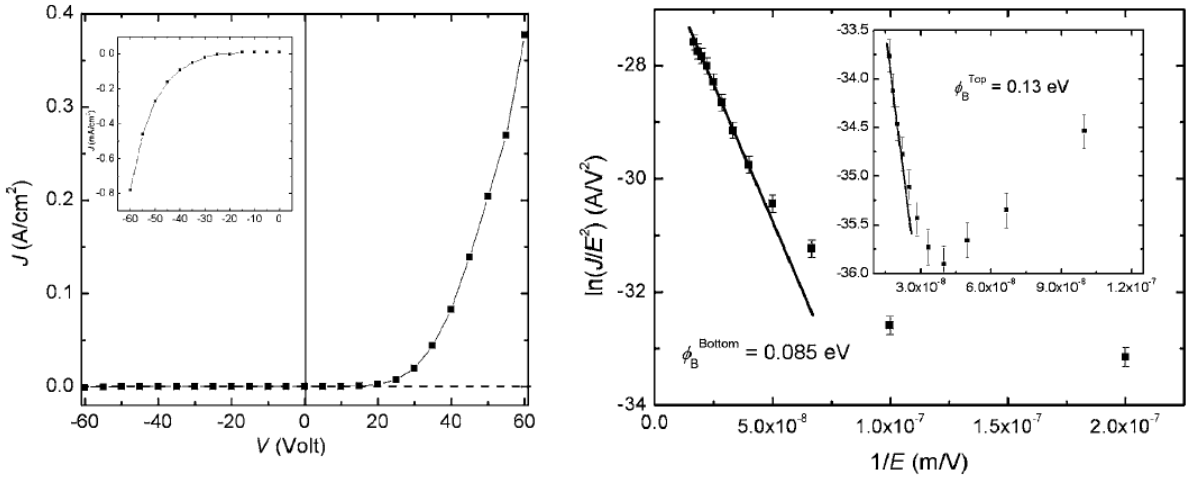

(a) (b)

Figure 21: (a) J-V characteristics of the Au (bottom)/P3HT/Au (top) sandwich cell. The inset shows reverse data on an expanded scale. (b) FN plot for forward biased data. The inset shows an identical plot for the reverse biased data. The author uses E to describe the electric field as F in the thesis. Reproduced from ref. [55]

Observation of straight line fits of $J(V)$ data in FN plots [$\ln(J/F^2)$ versus $1/F$] is usually taken as confirmation that the phenomenon of FN tunnelling of charge carriers dominates the conduction mechanisms of a given single carrier device. Figure 21(b) is an example of FN plots for Au/P3HT/Au data in forward and reverse bias. [55]

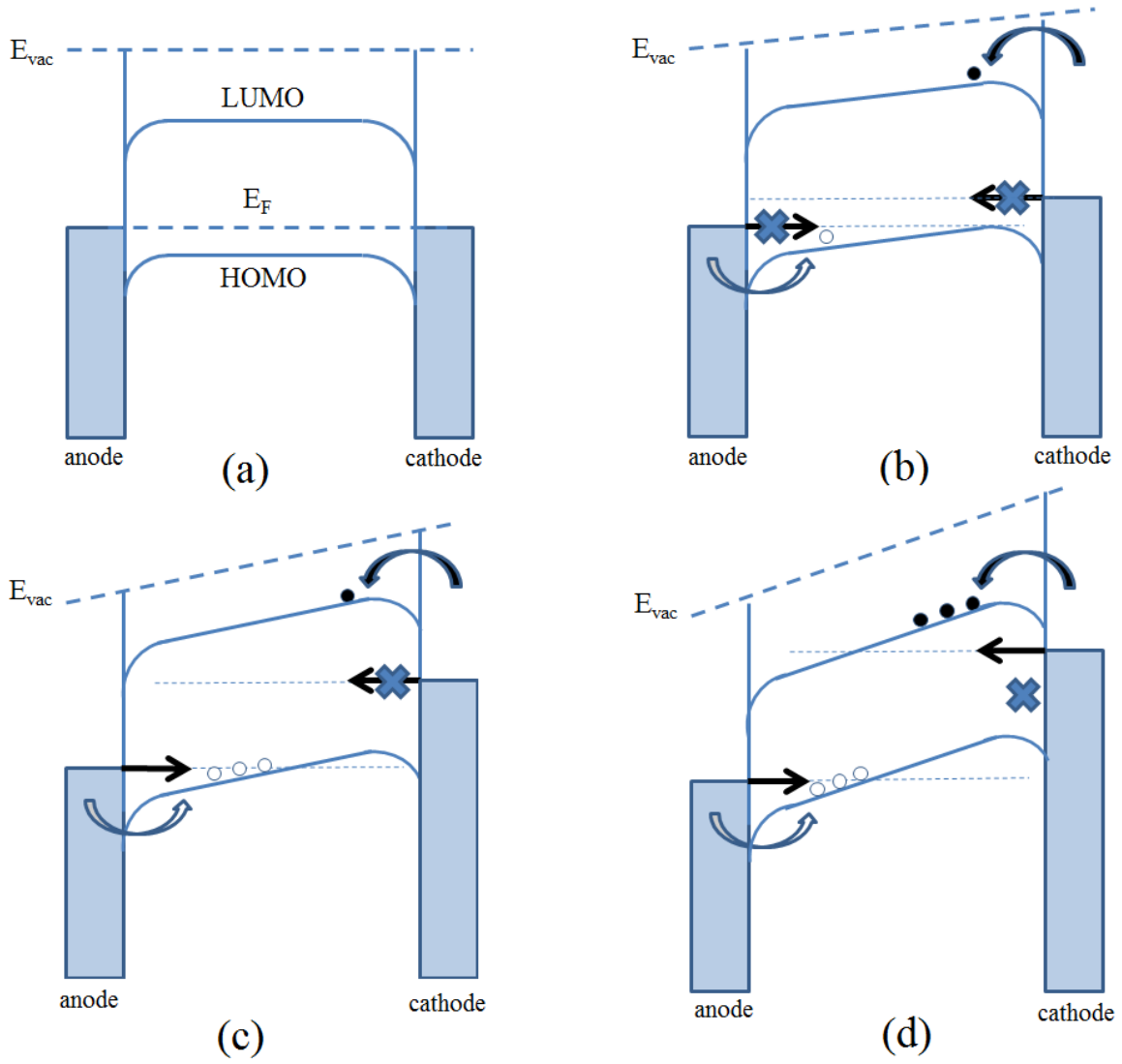

Figure 22: (a) Typical energy diagram of a metal/p-type organic semiconductor/metal device with symmetric electrodes in short circuit. The hole injection barrier is smaller than the electron injection barrier. (b) At low fields, both electrons and holes can be injected by thermionic emission. The effective tunnelling distance is the same as the film thickness and tunnelling is negligible. (c) At intermediate fields, the effective thickness for hole tunnelling is smaller than the device thickness and holes are injected by Fowler-Nordheim tunnelling (hole-only device); (d) At high fields, tunnelling takes place from both electrodes leading to ambipolar conduction.

Figure 22 shows that in a p-type diode with symmetric electrodes at low fields, only thermionic emission dominates charge injection. At intermediate fields both thermionic emission and tunnelling will appear. At high fields,

tunnelling of charge carriers from the electrode through a triangular barrier into unoccupied states of organic semiconductor will dominate the charge carrier injection. The band-bending will decrease the barrier for tunnelling.

Above all, both thermionic emission and FN tunnelling mechanisms can be used to describe charge injection in metal/organic semiconductor/metal based devices. Controlling the drive conditions will make it possible to tune the domination mechanism for charge injection. In the research, an Au/P3HT/Al diode is chosen in section 3.1 to discuss the injection mechanism change under different drive conditions.

1.2.2 Charge transport

In classic semiconductors, free, delocalized electrons (or holes) travel in extended bands. The charge carriers are only hindered by lattice vibrations (phonons) whose number increases with temperature and makes charge carrier mobility lower with increasing temperature. The bands are either completely filled or completely empty and separated by energy gaps. This makes them intrinsically unconducive, and either charge carriers have to be excited thermally or with light into the empty bands to make them conductive, or dopants have to be brought into the material and provide additional levels in the gap.

The situation in organic semiconductors is very different. Molecules are only weakly bound to each other (mainly van der Waals Forces), and no extended band structure can form. The charge carriers are localized to their sites and have to “hop” from site to site as shown in figure 23 to enable charge transport. Unlike the case of band transport, this “hopping” is aided by phonons, which causes mobility to increase with temperature. To describe these physical processes, at first existing models from amorphous inorganic semiconductors, like hydrogenated amorphous silicon were used and transferred to the organic systems. Also, most models which exist nowadays are based on such charge transport descriptions. Thus in the last decades, starting from different approaches, many models for charge transport in organic semiconductors were developed, resulting in different predictions of the charge carrier mobility. In the publications that present the models, all of them were checked on experimental data for the mobility variation with temperature, and were proven

to hold true for the respective material system tested. In many models, the mobility was shown to depend not only on temperature, but also parameters like electric field strength, charge carrier density, and related to this on parameters like ordering and the shape and width of the density of states (DoS).

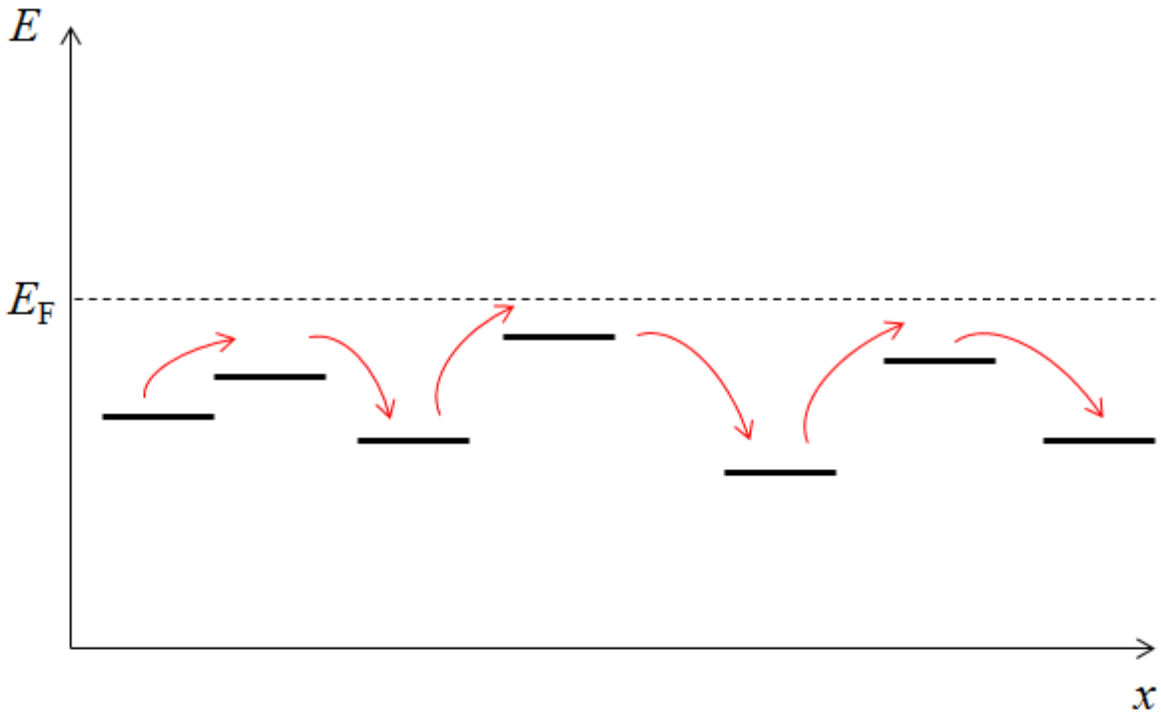

Figure 23**:** Schematic of hole polaron hopping transport in a one-dimensional system. E_F represents the Fermi level of the system.

Abundant research has been carried out on the mobility parameters of π-conjugated polymers like PPV, P3HT and their derivatives. For the derivative of PPV like OC_1C_{10}-PPV, the research had especially focused on hole mobility. [56-58] In order to investigate hole mobility, devices were fabricated with an electron blocking top contact. In this case, only holes from the bottom contact would be injected, and such a structure was normally called unipolar (hole only) device. At first a measurement of the hole current in OC_1C_{10}-PPV gave a quadratic relation between current and voltage at low biases, indicative of a space charge limited current. [56] At higher biases, the current started to increase more rapidly with voltage, implying an increase of the mobility. Varying the temperature, it was found that the mobility was also strongly temperature dependent and, as a result, a phenomenological relationship for mobility is: [58]

$$\mu_p(F,T) = \mu_0(T)\exp(\alpha\sqrt{F}) = \mu_* \exp(-\frac{\Delta}{kT})\exp(\alpha\sqrt{F}) \qquad (19)$$

Where $\mu_0(T)$ is the zero field mobility, α is the coefficient which is material dependent and comparable to the Pool-Frankel effect, [59] μ_* is the material mobility dependent prefactor, k is the Boltzmann constant, Δ is the activation energy.

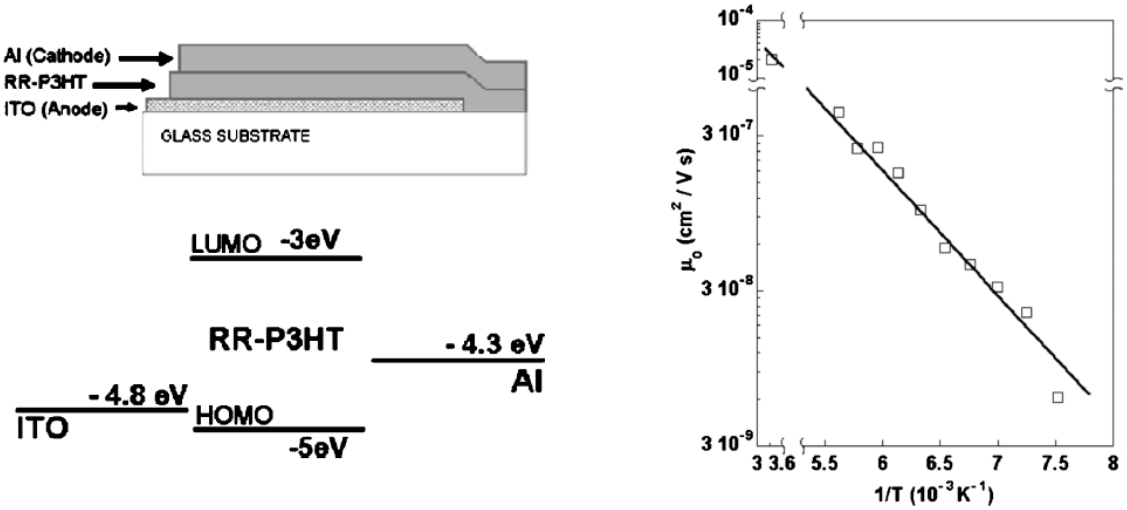

Figure 24: (a) Device structure and band energy level diagram of ITO/P3HT/Al. (b) Hole mobility (μ) as a function of reciprocal temperature (1/T). Reproduced from ref. [60]

The temperature dependence of mobility has also been reported in P3HT based devices. Figure 24(a) device structure and band energy level in an ITO/P3HT/Al device. The temperature dependence of the zero-field mobility μ_0 is shown in figure 24(b). For the calculated $\mu_0(T)$, the activation energy Δ was found to be 160 meV. [60]

The stretched exponential form of mobility as equation 19 is first observed for poly(N-vinyl carbazole) (PVK) by Gill in 1972. [61] Numerous experimental studies on molecularly doped polymers, pendant group polymers, and amorphous molecular glasses revealed a similar behaviour. [62-64] Charge transport in disordered organic semiconductors is thought to proceed by means of hopping in an energetically disordered environment. The hopping rate for an upward jump is given by the attempt frequency, multiplied by the probability for a carrier to get a certain amount of energy E, given by the Boltzmann distribution $exp(-E_a/kT)$, and multiplied by the probability to jump over a certain distance x, with the tunnelling factor $exp(-2\gamma x)$ given by:

$$\nu = \nu_0 \exp(-2\gamma x) \exp(-\frac{E}{kT}) \tag{20}$$

For a jump downward, it is considered that the charge carrier can always create a phonon to lose its energy. This is thought to be a reasonable assumption in view of the rich phonon spectra of conjugated polymer. [65] Therefore, the downward jump rate is given by:

$$\nu = \nu_0 \exp(-2\gamma x) \tag{21}$$

This combined in the Miller-Abraham rate for carrier hopping: [66]

$$\nu_{ij} = \begin{cases} \nu_0 \exp(-2\gamma x) \exp(-\frac{E_j - E_i}{kT}) & E_j - E_i \geq 0 \\ \nu_0 \exp(-2\gamma x) & E_j - E_i < 0 \end{cases} \tag{22}$$

In equation 22, ν_0 is the phonon vibration frequency, x is distance between site i and site j, γ is the inverse localization radius, E_i and E_j are the energy of site i and site j.

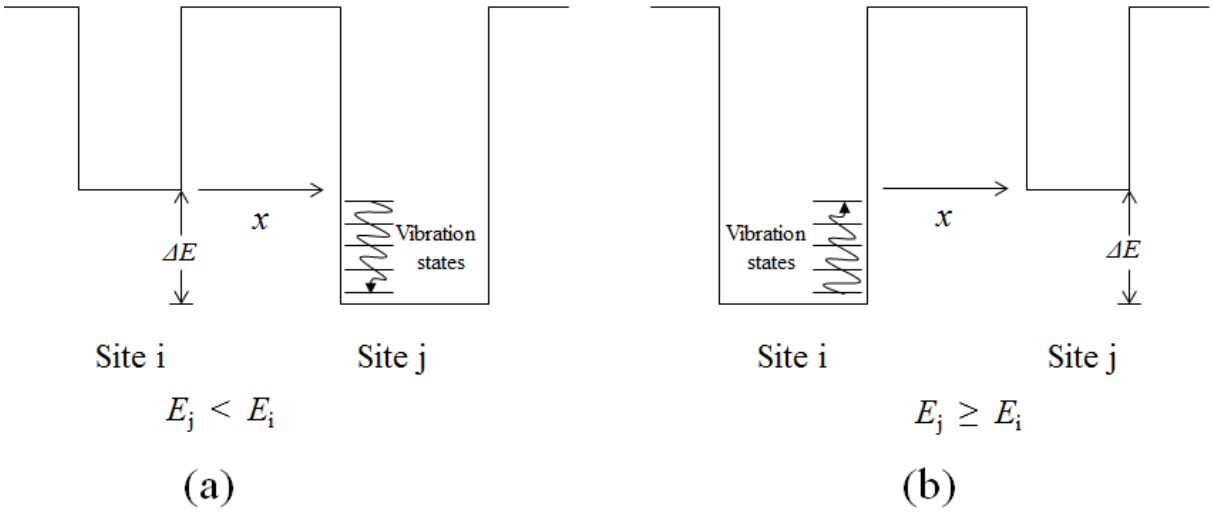

Figure 25: Schematic of Miller-Abraham model for hopping process. (a) $\Delta E=E_j-E_i$ <0. (b) $\Delta E=E_j-E_i$ $\geqslant$0.

The schematic in figure 25 describes the hopping process. Bässler et al. [65] performed numerical simulations of charge transport in a regular array of hopping sites with a Gaussian distribution of site energies $g(E)$ as shown in equation 23:

$$g(E) = \frac{N_{sites}}{\sigma\sqrt{2\pi}} \exp\left[-\left(\frac{E - E_0}{\sqrt{2}\sigma} \right)^2 \right] \tag{23}$$

Where N_{sites} is the site density, σ is the energy width, and E_0 is the centre of the Gaussian distribution.

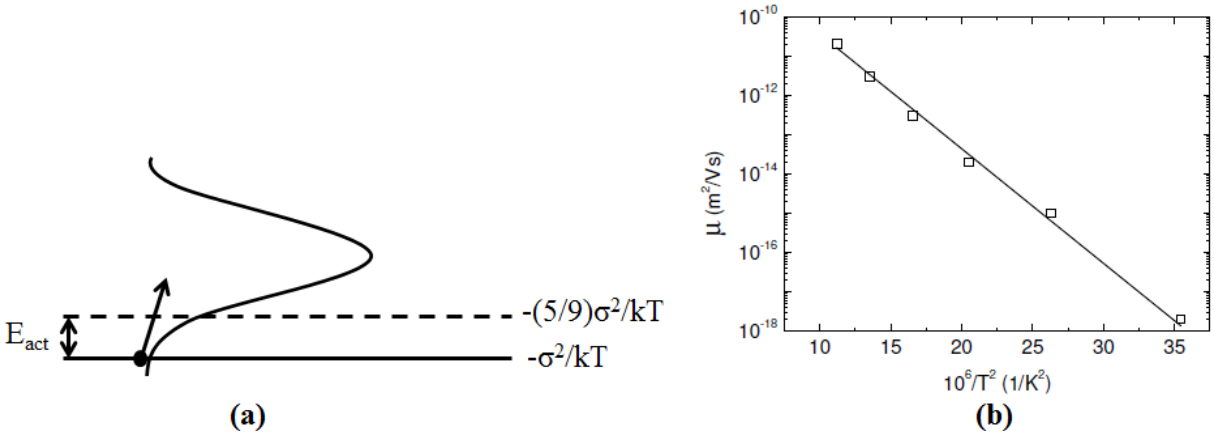

Figure 26: (a) Gaussian Density of States, where vertical axis corresponds with energy, horizontal axis reflects the site density. (b) The zero-field mobility of OC_1C_{10}-PPV found from the experiment is plotted as a function of T^{-2}. Reproduced from ref. [56]

The density of states (DoS) reflects the energetic spread of transport sites, as demonstrated in figure 26(a). The transport sites are conjugated chain segments in an environment of broken up conjugation due to twisting of the chain, and the energetic disorder arises from fluctuations in conjugation lengths. Positional disorder is included by a distribution of the charge localisation radius. In the Gaussian disorder model (GDM), the following functional dependence of μ is proposed by equation 24: [65]

$$\mu_{GDM} = \begin{cases} \mu_\infty \exp\left[-\left(\frac{2\sigma}{3kT} \right) + C\sqrt{F}\left(\frac{\sigma}{k\,T} \right)^2 - \Sigma^2 \right] & \Sigma \geq 1.5 \\ \mu_\infty \exp\left[-\left(\frac{2\sigma}{3kT} \right) + C\sqrt{F}\left(\frac{\sigma}{k\,T} \right)^2 - 2.25^2 \right] & \Sigma < 1.5 \end{cases} \tag{24}$$

Where μ_∞ is the mobility in the limit $T \to \infty$, $F \to 0$ and C is a constant (depending on the site spacing). F is applied electric field, T is temperature, k_B is the Boltzmann constant, Σ is positional disorder and σ is energetic disorder.

Their simulations revealed that at low electric field the carriers relaxed to an equilibrium level $-\sigma^2/kT$. Furthermore, charge carriers that contributed to the

transport would search for the fastest pathway. In the tail of the DoS few sites were available for hopping, and therefore the carriers would be activated to higher energy levels where the site density was high enough. The actual energy level, to which they jumped on average, was a trade-off between the number of available sites and the activation energy. It was found that the energy level to which most carriers were activated was independent from the starting energy of the charge carriers, and was therefore called the transport level. [67-68] The transport level was a well-known concept for amorphous organic semiconductors, concerning hopping motion in the band tail. [69]

The *T*-dependence of the zero-field mobility can be related to the thermal activation of a charge carrier in the Gaussian DoS: if all carriers are located at the equilibrium energy level $-\sigma^2/kT$, and a transport level exists exactly at the centre of the DoS, the zero-field mobility will follow $\mu_0 \sim \exp(-\sigma^2/kT)$. The Monte Carlo studies indicates that this *T*-dependence is actually recovered, but with a prefactor in the exponent that is less than unity, $E_{act} = -(4/9)\sigma^2/kT$. The transport in the Gaussian DoS can be thought of as governed by two energy levels: the equilibrium level and a transport level E_{tr} located at $-(5/9)\sigma^2/kT$, as shown in figure 26.

More recent calculations carried out by Arkhipov [70] showed that, although most charge carriers were located around $-\sigma^2/kT$, activation from this level was very unsuccessful, and most carriers immediately fell back. The largest contribution to the transport comes from carriers that were located around $-(1/2)\sigma^2/kT$, whereas on average they jumped to the centre of the Gaussian. With the activation energy of $-(4/9)\sigma^2/kT$, this left $-(1/18)\sigma^2/kT$ for the transport level, as shown in figure 27.

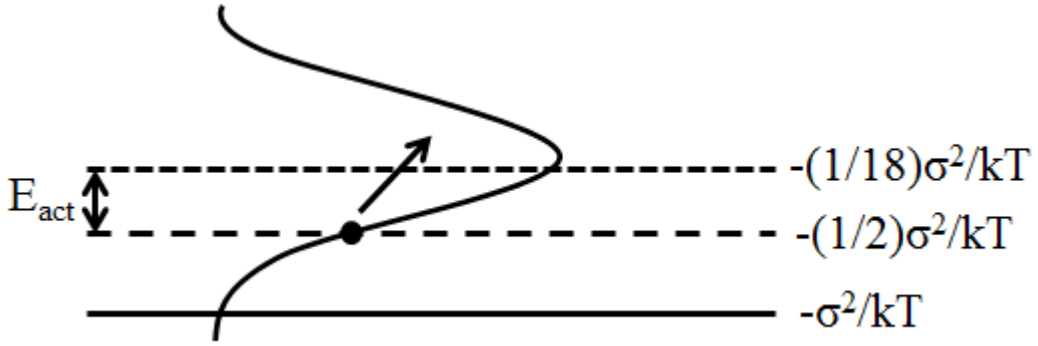

Figure 27: Gaussian Density of States. The start level for a jump is now different from the equilibrium level, $E_{start} = -(1/2)\sigma^2/kT$. The transport level amounts to $E_{tr} = -(1\ /18)\sigma^2/kT$ in this case.

Although there is a difference in the actual effective energy levels involved in the activation process (figure 26 and 27), it is clear that the mobility is strongly temperature dependent. The activation energy amounts to $E_{act} = -4\sigma^2/9kT$. It is shown in figure 26(b) that the T-dependence of the zero-field mobility of OC_1C_{10}-PPV is in agreement with the GDM. From this a disorder of σ = 0.11 eV is obtained. Due to the limited temperature regime, it is hard to distinguish between an $\ln\mu \sim 1/T$ and $\ln\mu \sim 1/T^2$ behaviour. However, the most important message here is that the strong T-dependence of the measured mobility reveals that charge carriers in organic semiconductors are hopping in an energetically disordered medium.

It is energetically favourable for a material to deform its lattice around an excess electron/hole, which can be imagined as a cloud of phonons around the charge carrier. Such an electron/hole surrounded by a phonon cloud is known as a polaron. A transition rate for polarons is given by: [71]

$$\nu = \nu_{matrix} \exp\left[-\frac{E_a}{kT}\right] = \nu_{matrix} \exp\left[-\frac{(\lambda - eaF)^2}{4\lambda kT}\right] \qquad (25)$$

Where a is the parameter related to inter-site distance, e is the charge, F is the electric field, λ is the energy for the charge carrier to jump to its new position, ν_{matrix} contains the matrix-element $|J|$ for the transition: [71]

$$\nu_{matrix} = \frac{|J|^2}{\hbar}\sqrt{\frac{\pi}{\lambda kT}} \qquad (26)$$

Where E_a is total the activation energy, k is the Boltzmann constant, T is the temperature and $\hbar$ is the Planck constant.

Marcus developed a theory for chemical reactions in solvents involving charge transfer. [71] Solvents were more or less polar and a jump by a charge carrier from a donor to an acceptor involved a change of the energy of the system (stronger for more polar solvents). If the system was frozen so that the solvent dipoles could not rearrange, it would cost the system a lot of energy to transfer the charge carrier. However, the system would rearrange itself in order to minimise the energy for the charge transfer. It was thought that the principle of rearrangement could be transferred to the charge transfer in solids, [72] where the rearrangement was governed by the vibrational relaxation.

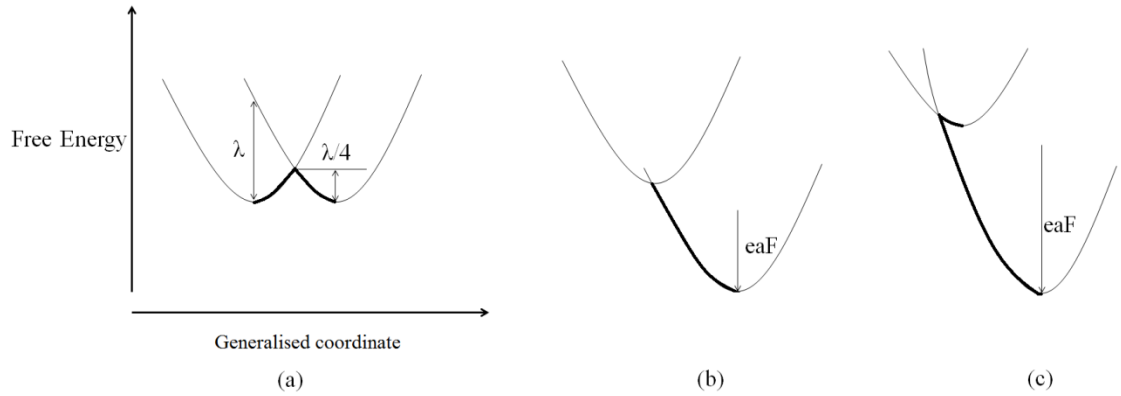

Figure 28: Schematic picture of polaron hopping, where vertical axis corresponds to the free energy and the horizontal axis corresponds to the reaction coordinate. (a) No electric field; (b) and (c) under electric field F.

Figure 28 graphically explains what Marcus [71] meant for polarons in conjugated polymers. The energy provided the gain in potential energy of the system when there was no rearrangement (no phonon cloud) upon moving the charge carrier. No rearrangement corresponded to an equal reaction coordinate before and after the charge transfer. This meant the charge carrier had to be activated by an amount λ in order to jump to its new position. However, Gerhard et al. [73] pointed out that it was energetically favourable when the system reorganised itself when the charge carrier moved.

The accompanying activation energy reduced to $\lambda/4$. For an applied field, the activation included the difference in free energy from start (E_i) and destination site (E_j), $E_a = (E_j - E_i + \lambda)^2/(4\lambda)$. This activation energy was used in the transition rate in equation 25. The destination site had a minimum free energy which was lower by $E_j - E_i = -eaF$. Using the transfer rate (equation 25), an analytical expression for the mobility could be derived. It consisted of a term for the forward motion, governed by $\exp[(\lambda - eaF)^2/4\lambda kT]$, and a term for backward motion, where the transition rate was given by $\exp[(\lambda + eaF)^2/4\lambda kT]$. The result is shown in equation 27:

$$\mu = \mu_0 \exp\left[-\frac{\lambda}{4kT} - \frac{(eaF)^2}{4\lambda kT}\right]\frac{\sin(eaF/2kT)}{eaF/2kT} \qquad (27)$$

In figure 28(a), the electric field is zero, and the resulting charge transfer rate corresponds with the zero-field activation. It was observed that the start site would reorganise itself until its free energy crossed the free energy curve of the destination site (first half of the thick line). This was a resonant state. The (thermal) energy required to obtain this state was $\lambda/4$, as previously pointed out.

Now the charge carrier was able to transfer from the start site to the designation site, and then the system relaxed back to its minimum free energy (second half of the thick line).

In figure 28(b), the system is already in resonance without any (thermal) activation. This corresponds with a mobility that does not depend on temperature. However, what is more striking is that for an even larger electric field the resonant state requires activation again. As shown in figure 28(c), this means that activation will reappear. This is called the Marcus inversion and was confirmed for chemical reactions in solvents. [73]

When the Marcus inversion is applicable to the mobility in conjugated polymers, it means that at higher electric fields the mobility would be lower, due to the increase of activation with field. Some evidence was found for the Marcus inversion in mobility measurements [72] for a molecularly doped polymer. A serious objection against the use of a Marcus based mobility in conjugated polymers was the insignificance of the polaron-contribution to the activation of the mobility. The activation by the polaron amounted to $\lambda/4$, whereas the activation by the disorder amounts to $8/9\sigma^2/kT$. The binding energy parameter λ was 100~300 meV, E_a was 25~75 meV. [72] Whereas the contribution from the disorder parameter (σ~110 meV) resulted in activation energy of E_a was ~420 meV.

It was observed from the transport characteristics of conjugated polymers like PPV that the energy levels in these materials were broadened due to disorder. The transport was governed by thermally activated hopping between transport sites. It was therefore not straightforward that the classical injection models could be applied to conjugated polymers, as the classical injection models essentially describe delocalised charge carriers.

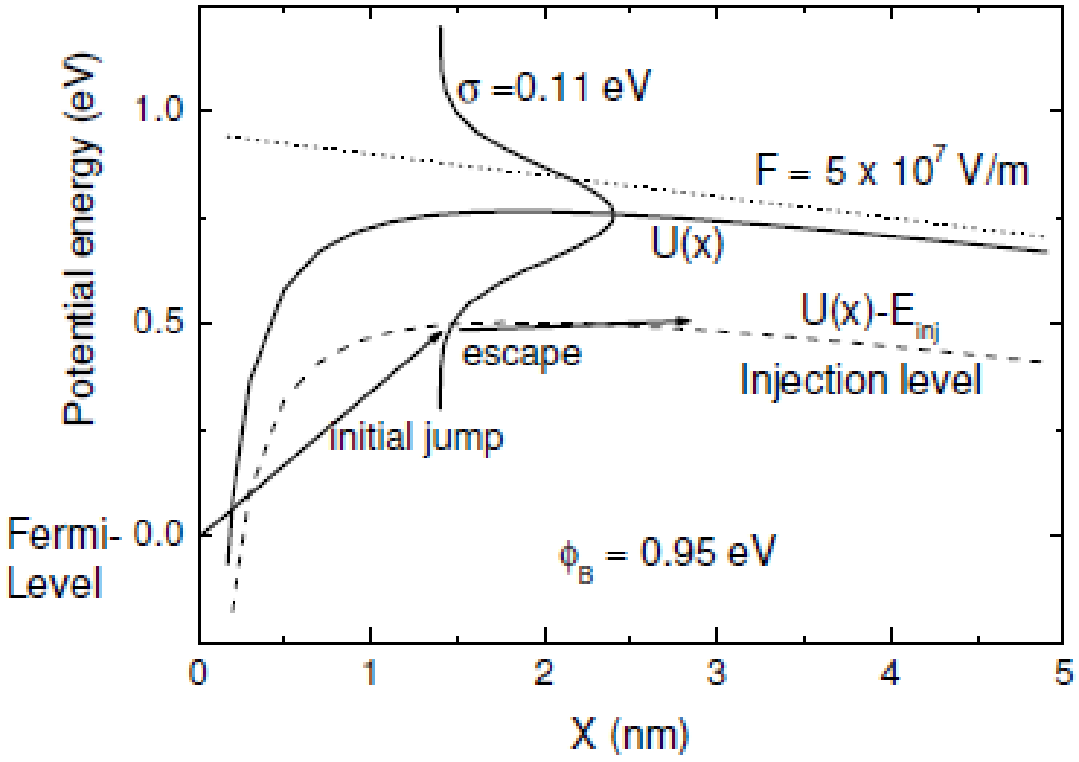

Figure 29: Schematic representation of the initial carrier jumps at the metal-polymer interface, together with their escape as indicated in the graph with arrows. The solid line represents the potential distribution due to tow components: the applied filed (dotted line) and the image force. The dashed line represents the effective injection energy level. The Gaussian DoS reflects the energetic distribution of sites to where a carrier can be injected. Reproduced from ref. [74]

To take account of the hopping nature of the charge transport, a model was formulated by M. A. Abkowitz, based on thermally assisted tunnelling of carriers from the contact into localised states of the polymer. [75] This model was further investigated by including energetic disorder and the image force effect in Monte Carlo simulations. [76-77] These simulations indicated that, in conjugated polymers, an increase of *J* with *V* was due to the field dependence of the mobility, and to an additional increase of the carrier density at the contact caused by the image force. Moreover, analytical treatment explicitly investigated the injection process by a first jump from the contact level into a random hopping system, followed by either a diffusive escape from the interface or a back-flow to the electrode. This approach was validated by the Monte Carlo simulation, which showed that the primary injection event was essential, and determined the temperature and field dependence of the injection process. The injection current was therefore a two-step process, as shown in figure 29. First, a carrier jumped into the organic semiconductor, and

subsequently it had a certain probability to escape or fall back into the electrode. [74]

The Injection Limited Current (ILC) is then given by:

$$J \propto \int_a^{\infty} dx_0 \cdot \exp(-2\gamma x_0)\omega_{esc}(x_0) \cdot \int_{-\infty}^{\infty} dE \cdot Bol(E) \cdot g\left[\frac{U(x_0)}{e} - E\right] \qquad (28)$$

Where $exp(-2\gamma x_0)$ is the tunnelling probability to distance x_0, and γ is the inverse localisation radius. The charge carrier can hop from the contact onto arbitrary sites in the conjugated polymer that are at a distance x_0 larger than the nearest neighbour distance of a. Furthermore, ω_{esc} is the probability to completely escape and reach the other side of the device. The Boltzmann function in equation 29 represents the energy part of the Miller-Abrahams jump rate:

$$Bol(E) = \begin{cases} \exp(-\frac{\Delta E}{kT}), & \Delta E > 0 \\ 1, & \Delta E < 0 \end{cases} \qquad (29)$$

E is defined according to the Fermi level of the metal. In the polymer, the density of transport states is described by a Gaussian distribution of transport sites $g[U(x_0)/e\text{-}E]$, characterised by the energy width σ. The Gaussian distribution is centred on the electrostatic potential, $U(x_0)/e$ given by equation 23.

$$\omega_{esc} = \frac{\int_a^{x_0} dx \exp\left[-\frac{1}{kT}(Fx + \frac{e}{16\pi\varepsilon x})\right]}{\int_a^{\infty} dx \exp\left[-\frac{1}{kT}(Fx + \frac{e}{16\pi\varepsilon x})\right]} \qquad (30)$$

Equation 30 is the well-known Onsager escape formula. [74][78] The Onsager escape describes the diffusive separation of an ion pair or charge pair. It is applied to the charge carrier injected from the metal electrode, because this carrier is accompanied by its mirror image in the metal. This escape function is a strong function of the electric field, but only weakly depends on temperature.

The temperature dependence of the injection current is a key parameter in distinguishing between the classical models based on thermionic emission and

the modern model that describes the hopping injection in an energetic disordered medium.

1.3 Doping effect on organic semiconductors

Doping is an efficient way of device functionalisation for semiconductors, although organic semiconductors are not intrinsically doped. It adjusts the position of the Fermi level relative to the transport levels and tunes the energy barriers for charge injection. At the same time, even under low doping levels, the Ohmic loss (voltage drop due to internal resistance) will be reduced in charge transport layers and increase the conductance of devices. Over the last few decades, many possible combinations of materials and dopants have been reported, such as phthalocyanines (Pc) doped by organic acceptor molecules like ortho-chloranil, [79] tetracyano-quinodimethane (TCNQ) [80] or dicyano-dichloro-quinone (DDQ). [81]

The basic principle of the doping effect in organic semiconductors is based on concepts adopted from inorganic semiconductor physics, including p-type and n-type. As shown in figure 30, p-type doping (p-doping) mixes strong molecular acceptors into organic semiconductor materials, with electron affinity (*EA*) of the dopant molecule in the range of the ionisation energy (*IE*) of the materials. The p-dopants extract electrons from the HOMO states. N-type doping (n-doping), on the other hand, is realised through admixing dopants as donors into the organic semiconductors with the *IE* of the dopants in the range of the *EA* of the organic semiconductors. The n-dopants then donate electrons into the LUMO states.

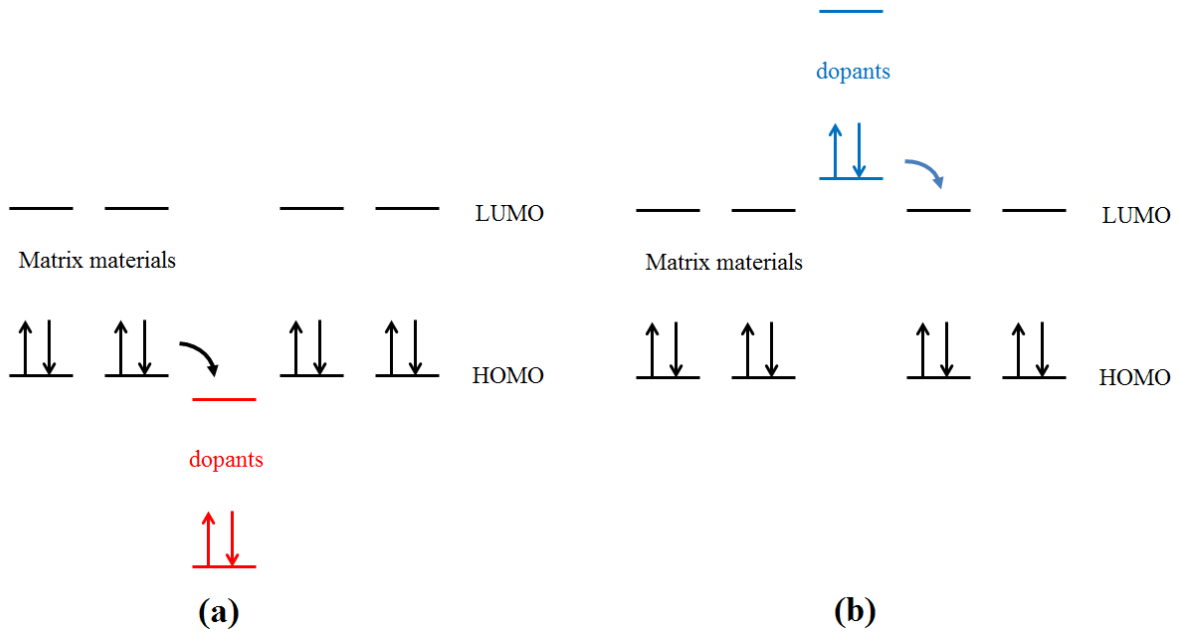

Figure 30: Schematic of doping process for (a) p-type and (b) n-type doping. The dopant acts an acceptor in p-type doping and a donor in n-type doping.

However, the microscopic process of doping effect in organic semiconductor is still not clear. In inorganic semiconductor, the dopant impurities used in controlling the conductivity type of a semiconductor usually have very small ionization energies (*IE*), and hence, these impurities are often referred to as shallow impurities. The energy required to remove an electron from a shallow donor impurity can be estimated based on the Bohr model of the hydrogen atom [82]. The ionization energy of hydrogen is given by:

$$IE = \frac{m_{effective} q^4}{8\varepsilon^2 h^2} \tag{31}$$

Where, $m_{\text{effective}}$ is the effective mass of the electron, q is the elementary charge, ε is the dielectric constanct, h is the Planck constant.

However, the dielectric constant ε, with the value of 3~4, of organic semiconductor is much lower than that of the inorganic semiconductor. Additionally, the effective mass in organics is higher, causing the *IE* higher than that in inorganics according to equation 31. Finally, neither the matrix materials nor the dopants have the symmetry of a single atom and are also usually quite different structures, thus raising the question on what the detailed microscopic arrangement is in organic semiconductors.

Recently, an alternative model was promoted, as shown in figure 31, for the fundamental process of molecular electrical doping, [83] in which pentacene was chosen as the matrix material and 2,3,5,6-tetrafluoro-7,7,8,8-tetracyanoquinodimethane (F4-TCNQ) was chosen as a p-type dopant. The frontier molecule orbital hybridisation between the HOMO of pentacene and the LUMO of F4-TCNQ resulted in the formation of a ground-state charge-transfer complex, with a reduced energy gap between a doubly occupied bonding and an unoccupied anti-bonding hybrid orbital. Additionally, frontier molecular orbital hybridisation contributed to a substantial intermolecular binding energy, which acted as a driving force for complex formation.

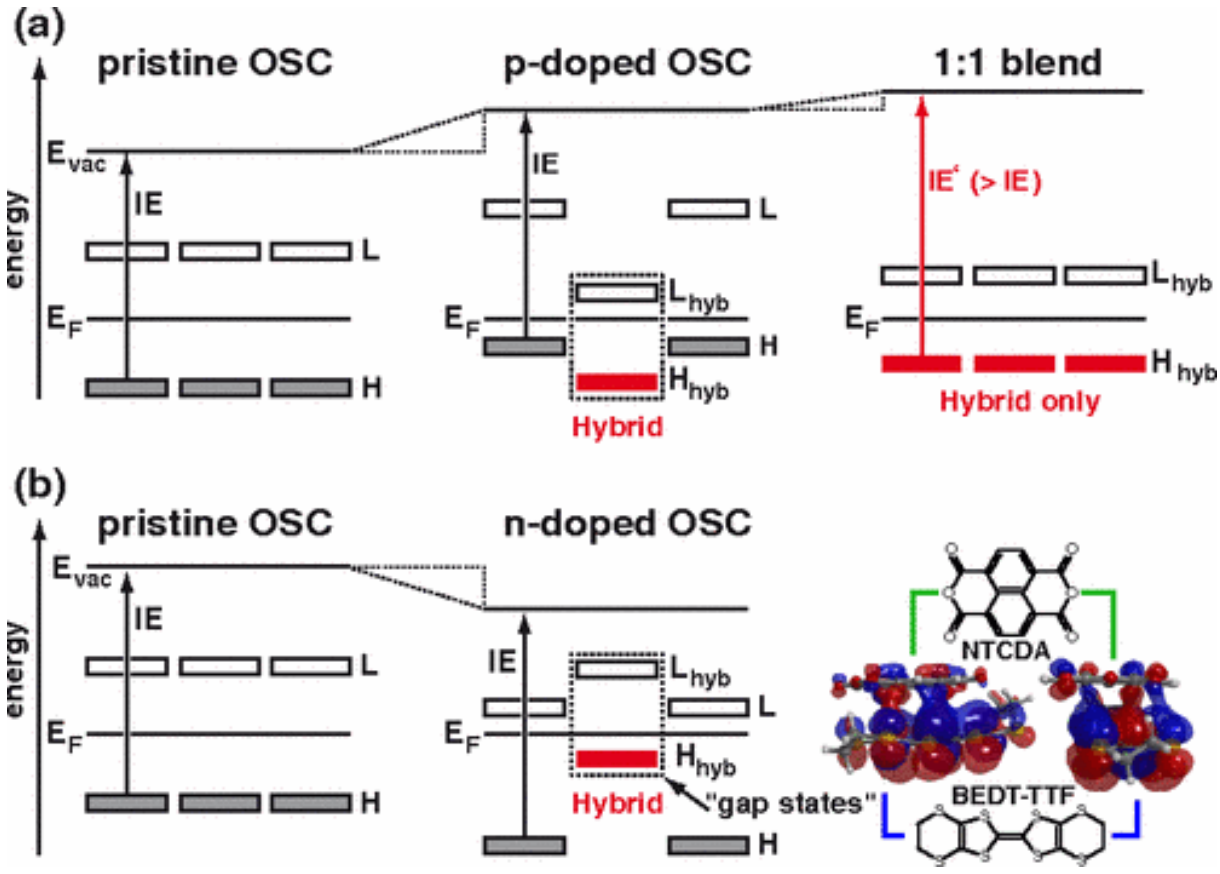

Figure 31: (a) Schematic energy-level diagram for molecular electrical p-doping via OSC-dopant frontier-orbital hybridisation. (b) n-type doping proceeds in full analogy to (a) right: chemical structures and calculated bonding hybrid orbitals for the prototypical material pair NTCDA and BEDT-TTF. Reproduced from ref. [83]

In the following sections, p-type doping, n-type-doping and the impurity doping effect will be discussed on both small molecules and polymers.

1.3.1 P-type doping:

Phthalocyanines (Pc) are stable organic semiconductors with a high lying HOMO, making them well suited for matrix materials in p-type doping research. F4-TCNQ, due to its band structure, is chosen as the acceptor (dopant) for the p-doping experiment. Figure 32 shows the conductivity of two different sample series of zinc phthalocyanine (ZnPc) doped with F4-TCNQ as a function of the molecular doping ratio. [84]

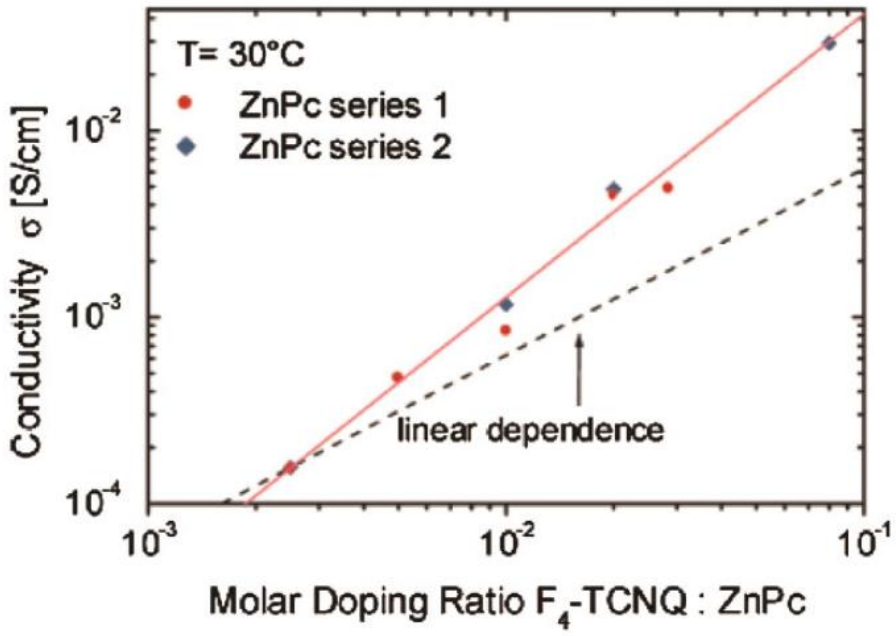

Figure 32: Conductivity of two different sample series of ZnPc doped with F4-TCNQ as a function of molecular doping ratio. ZnPc series 1 is a polycrystalline film (α-phase) grown when the substrate was held at room temperature and ZnPc series 2 is an almost amorphous film grown when the substrate was cooled down to at least -100 ℃. Reproduced from ref. [84]

The two most important points in figure 32 are that the conductivity could be reproducibly controlled over more than two orders of magnitude by the doping ratio, and the conductivity is many orders of magnitude higher than the background conductivity of nominally undoped ZnPc.

A similar experiment was carried out by Olthof et al. [85] with N,N,N’,N’-tetrakis (4-Methoxy-phenyl) benzidine (MeO-TPD), as shown in figure 33. The conductivity increases as the concentration of F4-TCNQ increase. After doping, free charge carriers are produced due to the charge carriers’ transference.

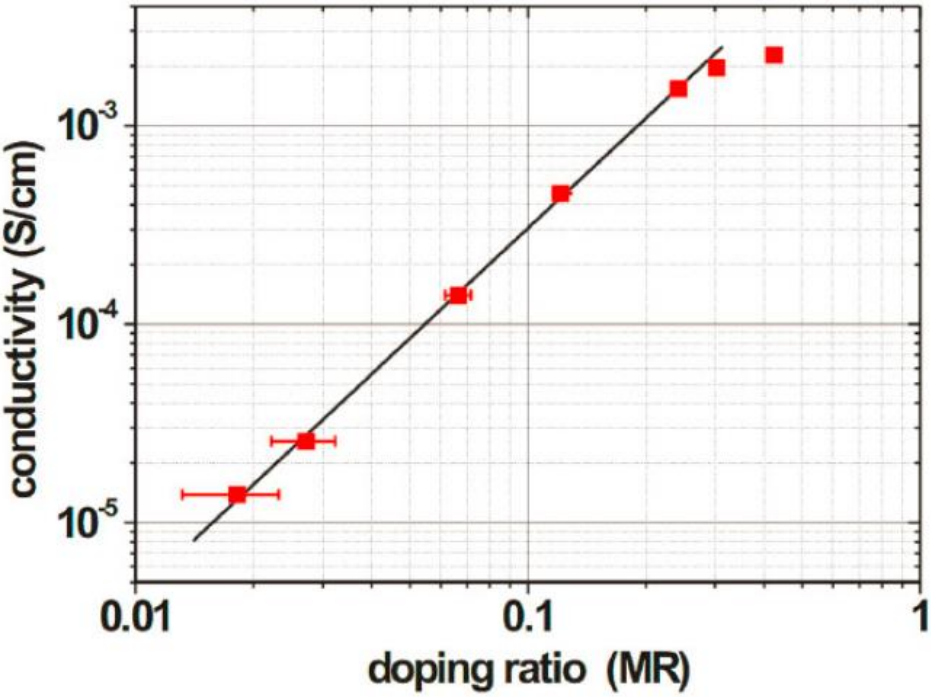

Figure 33: Conductivity of MeO-TPD doped with F4-TCNQ as a function of the doping ratio. Reproduced from ref. [85]

After doping, the population of free charge carriers increases and the Fermi level of the organic semiconductor shifts towards the transport level. For p-type doping, the Fermi level shifts towards the HOMO of the organic semiconductors. Thermoelectric effect was chosen by Seebeck, [86-87], also known as the Seebeck-effect, to measure the distance between the shifted Fermi level and the transport level (HOMO).

The Seebeck effect is a useful and simple tool to measure the distance between the transport states (E_μ here) and the Fermi level, E_F. In a simple analysis, it turns out that the Seebeck coefficient, $S(T)$, is the relation between thermal voltage and temperature difference between the contacts and can be expressed as:

$$S(T) = \frac{k_B}{e}\left[\left(\frac{E_F(T) - E_\mu}{k_B T}\right) + A\right] \tag{32}$$

The parameter A is a numerical factor that accounts for the kinetic energy of the charge carriers, and can be assumed to be negligible in low mobility organic materials.

For the F4-TCNQ doping experiment in ZnPc, the position of the Fermi level in ZnPc as a function of F4-TCNQ concentration is shown in figure 34. It

is obvious that the Fermi level shows the typical behaviour of a doped semiconductor. The result suggests the shift of the Fermi level to the transport level (HOMO) with the increase of F4-TCNQ doping concentration. For n-type doping the similar shift happens and the details are introduced in section 1.3.2. The temperature dependent detection is carried out as in figure 34(b), which is following the theory in equation 32. Another model also suggests the transport level would slightly move with temperature and doping level, as well as the Fermi level. [87]

However, only qualitative conclusions can be drawn from the thermoelectric measurement, assuming a discrete transport level. Ultraviolet photoelectron spectroscopy (UPS) was chosen by Olthof et al. [85] to resolve the distribution of transport (HOMO) states, and to determine the position of the transport states in relation to the Fermi level, leading to a deep understanding of the doping mechanisms.

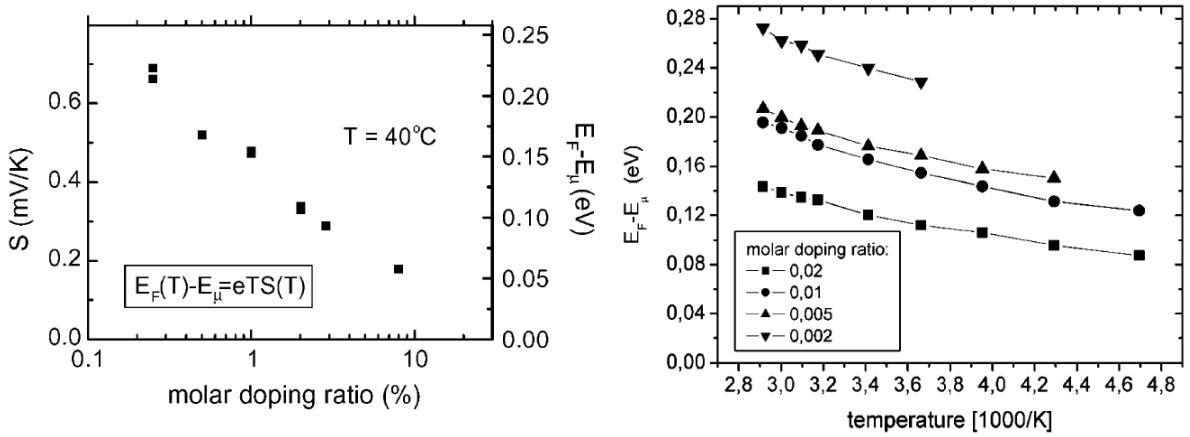

Figure 34: (a) The Seebeck coefficient, S (left axis), and distance (right axis) between the Fermi level, E_F, and the dominant transport energy level, E_μ, at 40 ℃ for ZnPc layers doped with F4-TCNQ as a function of the doping concentration. (b) Measured Fermi level shift as a function of the temperature. Reproduced from ref. [88]

Figure 35 shows the energy level alignment of a metal/p-doped organic layer junction. Following the establishment of the contact between the semiconductor and the metal, the Fermi level E_F of the organic layer aligns with the work function of the metal (Φ_M). The hole injection barrier at the interface Φ_0 is determined according to equation 33:

$$\Phi_0 = IE + \Delta - \Phi_M \tag{33}$$

Where Φ_M is the metal work function, *IE* is the ionisation energy of the semiconductor and Δ is the interface dipole.

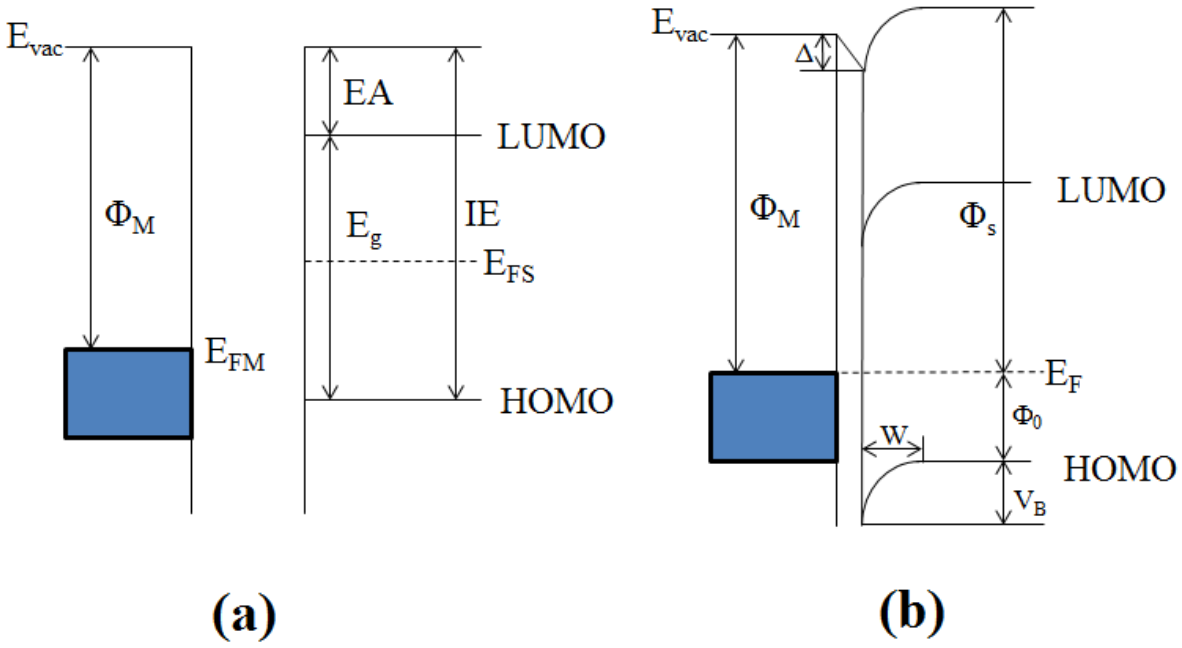

Figure 35: Energy level alignment in a metal/p-doped organic semiconductor junction before contact (a) and after contact (b).

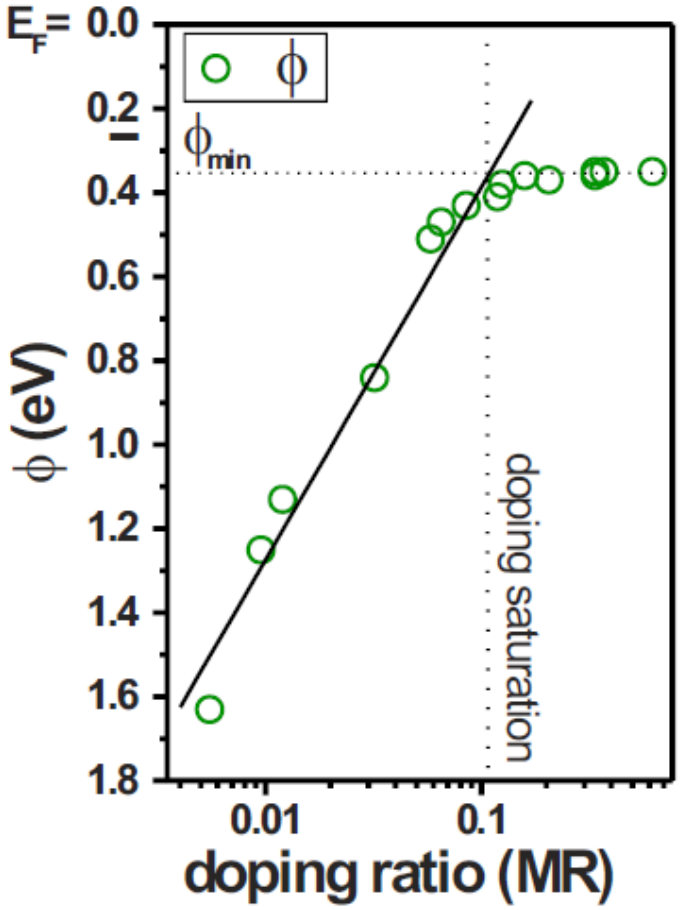

Figure 36: Change in hole injection barrier as a function of the doping ratio. Reproduced from ref. [85]

The formation of the charge depletion zone at the interface led to the HOMO states bending upwards. At the same time, the distance between the HOMO and the Fermi level decreases with the increase of the distance from the interface. At the end of the charge depletion zone, the distance between HOMO and E_F saturates at its bulk value Φ_{min} (which is the barrier Φ_0 in equation 33).

All these parameters can be determined by UPS. Thus, it is possible to get a full characterisation of the contact and position of the Fermi level in the bulk. Also, for the F4-TCNQ doped results in MeO-TPD, the distance Φ of the Fermi level and HOMO of MeO-TPD is plotted as a function of the doping ratio of F4-TCNQ. For pure MeO-TPD, the Fermi level is close to the (Φ = 1.68 eV). As shown in figure 36, Φ decreases as the doping ratio increase, and saturates at the value of 0.35 eV.

The comparison of F-4TCNQ and another two materials NPD2 and NPD9 doping into MeO-TPD was also carried out to detect the p-doping effect. [85] All dopants, F4-TCNQ, NDP2 and NDP9, with different doping strengths and electron affinities, resulted in the same saturation distance Φ_{min} at 3.5 eV when doping into MeO-TPD, as shown in figure 37.

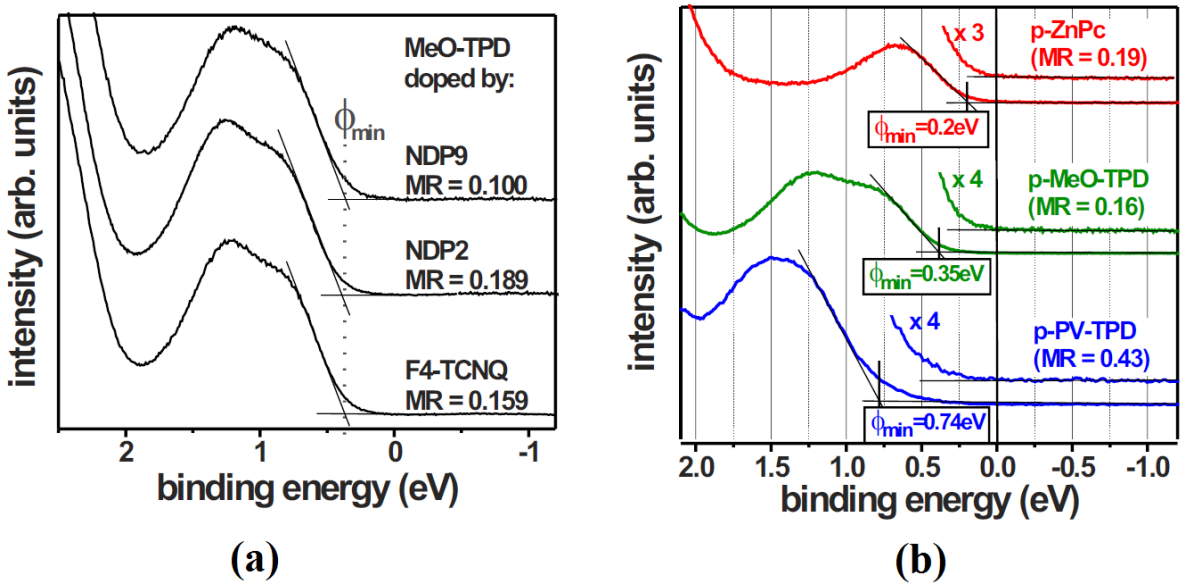

Figure 37: (a) HOMO region of the UPS spectra of MeO-TPD highly doped by three different dopants. (b) HOMO region of the UPS spectra of three different host materials, all highly doped by F4-TCNQ. Reproduced from ref. [85]

At the same time, MeO-TPD, ZnPc, and PV-TPD were doped by F4-TCNQ, for comparison. As shown in figure 37, the variation of the matrix material had a strong influence on the saturation behaviour. When doped by the

same material, F4-TCNQ and MeO-TPD saturated around 0.35 eV, while PV-TPD already saturated at 0.74 eV and ZnPc at 0.2 eV.

The dependence of the saturation effect on the matrix material can be understood by figure 37(b), which shows an enlarged view of the UPS signal between the HOMO energy and the Fermi level. Commonly, the HOMO cut-off energy is defined as the intersection of a tangent and the background. However, as shown in figure 37(b), there is a significant density of states that extends into the gap and reaches up to the Fermi level at saturation.

Another interesting p-type doping is oxygen doping in organic semiconductors. The same as chemical doping, oxygen doping also introduces some trap states, leading to the generation of free charge carriers and the Fermi level shift. Here, P3HT is chosen as the matrix material to discuss the oxygen doping effects. Oxygen doping in P3HT was reported including two reaction routes, as shown in figure 38. One was fully reversible; forming charge transfer complexes (CTC), [89] and the other was related to the formation of singlet oxygen with participation of triplet excitons on the polymer chain.

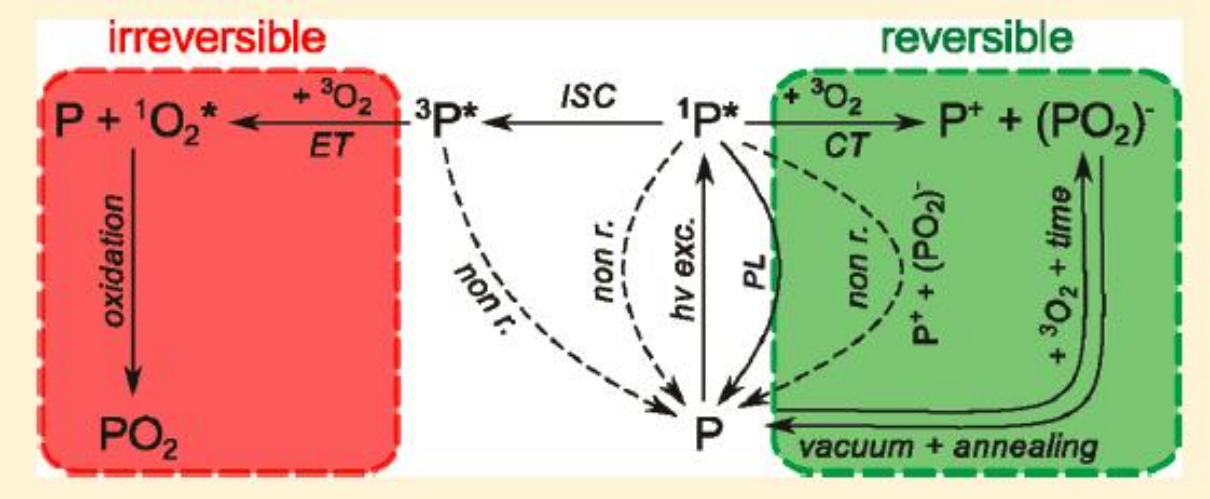

Figure 38: Reversible and irreversible oxygen doping effects in P3HT. Reproduced from ref. [89]

It was reported that oxygen doping in P3HT only carried on efficiently with light irradiation. [90] When P3HT was exposed to oxygen for 30 minutes in the dark, no significant changes in the position of the energy levels were observed. However, upon simultaneous exposure to light and oxygen, all core level peaks of the polymer shifted towards lower binding energies.

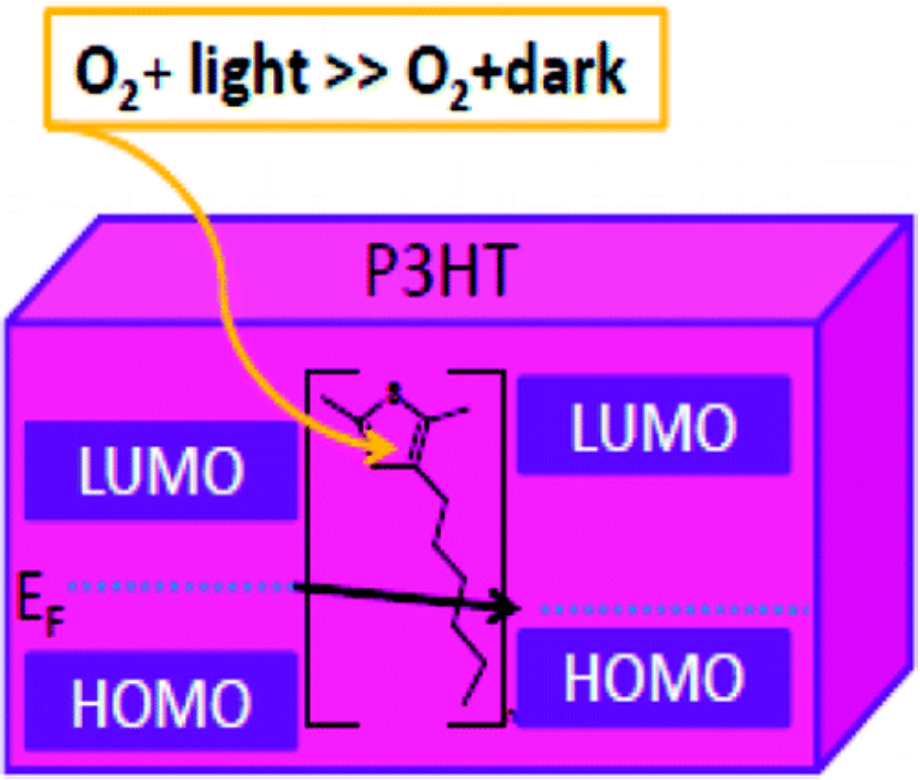

Figure 39: The influence of oxygen and light on the energy level alignment of poly(3-hexylthiophene) thin films. Reproduced from ref. [90]

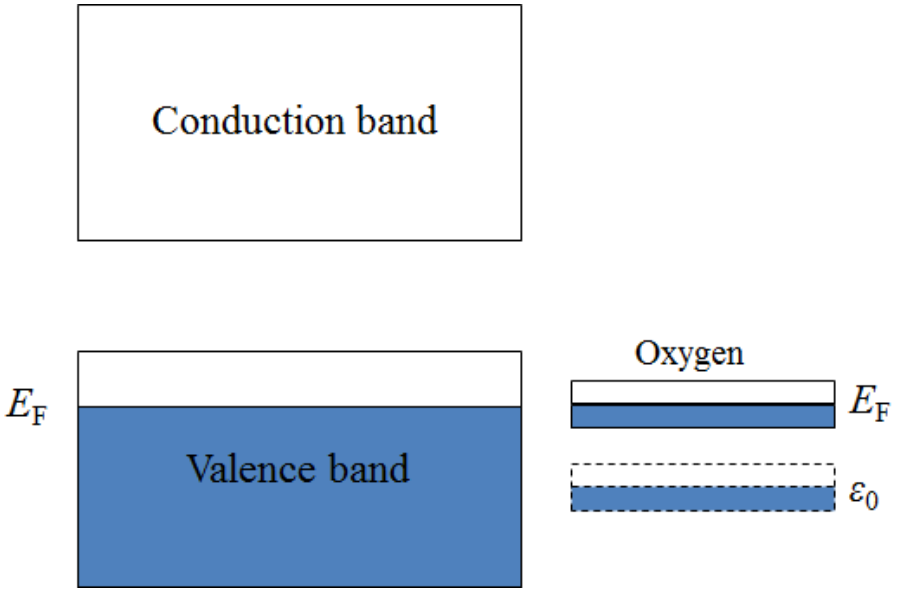

Figure 40: Schematic plot for the valence and conduction bands for an organic semiconductor. Due to the electron transferred to O_2, the oxygen band is shifted upward as a result of increasing Coulomb repulsion. Reproduced from ref. [91]

Annealing above the glass transition temperature of P3HT (150^{o}C) led to a reversible shift of the Fermi level. The oxygen content in P3HT consisted of irreversibly and reversibly bound oxygen fractions. The reversible fraction correlated with the observed p-doping, whereas the irreversible part did not alter the electronic structure. The theory of doping effects [91] suggested that when

P3HT was isolated from the O_2 chain, the top of the valence band lay above the oxygen band, because P3HT had an *IE* of 5.2 eV, while the oxygen band lay below the vacuum at 5.8 eV, as shown in figure 40. Once the coupling was turned on, the electrons occupying the top of the valence band may transfer to the lower oxygen band, causing a lift of the oxygen band according to its on-site energy, as shown by the arrow in figure 40. Due to the hybridisation of O_2 and polymer, the Fermi level was pushed into the valence band and pinned with the oxygen band due to charge transfer to O_2. The doping depended on the oxygen density in a highly nonlinear way.

The reversible oxygen doping would also make it possible to control the charge injection barrier, leading to the possibility of tuning the conductance in a P3HT based device. [92] Annealing above the glass transition temperature for de-doping will increase the barrier leading to a drop of the current, and re-doping will increase the current under the same bias, as shown in figure 41.

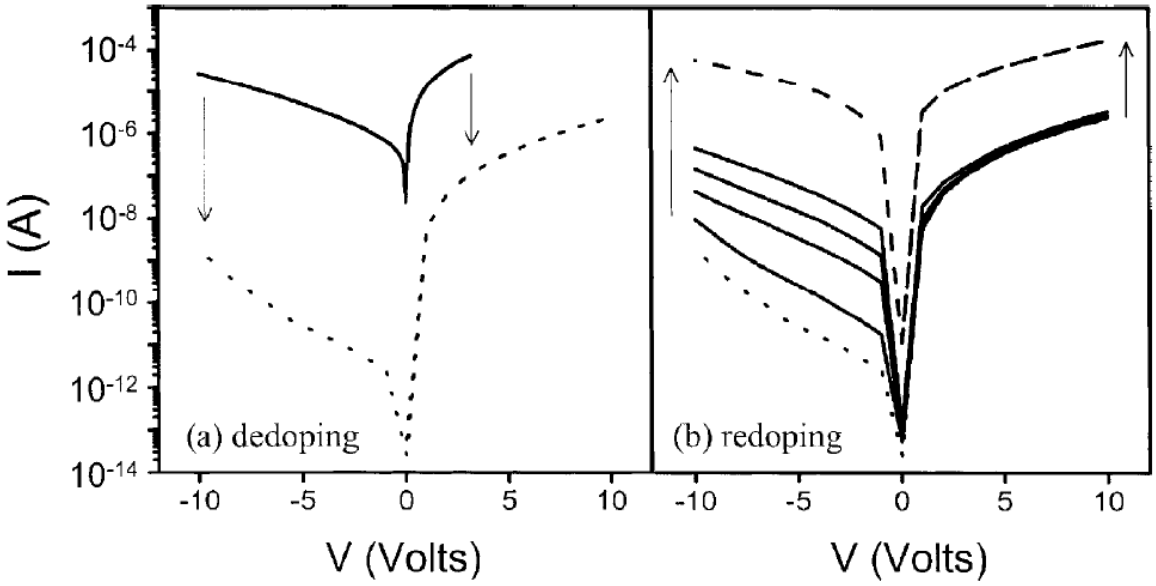

Figure 41: Current versus voltage characteristics of a Ti/P3HT/Au device at different doping levels. Bias voltage is applied to the Au (bottom) electrode, while the Ti (top) electrode is kept at ground. Reproduced from ref. [92]

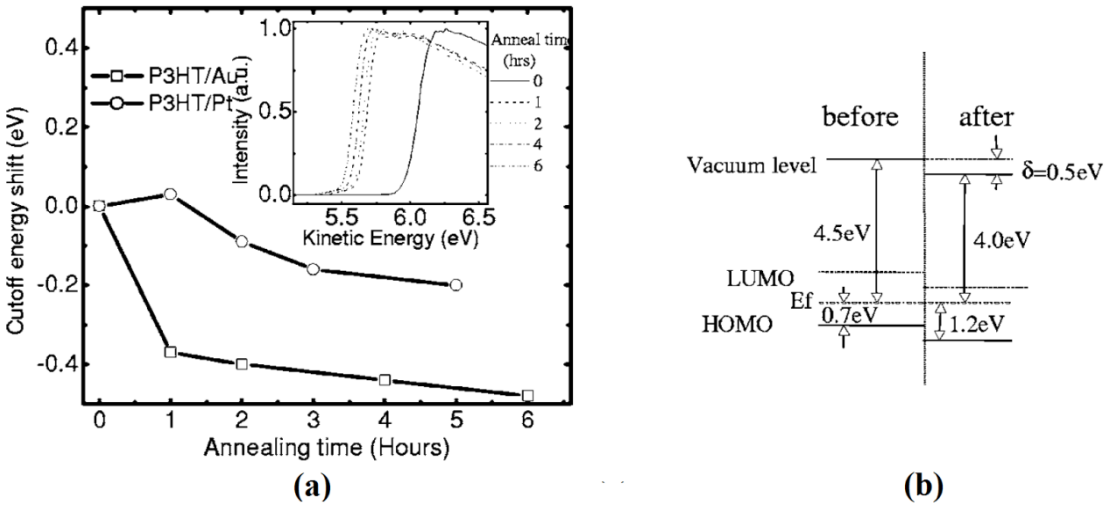

Figure 42: (a) UPS cut-off energy shift as a function of annealing time for both P3HT/Au and P3HT/Pt. Inset: UPS cut-off of a P3HT/Au sample for different annealing times at 350 K. (b) Energy level diagram of band alignment, based on the results of the UPS data for Au/P3HT before and after the annealing process, showing the large change in the barrier for hole injection. Reproduced from ref. [93]

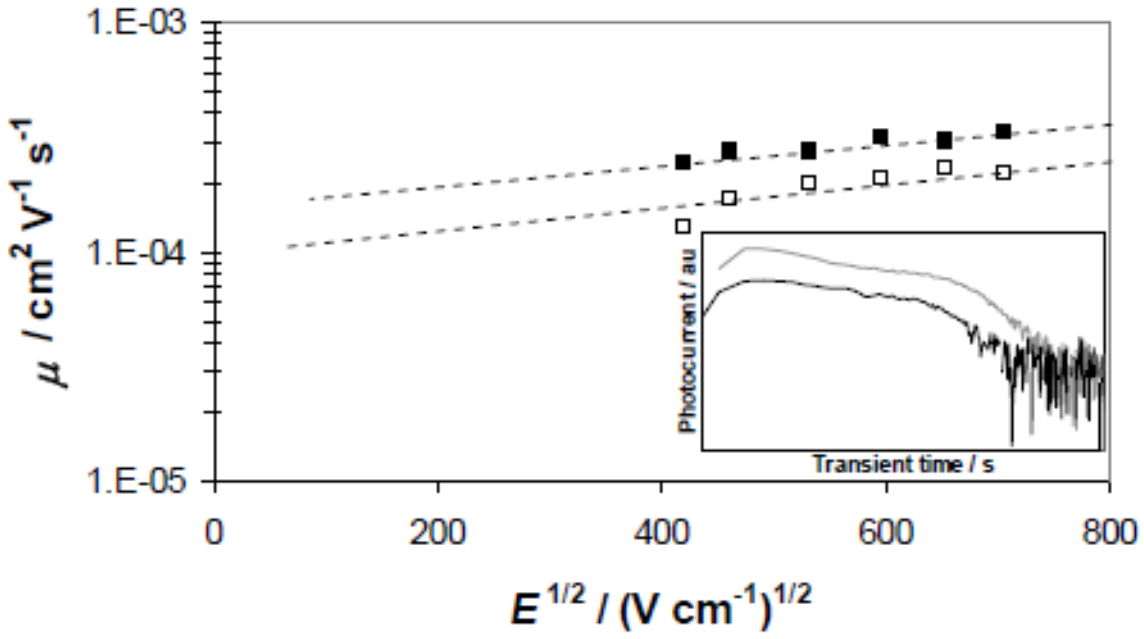

Figure 43: Electric field dependence of hole mobility before (hollow squares) and after (filled squares) annealing at 140 ℃ in a device with P3HT film thickness of 1.5 μm and a TiO_2 blocking layer. Reproduced from ref. [53]

The UPS data, as shown in figure 42, revealed that upon de-doping, the energy levels shifted at the interface, leading to an increased barrier for hole injection. [93] These results demonstrated that doping can profoundly affect the physics of charge injection in such systems, by strongly altering the band alignment between the metal and the organic. The scale of the interface dipole

shift could significantly exceed the dopant-induced broadening of the density of states.

Meanwhile, the annealing effect on P3HT resulted in an enhancement of π-π stacking in the crystal domain [94] and improved the degree of crystallinity, [95] leading to better charge transport, due to improvement in charge carrier mobility in different kinds of devices.

As shown in figure 43, Jenney Nelson et al. [53] reported measurement of the mobility of P3HT. The insert of the TiO_2 layer reduced the dark background current of the photocurrent. The hole mobility of P3HT slightly increased after annealing above the glass transition temperature.

P3HT was fabricated in different kinds of device structures, such as organic field effect transistors and organic solar cells. Morphology studies and analysis of the channel resistance demonstrated that the annealing process increased the crystallinity of rr-P3HT, and improved the contact between the electrodes and the P3HT films, thereby increasing the field effect mobility in OFET devices. For the solar cells based on P3HT, the results indicated that the most important factor leading to a strong enhancement of the efficiency, compared to non-annealed devices, was the increase of the hole mobility in the P3HT phase of the blend with PCBM.

1.3.2 N-type doping:

N-type dopant, due to high HOMO above the LUMO of matrix material, has low stability against oxidisation. There are several ways for the n-type doping of organic semiconductors. Here, three types of dopants: alkali metals, high HOMO compounds, and precursors will be discussed.

Ivory et al. [96] reported the first n-type doping using alkali metals like potassium (K) or sodium (Na) in the 1970s. Lithium doping into a cathode was first reported in OLEDs. Yoshikazu et al. [97] and Kido [98] reported LiF could act as a buffer layer for electron injection. The most investigated interface was Alq_3/LiF/Al, because of its frequent use in OLEDs, and figure 44 shows the UPS studies on this interface by Mori et al. [99] It showed that the Fermi level aligned well in the presence of the LiF interlayer. This better alignment improved the electron injection with an injection barrier decrease. The driving

voltage for the onset of the light emission decreased, and the efficiency was improved under the same bias. An XPS measurement was carried out to determine the species responsible for the Li doping in OLEDs, showing that following the LiF layer deposition, the LiF remained undissociated. After Al was subsequently deposited onto the LiF, an exothermic reaction on Alq_3 appeared with LiF and Al. However, in this detection no Li^+ ion was discovered. Other groups reported different results by lifting off the Al electrode after deposition. They found both Li-F and C-F bonds, indicating dissociation of LiF.

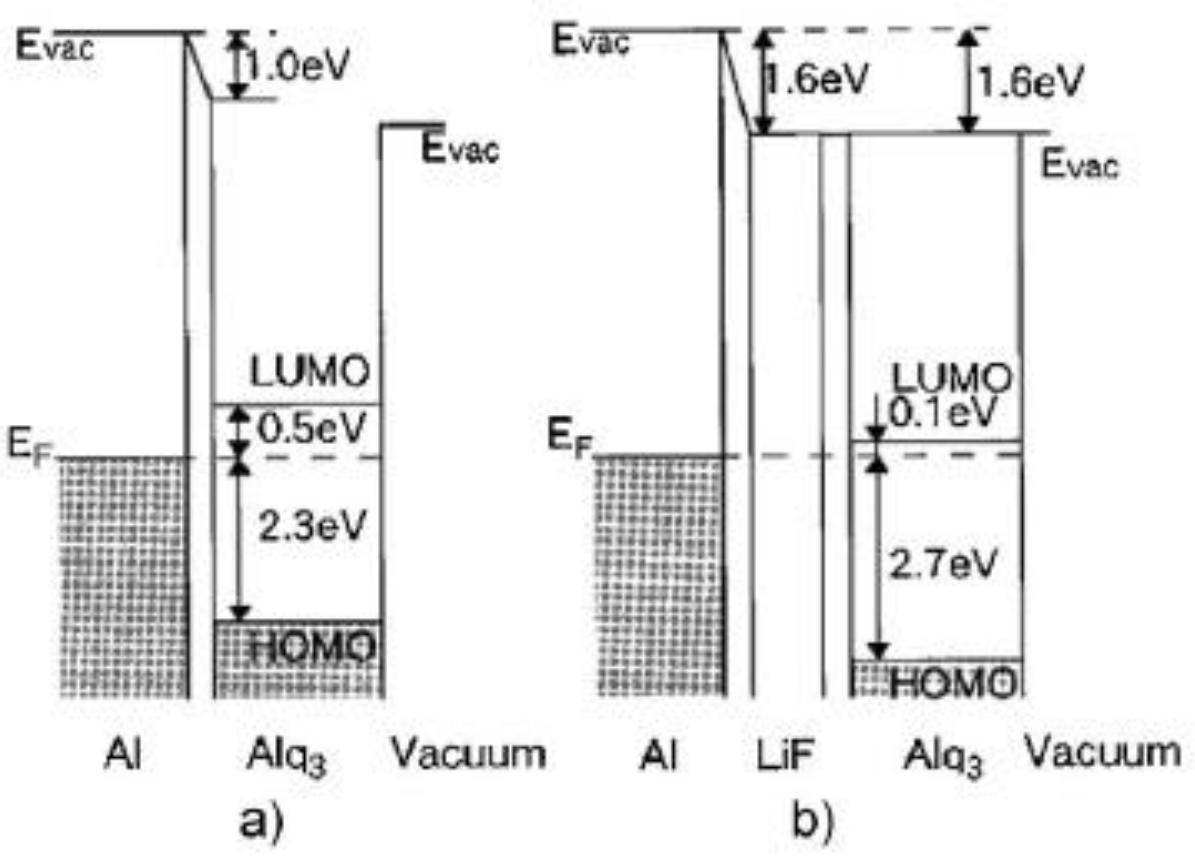

Figure 44: The results of a UPS on the interface between Alq_3 (1.7 nm) and Al (50 nm) without (a) and with (b) a 0.5 nm LiF inter layer. The energy diagrams show the difference between the undoped (a) and doped (b) interface. Reproduced from ref. [99]

Parthasarathy et al. [100] carried out a study of Li doping from the interface layer and its diffusion into the bulk of the OLED's common materials: BPC, CuPc and Alq_3. They proved that Li diffused nearly up to 100 nm into the bulk for BCP and CuPc after evaporation of a metal electrode. How much exactly Li diffused into the bulk very much depended on the matrix and the preparation conditions, as another study determined that Li diffused from a 0.8 nm layer only 10 nm into BPhen without the deposition of a metal electrode. An alternative to n-type doping by diffusion from the interface was co-evaporating

Li with an organic material typically at high doping ratios, leading to bulk doping. The thickness of the initially doped layer was more controllable, but could lead to a good Fermi level alignment at the interface as well. Kido and Matsumoto showed efficient OLEDs with a Li-doped Alq_3 or BPhen as the electron injection layer. [101]

Other alkali metals like Cs and their salt or alloy compounds could also be used for efficient n-doping of organic materials. Cs was often co-deposited with organic electron transport layers (ETLs) and could lead to highly efficient OLEDs. [102] However, in their experiment, they have never controlled the n-type doping ratio through co-evaporation.

Nollau et al. [103] first reported the controlled n-type doping using naphthalene tetracarboxylic dianhydride (NTCDA) as the matrix material doped by the electron donating molecule bis(ethylenedithio)-tetrathiafulvalene (BEDT-TTF). The proof of n-type doping was a clearly observable shift of the Fermi level towards the electron transport level, and an increase in conductivity by one to two orders of magnitude. This study showed that it was possible to carry out n-type doping organic semiconductors using molecular compounds, which had the potential to be much more thermally stable than using alkali metals due to reduced diffusivity.

Senku et al. [104] showed the molecule tetrathianaphthacene (TTN) with HOMO ~4.7 eV in a UPS study to be doped well into hexadecafluoro-zinc-phthalocyanine (F16ZnPc), but not Alq_3. Given the energy levels of F16ZnPc with LUMO ~4.5 eV and Alq_3 with LUMO ~2.5 eV, it was not surprising that TTN worked more efficiently as the electron donor for the former matrix molecule, highlighting that the HOMO level of a dopant had to lie above the LUMO of the matrix for direct n-doping.

Another compound for n-doping was reported by Chan et al. [105] on the molecule bis(cyclopentadienyl)-cobalt(II) (cobaltocene, $CoCp_2$). The thorough investigation included conductivity measurements, X-ray studies and UPS. Their matrix material was a tris(thieno)hexaazatriphenylene derivative, acting as the electron transporter. $CoCp_2$, with an ionisation potential of only ~4 eV, was able to shift the Fermi level of their matrix material by more than 0.5 eV towards the electron transport level (LUMO), indicating a clear proof of n-type doping. Consequently, the conductivity of the investigated films was found to

increase by about three orders of magnitude, making $CoCp_2$ an interesting n-dopant and leading to further work with this material class.

Using metal complexes in general appeared to be a good approach for n-doping, as they were also the basis for other n-type dopants. Bloom et al. [106] proved that the compounds $[Ru(terpy)2]^0$, $[Cr(bpy)3]^0$, and $[Cr(TMB)3]^0$ could act as n-dopants. The electron donating character of these compounds was strong enough to dope materials used in OSCs, [107] but was found to be not sufficiently n-doping for general application in OLEDs due to the higher lying LUMO values of the electron transporting materials. However, the general drawback of these approaches for n-type doping was the increasing instability of the dopants with respect to oxygen for higher HOMO values, requiring a continuous handling of the materials under inert conditions.

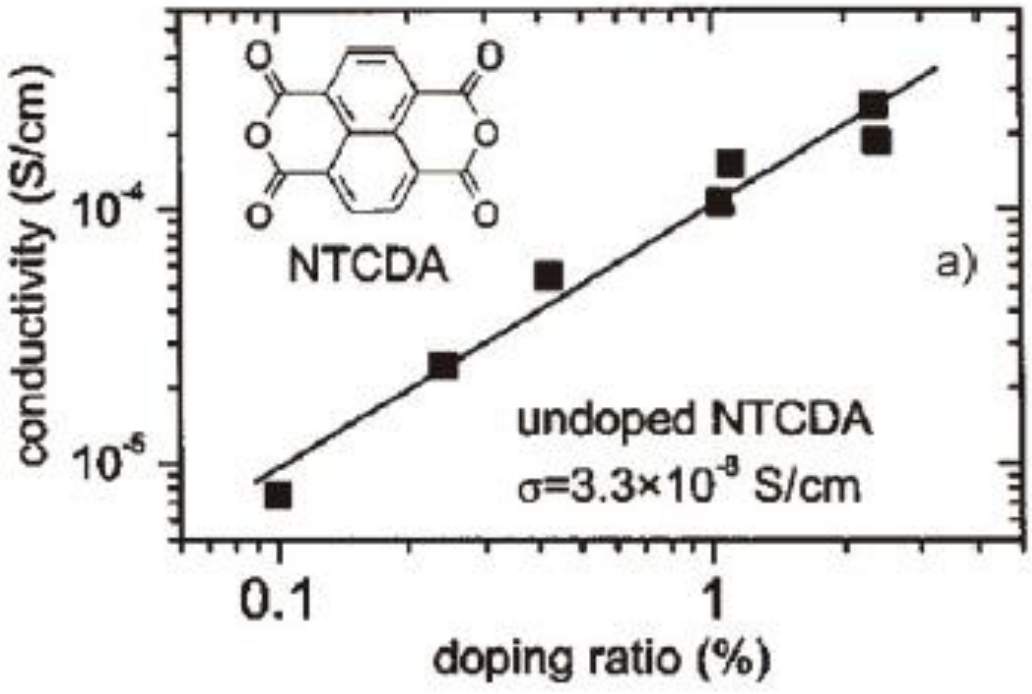

Figure 45: The conductivity of NTCDA layers as a function of pyronin B doping concentration. Reproduced from ref. [108]

Another possible approach was to use precursors that donate an electron to the matrix by being activated by heat or illumination. Werner et al. [108-109] showed that cationic dyes like pyronin B chloride could be used as stable precursors for strong molecular donors. Figure 45 shows the effect of pyronin B chloride co-evaporated with the matrix material NTCDA, where it turns into the strong donor pyronin B and the conductivity of NTCDA increases by about four orders of magnitude up to 10^{-4} Scm^{-1}.

The doping process of pyronin B in NTCDA was also investigated in great detail through UPS, IPES and I–V measurements. The n-type doping process was confirmed by observing a shift in the Fermi level towards the electron transport level, and an increase in conductivity by more than four orders of magnitude. Combining the experimental data with calculations using density functional theory (DFT), it was concluded that two species of pyronin B were present in the deposited thin film: the leuco and the neutral radical of pyronin B, whereas they attributed the doping effect to the neutral radical.

Recently, another material class for efficient n-type doping via a precursor was reported, in which (4-(1,3-dimethyl-2,3-dihydro-1H-benzoimidazol-2-yl)phenyl)dimethylamine (N-DMBI) was introduced as a solution process n-dopant, [110] and its cationic derivative, 2-(2-methoxyphenyl)-1,3-dimethyl-1H-benzoimidazol-3-ium iodide (o-MeO-DMBI-I) was introduced as a vacuum process n-dopant [111] for fullerenes (C_{60}). Using the n-type dopant o-MeO-DMBI-I, the conductivities of more than $1 Scm^{-1}$ were obtained for vacuum deposited C_{60}. The hypothesis for this stable doping process was that, during evaporation, o-MeO-DMBI-I was reduced to its neutral radical. This reduction would result in a much higher HOMO level. An electron transfer to the LUMO of C_{60} would take place, and thus the neutral radical was assumed to be responsible for the strong n-type doping effect in C_{60}. However, the exact mechanism was still under discussion.

1.3.3 Impurity doping

The dopant can also act as an impurity in the matrix materials, which may block the charge transport, leading to mobility decrease. Here, the hole trapping effect introduced by doping is discussed in the charge transport of the matrix materials.

As shown in the inset of figure 46, the impurities can be introduced as obvious trap states in the energy gap because of the relatively clear mid-gap states. This deteriorates charge transport in liquid crystals, which is very similar to the case of crystalline materials. Ahn et al. [112] reported that chemical impurities of less than 1 ppm can deteriorate the charge carrier transport in liquid crystals.

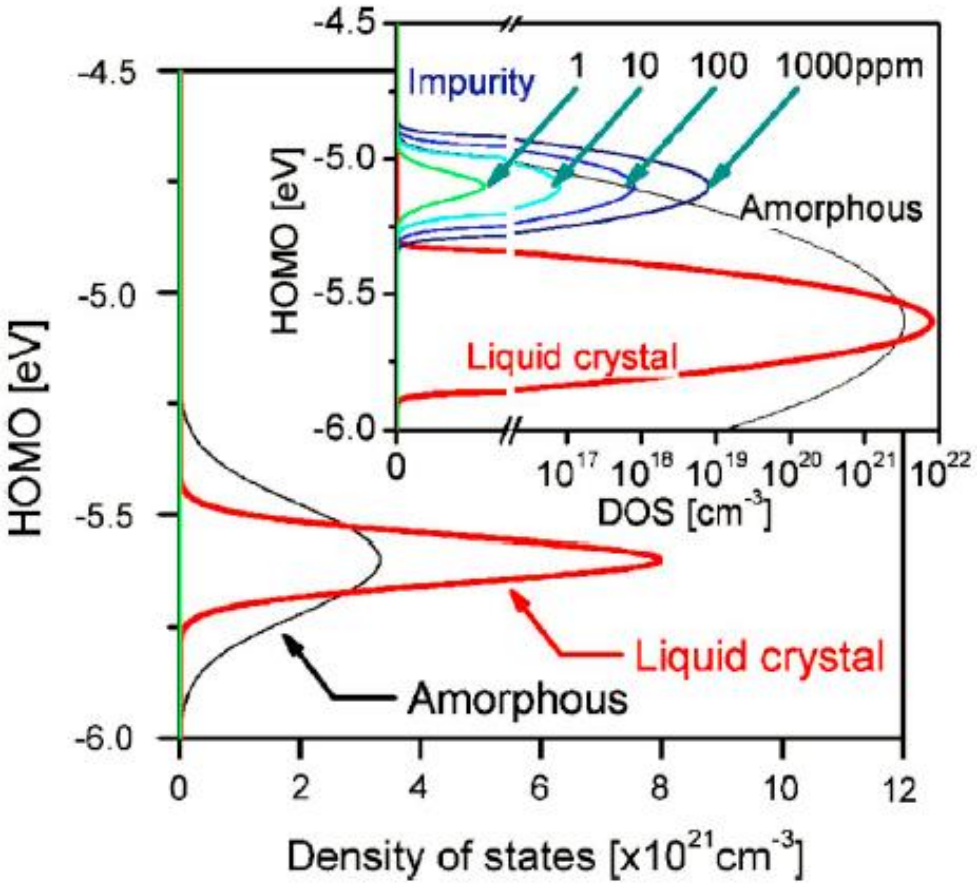

Figure 46: Schematic illustration of density of states (DoS) in organic amorphous (thin line) and liquid crystalline (thick line) semiconductors, whose positions relative to a small amount of impurity are shown as a function of their concentration (inset). Reproduced from ref. [112]

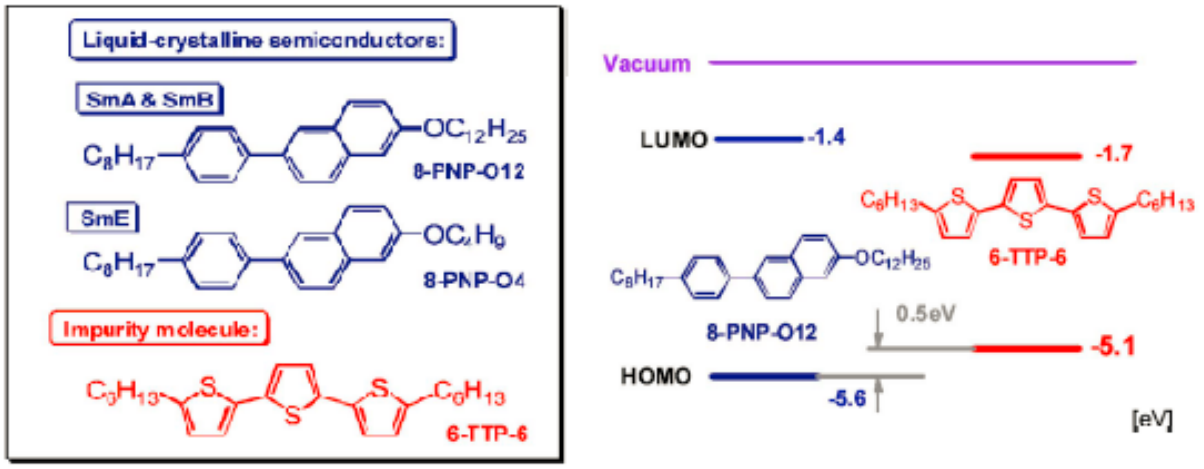

Figure 47: Schematic of molecule structures and energy levels. Reproduced from ref. [112]

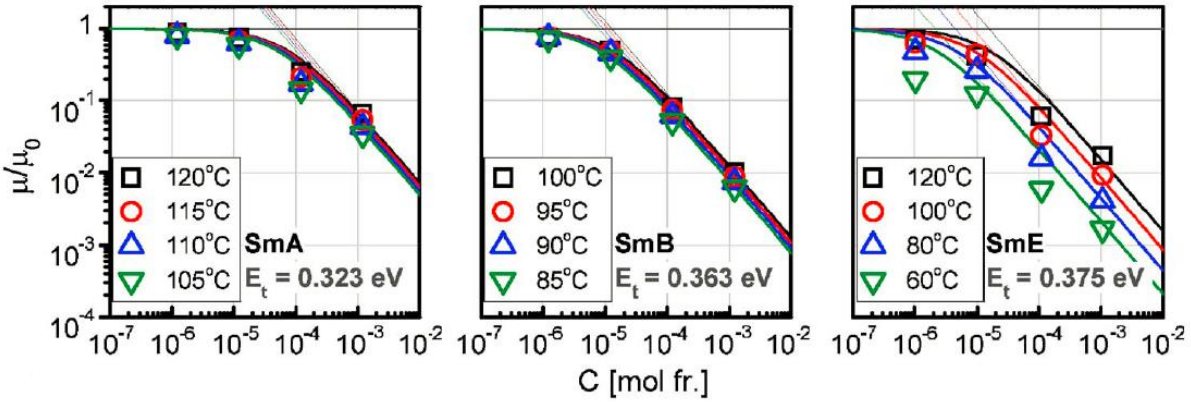

Figure 48: (a) Impurity concentration dependence of relative mobility μ/μ_0 for Smectic A (SmA), Smectic (SmB), and Smectic (SmE). Reproduced from ref. [112]

In the doping experiment, two 2-phenylnaphthalene derivatives, 8-PNP-O12 (SmA and SmB) and 8-PNP-O4 (SmE) with narrow DoS, whose charge carrier transport properties had been well studied, were selected as model liquid crystalline semiconductors. A terthiophene derivative ω,ω'-dihexylterthiophene (6-TTP-6), was selected as an impurity molecule with a good miscibility with 8-PNP-O12 and 8-PNP-O4. The molecule structures and energy levels are shown in figure 47.

The effects of chemical impurities in different smectic mesophases on hole transport were investigated by transient photocurrent measurements as shown in figure 48. In the less-ordered smectic mesophase, SmA, both ionic and hole conduction were observed, while only trap-controlled hole conduction was observed in the highly ordered smectic mesophases SmB and SmE. Impurity concentrations above 100 ppm showed completely trap limited charge transport. The trap depth in all the smectic mesophases investigated in this study was around 0.35 eV. The trap depth did not vary significantly with mesophase. Thus, the doping method could also potentially be used for the purity assessment of liquid crystal organic semiconductors.

The MC response in organic semiconductor diodes can also be enhanced by introducing trap states through different routes, both in small molecule and polymer based devices. In 2008, Niedermeier et al. [181] reported the enhancement of MC in poly (paraphenylene vinylene) (PPV) through electrical conditioning. They later attributed the MC change to the charge trapping effect, which can be removed by annealing in nitrogen. [182] In 2012, Wohlgenannt et al. [183] introduced the charge trapping effect through X-ray irradiation of aluminium tris(8-hydroxyquinolate) (Alq_3) and increased the MC, as well as

decreased the conductance. However, neither of these groups explained clearly the nature of these trap states and the mechanism by which they enhanced MC.

In 2013, Cox et al. [184] developed a chemical doping method using F4-TCNQ as the electron trap centre doping into PPV, and 4-(dicyanomethylene)-2-methyl-6-(dimethylaminostyryl)-4H-pyrane (DCM) as the intrinsic electron trap filling material in PPV. Their results showed that the MC response decreased through intrinsic electron trap filling by DCM, but kept constant with the F4-TCNQ doping. They proved the intrinsic electron trap was the origin of the MC, and filling the electron trap states would suppress the MC response.

Pentacene, due to its elevated Highest Occupied Molecular Orbital (HOMO), can act as a hole trap centre in P3HT. Figure 49 shows how pentacene with a smaller ionisation energy (*IE*) than P3HT, is introduced as hole trap states into P3HT. According to the literature, [185-186] 5.0 eV is taken as the average ionisation energy (*IE*) (HOMO position) and 3.0 eV as the electron affinity (*EA*) (LUMO position) of pentacene. Similarly, literature values [187] have been used as the HOMO and LUMO of P3HT, namely 5.2 eV and 3.0 eV respectively. By controlling the pentacene doping concentration, it is thus possible to investigate the hole trapping effect on MC, charge injection and transport in P3HT.

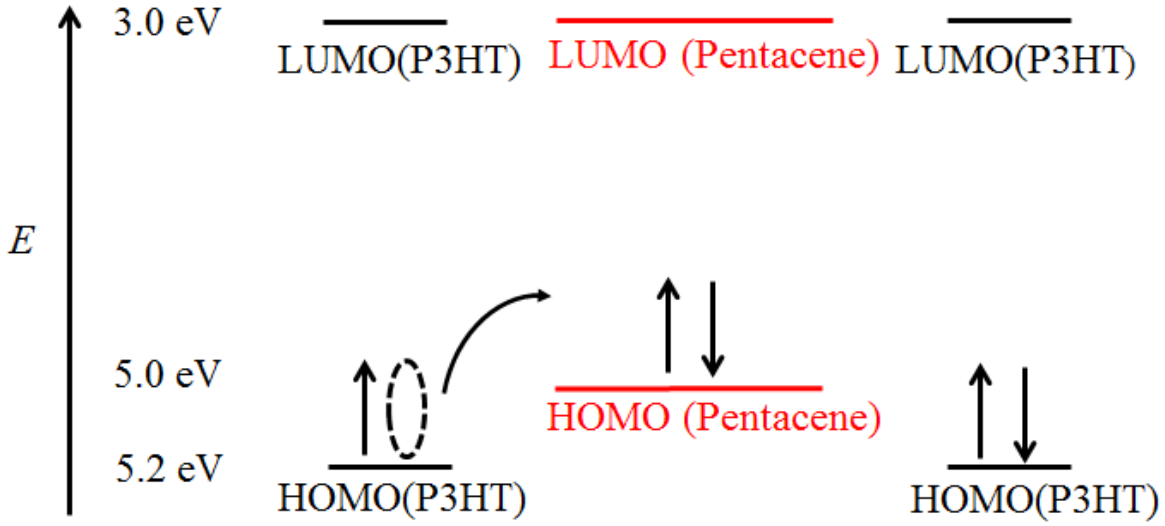

Figure 49: Band structure of pentacene as a hole trap centre in P3HT.

In the following sections, it will focus on the pentacene doping effect in P3HT consequent broadening the DoS. Annealing above the glass transition temperature of P3HT will also broaden the DoS. Meanwhile, pentacene can also act as a hole trap centre, which will both block the charge transport and broaden

the DoS of P3HT. Thus the pentacene doping effect will also result in the MC change. The detailed experiments are described in section 5 and section 6.

1.4 Organic Magnetoresistance

1.4.1 Early works on OMR

The studies of the magnetic field effect on the fluorescence properties of organic crystals can date back to 1967, when Merrifield's group showed the magnetic field dependence of the delayed fluorescence in anthracene crystals. [120] They observed that the intensity of delayed fluorescence, resulting from triplet-triplet annihilation (TTA), increased up to a maximum of 5% at a weak magnetic field of 35 mT and then decreased gradually, finally levelling off at 80% of its original value (B > 500 mT).

They also found that the magnitude of the high-field effect was a function of the relative direction between the field and the crystal axes. Initially, they assumed that four factors were possible to account for this phenomenon: absorption coefficient, triplet lifetime, TTA rate and singlet emission produced by TTA.

However, since there was no response on emission of singlet excitons generated directly from UV light, they eliminated the factor of singlet emission. They also excluded the factors of triplet lifetime and absorption coefficient by introducing pulsed-field techniques. The explanation was that if this effect was related to triplet lifetime or absorption coefficient, the build-up of the change in fluorescence intensity would follow the rapid rise-time and fall-time of the field pulse. Their results, however, showed that this field effect was independent of these two factors. At this stage, even without providing a detailed explanation of their observation, they believed that the physical factor should be the modulation of magnetic field on TTA rate.

To explain the magnetic field modulation of TTA rate, Merrifield et al. [121] presented a theory involving spin Hamiltonian terms for a triplet exciton. He stated that there were nine possible spin states for a pair of triplets (only six distinct pairs). There were two possible outcomes from the interaction of each triplet pair state: scattering which was independent of spin selection and annihilation which depended on spin selection. The reason is that only triplet

pairs that contained singlet component could undergo annihilation process. The general idea of Merrifields theory was that, when there was no magnetic field, only three triplet pairs among the nine possible pairs had singlet component. After the field was turned on, triplet pairs began to mix resulting in additional pair states possessing singlet component. As a result, more TTA would occur, which naturally led to an increase in delayed fluorescence intensity. While, at high field region, due to the large Zeeman splitting, spin states were quantized along the field and only two pair states had singlet character. Thus in the high field limit, there were fewer states with singlet character than that at zero-field, leading to a decrease in the delayed fluorescence intensity. In the same year, another work [122] from the same group reported a magnetic field dependence of triplet quenching rate. The triplet lifetime of anthracene at room temperature could be shortened significantly by low dosages of high-energy radiation. [123] It was believed that irradiation could introduce paramagnetic quenchers into target materials.

Merrifield et al. [123] irradiated anthracene sample with different dosages of X-Rays and found that a lifetime of 22 ms decreased to 1.5 ms after a dose of 4×10^{3} R. The irradiated sample was then going through a measurement of lifetime upon applying of magnetic field. An increase in triplet lifetime was found. Their qualitative understanding of an increase of lifetime was similar to the in magnetic field effect on TTA. They assumed that the interaction between a triplet exciton and a free radical (paramagnetic centre) would result in two outcomes: scattering which was spin selection independent and quenching which was spin selection dependent. They used a series of theories related to spin states, Hamiltonian and Eigen function to get a maximum quenching rate at zero-field.

In the 1970s further publications reported hyperfine field effect on the photo-physics of organic crystals. [124-125] It was found that under an external magnetic field, the intensity of delayed fluorescence firstly increased and then had a monotonic decay towards saturation, which was quite similar to that found in delayed fluorescence produced by direct optical excitation of anthracene, as reported in a previous work. [120] This phenomenon, observed in dye-sensitized anthracene, was obtained at a very low magnetic field. The maximum intensity was at 0.3 mT to 0.7 mT whilst the saturation was obtained at 20 mT to 30 mT. They attributed this to the field dependent surface recombination of electrons and holes. Owing to the different spin orientation

between singlet and triplet, only an unsymmetrical spin Hamiltonian can lead to a transition between them. They suggested that there were two components in the essential spin Hamiltonian of the present system, the unsymmetrical hyperfine interaction of the electron and the hole together with the symmetrical Zeeman term (electron and hole have the same *g* factors). At low field region, hyperfine interactions dominated the response so that singlet-triplet transition could appear, while at high fields region, the transition was only possible between singlet and $m = 0$ triplet state. This could explain the delayed fluorescence increased first and then decreased.

In 1975, M.Wittmer et al. [126] at the University of Basle reported their work on exciton trapped charge carrier interaction in anthracene crystal. It was the first example of investigated magnetic dependence of delayed fluorescence by electrical excitation. They studied the triplet trapped charge carrier interaction and singlet trapped charge carrier interaction with and without magnetic field. To remove the effect due to the free charge carriers, a high voltage supply was first used (to give a forward bias and inject charge carriers). Then, the forward bias was substituted by a reverse high voltage to remove free charge carriers in the bulk of the crystal. As a result, in the bulk only bound excitons and trapped charge carriers remained. It was found that trapped charge carriers could quench triplet excitons (since strong quenching of delayed fluorescence from the excited singlet state was found). As for the quenching of delayed fluorescence, it suggested that dissociation of triplet pairs in presence of charge carriers played a great role. These early works showed how magnetic fields affected exciton population and exciton/charge carrier interactions within organic materials. However, only fluorescence was discussed and more work needed to be done to explain the magnetic field effect clearly.

In the following part, a detailed review of the publications related to the origin of OMR will be given in terms of publication time as well as research group. Since different groups promoted different systems and different ways of characterizing a device, direct comparison of their data is quite difficult. Thus, the models used to explain OMR effects will be described separately.

1.4.1.1 Kalinowski's Polaron Pair model

In the first work, Kalinowski [127] carried out MR measurement on OLED devices with a structure of ITO(anode)/TPD:PC(HTL)/ Alq_3 (ETL)

/Ca/Ag(cathode). Light emission and current were found to increase by up to 5% and 3%, respectively as the external magnetic field increased to 300 mT. An increase of quantum efficiency (~3%) was also observed. Kalinowski characterized the current and the luminescence with a percentage change treatment that included the values measured with and without field (B):

$$\frac{X(B) - X(0)}{X(0)} \times 100\% \tag{34}$$

Kalinowki proposed a mechanism to explain these phenomena, which was known as the Polaron Pair model. Figure 50 shows the scheme used to describe his model. Electrons and holes injected from electrodes meet in the Alq_3 emitter forming singlet and triplet pair states with the probability of P_1 and P_3 respectively. They form singlet (S_1) which can come back to ground state (S_0) through light emission and triplet (T_1) which can relax non-radiatively to the S_0 state. Besides that, both singlet and triplet are expected to diffuse to the Ca cathode and dissociate there, releasing electrons back to the bulk. There is a mixture between singlet and triplet pair states with an effective rate constant k_{ST} due to hyperfine interaction, the results from this process can be considered as a pure transformation between singlet and triplet excitons. When there is no external field, the triplet states (T_+, T_-, and T_0) are degenerate, the mixing is therefore possible between singlets (S_1) and all components of triplets, the mixing rate is solely determined by hyperfine coupling. In the presence of a magnetic field bigger than the hyperfine strength, the degeneracy between singlet and triplet is removed. As a result, the mixing of S_1, T_+ and T_- is affected by the external field. However, when the magnetic field is much bigger than the hyperfine strength, there is no more mixing between S_1, T_+ and T_-, mixing can just occur between S_1 and T_0, which could explain that there is only a slight increase of light emission at high field regions.

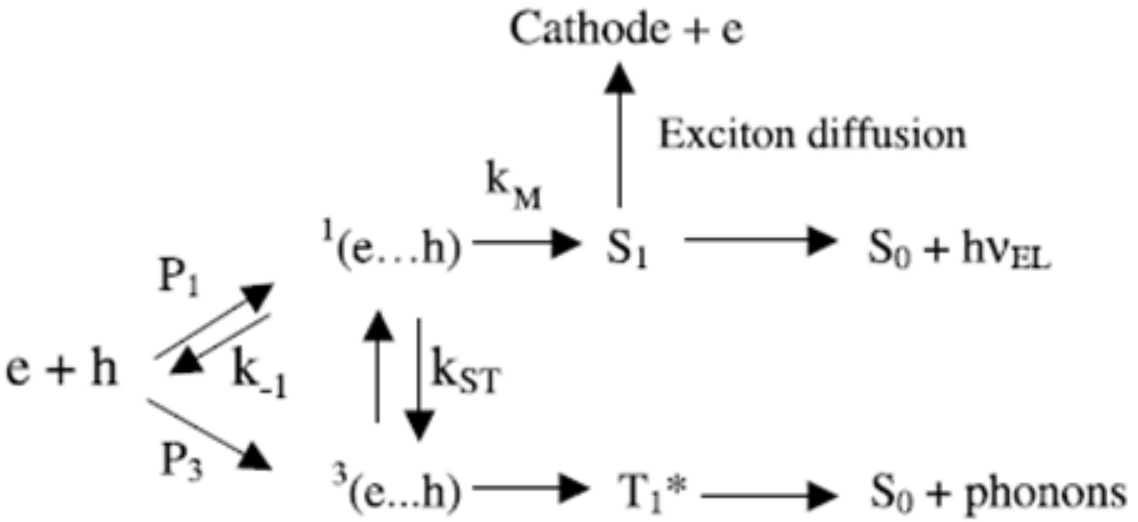

Figure 50: Schematic of Polaron Pair model. S_1 represents singlet and T_1^* represents triplet. Reproduced from ref. [127]

The main theory behind this model is that, when there is no field, mixing can happen among singlet and all triplet components, the rate k_{ST} is determined by hyperfine coupling between electron (hole) and the nucleus. Meanwhile, the Zeeman splitting energy is ~ μeV too small to remove the degeneracy. Instead, an applied external field allows only the mixing between singlets and some of triplets, which gives a smaller k_{ST} resulting in an increase of singlet exciton population and light emission. The positive magnetic field effect (MFE) on device current is attributed to the electrons released back to the bulk by dissociation of singlets at the cathode. Since the external magnetic field delivers more singlets which improves the dissociation component, finally giving a rise to an increase in the current density.

There are two aspects not clear in their model: one is that Kalinowski didn't explain why he assumed that the mixing was occurring in pair states rather than exciton states; the other one is that both singlet and triplet are expected to diffuse to the cathode and dissociate there. In their model the diffusion of triplet is neglected with the effective triplet-triplet and triplet-polaron interaction which contributing to OMR response. However, when considering the electrically pumping ratio of singlet and triplet and the triplet with a much higher lifetime than singlet, the contribution of MR response due to triplet cannot be neglected.

In 2004, Kalinowski et al. [128] extended their investigation of MFE on organic devices to the MFE on organic electrophosphorescence. They doped molecules containing heavy metal atoms into emissive layer producing

phosphorescence. It was possible to get triplet emission within the metal-organic complexes system. MFEs were compared among three types of devices: ITO/TPD:PC/PBD/Ca, ITO/TPD:PC($Ir(ppy)_3$)/PBD/Ca and ITO/TPD:PC(PtOEP)/Ca. There was a different line shape in the responses between the doped and undoped samples. It was found that there was a rapid increase in quantum efficiency at very low field regime around 10 mT, followed by a gradual increase under high fields. It was worth noticing that there was ~4% increase in quantum efficiency at a field of 500 mT (without a trend showing saturation). The other two devices with doped metal-organic complexes showed similar field response, with the quantum efficiency that firstly increased and then decreased. Both had a maximum increase by up to 6% and 2% separately at a field around 500 mT.

1.4.1.2 The Iowa group and mathematical fitting of OMR

In the year 2004, Wohlgenannt et al. [129] reported their work of MFE on OLED device based on a polymer, PFO. In that paper, they defined the magnetic field effect as a percentage change in device resistance before and after applying field, named as MR:

$$\frac{\Delta R}{R} = \frac{R(B) - R(0)}{R(0)} \tag{35}$$

Where $R(B)$ is the device resistance at an applied field and $R(0)$ is the device resistance at zero-field.

They investigated many aspects of the performance of a device in the presence of an external field by varying the electrodes (for example PEDOT:PSS/PFO(100 nm)/Ca and ITO/PFO(100 nm)/Ca), the thickness of the active layer, the temperature, and the direction of the field. OMR measurements were tested on a PFO sandwiched device at room temperature at the range from -100 mT to +100 mT. It was found that the OMR traces were independent of the angle between the film plane and applied field. Using PEDOT:PSS as an anode resulted in a significant reduction in the onset voltage and an increase in the observed OMR effect. This difference was attributed to the improved hole injection and reduced interface series resistance. For devices with other electrodes, there was difference in either thickness and anodes or thickness and cathode, which made the comparison inaccurate. They stated that the observed

OMR was largely independent of the cathode material and occurred also in a unipolar device (Au as cathode and ITO as anode), interestingly, they discovered a weak electroluminescence in this unipolar device. As a result, they concluded that the OMR effect was only due to hole transport without electron or electron-hole recombination processes. The observed MFE appeared to be independent of exciton processes presented in OLEDs.

For the thickness study, they found a proportional relationship between the onset voltage and polymer thickness, which suggested a shift in the voltage to drive these devices. When they ignored the shift of the operating voltage, they discovered a similar MR response in devices with thickness of 60 nm, 140 nm, and 300 nm. Therefore, they concluded that MR was a bulk rather than an interface effect. This conclusion was also supported by the fact that MR effect was also observed for devices with an anode of PEDOT:PSS, ITO and Au. Their study of MR from 10 K to 300 K suggested that the magnitude and width of the MR were not sensitive to the change of temperature.

After investigating the MR on PFO, Wohlgenannt et al. [130] extended their research to small molecule devices. They chose Alq_3 as the active layer, and performed a similar work of MR. [130] Similar results were obtained and similar conclusions regarding MR on temperature, active layer thickness and direction of the field were reported. As for the MR dependence of electrodes, unlike that stated in PFO devices, it was found that both I-V and OMR responses critically depended on the choice of the cathode material. A Ca cathode resulted in low onset voltage and large OMR response, whereas Al resulted in a drastic increase in the onset voltage and decrease in OMR magnitude at small currents. At high voltages, the OMR response became as large as that in Ca cathode device. This situation was even more obvious in Au cathode device. The increased onset voltage and decreased OMR response could be rationalized regarding the increase of interface series resistance in Al and Au compared to that of Ca. In their early work, [129] they concluded that, in the case of PFO devices, no cathode dependence of OMR effect was present.

Considering PFO is a hole transporting material, there may be no anode dependence of OMR in Alq_3 device, because Alq_3 is an electron transport material. However, they found considerable change in the onset voltage by changing the anode from PEDOT:PSS to ITO. It seems that holes are also important in Alq_3 device, but it is not clear the role of holes or electrons in OMR or at least which role dominates the MR response in different materials.

The percentage change in EL is commonly investigated by keeping the voltage constant ($\Delta EL/EL|V$). Wohlgenannt et al. [130] investigated this percentage change also by keeping the current constant ($\Delta EL/EL|I$). Results showed that $\Delta EL/EL|V << \Delta EL/EL|I$, suggesting that the magnetotransport effect was the primary effect, whereas the magnetoluminescence effect was secondary. The normalized traces in PEDOT:PSS/Alq_3/Ca and PEDOT:PSS/PFO/Ca devices overlaps each other quite well, which indicates that the explanation of the OMR effect must be quite general and simple, since PFO and Alq_3 has different chemical structures and transport properties but possessed identical OMR line shape.

In 2005, Wohlgenannt et al. [131] published a review of the OMR effect, including both polymers and small molecules. The OMR measurements were carried out over a range of temperatures and voltages. They used the regioregular (RR) and regiorandom (RRa) P3HT to test the effects of disorder and mobility on magnetoresistance and found that the MR response was larger in more disordered polymers.

They also carried out the MC response on metal-organic complexes. According to Kalinowski's idea of magnetically reduced intersystem crossing, large fields were needed to observe the OMR effect in 5,8-diethynyl-2,3-diphenylquinoxaline unit and its platinum-containing polymer (Pt-PPE) device. However, such an effect was not observed, therefore, they concluded that there was no spin orbital effect.

They plotted all the normalized OMR values, obtained from each material at room temperature, in one graph at a field range from -50 mT to +50 mT as shown in figure 51. The line shape of these data fell into two groups, namely "fully saturated" group including materials of pentacene, RR-P3HT and RRa-P3OT; the "weakly saturated" group including the remaining materials of PFO, Alq_3, Pt-PPE and PPE.

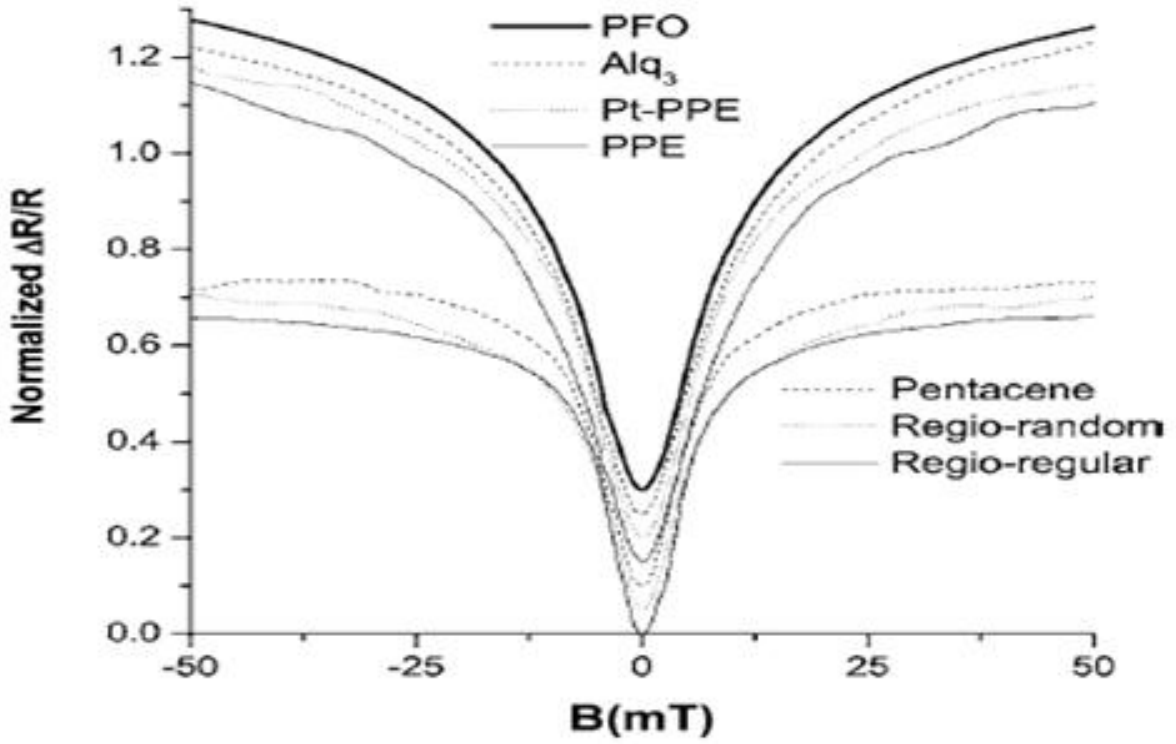

Figure 51: Fully saturated and weakly saturated OMR line shape. Reproduced from ref. [131]

To explore the function dependence of OMR on B(mT) , PFO and RR-P3HT data (representing "fully saturated" and "weakly saturated" group respectively) were presented and this time the $\Delta I/I$ was presented. They found that data of "fully saturated" RR-P3HT could be fitted accurately by an empirical function named as Lorentzian function:

$$\frac{\Delta I}{I} = \left(\frac{\Delta I}{I}\right)_{\max} \left(\frac{B^2}{B^2 + B_0^2}\right) \tag{36}$$

Where $(\Delta I/I)$ max denotes the percentage change in current at infinite field and B_0 is positive and denotes the half-saturation field. While data from "weakly saturated" group can be fitted by another empirical law named as non-Lorentzian function:

$$\frac{\Delta I}{I} = \left(\frac{\Delta I}{I}\right)_{\max} \left(\frac{|B|}{|B| + B_0}\right)^2 \tag{37}$$

Where $(\Delta I/I)_{\max}$ has the same meaning as that in equation 36, B_0 is positive in this case and denotes quarter-saturation field.

It was stated that data from each group could also be fitted by the corresponding empirical law function. They noted that equation 36 was predicted by simple theories of classical magnetoresistance. [132] The authors showed favour to models involving pairs of electrons and holes as a possible mechanism for organic magnetoresistance. The dipole field between such pairs was an order of 10 mT. They also considered the possibility of spin-dependent bipolaron formation as a mechanism, but did not elaborate.

1.4.1.3 Ohio group MIST model

In 2006, Prigodin et al. [133] in Ohio group studied the MR effect on Alq_3 based devices with similar structure as that used in Iowa group. Devices of pure Alq_3, $Ir(ppy)_3$ doped and Pt-OEP doped were fabricated. The conducted MR measurements were carried out with different voltages and temperatures over a field range from – 100 mT to +100 mT. For the device of pure Alq_3, it was found that the MR was negative at all temperatures and voltages. There was a decrease in magnetoresistance as temperature decreased. By comparing with the MR effect from $Ir(ppy)_3$ doped and Pt-OEP doped samples at room temperature, there was a decrease in $Ir(ppy)_3$ doped sample with a factor of ~10, while there was no MR effect in Pt-OEP doped sample. They stated that large spin-orbit coupling in the semiconductor would diminish the MR response. The larger reduction of MR in the Pt-OEP doped film over the $Ir(ppy)_3$ doped film was in agreement with more efficient energy transfer from triplets in the Alq_3 host to the phosphorescent guest. [134]

Their work continued in 2008, [135] they fabricated devices using sexithiophene (*α-6T*) as an active layer with different thickness, temperature and driving voltage. Both positive and negative MR responses were discovered in their experiments. They proposed the MR controlled by inter-conversion of singlet and triplet (MIST) model in their first work [133] and further discussed it in another one. [135]

The main idea of this model is quite similar to that demonstrated by Kalinowski, however it is implied in this case that the source of current is from triplet dissociation, which is temperature dependent. In this model, polaron pair states residing on one molecule or neighbouring molecules can dissociate back to charge carriers and contributed to current or light emission through radiative

decay. In the MIST model, the MR response appears due to the sensitivity of carrier recombination to magnetic field. Uncorrelated electrons and holes form Coulomb bound pairs with equal probability of forming a singlet (S_1) or one of the three triplet configurations (T_-, T_0 and T_+). Hyperfine interaction allows the mixing between degenerate singlet and triplet states. At zero-field, the singlet level is degenerate with the entire triplet manifold and spin-mixing appears among the four states. However, in the presence of a magnetic field, the degeneracy of the triplet states is lifted by Zeeman splitting, and inter-conversion only occurs between the $m = 0$ states, while the long-lived triplets in the $m = \pm 1$ states no longer interconvert with the singlet and will probably dissociate.

Based on early work, in the following section, Electron-Hole Pair model, Bipolaron model and Triplet-Polaron Interaction model will be introduced and discussed.

1.4.2 Electron-Hole Pair model

Hu et al. [136] released their first work on MFE in 2006 studying spin-orbit coupling and MR in organic devices. Devices with MEHPPV active layer, ITO as anode and Al or Au as cathodes were fabricated. MR measurements were carried out from reverse to forward bias. Their results showed a dependence of MR on driving voltage. In forward bias, the results revealed smaller dependence of MR and MEL on field with respect to that of reverse bias. Based on the work function explanation, they stated that in forward bias, the electron-hole recombination zone was close to metal/organic interface while that in reverse bias it was close to ITO/organic interface. They proposed that the deposited metal electrode increased the spin-orbit coupling effect of MEHPPV due to the penetration of delocalized electrons into the orbital field of metal atoms upon the interfacial diffusion of metal atoms during vacuum deposition.

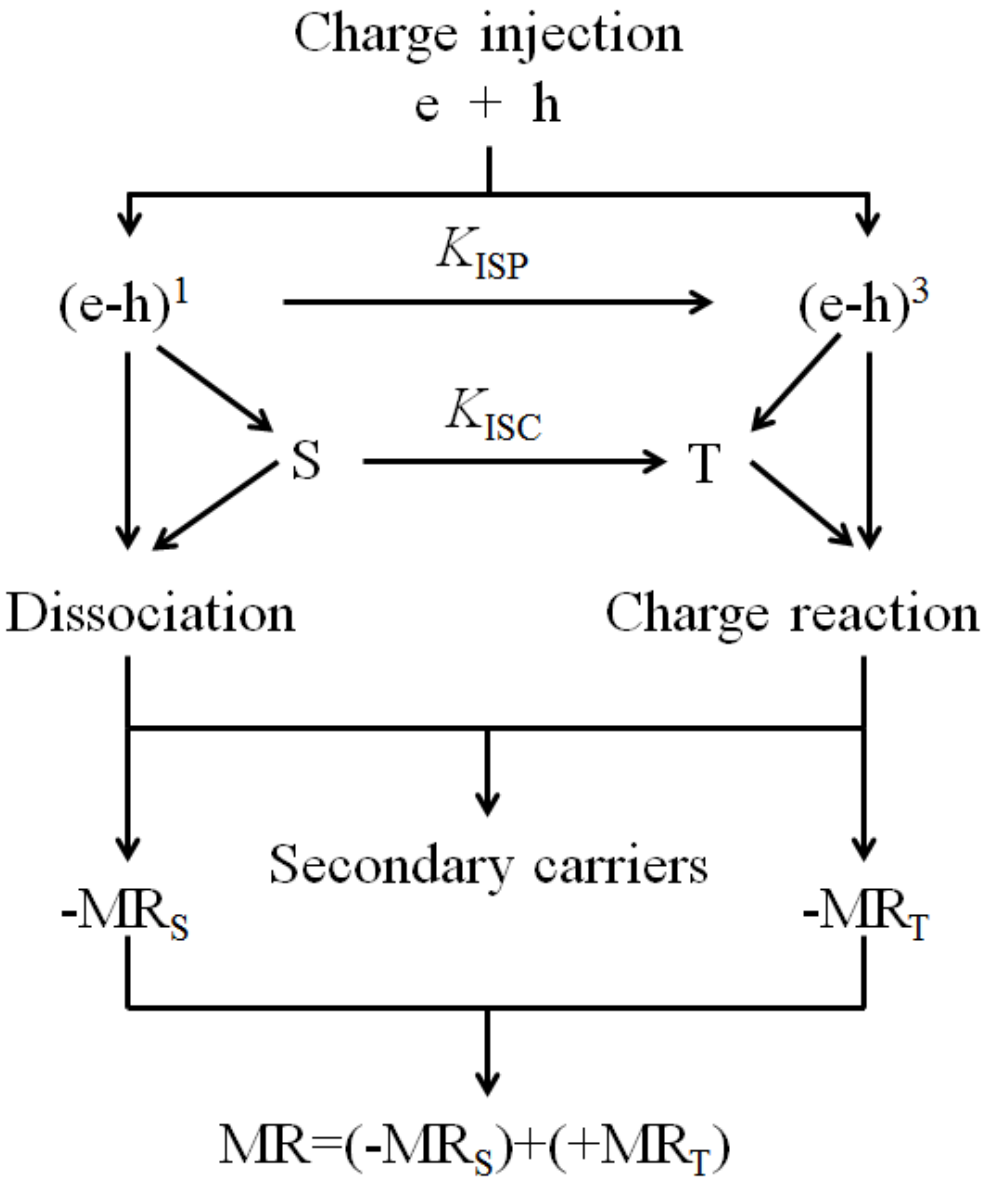

Figure 52: Schematic of electron-hole pair model: e and h represent electron and hole polarons, (e-h)^1 and (e-h)^3 represent singlet and triplet polaron pairs, S and T represent singlet and triplet excitons, negative magnetoresistance (MR) component (–MR$_S$) is from the dissociation dominated by singlet excited states, positive MR component (+MR$_T$) is from the charge reaction dominated by triplet excited states, K$_{ISP}$ and K$_{ISC}$ are intersystem crossings in e–h pairs and excitons. Reproduced from ref. [137]

They suggested that it was the competition between the internal Zeeman splitting (with the energy of ~meV) induced by spin-orbit coupling and the external Zeeman splitting caused by an external magnetic field that determined the intersystem crossing rate and the singlet/triplet ratio. Therefore, the enhanced spin-orbit coupling in the metal/organic interface weakened the dependence of the singlet/triplet ratio on magnetic field, which induced a weak dependence of MR and MEL on external field.

When the electron-hole recombination zone was pushed away from the metal/organic interface, they experienced weak spin-orbit coupling, as thus the singlet/triplet ratio could be modulated more strongly by an applied field, giving a higher MR response. By introducing a buffer layer between the metal and organic material, they observed an improved MR supporting their assumption. Compared to Al, Au as a cathode showed an even weaker MR in forward bias. This was also in agreement with their view of spin-orbit coupling since Au could introduce larger spin-orbit coupling in the metal/organic interface.

One year later, Hu et al. [137] discussed the mechanism they used to explain MR, namely the secondary charge carrier model. Figure 52 shows the schematic used to demonstrate this model. The main idea is that the electrons and holes resulting from the field dependent excited states or polaron pair states dissociation and triplet-charge carrier interaction gives a rise to the observed MR. An applied external field decreases the inter-conversion of singlet and triplet leading to an increase in singlet population and a decrease in triplet population. The increase of singlet leads to an increase of charge carriers with singlet dissociation, yielding a negative MR. Secondly, the decrease of triplets reduces the triplet-charge carrier interaction for the generation of free charge carriers, therefore, generates a positive MR. The overall MR is a combination of the two components.

Based on this idea, they carried out experiments to tune the MR between positive and negative by changing the charge carrier balanced injected into the active layer. When tuning charge carriers from an unbalanced state to a balanced state, the role of triplet-carrier interaction became weaker while the role of singlet dissociation became stronger, therefore, a negative trend of MR could be achieved. On the other hand, by tuning an already unbalanced system towards even more unbalanced state, bigger positive components in MR could be achieved. Their devices were based on MEHPPV, Alq_3 and PVK active layers, PMMA as an insulation buffer layer, ITO as anode, Al or Au as cathode. Experimental results were consistent with their predictions.

However, they did not clearly explain why the singlet pairs undergo a dissociation process instead of radiative decay and did not mention why the triplet dissociation did not contributed to MR in the device.

1.4.3 Bipolaron model

In 2007, the model for OMR based on spin dynamics was established by groups from the University of Iowa, USA and University of Eindhoven, Netherland. [138] The bipolaron intermediate will be formed if two electrons have different spin states. This kind of bipolaron can be described as an electron trap site. As shown in figure 53, charge carriers can either hop onto an empty site forming a polaron or hop onto an occupied site forming a bipolaron. For bipolaron formation, there are spin selection rules that determine whether or not a charge can hop onto the site which is already occupied by a polaron. Namely, two polarons having the same spin component along a common quantization axis have no probability and cannot form a bipolaron. This "spin blocking" mechanism is the basic notion of their theory. According to Pauli Exclusion Principle, [1] bipolarons can only be formed in a singlet configuration. The hydrogen atoms generate a very small hyperfine field which is totally random. The spin state of the injected charges can flip to any possible direction due to the random hyperfine field.

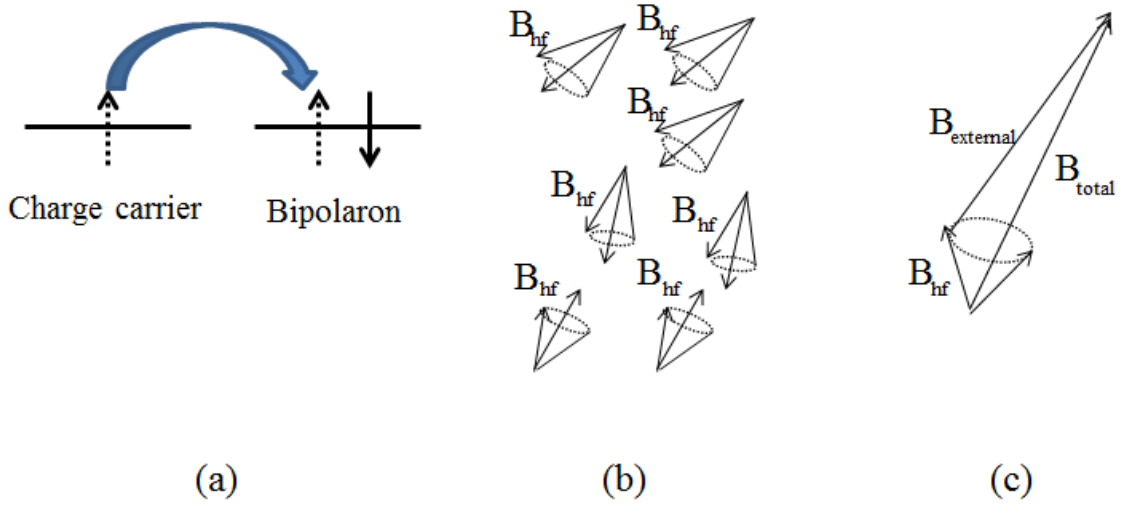

Figure 53: Schematic of bipolaron, hyperfine, and precession and total magnetic field precession of injected charge carriers. (a) bipolaron formation, (b) hyperfine precession and (c) injected charge precession under total magnetic field.

In this model, the OMR depends upon the probability of forming a singlet like bipolaron. The singlet bipolaron formation is defined by the local magnetic field which is the sum of the fields due to hydrogen dipoles and the external magnetic field, $B_{external}$. Polarons are exposed to a local hyperfine field produced by the hydrogen nuclei, which can be treated as a random classical field B_{hf}. As a result, the total field experienced by a polaron is a combination of $B_{external}$ and

$B_{hf} : B_{total} = B_{external} + B_{hf}$. The transport behaviour of a polaron α is either hop to a site β which is already occupied by a carrier with opposite spin to form a bipolaron or hop to another empty site. Assuming that the probability of situation is P, then P equals to 1/4 when there is no $B_{external}$, when there is a large $B_{external}$, P equals to 1/2.

The authors suggested that it was the field dependent branch ratio of these two situations that accounted for the MEF. To test this model, Monte Carlo simulations were employed to modify the MR of a system. A randomly oriented hyperfine field of strength B_{hf} is attributed to each site with the site energy of Gaussian DoS. The simulation also took into account the intra-site Coulomb repulsion U and a spherical region of long-range Coulomb repulsion around each carrier. Both positive and negative MR responses were achieved, as well as the empirical function fitting results.

However, this model does not take into account the formation of excitons. In their model, it is easy for us to see the OMR in any unipolar material. The absence of electron injection (or hole injection) will not affect the formation of the bipolaron.

1.4.4 Triplet-Polaron Interaction model

Based on the preliminary work by Pratik Desai and Sijie Zhang from Queen Mary University of London, [139-143] the observation of OMR measurements on OLED structured devices strongly suggested excitons lay at the origins of OMR. They chose the small molecule Alq_3 to carry out the MR measurement. In their results, OMR was only visible when both holes and electrons were injected into the device. Alq_3 was always used as an electron transport layer, and the "turn on" voltage was defined as the voltage where electron started to inject into the device. Their results showed that no OMR could be seen below the "turn on" voltage. Then they also introduced singlet excitons by illumination and observed the effects of a magnetic field. [144] In that case, OMR appeared even below the "turn on" voltage which strongly suggested OMR effect device was due to the magnetic field modulation of the photo-generated excitons.

In order to explain the mechanism of OMR based on exciton formation, they promoted a simple schematic diagram of the processes controlling the

population of singlets and triplets within an organic material in figure 54. Both electrical pumping and optical pumping lead to the formation of the excited states (excitons) in the organic material. If the excitation is optical pumping, no triplets can be produced under illumination, which means *B* is equal to 0 and *A* is equal to 100%.

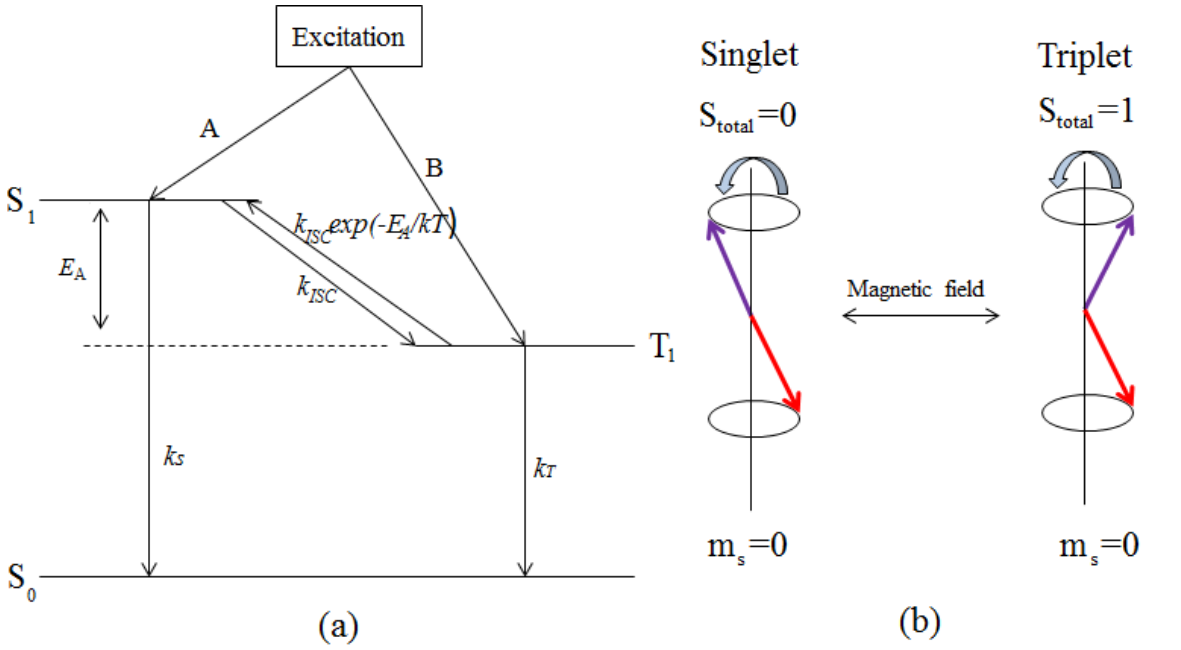

Figure 54: (a) Schematic of the excitation and recombination pathways in the organic molecule. (b) Schematic of intersystem crossing between singlet and triplet through magnetic field.

In their experiment, the excitation was caused by the interaction of holes and electrons. As explained in section 1, there are four kinds of results and one fourth of them are singlets and the other three are triplets. So in this condition, *A* is equal to 25% and *B* is equal to 75%, if there is no external influence. As radiative recombination of triplets is forbidden, the life time of triplet is many times longer than that of the singlet, which means the rate constant of the singlet decay is higher than that of the triplet ($k_S >> k_T$). The term k_{ISC} is introduced to denote the intersystem crossing from singlet to triplet. As the existence of the energy barrier E_A to undergo, the intersystem crossing term is modified as $k_{ISC}exp(-E_A/kT)$ for a finite temperature *T*. After electrical excitation, the system reaching a steady state, the change of triplet (T_1) in the intersystem crossing process in figure 54(a) can be described in equation 38:

$$\frac{dT_1}{dt} = k_{ISC}S_1 - k_T T_1 - k_{ISC}\exp(\frac{-E_A}{kT}) \tag{38}$$

Where S_0, S_1 and T_1 represent the population of the ground state, singlet state and triplet state respectively, k_S and k_T are the recombination rates for singlet and triplet states, k_{ISC} is the rate constant for intersystem crossing, k is the Boltzmann constant, and E_A is the activation energy for the interchange from the triplet to the singlet.

In this system, a triplet can be changed into singlet if there is large population of triplets and the temperature is sufficient enough to overcome the energetic barrier. Theoretically for electrical excitation, the triplet to singlet ratio will be 3:1 if there is no external influence. As shown in figure 54(b) a vector diagram to describe the magnetic field alter the intersystem crossing between singlet states and triplet states, the effect of this magnetic field induced mixing will be able to increase k_{ISC} and will depend on the relative concentration of singlet and triplet as well as the temperature (to overcome the activation energy E_A) of the system. So the triplet concentration will decrease under the magnetic field.

Hence, if there is an accumulation of triplets in the device due to the electrical injection, the MEFs decrease their concentration by intersystem crossing, so that there are fewer interactions of the free carriers with the triplets, which increased the mobility of the free carriers. It has become clear that from the preliminary study of OMR in Alq_3, there are many important processes and parameters which are involved in causing changes in current, efficiency and light output. In addition to hyperfine scale interaction of the singlet and triplet intersystem crossing at low magnetic fields, the triplet-carrier interaction becomes important at high magnetic fields. In the triplet-carrier interaction process, the trapping and scattering of carriers are found to be magnetic field dependent and this affects the mobility of the free carriers significantly.

The preliminary work by Jinyao Song [145] from Queen Mary University of London proved the function of this model through measuring the mobility ratio. He applied an offset voltage to both of the small molecule based unipolar device (ITO/TPD/Au) and the ambipolar device (ITO/TPD/Al) to detect the change of the mobility. Excitons, generated only in the ambipolar device, would block the charge carrier transport to reduce the mobility of TPD. So the mobility began to drop after the “turn on”. Then they applied a magnetic field (500 mT) after “turn on” and discovered an increase of the mobility. This phenomenon can be well explained by the model in figure 54. After electrical excitation, the system reaches a steady state and the triplet concentration will decrease with the

application of the magnetic field based on the intersystem crossing mechanism. So the mobility ratio will increase.

However, the triplet-polaron interaction model cannot explain the negative MC response under low bias in polymers [146] and the large negative MC response in zeolite materials. [147] Under low bias, there are not enough excitons to dissociate in PPV or P3HT leading to negative magnetoconductance (MC). Thus, the negative MC must be attributed to other mechanisms such as the bipolaron model.

Above all, no single model can explain the MC response both in small molecule and polymer based organic semiconductors. In the following experiment section, it is proposed to use a combination of different mechanisms to explain the MC response in different conditions.

2. Experimental and Measurement Techniques

2.1 Material selection:

The major materials tested in the experiment were P3HT (Mw 652000, Mn 296000 and regioregularity 95.7%) supplied by Ossila and pentacene (purity >99.9%) supplied by Sigma Aldrich. The solvent to dissolve P3HT and pentacene was 1,2-dicholorobenzene (purity > 99%) supplied by Sigma Aldrich.

The electrode materials were ITO (thickness 100 nm, resistance 15 ohms/sq) supplied by Visionteksystems, Au (purity >99.99%) supplied by Sigma Aldrich and Al (purity >99.999%) supplied by Kurt J. Lesker Company.

The buffer layer for hole injection was poly(3,4-ethylenedioxythiophene) polystyrene (PEDOT:PSS) (2.8% wt dispersion in water) and for electron injection was LiF (purity >99.995%) supplied by Sigma Aldrich.

The solvents for substrate cleaning were acetone (purity >99.8%) and chloroform (purity >99.9%) supplied by ROMIL.

2.2 Device Fabrication

Three main device architectures were fabricated in the experiment: Au/P3HT/Al, Au/P3HT/ITO and ITO/PEDOT:PSS/P3HT/LiF/Al.

2.2.1 Solution preparation

For P3HT solution, 30.0 mg P3HT was weighted and dissolved in 1 ml 1,2-dicholorobenzene. The solution was warmed to 60 ^{o}C using a magnet rod, stirred for 6 hours and filtered using 1 ml syringe and filter (0.2 μm).

For pentacene solution, 6.0 mg, 15.0 mg and 30.0 mg pentacene were weighted and dissolved in 10 ml 1,2-dicholorobenzene. The solution was warmed to 120 ^{o}C and stirred for 24 hours. The solution colour changed to yellow as the pentacene dissolved and the colour became deeper as the concentration increased.

For P3HT and pentacene mixed solution, 1 ml pure pentacene solution was selected as the solvent for P3HT. 29.4 mg, 28.5 mg and 27.0 mg P3HT

were separately weighed and dissolved in the solvent resulting in the pentacene doping concentration of 2%, 5% and 10%. All solutions were warmed to 60 ^{o}C and stirred for 6 hours and filtered using a 1 ml syringe and filter (0.2 μm).

2.2.2 Substrate preparation

2.2.2.1 Substrate cleaning

The cleaning process was crucial. Any failure in the cleaning procedure would result in poor performance of devices. To achieve the proper cleaning requirement, the substrates coated with 100 nm ITO were cleaned in detergent and solvents using an ultrasonic bath. The substrates were first washed with the detergent in distilled water. They were then transferred to specially designed holders and inserted into the beaker containing the solution of detergent and distilled water. The beaker was then placed in an ultrasonic bath for about 20 minutes. This process was called ultrasonication. The sonicator induced a high frequency acoustic wave in the liquid, which led to the formation of microscopic gas bubbles. When these bubbles collapsed, the energy would transfer to the substrate surface to remove the microscopic impurities. Further ultrasonications were repeated three times, with the substrates being immersed in distilled water for five minutes per rinse. After this, the substrates were ultrasonicated in acetone and chloroform for five minutes and repeated twice. Finally the ITO substrates were dried using a nitrogen gas gun. Once cleaned, the ITO substrates were subjected to a series of photo-chemical processes to pattern to get the designed structures.

2.2.2.2 Substrate patterning

The first step of this process was to spin-coat a layer of Shipley 1818 sp16 photoresist onto the surface of ITO substrate. This was done to ensure a uniform layer of photoresist. The substrate was mounted onto the chuck of the spin-coater with the ITO surface facing upward. The vacuum generated by the pump was to hold the substrate while it was spinning. About 7 drops of photoresist solution were dropped onto the ITO substrate using a pipette. The wetting of the substrate was carried out at 500 rpm for 18 seconds and then accelerated up to 6000-7000 rpm and maintained for 60 s. The substrate was then cured for 15 minutes in the oven at 90^{o}C.

Next, the pattern of the electrodes needed to be exposed onto the photoresist. The substrates were laid, photoresist solution side down, upon the mask as shown in figure 55 in a black box UV exposure unit. The substrates were then exposed to the light source for 60 seconds. Next, they were immersed in the NaOH based developing solution with the density of 0.33 g/ml. The substrate was submerged for 60 seconds, then rinsed with distilled water in the sonic bath for five minutes and dried with a nitrogen gas gun.

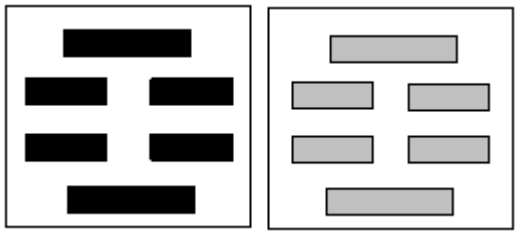

Figure 55: Schematic of mask (left) for UV light and patterned substrate (right).

The final step was to remove the exposed ITO. The etching solution was a mixture of 50% distilled water, 48% hydrochloric acid and 2% nitric acid. Using a beaker, it was heated in a water bath to between 48^{o}C and 50^{o}C, after which the substrate was soaked in the solution for 1 minute 45 seconds then immediately rinsed with distilled water in the sonic bath. To remove the remaining photoresist, the sample was cleaned by acetone in the sonic bath for five minutes. The ITO substrates went through another cleaning process (in detergent, acetone and chloroform) and then dried with nitrogen gas gun for next step of plasma treatment.

2.2.2.3 Plasma treatment

For ITO/P3HT/Au and ITO/PEDOT:PSS/P3HT/LiF/Al devices, the plasma treatment was carried out to remove impurities from the patterned ITO and increase the work function of the ITO. The cleaned ITO substrate was transferred into a Diner Electronic Femto plasma system with the ITO facing up. Oxygen gas was allowed to flow through this chamber and kept at a pressure of about 2 mbar for five minutes to ensure the system was oxygen rich. The power of the plasma system was adjusted to 30 W, and the treatment time was 4 minutes. When the pressure of oxygen gas was lowered to about 0.2 mbar, the generator was switched on and the ITO substrates were treated for the desired time. Once the treatment was completed, the ITO substrate was mounted onto a

sample holder with an aperture in the middle allowing materials to be evaporated onto the substrate.

For Au electrodes, 50 nm Au was evaporated directly onto ITO and the detail of evaporation will be described with LiF and Al in the thermal evaporation sections.

2.2.3 Material spin-coating

For the ITO/PEDOT:PSS/P3HT/LiF/Al device, the PEDOT:PSS layer was spin-coated at room temperature with the speed of 3000 rpm for 60 seconds. After baking at 120 ^{o}C for 15 minutes on the hot plate, the thickness of PEDOT:PSS was around ~100 nm confirmed by the Dektak profilometer. For other devices, P3HT was directly spun coated onto the electrode.

Both the pure and pentacene doped P3HT solutions were heated to 60 ^{o}C on the hot-plate before spin-coating. The pre-speed was set to 1000 rpm with the time 3 seconds and the rotation speed was also 1000 rpm with the time 60 seconds.

The patterned substrate was mounted on the chuck of the spin-coater with the ITO or Au surface facing upwards. The substrate was securely held by the vacuum generated by the pump. About 12 drops of P3HT solution were dropped onto the patterned substrate using a glass pipette. Single layer P3HT was ~150 nm as confirmed by the Dektak profilometer. To build up a thicker P3HT layers, 5 layers of pure P3HT or pentacene doped P3HT solution were successively spin-coated. The thickness was confirmed between 300 nm and 350 nm using the Dektak profilometer.

2.2.4 Thermal evaporation

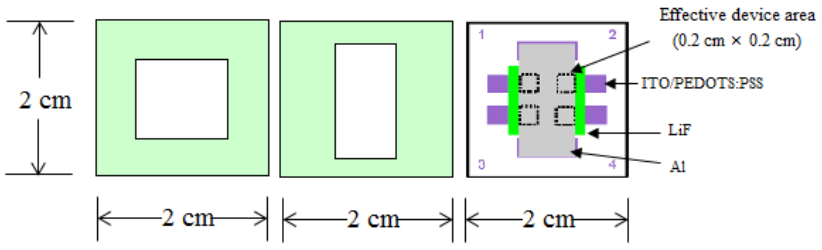

Figure 56: Schematic of evaporation mask for LiF (left) and metal (middle) and proposed diode structure (right).

The metal electrodes Au, Al and the electron buffer layer LiF were completed through thermal evaporation using mask shown in figure 56 in a Kurt J. Lesker Spectros evaporation system.

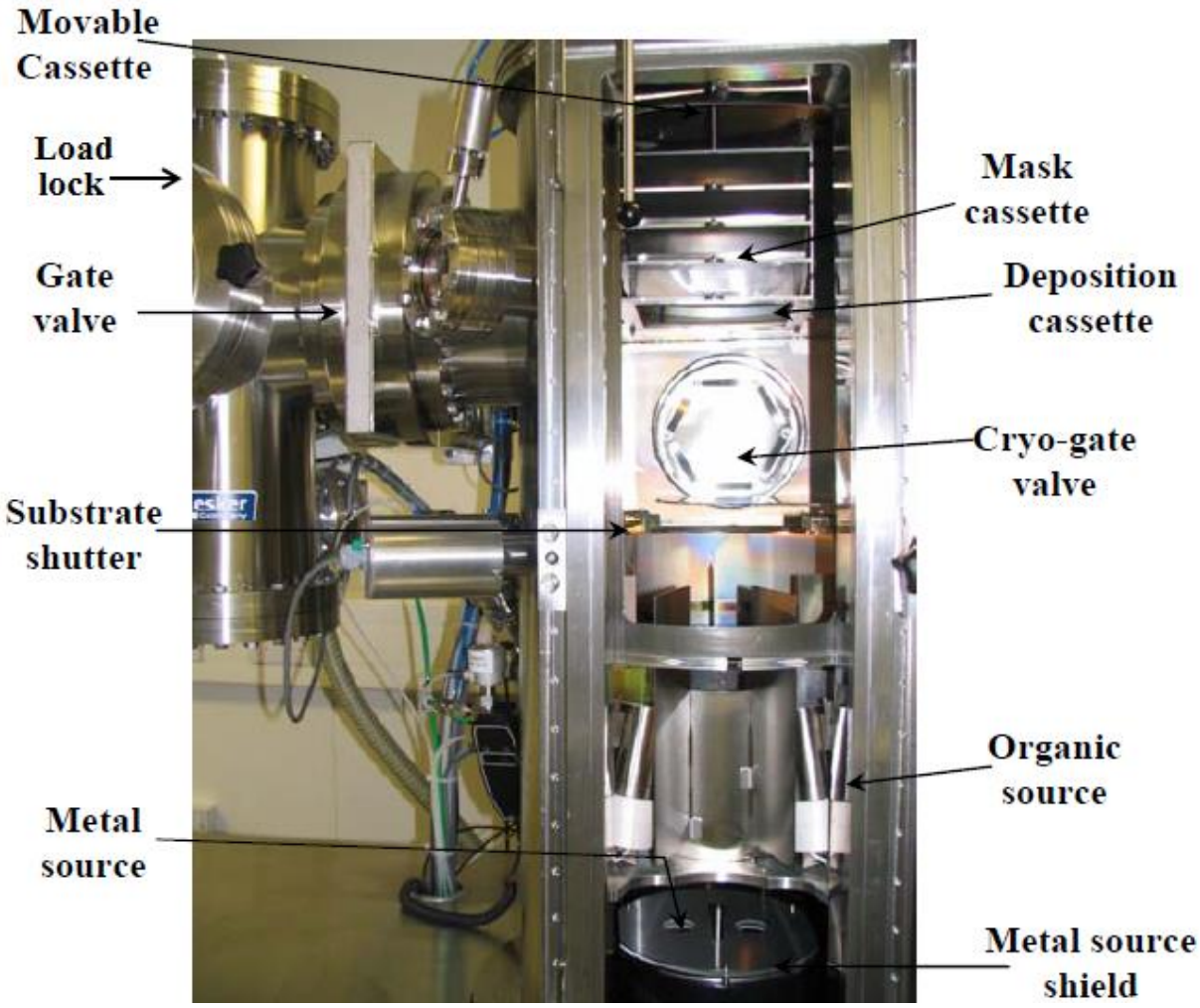

Figure 57: The photograph of a Kurt J. Lesker Spectros evaporation system.

The Kurt J. Lesker Spectros as shown in figure 57 consists of two vacuum chambers, one acting as a load lock, used for loading the substrates to the ultra-high vacuum evaporation. The substrate sample holder is loaded onto an arm for transference in the load lock, which can be evacuated using scroll and turbo-molecular pumps to produce a pressure of ~10^{-7} mbar. The main chamber is evacuated using a scroll pump and a helium cryo-pump to a pressure of ~10^{-8} mbar which increases to ~10^{-7} mbar during thermal evaporation. Inside the main chamber are six boron-nitride crucibles for organic crucibles for organic sublimation and two sources for metal (Au or Al) and LiF evaporation. Above the crucibles is one cassette to support the substrate holder. The cassette can be moved in height and contained the masks designed for organic and metallic layer growth. In this section, only metal and LiF sources are used.

During evaporation process, the cassette was rotated in order to improve the uniformity of the layers. Evaporation rate was controlled through a calibrated quartz crystal monitor. The rate for LiF was controlled to 1 Å/s with thickness of 10 Å. Both the rates of Al and Au evaporation were controlled to 1 Å/s for the first 100 Å and changed to be 6 Å/s for the rest. Once the electrode had been deposited, the whole evaporation process was completed. The rate can be controlled by tuning the heating temperature to make sure reaching a steady rate finally.

2.2.5 Vacuum annealing

Figure 58: The photograph of a vacuum annealing system.

The vacuum annealing experiments were carried out in a purification column composed of a glass boat and a Pyrex glass tube (diameter 2.5 cm) as shown in figure 58. The prepared device was put into the glass boat. The Pyrex glass tube was used as an inner tube. An additional Pyrex test tube was used as housing for the purification column. One end of the housing was inserted into the furnace tube of a Carbolite Furnace close to the centre. The temperature was set to be 80 ^{o}C, the hearting rate was set to 10 ^{o}C/min and the time was 15 minutes for drying solvent. For annealing experiments, the temperature was set to be 150 ^{o}C, the hearting rate was set to 10 ^{o}C/min and the time was 30 minutes.

A thermocouple was also inserted inside the furnace to monitor the temperature in the purification column. A Turbotronik NT 10 turbo pump and Trivac rotary pump, attached at the other end of the housing column, maintained the vacuum in the system, while a combined Penning/Pirani gauge was used to measure the pressure inside. The vacuum in the system was kept at $<10^{-6}$ mbar during the solvent drying and annealing experiment.

2.2.6 Visible light irradiation

For re-doping experiments, an incandescent light (40 W) was chosen for visible light irradiation in the fume cupboard (humidity 46%, light intensity at the sample 3.75 mW/cm^2 and temperature 22 ^{o}C). The sample was separately exposed under light irradiation for 15 minutes, 30 minutes and 60 minutes for re-doping experiment and after that the samples were kept under vacuum for further test.

2.3 Measurement Techniques

2.3.1 Current-Voltage-Luminescence (I-V-L) measurement

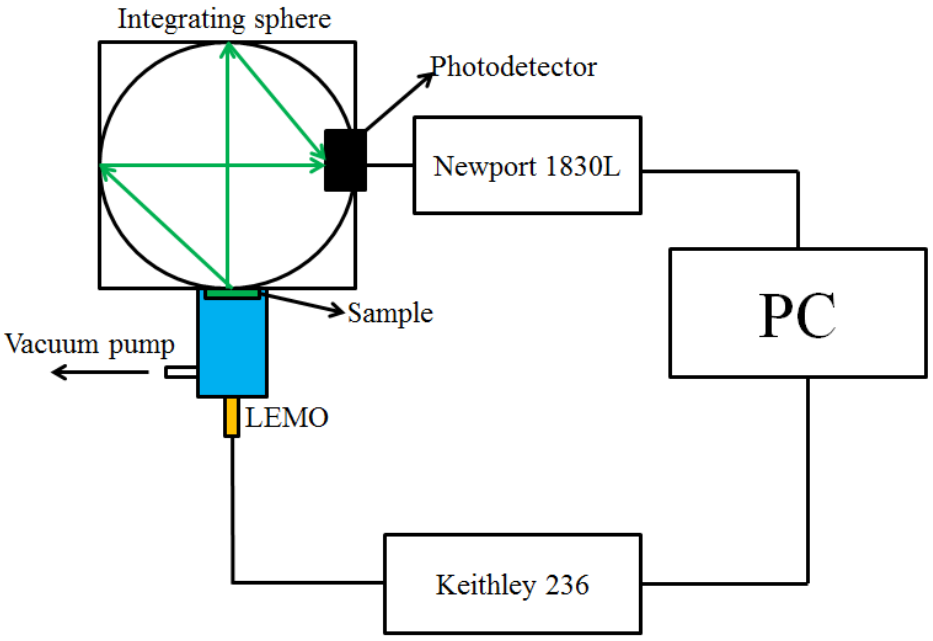

Figure 59: Schematic of the I-V-L characteristic measurement system: Newport 1830L is the optical power meter, PC is the personal computer, Keithley 236 is the source measurement unit, capable of sourcing and measuring voltage or current simultaneously, LEMO represents the connector connecting the sample holder with the source measurement unit Keithley 236.

The quality of the devices needs to be assessed by measuring the I-V-L characteristics of all the diodes. The efficiency of the diode is one factor when comparing the quality of different devices especially for the ambipolar device. The efficiency can be calculated by dividing the electrical power ($I \times V$) input by the light output (L).

As shown in figure 59, a Keithley 236 source-measure unit was chosen (averaging 4 readings for each measurement) which provided a series of constant voltages while recording the current through the device. The sample was connected with the source-measure unit by a LEMO connector. This setup allowed for measurements of current from 10^{-12} to 10^{-1} A. [148] Luminosity was measured by a Newport 1830C optical power meter. For measuring luminosity there was a silicon photo-diode (818-SL) and matching integrating sphere (819M). This setup came pre-calibrated and allowed for absolute measurements of luminosity at a certain wavelength. As the luminescent spectra of diodes were broad, the power meter should be set to the peak wavelength of the emission spectra of the sample. As this work was mainly focused on the same structure of certain device, the problems regarding power measurements were negligible since the devices were not being compared to other devices with different emission spectra. So the wavelength was set to be 520 nm in this experiment for comparison. The instruments were interfaced to computer (PC in figure 59) using intensity software written in visual basics.

2.3.2 Magnetoresistance (MR) measurement

The MR measurement was taken with the device operated in the constant voltage mode. The Keithley 236 source-measure unit was used averaged over 16 readings current measurements. Magnetic field effect measurements were carried out using the field from 0 to ~300 mT.

As shown in figure 60, the device was mounted onto a sample holder and placed between two poles of the electromagnet, with the magnetic field perpendicular to the direction of current flow in the device. A calibrated silicon photo detector of a Newport 1830C: EL was placed directly in front of one of the holder windows and stop light affecting from outside. The magnetic field was generated by an electromagnet. The power supply varied the current through the electromagnet in order to change the magnitude of the magnetic field from 0 to ~300 mT. A Hall-probe gaussmeter (GM 05 Gaussmeter) was

placed close to the sample holder to measure the strength of the electromagnet. The power supply unit (PSU) supplies a positive current for magnetic field measurement and a negative current for null field in order to counteract the remnant field of the electromagnet.

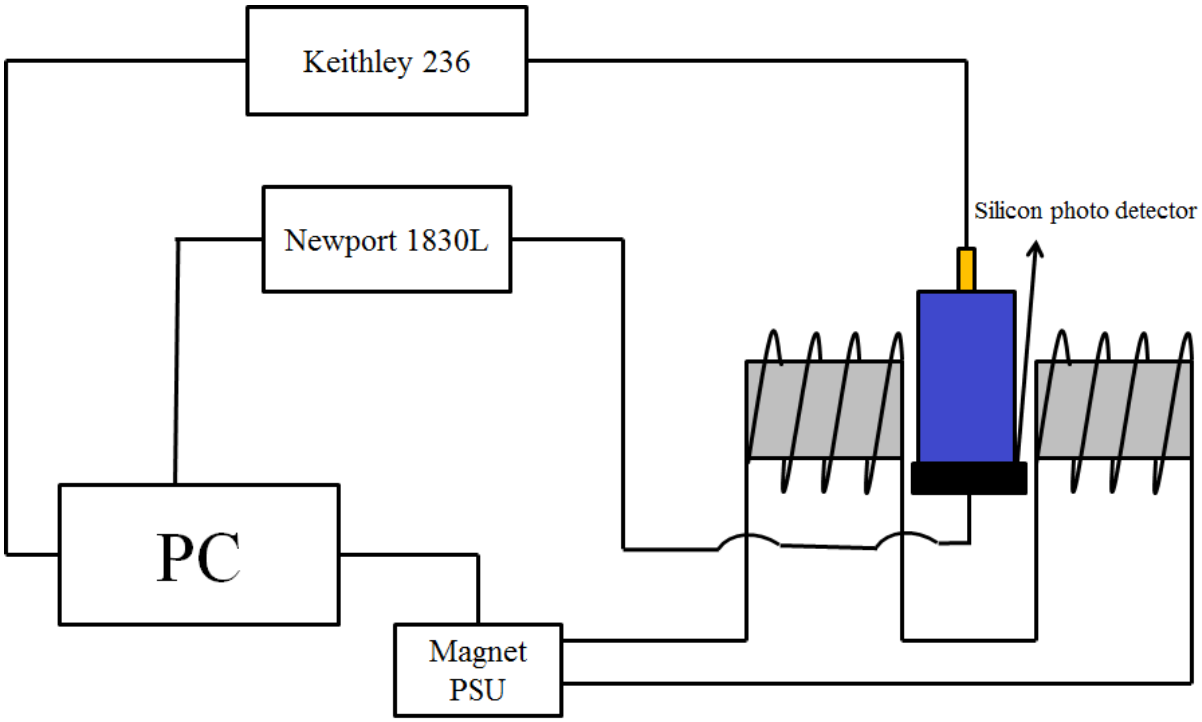

Figure 60: Schematic for organic magnetoresistance measurement system for P3HT based devices.

The MR test needs to take into account the device degradation during device operation. Degradation can occur after the device has been operated for a long time, and causes some parts of the device to stop working, thus reducing the effective area of the sample. Therefore, a drift in current through the device will occur at a given voltage. In order to remove any effects, due to drifting, in the device characteristics, the OMR is simply calculated using equation 39:

$$\frac{\Delta I}{I} = \frac{I_{Bn} - I_{null}}{I_{null}} \times 100\% = \frac{I_{Bn} - \left(\frac{I_{B(n-1)} + I_{B(n+1)}}{2}\right)}{\left(\frac{I_{B(n-1)} + I_{B(n+1)}}{2}\right)} \times 100\% \tag{39}$$

Where I_{Bn} is the measured current in the device with a magnetic field B, $I_{B(n-1)}$ and $I_{B(n+1)}$ are the current through the device with null field. I_{null} is the average value between $I_{B(n-1)}$ and $I_{B(n+1)}$.

2.3.3 Dark injection (DI) measurement

The dark injection transient current technique (DI) [149] was carried out to measure the charge carrier mobility. It is based on applying a step voltage to the sample sandwiched between two electrodes and recording the current flow through the device. The process of the dark injection experiment is shown in figure 61. When charge carriers are injected into a unipolar device, the current density will increase. When the front edge of charge carriers almost reaches the counter-electrode, there is a reduction in charge injection which causes a reduction of the dark current. Then the dark current will reach the steady state dark current I_{SCL} eventually. In an ideal case, the current density peak will appear on the oscilloscope, as shown in figure 61(c). The frontier charges are injected and drifted to counter electrode leading to an increase of the current density. But the amount of the charge that can be injected into the organic semiconductor is limited by the columbic repulsion from the charges already injected into the sample. This finally forces the current to drop down until it finally reaches the steady state I_{SCL}. The time at which the peak of the dark current occurred, is called the dark injection transient time and this relates to the time it takes for the frontier charge carriers to drift across the device.

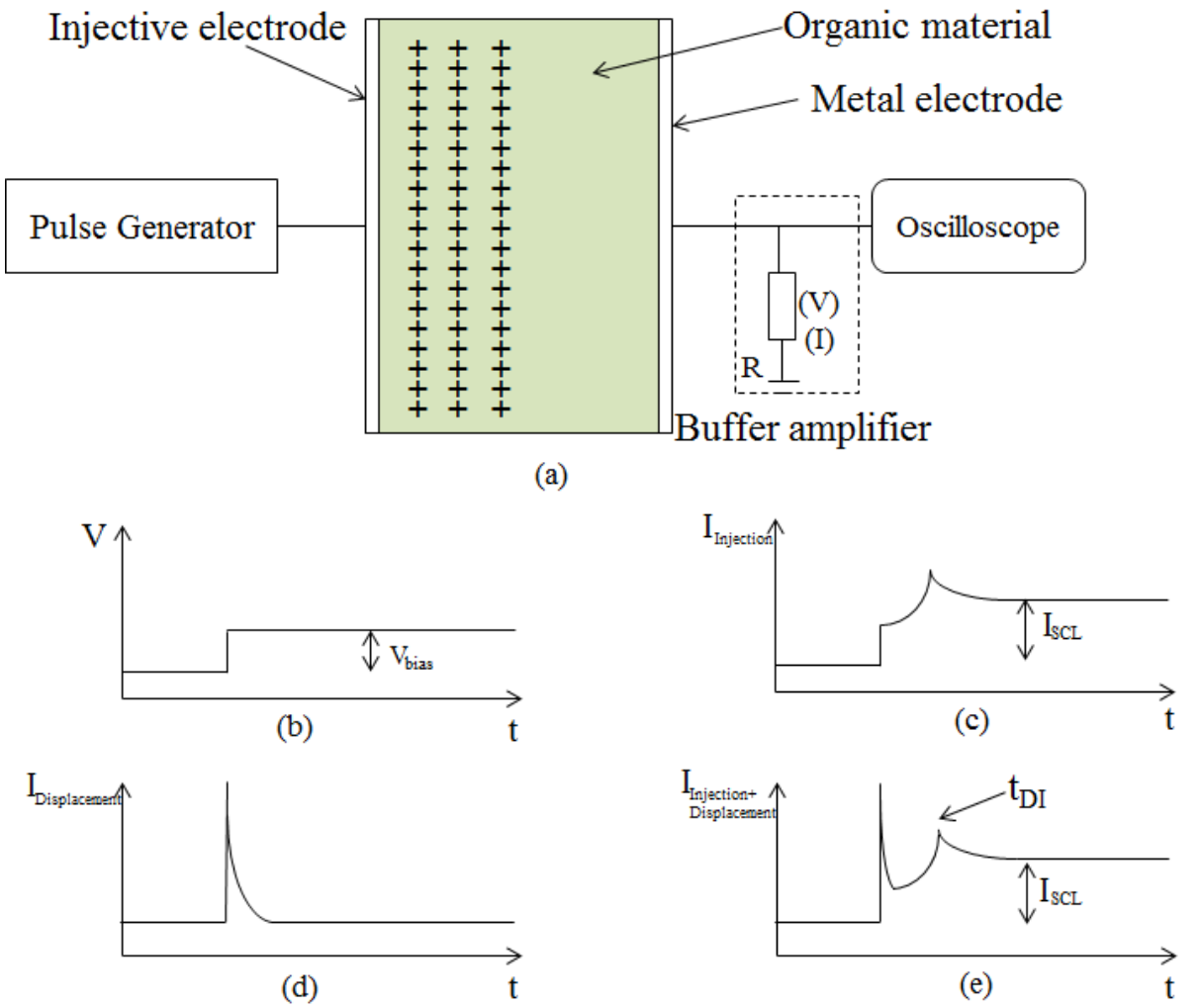

Figure 61: Schematic of the dark injection measurement. (a) The dark injection experiment setup. (b) The applied step voltage as a function of time. (c) The injected current flowing through the device as a function of time, (d) the RC displacement current as a function of time. (e) The resultant RC displacement and injected current through the device as a function of time.

The curve in figure 61(e) is considered as an ideal model, which is based on the assumption that during the charge drift across the material there are no traps and no diffusion. Furthermore the contact should be Ohmic which means no injection barrier and unlimited charge carriers can be injected until reaching the space charge limited (SCL) regime. This contact can sustain the space-charge-limit current (SCLC) through the sample, and acts as an infinite reservoir of charges. A buffer amplifier is used to protect the oscilloscope, in case the sample short-circuits resulting in a large current passing through the sample and damaging the oscilloscope. It also allows the load resistor, which determines the RC time constant, to be varied.

The mobility in this experiment can be calculated by:

$$\mu = \frac{d^2}{Vt_{trans}} = \frac{v_d}{E} \tag{40}$$

Where μ is the charge carrier mobility, d is the distance between two electrodes, V is the voltage drop across the electrodes, v_d is the drift velocity of the carriers and t_{trans} is the transit time.

The relationship between the dark injection transit time (t_{DI}) and space-charge-free transit time (t_{trans}) is shown in equation 41:

$$t_{DI} = 0.786 \cdot t_{trans} \tag{41}$$

In equation 41, t_{DI} indicates the dark injection transient time, and the factor 0.786 relates the DI time to the space-charge-free transient time. [150]

In the real dark injection experiment, the curve of the DI peak in figure 62 is different from the ideal one in figure 61(e) due to the existence of the RC displacement, trap filling, and diffusive broadening the field-dependence of the carrier mobility. Strong charge trapping may even cover the DI transient peak. The diode used in the experiment had a capacitance and there were also resistors in the circuit. So the RC displacement current will be observed at the short time in a real DI experiment. Whether the decay time will mask the DI peak depends on the RC decay time. The decay time, τ is decided by total resistance in the circuit and capacitance (C) of the sample.

$$\tau = C \sum R \tag{42}$$

As shown in equation 42, τ is the RC displacement time constant, and R is the total resistance of the measuring circuit, including the cable, the electrode, the sample, and the load. C is the capacitance of the device.

During the DI experiment, reducing the duration of RC displacement current as much as possible will support to get the DI peak. Under high bias voltage, it is possible to get the fast charge carriers under the high electric field, which will result in the DI transient peak moving towards the RC displacement peak. According to equation 42, either decreasing the capacitance of the sample, which can be achieved by decreasing the electrode area or increasing the sample thickness, or reducing the resistance in the whole experimental circuit will help to reduce effect of the RC decay.

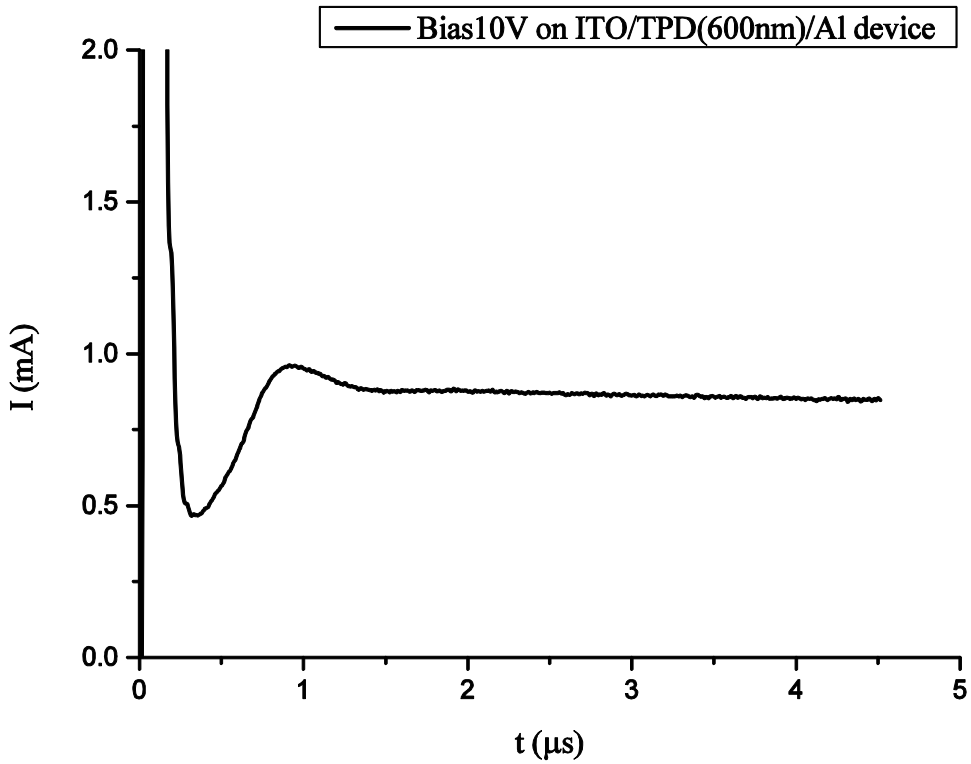

Figure 62: A typical dark injection current transient curve in ITO/TPD (600 nm)/Al.

In the measurement, a bridge circuit was employed as shown in figure 63(a), which was firstly proposed by Helfrish and Mark and later used by J.C. Scott. [151-152]

The key element of the circuit is a differential amplifier with one input connected to the resistor R_1 in series with the sample, while the other input is connected to another, ideally identical, resistor R_2 in series with the variable capacitor. The variable capacitance should be tuned to make sure it is equal to the capacitance of the sample, then it will get the same RC displacement signal as the sample and it can be set as an inverting signal (V_{in}) and the sample signal as the non-inverting signal ($V_{non\text{-}in}$). The output will be the only dark injection transient time curve which is shown as the red curve in figure 63(b). Figure 63(b) shows the comparison between the signal with differential amplifier and the one without differential amplifier. It is possible to effectively remove the RC displacement as well as remove any other distortions of the signal due to impedance mismatches in the measuring circuit and the noise from pulse generator by using the differential amplifier.

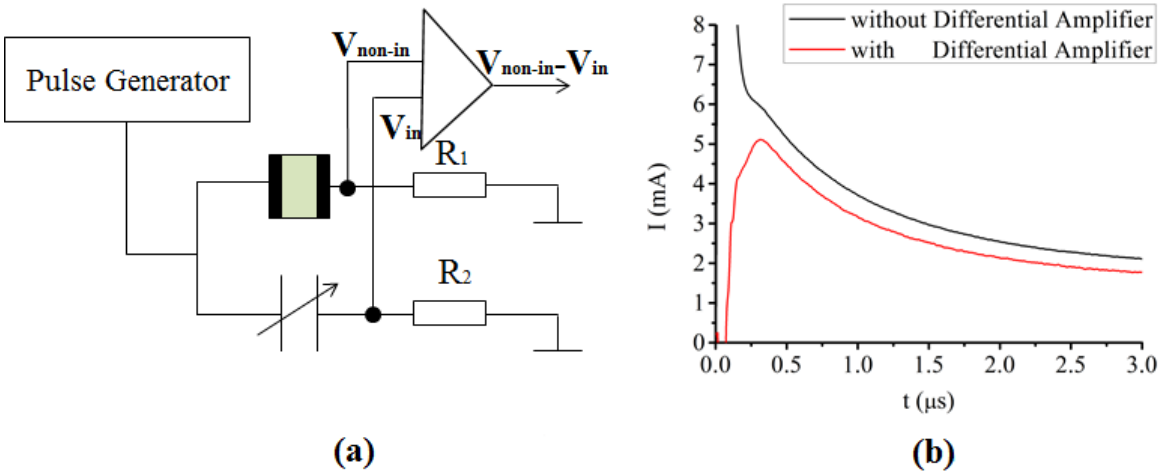

Figure 63: (a) The schematic of the dark injection circuit with a differential amplifier. (b) A typical dark injection measurement on TPD with and without the differential amplifier.

2.3.4 Photoluminescence measurement

Photoluminescence is a well-known and widely used technique for studying the optical properties in organic semiconductors. [153] When the P3HT sample is excited by a laser, a photon with energy greater than the band-gap (E_g) can excite the electron from the HOMO to the LUMO. The electron then loses energy through phonon emission before an exciton is formed. The luminescence will be detected when electrons and holes recombine in the gap as shown in figure 64.

In order to conserve angular momentum in the generation of excitons, the selection rules should be obeyed. In this case, the selection rules indicate that the orbital momentum $\Delta L = \pm 1$ and the spin momentum $\Delta S = 0$. The absorbed photon has integer angular momentum, which will change the orbital angular momentum while maintaining the spin. The only possible transition is that to the singlet state, thus photon absorption can only generate singlet excitons by exciting electrons from HOMO to LUMO. When an electron interacts with a photon, the electron must obey the conservation of angular momentum. The photon has an intrinsic angular momentum with a constant magnitude, h, the orbital angular momentum of the electron will not change when a photon of energy ($h\nu = E_2 - E_1$) is absorbed. E_2 is the emission energy and E_1 is the absorption energy. Therefore, photon absorption can only generate singlet excitons.

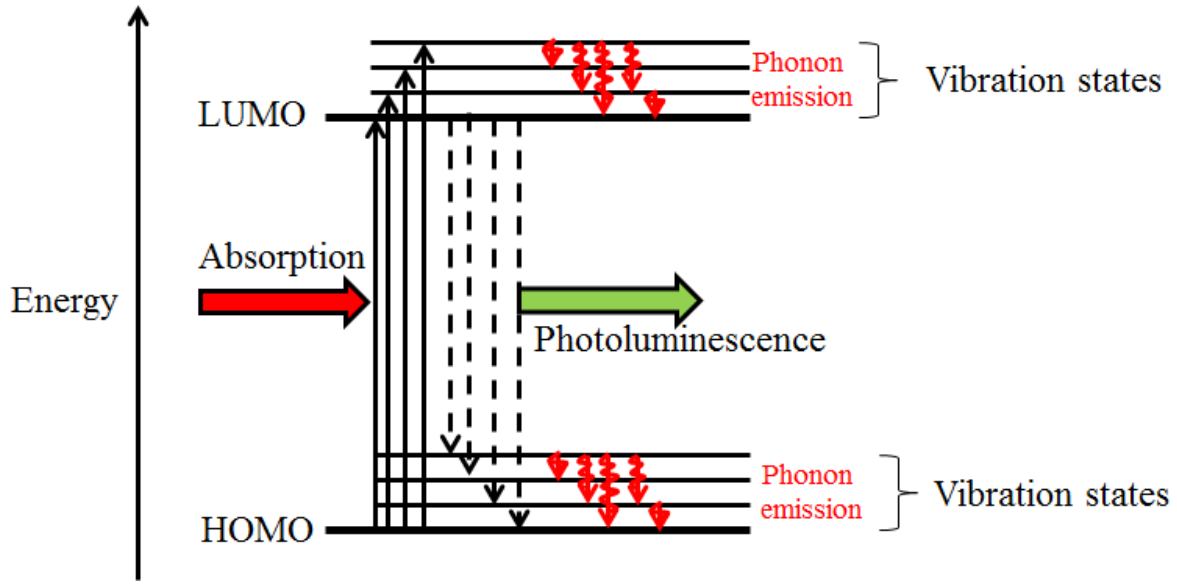

Figure 64: Schematic of mechanism of photoluminescence.

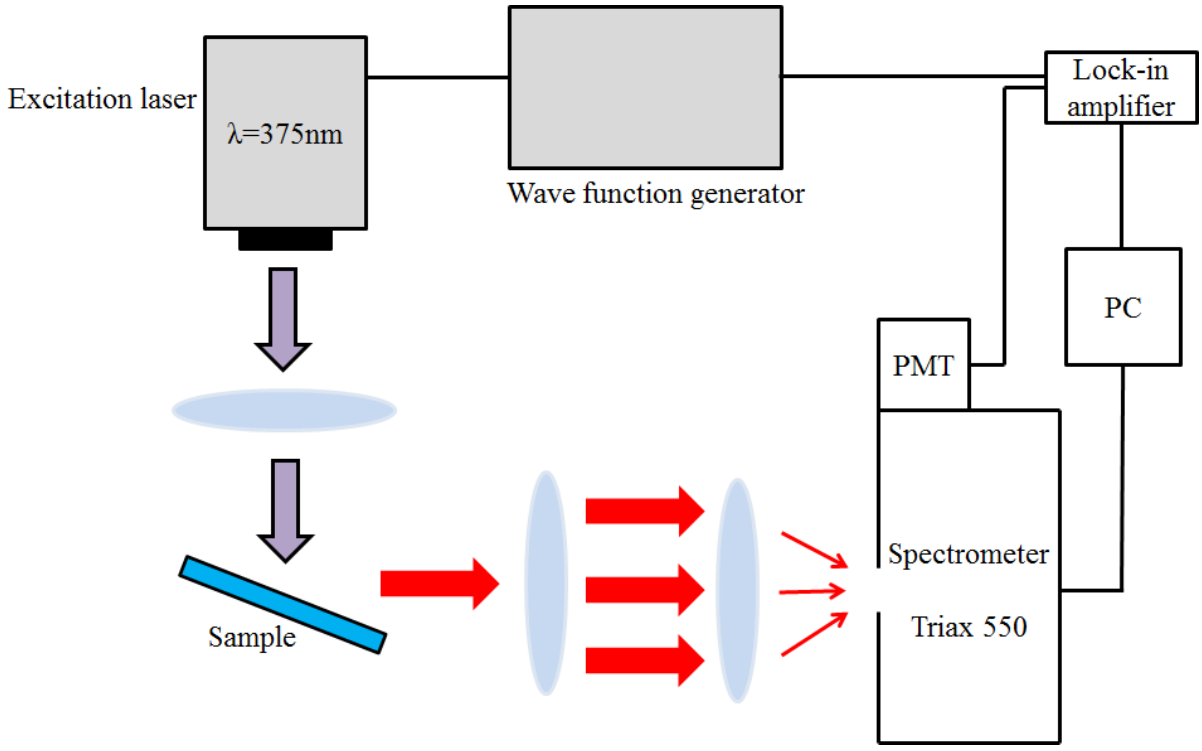

Figure 65: The schematic for PL measurement.

In the experiment, the P3HT samples were excited by a frequency-modulated laser. The modulation of the lasers could be achieved by a wave function generator. The luminescence from samples was focused into a Spectrometer Triax 550, the intensities of light were measured by a photomultiplier (PMT) detector and the signals were analysed with a lock-in amplifier. The spectra were extracted by the software (LabVIEW). The slit width could be adjusted from 20 to 2000 μm depending on the desired resolution.

In order to choose an appropriate slit width, it is possible to decrease the slit width and measure the spectra gain. If there is no significant change, the slit width is narrow enough. Grating of 600 lines/mm and 1200 lines/mm are usually selected to detect infrared and UV/visible light, respectively. The UV-visible spectra are detected by Hamamatsu 9113B PMT, and the near-infrared spectra is detected by Hamamatsu R5509-72 nitrogen-cooled PMT. As shown in figure 65, the sample is excited using a 375 nm laser that is focused onto a <0.1 mm spot diameter, by a microscope objective (Achro 4/0.1) onto the sample.

As shown in figure 65, the wave function generator not only provides a pulse signal to the laser to excite sample but also feeds a reference frequency to a lock-in amplifier (PerkinElmer 7265 DSP lock-in Amplifier). The use of such a reference signal ensures that the instrument will only track changes in the signal of the same frequency.

In the experiment, the purpose of the modulation was to increase the signal to noise ratio, furthermore by taking several measurements performing an average. The PL was dispersed in a spectrometer and detected using an S-20 photomultiplier. The lock-in amplifier was used to measure the output of the PMT. The spectrometer was used to disperse the luminescence. The characteristics of materials can be identified by measuring the wavelengths and intensity of the spectra. [154] The schematic diagram of a spectrometer is shown in figure 66, the luminescence is aimed at an entrance slit (A). The intensity and resolution of the luminescence can be adjusted by the slit (A). This luminescence is then focused on a collection mirror (B), which is named as collimator. In this case, the luminescence will be parallel. This process is denoted collimation. The collimated luminescence is diffracted by the diffraction grating (C) and then collected by a focussing mirror (D). The mirror (D) refocuses the dispersed luminescence with individual wavelengths on the different positions of the exit slit (*E*). At the exit slit, the wavelengths of the luminescence are spread out spatially. Therefore, when the diffraction grating is rotated, the intensity changes of a sample’s spectra can be seen at different wavelengths.

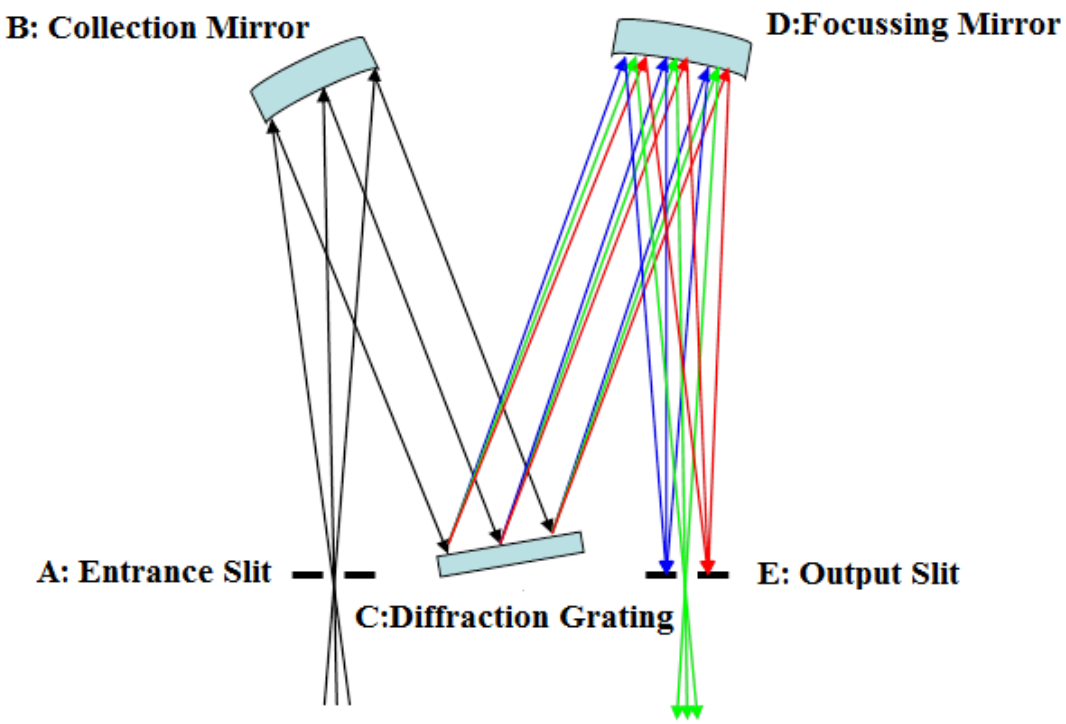

Figure 66: The schematic diagram of a spectrometer.

The dispersed luminescence is detected using a photomultiplier tube as shown in figure 67. A photomultiplier tube is an apparatus that multiplies the electrical signals caused by light; these multiplied signals are then measured by a lock-in amplifier. It is constructed from a glass envelope with a high vacuum inside. This tube is constructed by a photocathode, several electrodes, and an anode. When the incident photons strike the photocathode material, electrons are produced as a consequence of the photoelectric effect. These electrons are directed by the focusing electrode towards the electron multiplier. The electron multiplier consists of a number of electrodes. There is a 1 kV supply between electrode 1 and electrode 8. When the electrons move towards each electrode, they are accelerated by the electric field and arrive with much greater energy. Therefore, an increasing number of electrons are produced at each stage. Finally, the electrons reach the anode, where the accumulation of charge resulted in a sharp current, indicating the arrival of the photons at the photocathode.

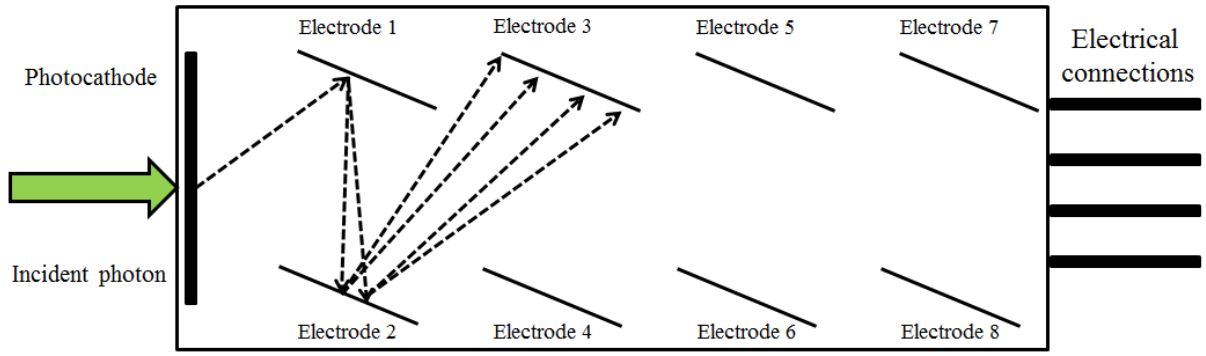

Figure 67: The schematic diagram of a photomultiplier tube.

Figure 68 is the schematic diagram of typical lock-in amplifier. The lock-in amplifier consists of a RC circuit filter, a signal amplifier and a phase-sensitive detector (PSD) to pick up the component of signals at a specific reference frequency and phase.

The measurement using lock-in amplifier requires a reference frequency. Typically, a signal is modulated at a fixed frequency and the lock-in amplifier detects the intensity of the modulated signal at the reference frequency. The lock-in amplifier can not only recover signals from a noisy background, but also enhances the resolution of relatively clean signals over several orders of magnitude and frequency. The output of phase-sensitive detector (PSD) is simply the product of two cosine wave functions, as follows:

$$V_{in} = A \times \sin(\omega t) \tag{43}$$

$$V_{ref} = B \times \sin(\omega t + \theta) \tag{44}$$

$$\theta = (\theta_{sig} - \theta_{ref}) \tag{45}$$

Where A is amplitude of the input voltage V_{in}, B is the reference voltage V_{ref}, ω is the modulated frequency of input signal and θ is the phase difference between input signal and lock-in reference. It is a user-adjustable phase-shift introduced within the lock-in amplifier.

$$V_{PSD} = V_{in} \times V_{ref} = A\sin(\omega t) \times B\sin(\omega t + \theta) = \frac{1}{2} \times AB\cos(\theta) - \frac{1}{2} \times AB\cos(2\omega t + \theta) \tag{46}$$

The output from the PSD then passes to a low-pass filter which removes the 2ω component. Consequently, the output of PSD is $1/2 \times AB\cos(\theta)$. Therefore, the largest output signal can be obtained when θ is 0, namely θ_{sig} is equal to θ_{ref}. This case is called the “In-phase”. [155]

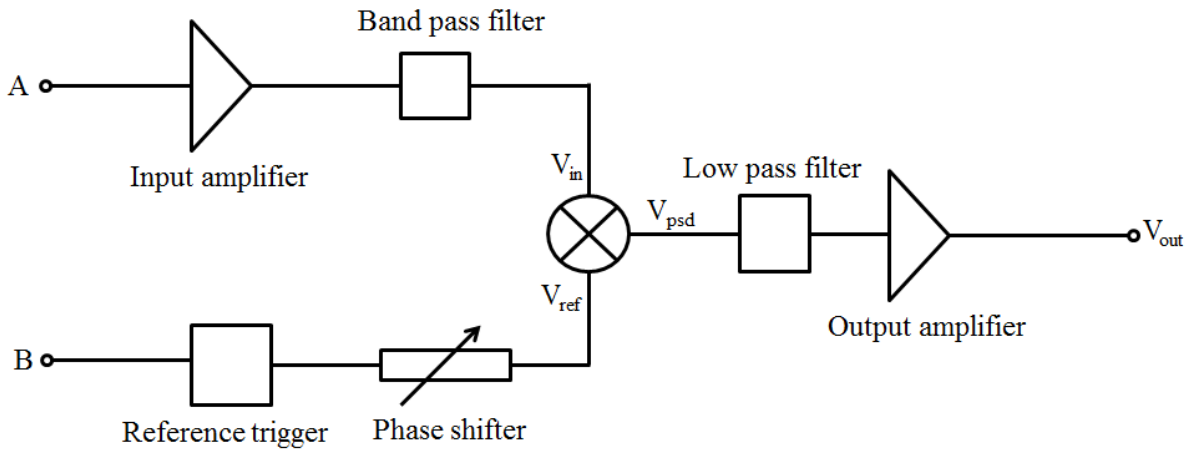

Figure 68: The schematic diagram of typical lock-in amplifier.

3. Results and discussion

3.1 Sign change of MC in P3HT diodes

3.1.1 Overview

The transition from negative MC at low voltages to positive MC at high voltages has been observed in the literature, [129][140][156-159] mostly in devices where poly (3,4-ethylenedioxythiophene)-poly(styrenesulfonate) (PEDOT:PSS) was used as a buffer layer for hole injection. However, the presence of a PEDOT:PSS layer can have pronounced magnetic interfacial injection effects. [160] Changes from negative to positive MC resulting from varying blend composition, [161] geometric factors [129][162] and magnetic field [163] have also been reported. Here the results from a simple sandwich structure device Au/P3HT/Al as shown in figure 69 are presented under different measurement conditions. The hole only (low reverse bias) behaviour corresponds to a negative magnetic effect on the current (negative saturation MC) fitted by a single non-Lorentzian function whereas the ambipolar behaviour (forward bias) appears to have a contribution from more than one process. The forward bias results depend strongly on the current density through the device showing a transition from negative saturation MC to positive saturation MC. The transition is due to the competition between the two mechanisms and the dominance of one over the other depending on drive conditions.

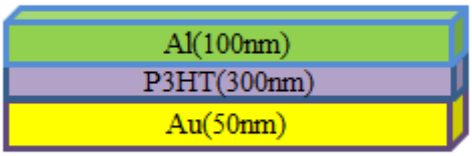

Figure 69: Schematic of an Au(50 nm)/P3HT(300 nm)/Al(100 nm) device.

3.1.2 Results

P3HT is known to be p-doped due to exposure to oxygen and this has been demonstrated to result in Schottky barriers with metal electrodes such as aluminium [164-167] or gold. [168-169] This can result in a contact with a very

low injection barrier between the metal and the Highest Occupied Molecular Orbital (HOMO) of P3HT and efficient hole injection from either contact at low operating voltages. Figure 70 shows the current voltage characteristic of the Au/P3HT/Al diode which demonstrates current injection at low voltages in both forward and reverse bias but with clear rectification, with approximately two orders of magnitude difference in the current density between forward and reverse bias. This rectification is due to the differences in the Schottky barrier heights for the two contacts.

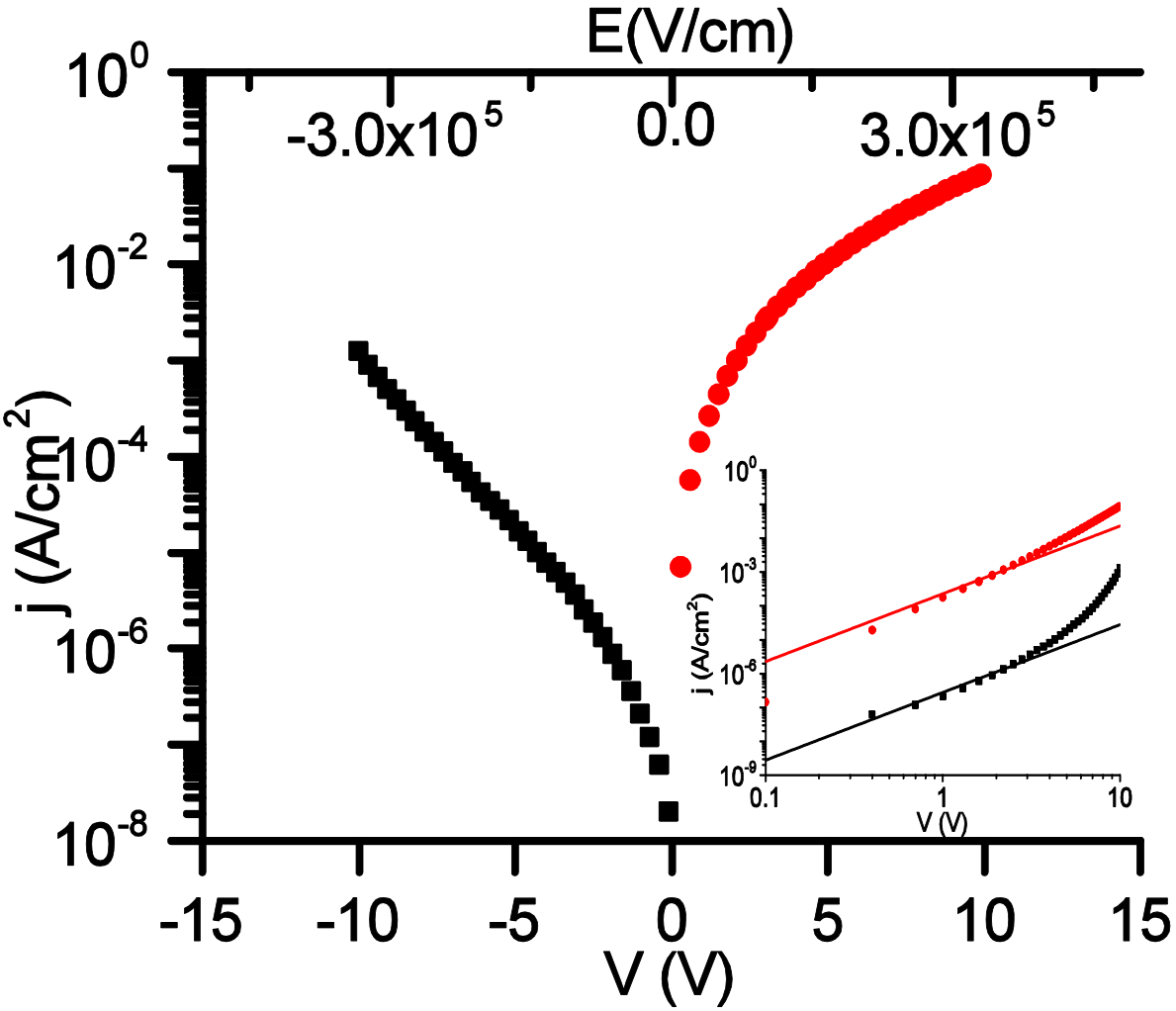

Figure 70: Current density versus voltage characteristics in forward (Au bottom electrode positive) and reverse (Al top electrode positive) bias. The inset shows double logarithmic plots of the forward and reverse bias results and the solid lines denote $j \propto V^2$ behaviour.

The inset shows double logarithmic plots of the forward and reverse bias current density versus voltage. The settling time in the scanning is set to 10 ms which is long enough compared to RC decay time τ to make sure the measurement is accurate. The solid lines indicate space charge limited current (SCLC) regions ($j \propto V^2$) and the majority of the forward bias results follow that

behaviour. In reverse bias, when the bias is smaller than 1 V, the slope is 1. When the bias is smaller than 2 V, the slope is ~2. However, the characteristic significantly deviates from SCLC behaviour, particularly at larger bias (>2 V). This is attributed to the electron injection from the cathode. (Al in forward bias and Au in revers bias) However, the slope above bias 2 V in reverse bias is larger than that in forward bias which is not clear here, as in theory Au should have larger injection barrier for electrons compared to Al.

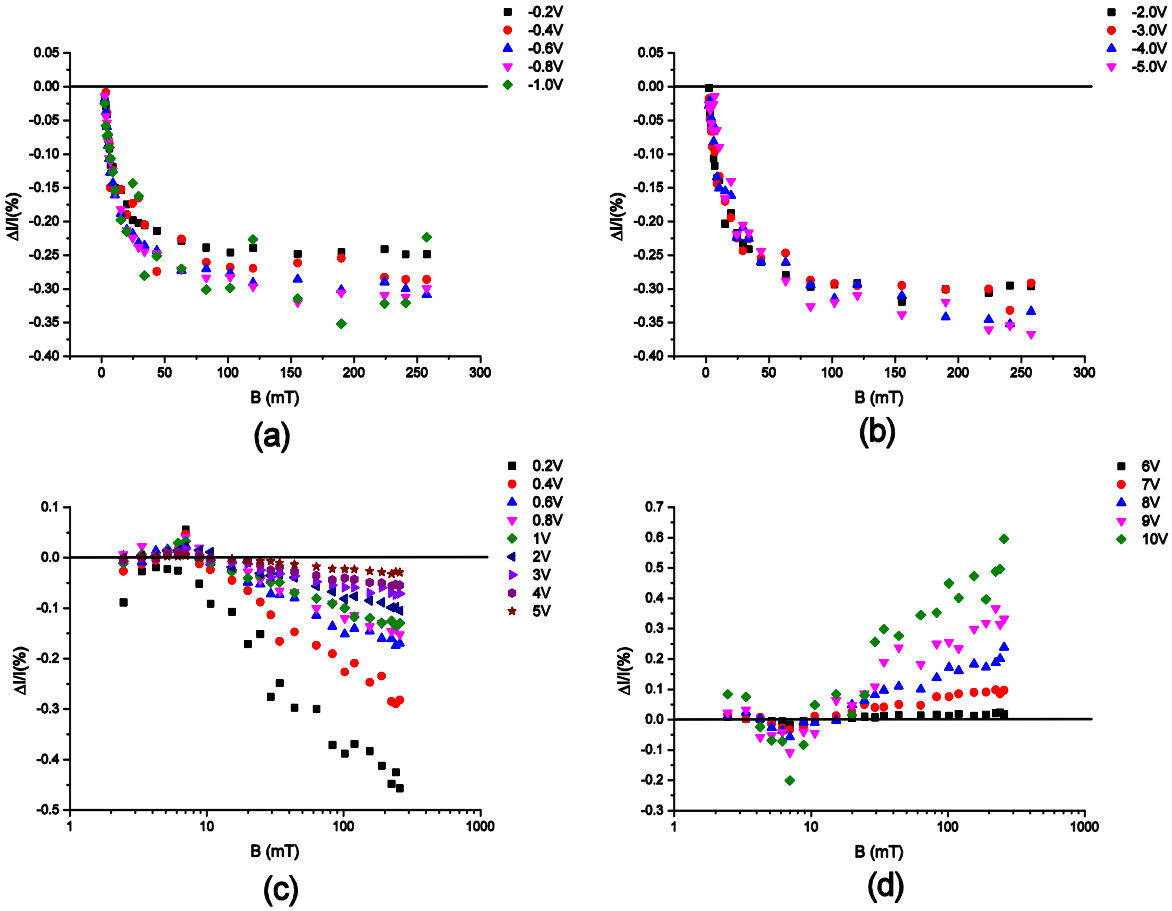

Figure 71: Variation of current versus magnetic field in reverse bias (a) from -0.2 V to -1 V and (b) from -2 V to -5 V. In forward bias, the variation of current is plotted using a logarithmic magnetic axis, (c) from 0.2 V to 5 V and (d) from 6 V to 10 V.

Figure 71, (a) and (b) show the MC of the device in reverse bias at low voltages (-0.2 V to -1 V) and high voltages (-2 V to -5 V). The MC plots in figure 71 (c) and (d) with different trends correspond to different forward bias. The negative (low bias) MC in figure 71(c) corresponds to the previously measured OMR in P3HT. [132] The overall magnitude of this effect at the fields measured is low, reaching a maximum value of ~ -0.4% at the up-limit field of 300 mT. As the applied bias is increased a switch appears from negative to positive MC in the high field region with the MC reaching a maximum value of

~ +0.6% at the up-limit field of 300 mT. Unlike the MC results at negative bias in figure 71(a) and (b), the MC results in forward bias are not in the same trend. For the negative MC low-bias (0.2 V to 5 V) results as shown in figure 71(c), there is a positive spike of magnitude 0.05% at a field of ~7 mT whereas for the positive MC high bias (from 6 V to 10 V) results as shown in figure 71(d), there is a negative spike of the same magnitude and position. These features are different to the ultra-low field features that have been seen in other experiments [132] and are most likely to be due to the interaction of two different processes, one positive and one negative, such as has been observed in thin Alq_3 devices. [142-144][170]

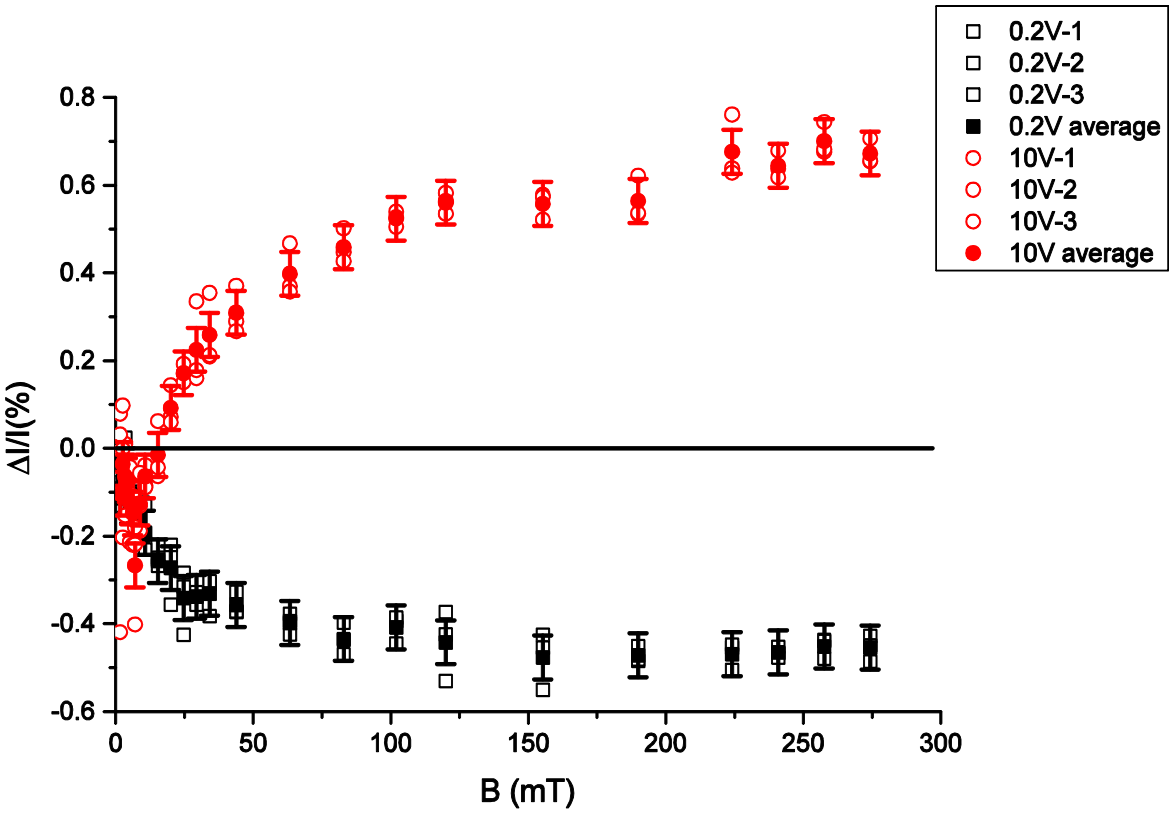

Figure 72: Repeated MC measurements on an Au/P3HT (300nm)/Al sample at low bias 0.2V (black square) and high bias 10V (red circle). The empty symbols are raw data repeated three times in each condition and filled symbols are the average results at each given magnetic field. A representative error of 0.05% is shown by the error bar on the filled points and describes the scatter of experimental points satisfactorily.

In order to quantify the experimental error, MC measurements at high (10V) and low (0.2V) bias are repeated three times. These are shown in figure 72. The average value for the differential current change is also calculated, as is the range of values for each magnetic field (also shown in figure 72). The range is taken to represent the error at each point and these errors vary between 0.033%

and 0.06%. As a result, a typical error of 0.05% is chosen as representative across all electric and magnetic field values, as shown by the error bars on the filled points in figure 72. Consequently, throughout the thesis the typical error bars in MC results are assumed to be of the order of 0.05%

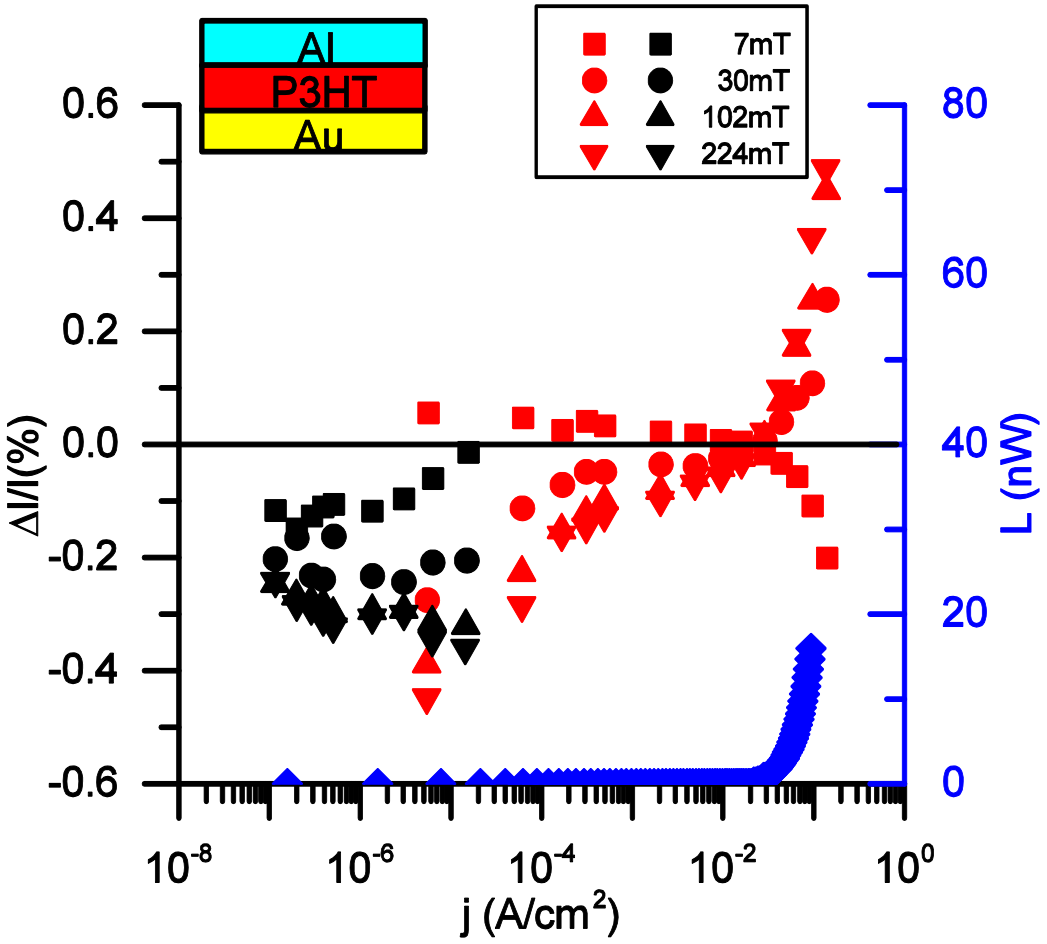

Figure 73: Differential current obtained under several magnetic fields (7 mT squares, 30 mT circles, 155 mT up-triangles and 258 mT down-triangles) versus current density for the Au/P3HT(300 nm)/Al diode in forward (Au bottom electrode positive, red symbols) and reverse (Al top electrode positive, black symbols) bias at room temperature (left hand axis). The corresponding electroluminescence (blue diamonds) versus current density in forward bias is plotted against the right hand axis.

The MC response is taken from figure 71 at a number of different magnetic fields (7 mT, 30 mT, 155 mT and 258 mT) and these fields are used to monitor the trends in the MC response as a function of different operating conditions as shown in Figure 73. The differential current measurements obtained under several magnetic fields are plotted against the current density through the diode; the measured electroluminescence is also plotted for forward bias only. The voltage range for negative bias measurements is -0.2 to -5V and for positive bias measurements is 0.2V to 10V. The reverse bias results (black symbols) are limited to low currents ($<10^{-4}$ A/cm^2) and always display negative

MC (the 7mT high bias results are too noisy and small to consider as evidence of any positive MC). The forward bias MC results (red symbols) clearly show a change of sign as the current density increases. The data under low magnetic fields (7mT) correspond to the "spike" seen in figure 71(c) and 71(d), and make a transition from positive MC to negative MC. The saturation MC, on the other hand, makes a transition from negative to positive with the increasing bias. Under high magnetic fields (155mT and 258mT), low current densities ($<10^{-2}$ A/cm^2) correspond to low forward bias (<6V) and display negative MC whereas high current densities ($>10^{-2}$ A/cm^2) correspond to large forward bias (>6V) and display positive MC. The onset for measurable electroluminescence in this device is at $\sim 2\times10^{-2}$ A/cm^2, corresponding to positive differential current and large forward bias conditions (>6V).

3.1.3 Discussion

Figure 74 shows schematic diagrams for the device under short circuit, small reverse bias and small and large forward bias conditions. Due to the presence of Schottky barriers at both interfaces, even at zero bias in figure 70(a), the device is expected to be in a "flat-band" condition. Therefore the onset of charge injection is not defined by the difference in the effective work functions for the two electrodes, as in traditional "undoped" organic semiconductors. In the presence of a modest reverse bias (<1 V) in figure 74(b) the device will operate in nearly unipolar conditions. Given the Schottky barrier at the Al/P3HT interface at low reverse bias voltages it is possible to get hole injection from the Al into the P3HT whereas there will be no electron injection from the gold due to the high work function of gold. As shown in figure 74(b), the P3HT LUMO states do not become available for electrons to tunnel into from the gold Fermi level until the applied bias (nominally) exceeds 2.2V.

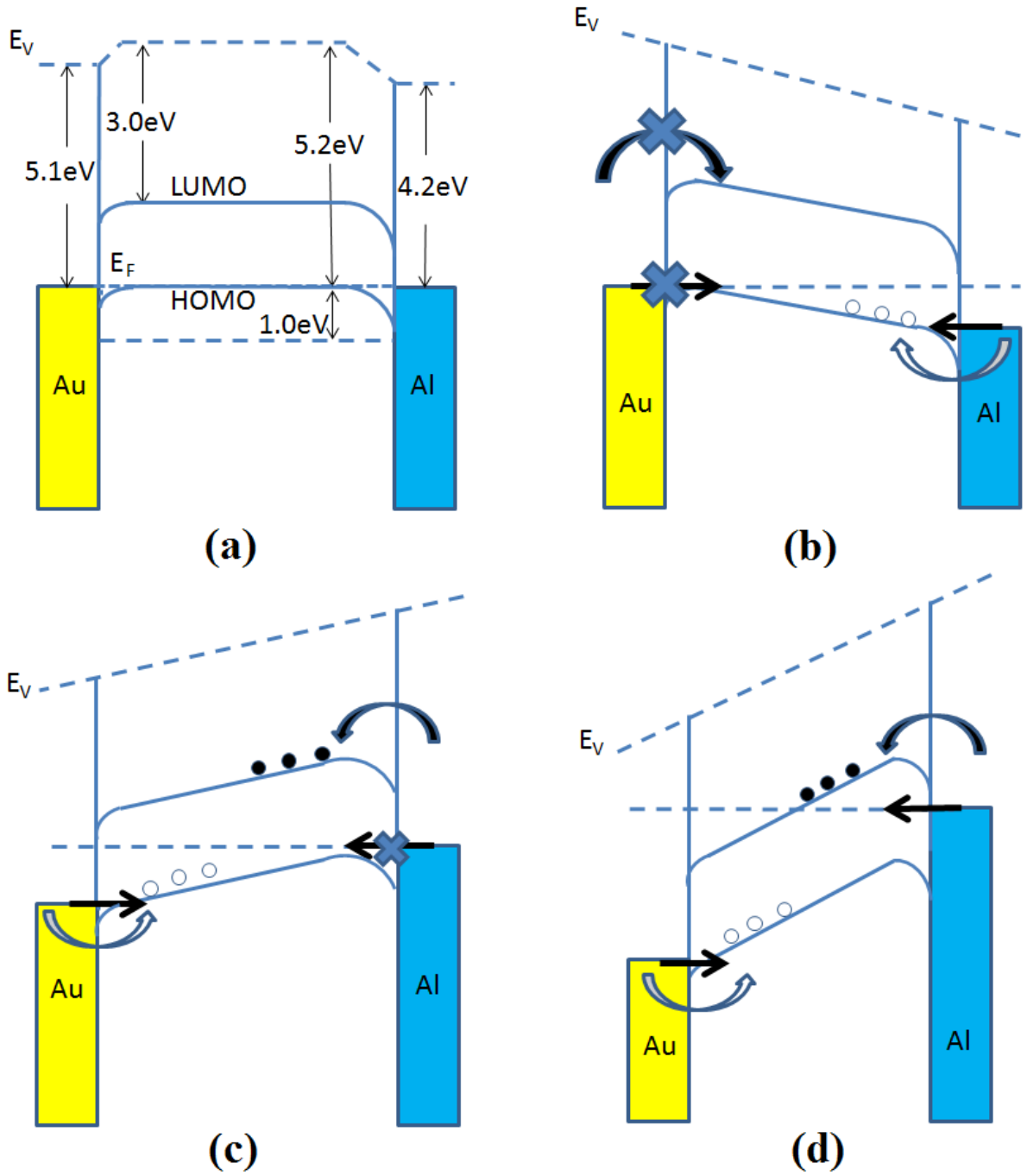

Figure 74: Energetic schematics of the Au/P3HT(300 nm)/Al device under different conditions. (a) Short circuit condition with Schottky contacts between P3HT and electrodes. (b) Under low reverse bias, holes can be injected by tunnelling and thermionic emission from Al but electron injection is forbidden from Au. (c) Under low forward bias, holes can be injected from Au and electrons can only be injected from the Al by thermionic emission. (d) Under high forward bias, tunnelling injection of electrons takes place from the Al, leading to ambipolar conduction.

Under low forward bias in figure 74(c), the large work function of gold [171] coupled with the Schottky barrier at the interface allows for very efficient hole injection from gold into P3HT.[172] In contrast to this, electron injection from the Al in these conditions is very inefficient as it is only possible via

thermionic emission. Although this thermionic emission is inefficient, it is expected that there may be some electron injection, even at low bias voltages as the energy barrier between the P3HT LUMO and Al is much smaller than for Au. Also at such low forward bias, electron tunnelling into the LUMO is not possible as there are no available states at the Al Fermi level. At large forward bias in figure 74(d) it becomes possible for electrons to tunnel into the LUMO of the P3HT from the Al and this tunnelling injection is expected to dominate over any thermionic injection. Therefore it is expected to see a significant increase in electron injection as the forward bias is increased and eventually the onset of light emission.

Three transport regimes can be defined within this device structure: Reverse bias in figure 74(b), essentially unipolar with holes injected from the Al contact; Forward bias at low voltages in figure 74(c), predominantly hole transport but with weak thermionic electron injection; Forward bias at higher voltages in figure 74(d), essentially ambipolar current transport.

Figure 75(a) shows the MC fitting results of the device in reverse bias at low voltages (-0.2 V to -1 V). In all cases the MC curves can be well fitted with a single non-Lorentzian function given in equation 47:

$$\frac{\Delta I}{I} = \frac{a_0 B^2}{\left(|B| + B_0\right)^2} \tag{47}$$

The characteristic fields (B_0) obtained in the MC response fits are consistent with those reported in the literature for P3HT [173] which are of the order of ~5 mT. The fitting results are consistent with the bipolaron theory [138], in which B_0 is a field related to hyperfine effect, in the presence of a single carrier type (hole) transport.

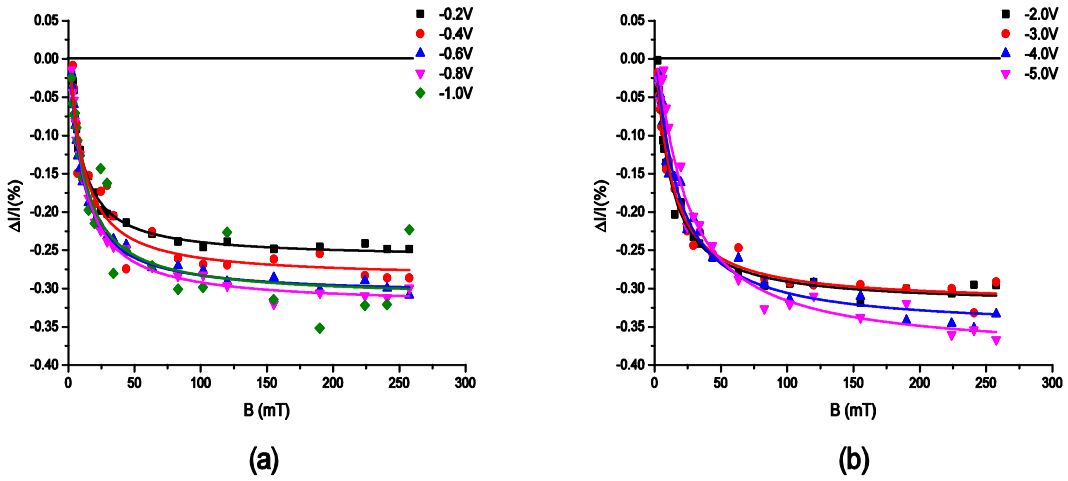

Figure 75: Typical room temperature MC results obtained from the Au/P3HT(300 nm)/Al device under different reverse bias conditions: (a) -0.2 V (black square), -0.3 V (red circle), -0.4 V (blue up-triangle), -0.5 V (magenta down-triangle), -1.0 V (olive) diamond; (b) -2 V (black square), -3 V (red circle), -4 V (blue triangle), -5 V (magenta down-triangle). The solid line represents the non-Lorentzian fitting results.

The solid lines are fits obtained using equation 47. Figure 75(b) shows the MC of the device in reverse bias at high-voltages (-2 V to -5 V). Under higher reverse bias, B_0 term starts to increase, as does the associated error in the fit; this may be due to the onset of weak electron injection from the gold. The weak electron injection will introduce another process, which will affect the quality of the fit. As shown in Table I, the characteristic field (B_0) is ~5 mT when the absolute value of negative bias is lower than 3 V. B_0 increases as the negative bias increases beyond 3 V, most probably due to perturbation of electron injection from the Au, and corresponds to significant deviation from SCLC behaviour in the *j-V* characteristic shown in the inset, figure 70.

Table I: Summary of fitting parameters in reverse bias.

Bias(V)	a_0	error a_0	B_0 (mT)	error B_0 (mT)
-0.2	-0.26	0.004	4.3	0.24
-0.4	-0.29	0.016	5.8	0.19
-0.6	-0.31	0.004	4.5	0.23
-0.8	-0.32	0.004	5.1	0.25
-1.0	-0.31	0.013	5.2	0.83
-2.0	-0.32	0.005	5.2	0.31
-3.0	-0.32	0.005	5.5	0.33
-4.0	-0.35	0.008	7.5	0.57
-5.0	-0.39	0.012	10.8	1.13

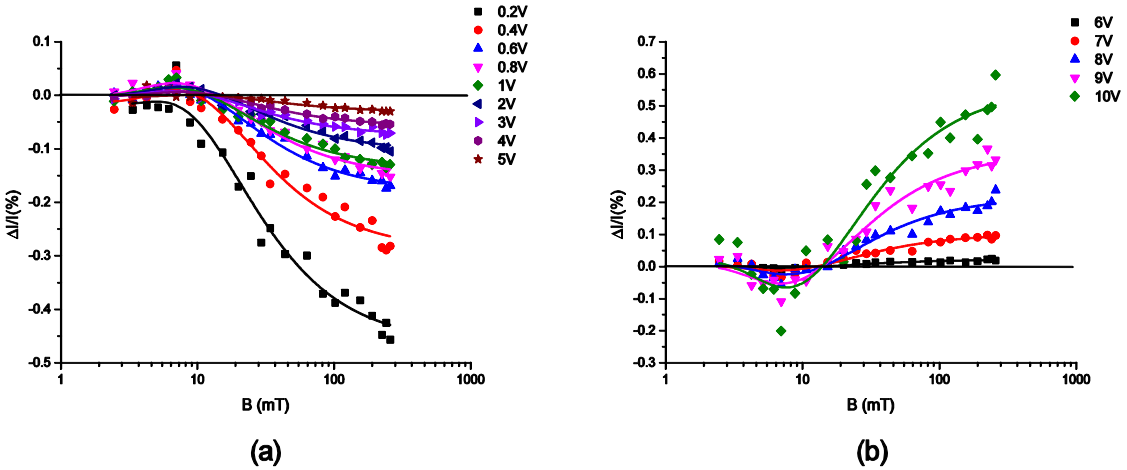

Figure 76: MC under different forward bias conditions plotted using a logarithmic magnetic axis. (a) 0.2 V (black square), 0.3 V (red circle), 0.4 V (blue up-triangle), 0.5 V (magenta down-triangle), 1.0 V (olive) diamond, 2 V (navy left-triangle), 3V (violet right-triangle), 4 V (purple hexagon) and 5 V (wine star); (b) 5 V (black square), 6 V (red circle), 7 V (blue triangle), 8 V (magenta down-triangle) and 9 V (olive diamond) . The solid line represents a sum of non-Lorentzian and Lorentzian fitting results.

In this work, there is a negative non-Lorentzian component due to the hole bipolarons that are measured in reverse bias but it is hard to specify precisely what positive components there may be. In figure 76, the detailed fitting of the MC is carried out using the sum of a Lorentzian and a non-Lorentzian function under low and high forward bias conditions. As the relative sizes and signs of the two functions vary with bias, however, they cannot be attributed to a specific process, and the fits are treated as purely empirical. The fitting results from Table I are chosen to fix B_0 to a value of 5mT for the non-Lorentzian function when using equation 48:

$$\frac{\Delta I}{I} = \frac{a_0 B^2}{\left(|B| + B_0\right)^2} + \frac{a_1 B^2}{B^2 + B_1^2} \tag{48}$$

The reason for this is that the “spike” occurs below 10 mT. As the Lorentzian function saturates more slowly than the non-Lorentzian, the high field behaviour is described by the Lorentzian component of the empirical fit. In order for a “spike” to appear, the non-Lorentzian function must dominate below 10 mT and the 5 mT value chosen satisfies this requirement whilst reducing the number of free fitting parameters to three. The fitting results under different forward bias conditions are shown in figure 76.

The MC results are separated in figure 76, the negative high field MC data in figure 76(a) and the positive high field MC in figure 76(b). The fitting

results are summarised in Table II. The sign of the non-Lorentzian prefactor, a_0 is always opposite to the high field (saturation) behaviour described by the prefactor, a_1. This means that it is impossible to associate the non-Lorentzian component to a single mechanism (for example, the bipolaron mechanism) as the sign of a given mechanism is not expected to change with bias. Also the empirical fits carried out here return characteristic fields (B_1) for the Lorentzian component of 5~6 mT and that it is the small difference between these and the fixed non-Lorentzian field that give rise to the "spikes". The overall MC approaches saturation slowly, over a scale of hundreds of mT, and it must be pointed out that the fitting carried out here is purely empirical. It can be expected a minimum of three different processes to be occurring simultaneously (triplet-polaron interaction, triplet dissociation and bipolaron site blocking). It is refrained from carrying out MC fitting with the large number of free parameters these processes would require, as any results would be viewed as meaningless.

Table II: Summary of MC fitting parameters in forward bias.

Bias(V)	a_0	error a_0	a_1	error a_1	B_1(mT)	error B_1(mT)
0.2	-0.95	0.082	0.48	0.071	5.7	0.52
0.4	-0.69	0.057	0.40	0.050	5.8	0.38
0.6	-0.43	0.024	0.24	0.021	5.3	0.27
0.8	-0.38	0.028	0.23	0.024	5.1	0.34
1	-0.33	0.028	0.19	0.025	5.2	0.41
2	-0.28	0.020	0.18	0.018	5.5	0.31
3	-0.18	0.014	0.11	0.012	5.3	0.36
4	-0.15	0.010	0.09	0.009	5.8	0.28
5	-0.09	0.022	0.05	0.020	6.0	1.05
6	0.06	0.013	-0.03	0.011	5.1	1.01
7	0.25	0.032	-0.15	0.028	5.1	0.60
8	0.58	0.054	-0.36	0.047	5.7	0.40
9	0.91	0.090	-0.55	0.079	5.2	0.45
10	1.46	0.185	-0.90	0.162	5.6	0.55

The data in figure 76(b) approaches saturation at fields of the order of hundreds of mT and it is possible to concentrate on high magnetic field MC in the majority of the analysis. As explained above, it would be expected to see some electron injection in forward bias, even at low voltages. There are a number of possible processes that the electron injection could contribute to the

MC, such as the positive pair-level interaction affecting the formation rate of singlets and triplets. [127][174] The change of formation rate of singlets and triplets then affect the device current, via site blocking or weak trapping, [139][175-178] which would be expected to give a positive Lorentzian MC. Alternatively, exciton dissociation at energetically favourable sites would yield a negative Lorentzian of similar form. Finally there could be a strongly coupled triplet-polaron or "trion" interaction which would be expected to be positive with a larger B_0 term. As previously discussed, the "spike" region cannot be unambiguously attributed to distinct processes and it is better to limit the further discussion to high magnetic field results (155 mT and 258 mT) i.e. to fields approaching the saturation region.

The positive bias results in figure 70 can be split into three distinct regions: Low bias, below ~1 V (10^{-4} A/cm^2), where the saturation MC response is negative and has a magnitude approximately the same as the saturation MC under negative bias. Under medium bias, from ~1 V to ~5 V (10^{-4} A/cm^2 to 2×10^{-2} A/cm^2), the saturation MC is negative and decreasing in magnitude as the bias increases. Under large bias, greater than 5 V (> 2×10^{-2} A/cm^2) the saturation MC becomes positive. In the first region, <1 V, the electron injection is expected to be negligible and hence the high field MC is dominated by the bipolaron process. Despite this there is some evidence of the positive "spike" at low fields which increases in magnitude as the bias is increased and this suggests that there is another process occurring, probably related to the fact that the electron injection is not zero. As the applied bias is further increased, the magnitude of the saturation MC decreases until at a bias of ~5 V the high field MC response becomes positive. This voltage corresponds to the point where it is possible to detect light emission from the sample in the system and hence where excitonic effects are expected to dominate. As mentioned previously, this does not mean that excitons are not present at lower bias values, just that the photo detector is not sufficiently sensitive to measure them.

In forward bias the negative saturation MC measured at low current densities (<4×10^{-4} A/cm^2) is in good agreement, both qualitatively and quantitatively, with previously published results [131] at room temperature. The high current (>2×10^{-2} A/cm^2) positive saturation MC agrees qualitatively with the reduced hole mobility due to the presence of excited states in P3HT reported by Song. [175] It is worth noting that positive MC has been previously reported in P3HT at high bias, [131] but at significantly reduced temperature compared

to the above results (200 K). Given that the samples reported by Nguyen [160] contained the hole injection layer PEDOT:PSS and that this material displays significant interfacial effects, the discrepancy may be due to the magnetic behaviour of the injection layer.

In this device the transition from negative saturation MC to positive saturation MC appears when the current density exceeds ~10^{-2} Acm^{-2}. The bipolaron theory [138] identifies two competing effects: (i) transport blocking through bipolaron states (negative MC), and (ii) increasing in polaron population at the expense of bipolarons with increasing magnetic field (positive MC). When the long-range Coulombic repulsion between polarons is sufficiently large, (ii) will start to dominate and positive MC will occur. In the experiment, however, the current density increase will not affect this long-range Coulombic repulsion between polarons, so the positive MC cannot be attributed to bipolaron theory. In contrast, the triplet-polaron theory predicts positive MC due to a decrease in triplet states resulting from a magnetic field dependent inter system crossing. This decrease in triplet states results in a decrease in site blocking or polaron trapping which in turn increases the current (positive MC). In the regime where the MC is positive (i.e. at current densities exceeding 10^{-2} Acm^{-2}) and assuming that the current is still hole dominated, using literature values for the hole mobility in P3HT, the hole density can be calculated in the device from the measured current density.

Equation 49 is used to calculate the hole carrier density of the device.

$$J = e \cdot n_{hole} \cdot \mu_{hole} \cdot \frac{V}{d} \tag{49}$$

Where J is the current density (10^{-2} Acm^{-2} at the transition from negative to positive MC), e is the electronic charge, μ_{hole} is the hole mobility of P3HT, V is the applied bias voltage and d is the thickness of P3HT.

Table III: Hole carrier density parameters at 10^{-2} Acm^{-2}

	Bias Voltage	Thickness	Hole carrier density
Au-P3HT-Al	V = 6V	$d = 3\times10^{-5}$ cm	$n_{hole} = 2.08\times10^{16}(cm^{-3})$

The hole mobility in P3HT has been measured separately using the dark-injection technique and $\mu_h = 1.5\times10^{-4}$ cm^2/Vs is obtained at the electric fields used. The bias voltage, thickness and calculated hole density for the device is shown in Table III.

When the current density is higher than 10^{-2} Acm^{-2}, the electron density should be taken into account. The hole carrier density at 10^{-2} Acm^{-2} in this device is ~10^{16} cm^{-3} when the transition of MC happens. The triplet concentration at the onset of measured electroluminescence can be calculated using the light detection lower limit of 10^{-10} W. Considering one second of operation, the number of singlets generated can be calculated using equation 50, and obtaining 2.6×10^{8} singlets generated in 1 second.

$$S = \frac{E\lambda}{hc} \tag{50}$$

Here, S is the singlet population, E is light emission energy (10^{-10} W) detected in 1 second, h is the Planck constant, c is the velocity of light and λ is wavelength of light detected (520 nm).

The electrical excitation results in a singet/triplet generation ratio of 1:3. The population of triplets decaying in 1s can be calculated using a literature triplet lifetime of 10 μs. [179] Assuming a steady state, the triplet population divided by the triplet life time will be equal to the rate of triplet generation minus the triplet decay rate (can be ignored compared to the generation rate), thus, obtaining a total triplet population of 7.8×10^{3}. Using the diode dimensions of 0.2 cm×0.2 cm×3×10^{-5} cm, a triplet density of ~10^{10} cm^{-3} can be obtained.

As shown in figure 76, the MC change is ~0.01% when the saturation region transition happens from 5 V in figure 76(a) (negative MC) to 6 V in figure 76(b) (positive MC). Meanwhile, the triplet density (~10^{10} cm^{-3}) is ~0.001% of the hole density (~10^{16} cm^{-3}) in P3HT. At the same time, both hole density and triplet density are lower than the theoretical upper limit of the hopping carrier site density. Using 1.1 g/cm^3 as the mass density of crystalline P3HT from the literature [180] and the molecular weight for a monomer unit of 176 g/mol, the monomer site density obtained is ~10^{21} cm^{-3}. Therefore the hopping site density has to be < 10^{21} cm^{-3} which is taken to be less than or equal to the density of monomer units, $n_{site} \leq n_{monomer} = 3.8\times10^{21}$ cm^{-3}, calculated using

literature values. [180] The site density is larger than the calculated hole density which suggests the result in Table III makes sense.

These results, based on the pre-doped Au/P3HT/Al device, show that under low reverse bias, where the device is operating under hole only conditions, the negative MC can only be explained by the bipolaron mechanism. This is confirmed by fitting using a single non-Lorentzian function. Under high magnetic fields (≥100 mT) the negative MC in low forward bias is also attributed to the bipolaron mechanism although there may be some small contribution from electron injection. The positive MC under high forward bias and high field conditions is explained using the triplet-polaron interaction mechanism and this is confirmed by the electroluminescence measurement. The high magnetic field MC transition from negative to positive occurs at a current density of ~10^{-2} Acm^{-2}. The triplet/hole density ratio (~0.001%) is comparable to the MC change (~0.01%), suggesting the perturbation effect of site blocking and other interactions with the system. Under appropriate drive conditions (10^{-4}-10^{-2} Acm^{-2}) both mechanisms occur simultaneously within the device and the overall sign of the MC results from competition between them.

3.2 Oxygen doping effects on P3HT

3.2.1 Overview

Photo-oxidation doping in P3HT includes two reaction routes. One is fully reversible, forming charge transfer complexes (CTC) [181] and the other is related to the formation of singlet oxygens under participation of triplet excitons on the chains of P3HT. [89] Annealing above the glass transition temperature can lead to de-doping and will also result in a reversible shift of the Fermi level (a rise of ~0.3 eV after de-doping), [90-91] an enhancement of the π-π stacking in the crystal domains [182] and an improvement of the degree of crystallinity. [95] This can result in an improvement in charge carrier mobility in different structures of devices. [53][167][183-184] In this section, the current density-voltage (J-V) and magnetoconductance (MC) response of a poly(3-hexyl-thiophene) (P3HT) device (Au/P3HT(350 nm)/Al) are compared as shown in figure 77 before and after annealing above the glass transition temperature of 150 ^{o}C under vacuum. There is a decrease of more than 3 orders of magnitude in current density due to an increase of the charge injection barriers after de-

doping through annealing. An increase, approaching 1 order of magnitude, in the negative MC response after annealing can be explained by a shift in the Fermi level due to de-doping, according to the bipolaron mechanism. The charge injection barrier is successfully tuned through re-doping by photo-oxidation. This leads to the charge injection and transport transitioning from unipolar to ambipolar, as the bias increases, and the MC response is modelled using a combination of bipolaron and triplet-polaron interaction mechanisms.

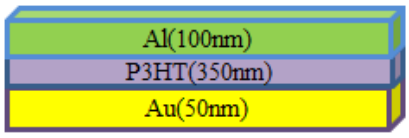

Figure 77: Schematic of an Au(50 nm)/P3HT(350 nm)/Al(100 nm) device.

3.2.2 Results

Figure 78 shows a double logarithmic plot of current density versus voltage (j-V) for the pristine (pre-doped), annealed and re-doped Au/P3HT(350 nm)/Al device.

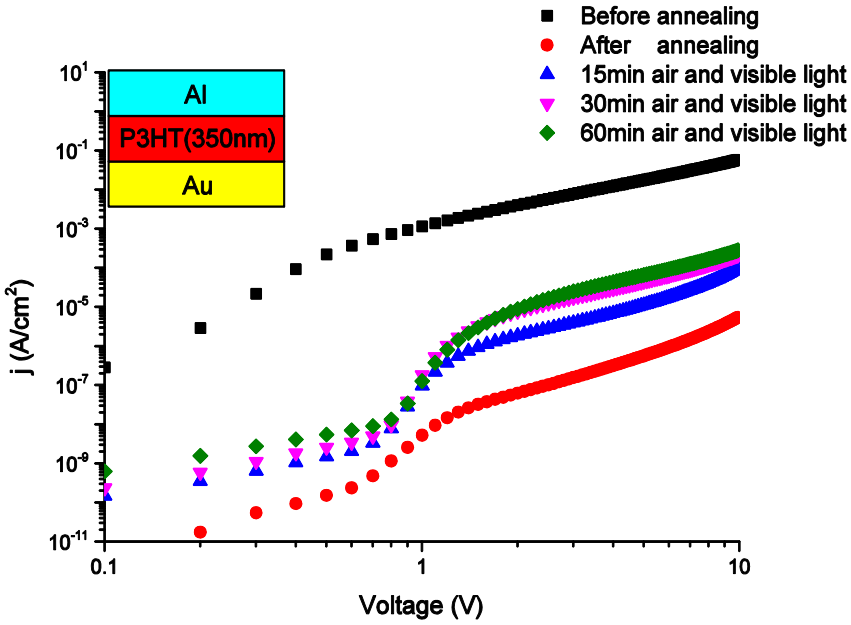

Figure 78: Current density versus voltage characteristics in the pristine (black squares), annealed (red circles) and re-doped samples. The re-doping exposure is varied: 15 minutes (blue up-triangles), 30 minutes (magenta down-triangles) and 60 minutes (olive diamonds).

Before annealing, as shown in figure 78, the j-V curve appears as an almost featureless straight line, with no sharp “turn on” transitions, confirming that the oxygen doping effect results in efficient hole injection and extraction. For both annealed and re-doped samples, a “turn on” appears at ~1 V suggesting an injection barrier has been overcome above that bias. Above ~2 V bias all samples display approximately quadratic j-V characteristics as expected for space charge limited transport (SCLC). In this region (bias > 2 V) there is a decrease of more than 3 orders of magnitude in current density under the same bias after annealing, compared to the pristine (pre-doped) results, which partially recovers after re-doping. These changes can be attributed to the disappearance of band bending through de-doping and the consequent charge injection barrier enhancement as reported in the literature. [92-93] There is a significant current density recovery through re-doping.

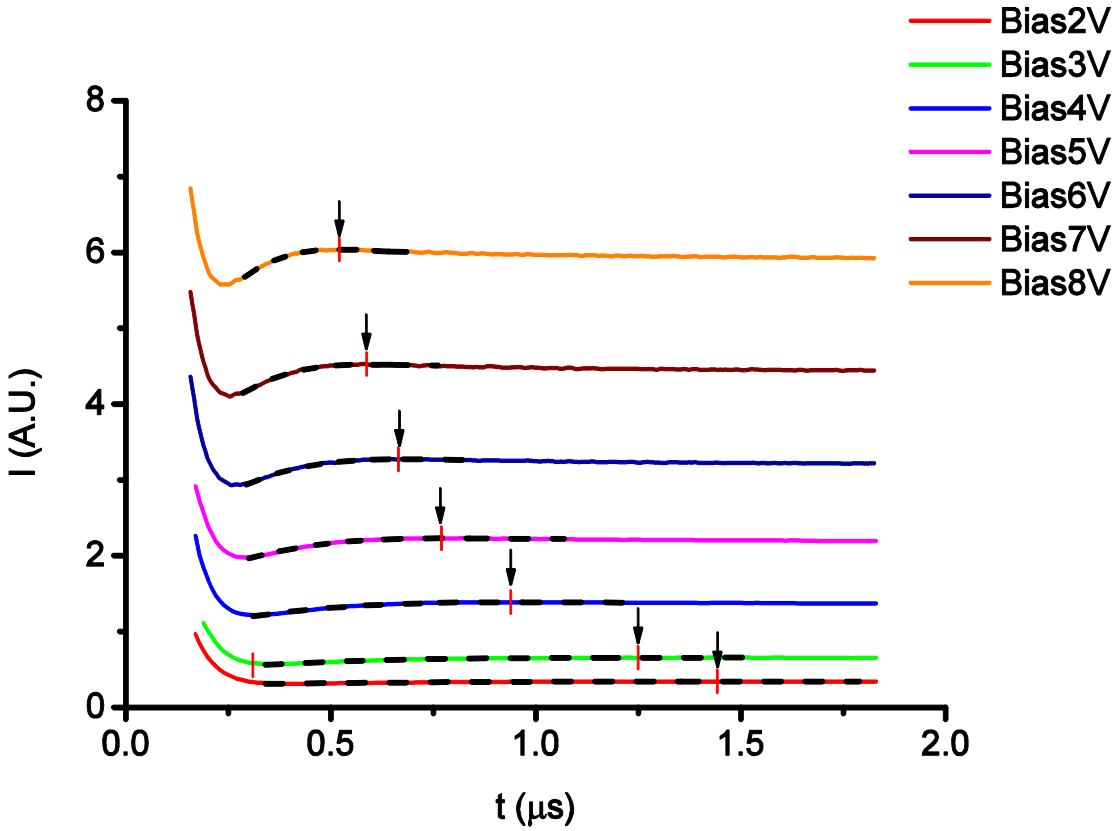

Figure 79: Dark injection results before annealing.

Dark injection (DI) for mobility measurement is carried out under different bias and the fitting results before annealing is shown in figure 79. A cubic polynomial function is chosen to carry out an empirical fitting of the dark injection transient peak and calculating the drift velocity v_d and electric field E

under different bias according to equation 40 and equation 41 in section 2.3.3. The summary of results is shown in Table IV.

Table IV. Summary of analysis results before annealing.

Bias	t_{DI}(μs)	v_d(cm/s)	error v_d(cm/s)	E(V/cm)	error E(V/cm)
2	1.46	18.85	1.35	5.71E+04	0.41 E+04
3	1.20	22.95	1.64	8.57E+04	0.61 E+04
4	0.95	28.94	2.08	1.14E+05	0.82 E+04
5	0.79	34.97	2.50	1.43E+05	1.02 E+04
6	0.66	41.51	2.97	1.71E+05	1.22 E+04
7	0.59	46.43	3.32	2.00E+05	1.43 E+04
8	0.54	50.99	3.64	2.29E+05	1.63 E+04

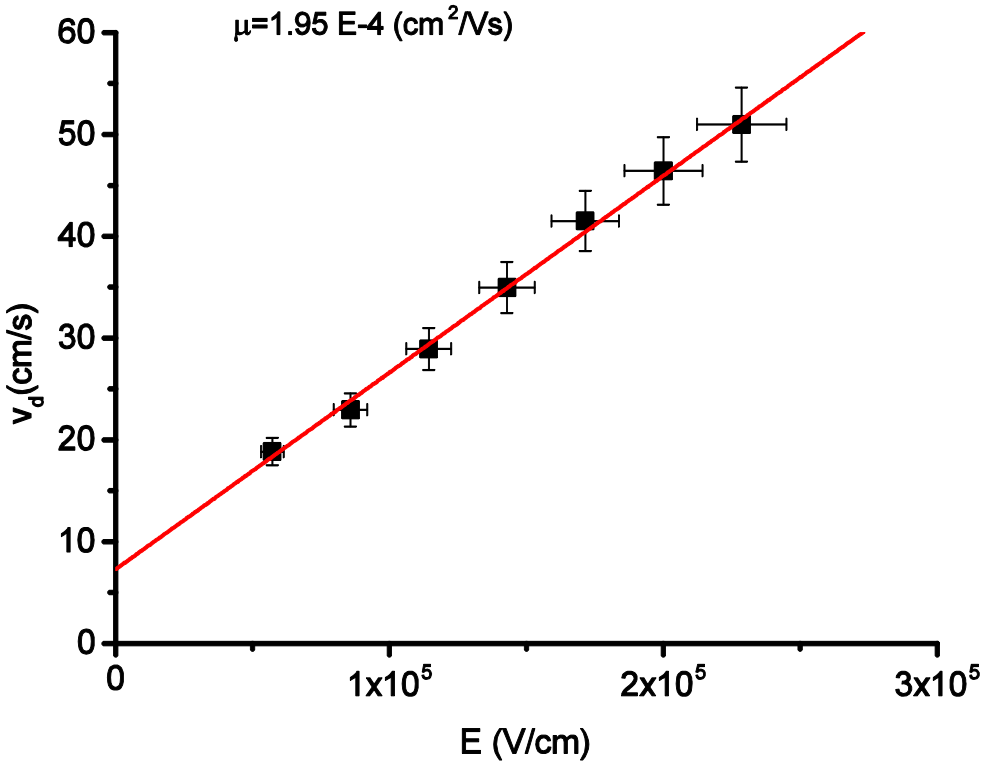

Figure 80: Charge carrier drift velocity versus electric field with error bars and the mobility fitting results.

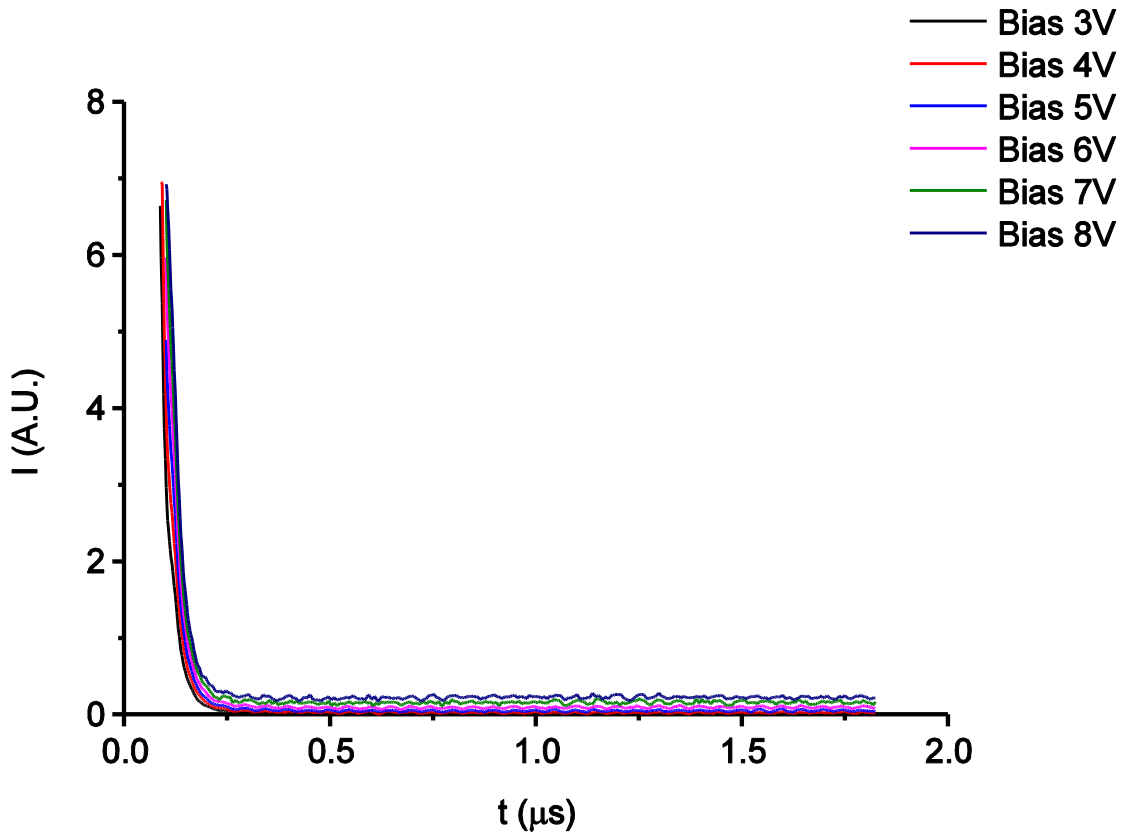

Figure 81: Dark injection results after annealing.

The drift velocity v_d is plotted versus electric field E in figure 80 and the slope of linear fitting is the hole mobility of P3HT before annealing. The result is ~10^{-4} cm^2/Vs as shown in figure 80. This is in agreement with mobilities reported in the literature. [53][175]

After annealing, however, the DI transient peak disappears, as shown in figure 81. This is entirely consistent with the re-appearance of a significant injection barrier at the anode, due to removal of the doping effect, since DI measurements require highly effective injection conditions. The steady state (long time) currents in figure 81 display a corresponding current density drop to that in figure 78.

After proving the oxygen doping and de-doping effect on conductance, the MR measurement is carried out on P3HT based device. The magnetoconductance (MC) response versus magnetic field (B) is plotted under different bias and sample conditioning. Figure 82 is the MC response before annealing for the Au/P3HT(350 nm)/Al device.

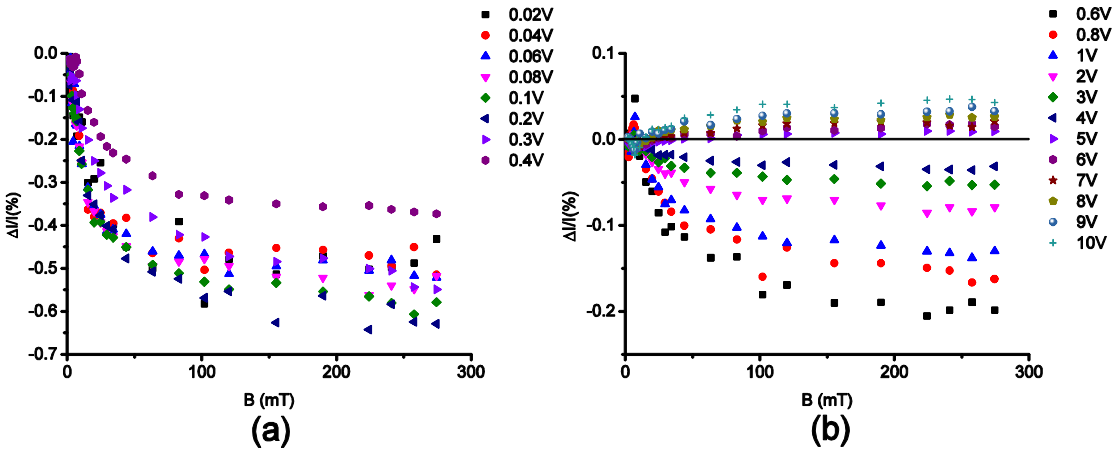

Figure 82: Variation in device current versus magnetic field before annealing.

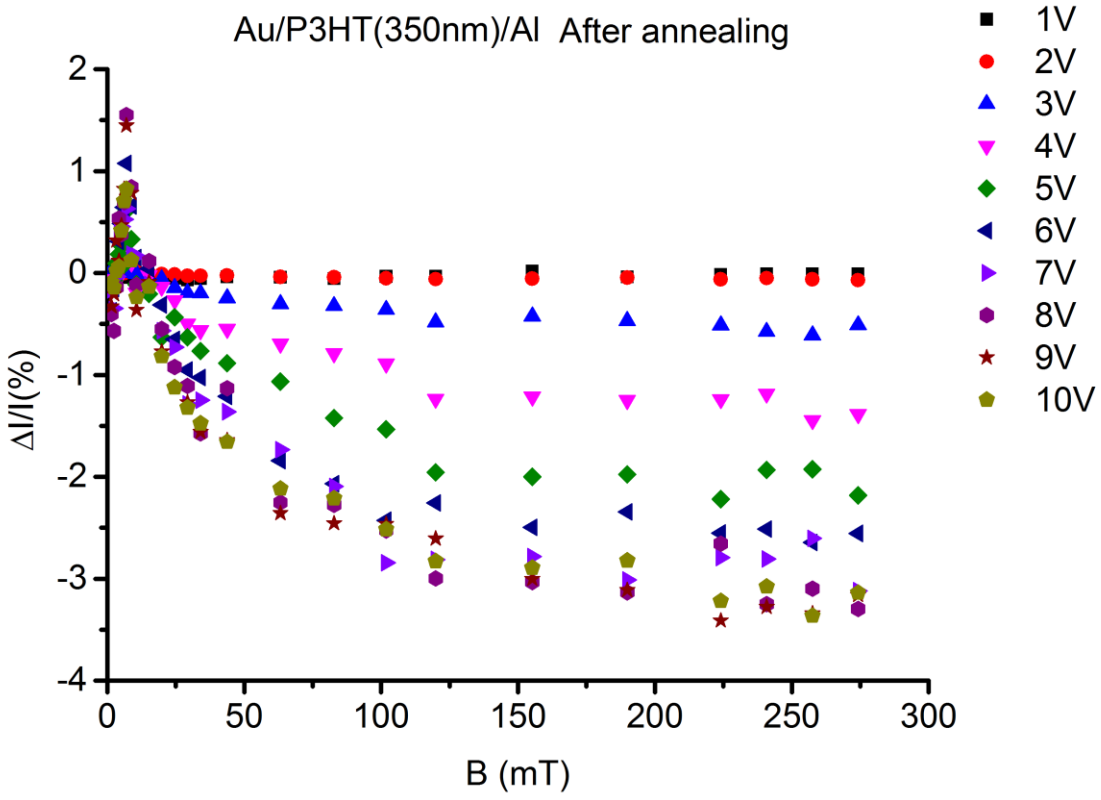

Figure 83: Variation in device current versus magnetic field after annealing.

The MC can be detected under a bias as low as 0.02 V in the pristine device as shown in figure 82. For the pristine sample, there is a transition under high magnetic field from negative MC to positive MC as the bias voltage increases, which is in agreement with the previous results in section 3.1. [146] The negative MC is attributed to the bipolaron mechanism [138] dominating and the positive "spike" below ~10 mT to the triplet-polaron interaction mechanism. [139]

After annealing (figure 83), there is negligible MC response below 1 V because of poor charge injection. The positive "spike" (below ~10 mT) increases with the drive voltage as does the negative (saturation) MC under high magnetic field. The negative response can be as large as -3% after annealing which is an increase of approximately 1 order of magnitude compared to that before annealing. After re-doping (figure 84) there is no low field "spike" under low bias (from 0.9 V to 1.9 V) and the positive "spike" appears above 2 V. The negative (saturation) MC under high magnetic field first decreases from 0.9 V to 2 V then increases from 2 V to 10 V.

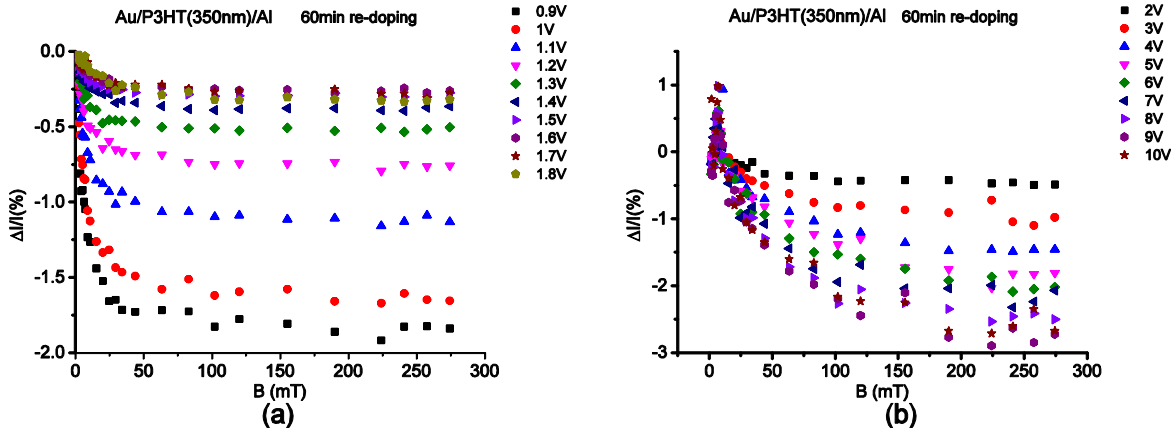

Figure 84: Variation in device current versus magnetic field after re-doping.

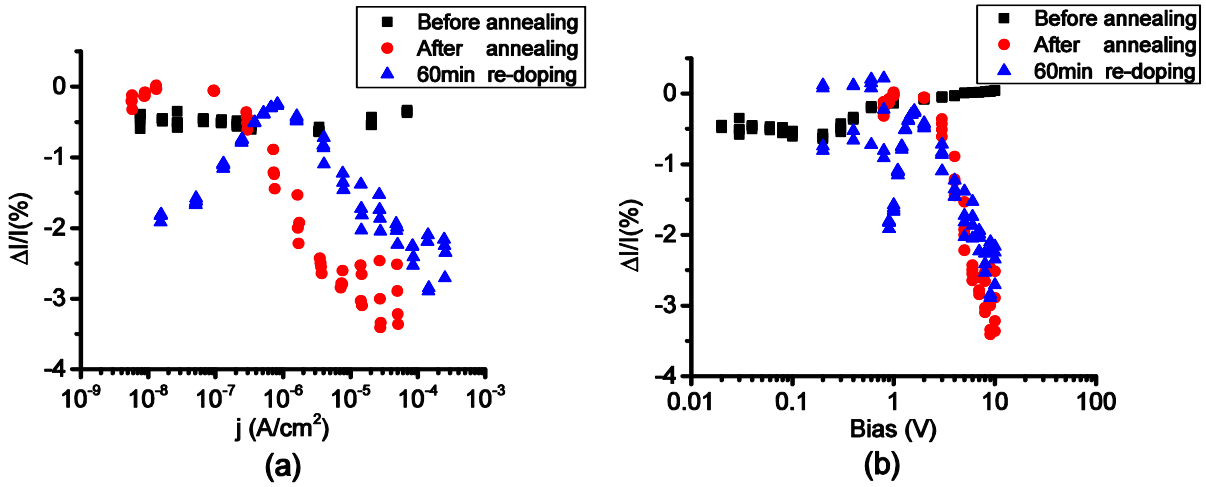

Figure 85: Saturation magnetoconductance (MC) response under high magnetic field (102 mT, 155 mT, 224 mT and 258 mT) before annealing (black squares), after annealing (red circles) and after 60 minutes re-doping (blue up-triangles). (a) MC versus current density. (b) MC versus bias.

In order to clarify the behaviour of the saturation MC, it has been plotted versus the current density in figure 85(a). The MC from 10^{-8}Acm^{-2} to 10^{-4}Acm^{-2}, is chosen and plotted at a number of relatively high magnetic fields (102 mT, 155 mT, 224 mT and 258 mT) under different drive conditions: before annealing 0.02 V to 0.4 V, after annealing 1 V to 10 V, and after re-doping 0.9

V to 10 V. The data (nearly around ~0%) after re-doping from 0.2 V to 0.8 V is also presented in figure 85(b), the negative MC suddenly appears when the bias reaches 0.9 V suggesting the initiation of hole injection. Below 10^{-6} Acm^{-2}, the pristine sample MC is constant and there is negligible MC response for the annealed device. Once sufficient current density is achieved (e.g. at $j > 10^{-5}$ Acm^{-2}) in the annealed device the negative MC far exceeds that obtained from the pristine sample.

3.2.3 Discussion:

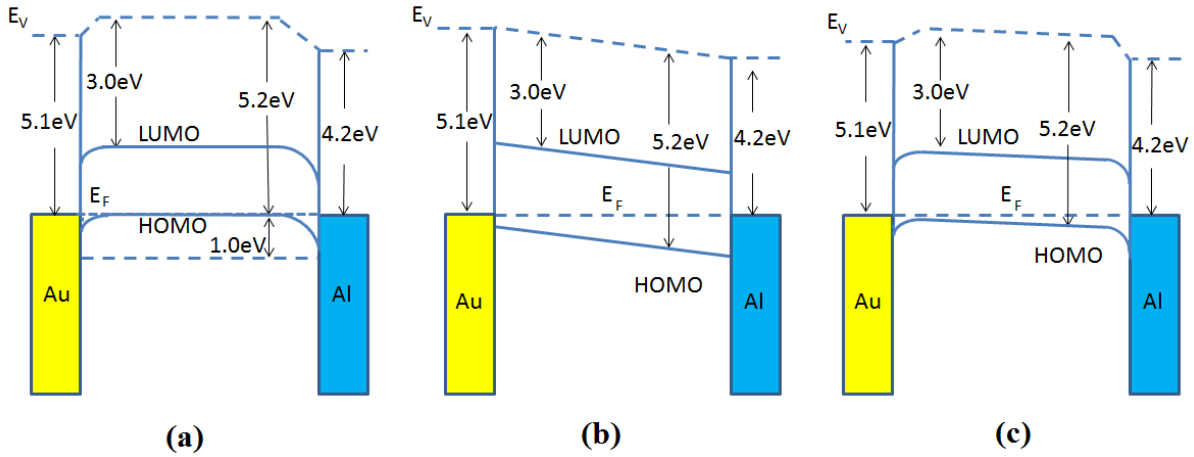

Figure 86: Energetic schematics of the Au/P3HT(350 nm)/Al device under different short circuit conditions. (a) Pristine (pre-doped) sample. (b) Annealed sample. (c) Re-doped sample.

Figure 86 shows schematic diagrams of pristine (pre-doped), annealed and re-doped Au/P3HTAl devices under short circuit conditions. Due to the oxygen doping effect on both interfaces, even at zero bias (figure 86(a)), device is expected to be in a "flat-band" state. After annealing (figure 86(b)), the removal of the dopants results in the return of significant Schottky barriers at both metal-organic interfaces, in agreement with the appearance of the "turn on knee" at ~1 V in figure 86. This is consistent with the "flat band" conditions requiring a bias defined by the difference in the effective work functions, 5.1 eV for Au [170] and 4.2 eV for Al [171] in the undoped case. After re-doping (figure 86(c)) band bending can occur, at least partly, at both interfaces in agreement with the current density recovery in figure 78. According to the bipolaron theory, [138] the magnitude of a negative MC will increase as the value of $-E_F/\sigma$ decreases, where E_F is the Fermi level and σ is the standard deviation of the DoS. As reported in the literature, annealing P3HT will result in a shift of the Fermi level ($|E_F|$ decreases) [90-91] and a broadening of the deep

trap DoS (σ increases). [95] Thus the overall effect of annealing is to reduce the ratio of $|-E_F/\sigma|$, which can explain the larger magnitude negative MC, post annealing, at the same current density (figure 84(a)). This effect has been simulated by Peter Bobbert et al. [138] see figure 113 in section 3.3.3. After re-doping, an increase in $|E_F|$ is expected, which can explain the smaller magnitude negative MC obtained after re-doping, compared to the annealed sample, at high current densities in figure 84(a).

For both pristine and re-doped samples, the negative MC response, when the current density is lower than 10^{-6} Acm^{-2}, is attributed to the bipolaron mechanism in a mostly unipolar system. For the re-doped data (blue up-triangles) the magnitude of the negative MC initially reduces with increasing current density before recovering. The low current density (< 10^{-6} Acm^{-2}) behaviour of the MC in the re-doped case is consistent with a decrease in MC with increasing electric field predicted by the bipolaron theory. [138] There is an obvious transition at 10^{-6} Acm^{-2} corresponding to the appearance of a low field "spike" in figure 83(b). When the current density is higher than 10^{-6} Acm^{-2}, the negative MC under high magnetic field is attributed to the bipolaron mechanism dominating in the presence of ambipolar based mechanisms.

The relatively high magnetic field (102 mT, 155 mT, 224 mT and 258 mT) MC data is plotted versus bias voltage in figure 85(b). The measurable MC at low bias (< 1 V) in the pristine case corresponds to the absence of significant injection barriers. For both annealed and re-doped samples significant MC cannot be detected at such low bias. The annealed sample requires large bias (> 2 V) in order to provide measurable MC (as required to overcome injection barriers). There is a clear barrier lowering effect as a result of re-doping, with the sample only requiring a bias larger than 1 V to provide measurable MC.

A single non-Lorentzian function, given in equation 47 in Chapter 3.1, is chosen to carry out an empirical fitting for the MC response before annealing in figure 87 (between 0.02 V and 0.4 V) and after re-doping in figure 88 (between 0.9 V and 1.9 V). The characteristic fields (B_0) under low bias obtained in the MC response fits as shown in Table V are consistent with that in reverse bias in Chapter 3.1 and those reported in the literature for P3HT which are of the order of ~5 mT.

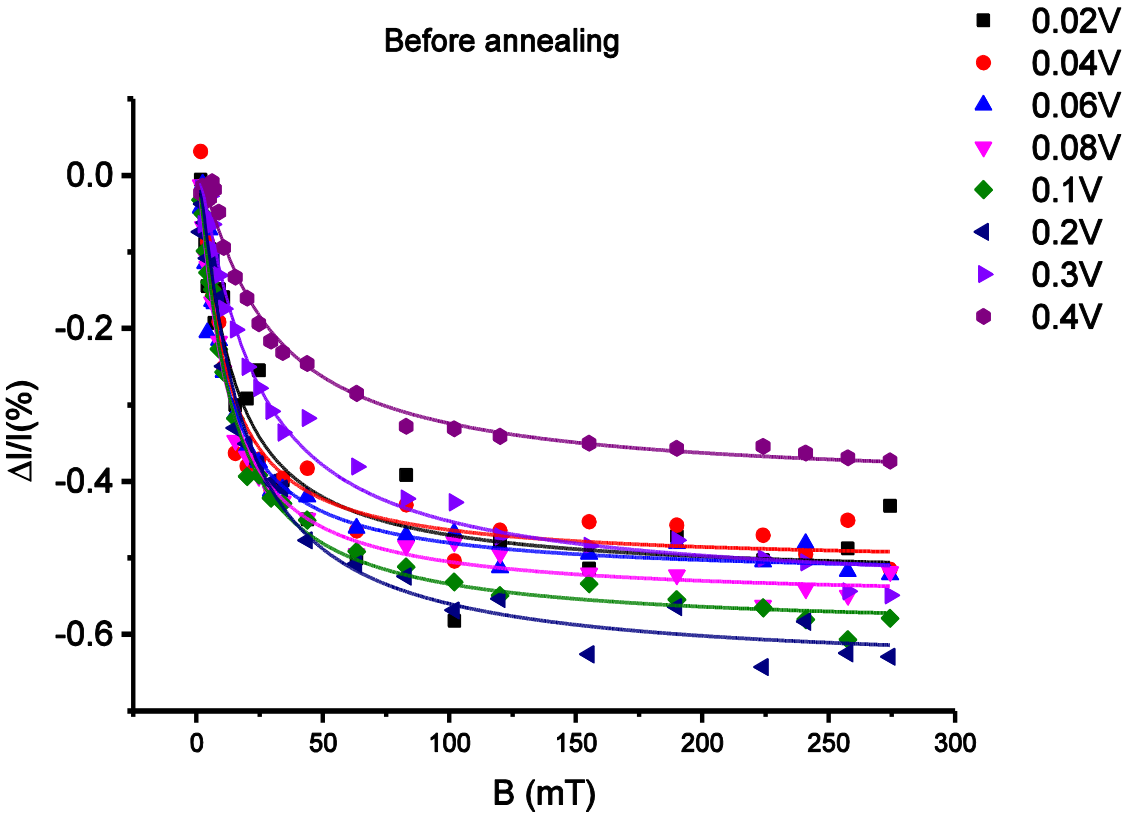

Figure 87: Differential current versus magnetic field (B) before annealing under bias from 0.02 V to 0.4 V.

Table V: Summary of fitting parameters before annealing.

Bias(V)	a_0	error a_0	B_0 (mT)	error B_0 (mT)
0.02	-0.53	0.019	6.06	0.77
0.04	-0.51	0.012	4.85	0.44
0.06	-0.53	0.011	4.73	0.37
0.08	-0.56	0.006	4.99	0.20
0.1	-0.60	0.006	5.65	0.20
0.2	-0.65	0.011	7.62	0.45
0.3	-0.55	0.011	10.18	0.65
0.4	-0.41	0.007	12.28	0.70

As shown in figure 87, the single non-Lorentzian function is chosen according to equation 47 to analyse the MC response under low bias and the summary of the results are shown in Table VI.

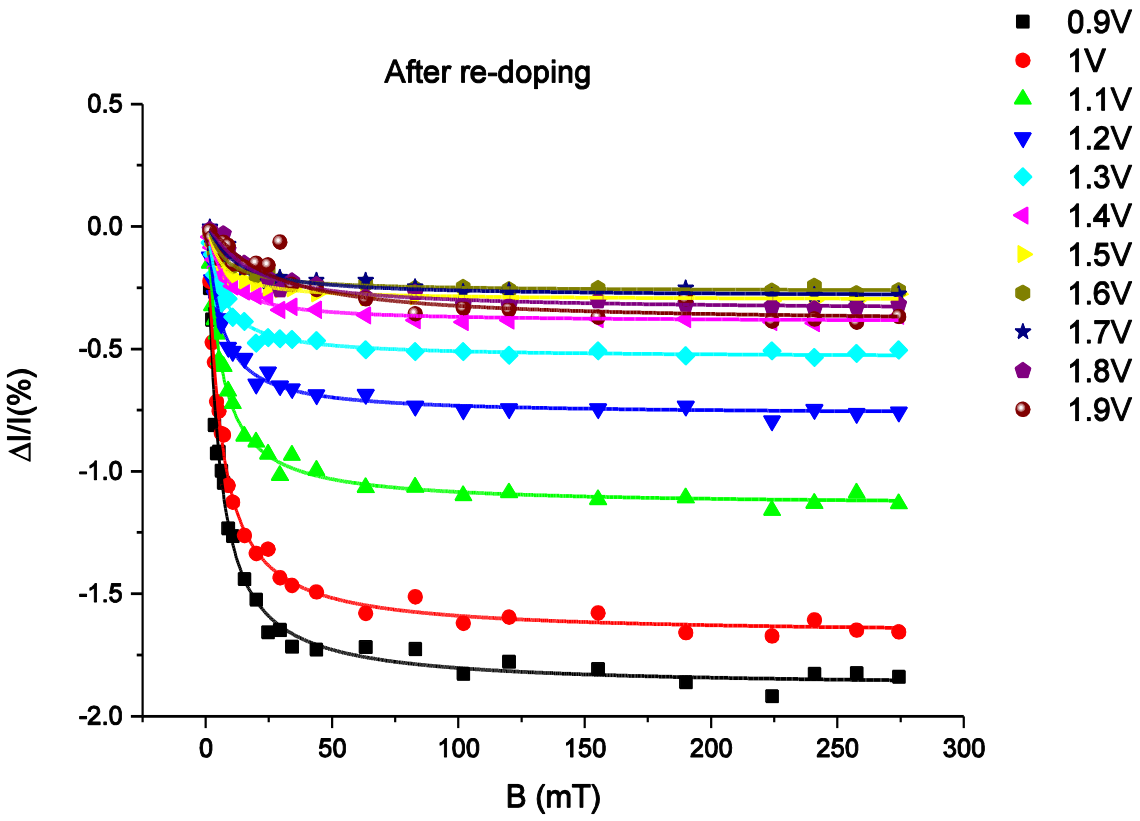

Figure 88: Differential current versus magnetic field (B) after re-doping under bias from 0.9 V to 1.9 V.

Table VI: Summary of fitting parameters after re-doping under low bias

Bias(V)	a_0	error a_0	B_0 (mT)	error B_0 (mT)
0.9	-1.88	0.019	2.19	0.10
1.0	-1.67	0.011	2.43	0.07
1.1	-1.14	0.009	2.57	0.09
1.2	-0.77	0.007	2.48	0.10
1.3	-0.54	0.007	2.51	0.14
1.4	-0.39	0.006	2.84	0.17
1.5	-0.30	0.003	2.55	0.12
1.6	-0.27	0.005	3.18	0.23
1.7	-0.29	0.009	4.80	0.54
1.8	-0.34	0.009	7.22	0.65
1.9	-0.40	0.022	10.46	1.95

As the bias increases, the absolute value of the parameter, a_0 decreases according to the bipolaron theory. Below 1.5 V, the characteristic field B_0 is 2.5±0.3 mT which is smaller than that before annealing. This may suggest the hyperfine field effect decreases after annealing leading to the crystallinity change. Above 1.5 V, the increase of B_0 is due to the electron injection and the single non-Lorentzian function does not fit well. The single non-Lorentzian fitting for negative MC proves that it is the hole bipolaron mechanism which dominates the MC response under low bias. The characteristic field B_0 obtained by fitting, which should be related to the hyperfine field effect, changes from ~5 mT (before annealing) to ~2.5 mT (after re-doping). This may be related to the increased crystallinity following annealing.In the cases where the MC displayed a low field "spike", namely, after annealing (from 2 V to 10 V) and after re-doping (from 2 V to 7 V), see figure 89 and 90(b) a sum of two functions is chosen according to equation 48 in Chapter 3.1. This sum consists of one Lorentzian and one non-Lorentzian function to empirically fit the data.

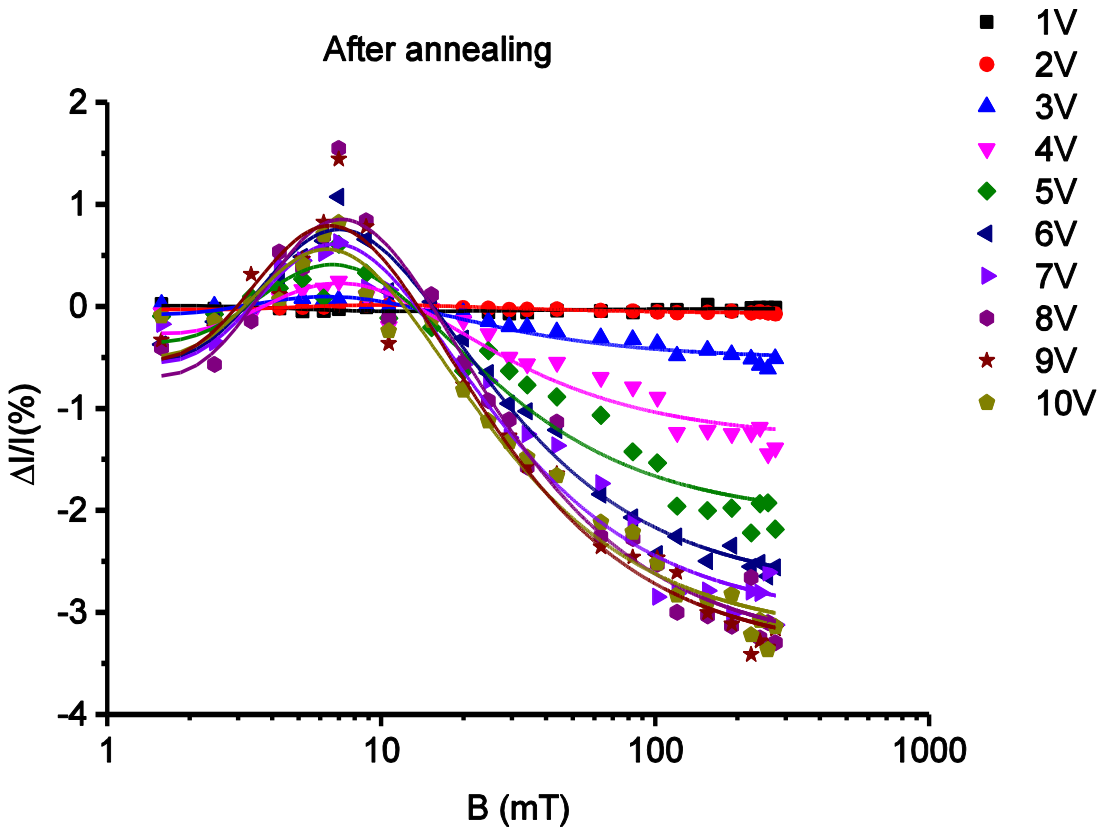

Figure 89: MC response after annealing plotted using a logarithmic magnetic axis.

Having obtained a characteristic field of ~2.5 mT from the single non-Lorenzian fitting to the low field re-doped data, the value of B_0 is fixed in equation 48 to 2.5 mT for subsequent fitting.

Table VII: Summary of MC fitting parameters after annealing.

Bias(V)	a_0	error a_0	a_1	error a_1	B_1 (mT)	error B_1 (mT)
1	0.18	0.07	0.20	0.07	4.77	0.45
2	-0.41	0.05	0.34	0.05	4.83	0.19
3	-2.12	0.20	1.60	0.19	3.75	0.21
4	-5.77	0.50	4.46	0.46	4.00	0.17
5	-8.89	0.73	6.81	0.68	3.84	0.17
6	-13.16	0.51	10.37	0.47	3.92	0.08
7	-13.37	0.77	10.30	0.71	3.89	0.11
8	-15.98	1.03	12.61	0.96	3.98	0.12
9	-14.74	0.92	11.33	0.85	3.77	0.13
10	-13.13	0.74	9.89	0.68	3.76	0.12

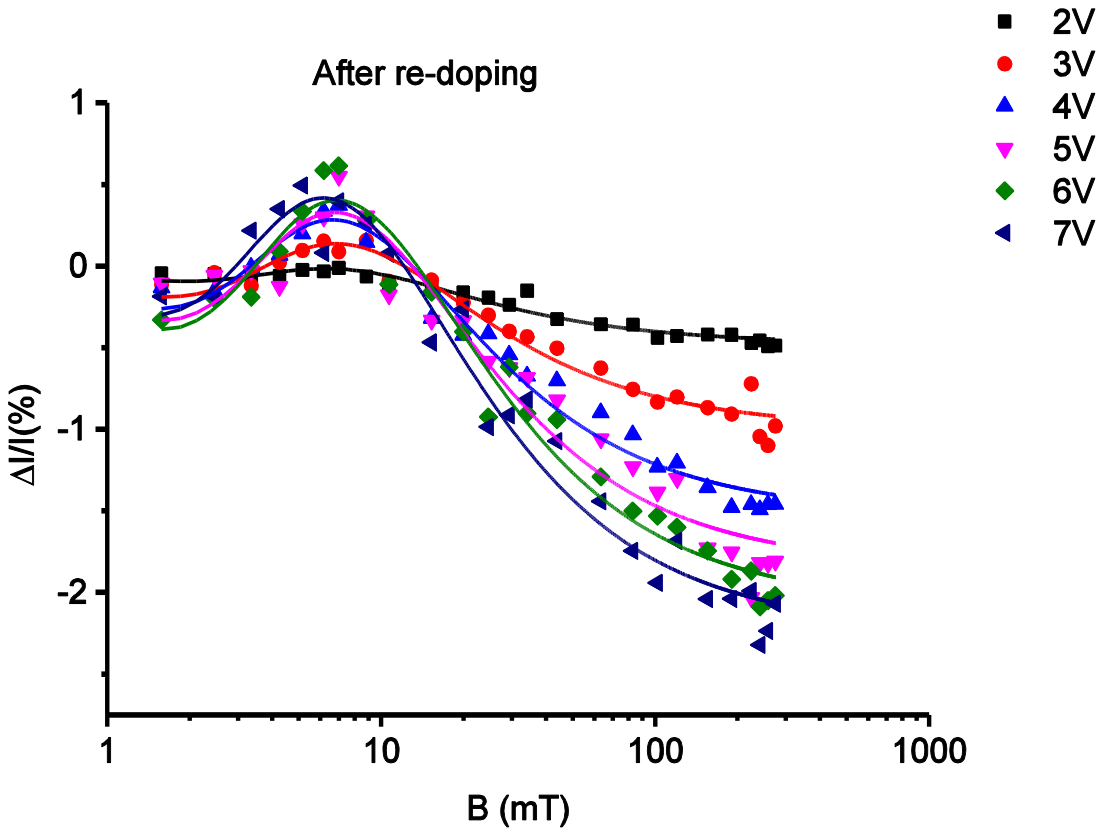

Figure 90: MC response after re-doping plotted using a logarithmic magnetic axis.

The summary of fitting results is shown in Table VII. The non-Lorentzian function can be explained by bipolaron mechanism and the Lorentzian function can be explained by the triplet-polaron interaction. The characteristic field B_2 after annealing is around ~4 mT. For the MC after re-doping under high bias,

equation 48 is chosen and B_0 (~2.5 mT) is fixed according to Table VI as shown in figure 90.

Table VIII: Summary of MC fitting parameters after re-doping under high bias.

Bias(V)	a_0	error a_0	a_1	error a_1	B_1 (mT)	error B_1 (mT)
2	-1.63	0.13	1.15	0.12	4.02	0.17
3	-4.15	0.28	3.16	0.26	3.97	0.14
4	-6.46	0.36	4.95	0.33	3.86	0.11
5	-7.88	0.64	6.04	0.59	3.91	0.16
6	-9.10	0.53	7.04	0.49	3.93	0.11
7	-8.92	0.57	6.70	0.52	3.69	0.14

The summary of fitting results is shown in Table VIII. The characteristic field B_2 after re-doping is still ~4 mT the same as that after annealing. This suggests the re-doping effect only change the barrier injection and the hyperfine field effect contributing to MC response stays fixed after annealing. The change of the characteristic field for bipolaron mechanism from 5 mT to 2.5 mT is probably due to the crystallinity increase which improves the interaction between P3HT molecules.

A summary table of the characteristic fields obtained by fitting is shown in Table IX.

Table IX: Summary of the parameters by empirical fitting.

Sample	a_0	B_0	a_1	B_1
Pristine	Negative	~5 mT		
Annealed	Negative	2.5 mT	Positive	~4 mT
Re-doped: 0.9 V-1.5 V	Negative	~2.5 mT		
Re-doped: 2 V-7 V	Negative	2.5 mT	Positive	~4 mT

The non-Lorentzian function, with negative coefficient a_0, can be taken to correspond to the bipolaron mechanism and the Lorentzian function, with

positive coefficient a_1, can be taken to correspond to a positive magnetoconductance contribution resulting from triplet-polaron interactions.

The triplet-polaron interaction mechanism [139] states that electrons injected from Al under high bias can interact with holes to form excitons. The spins of injected charge carriers from anode and cathode are random, without any external influences, exciton formation is solely governed by spin statistics, 25% of the excitons are singlets which will decay due to short life time and 75% are triplets which will interact with the polaron leading to positive MC. Thus, using the values shown in Table IX, the field can be attributed to triplet-polaron interaction to be ~4 mT. Since the magnitude of the MC is much larger post annealing, there is an increase of the parameters a_0 and a_1 compared to the parameter a_0 before annealing.

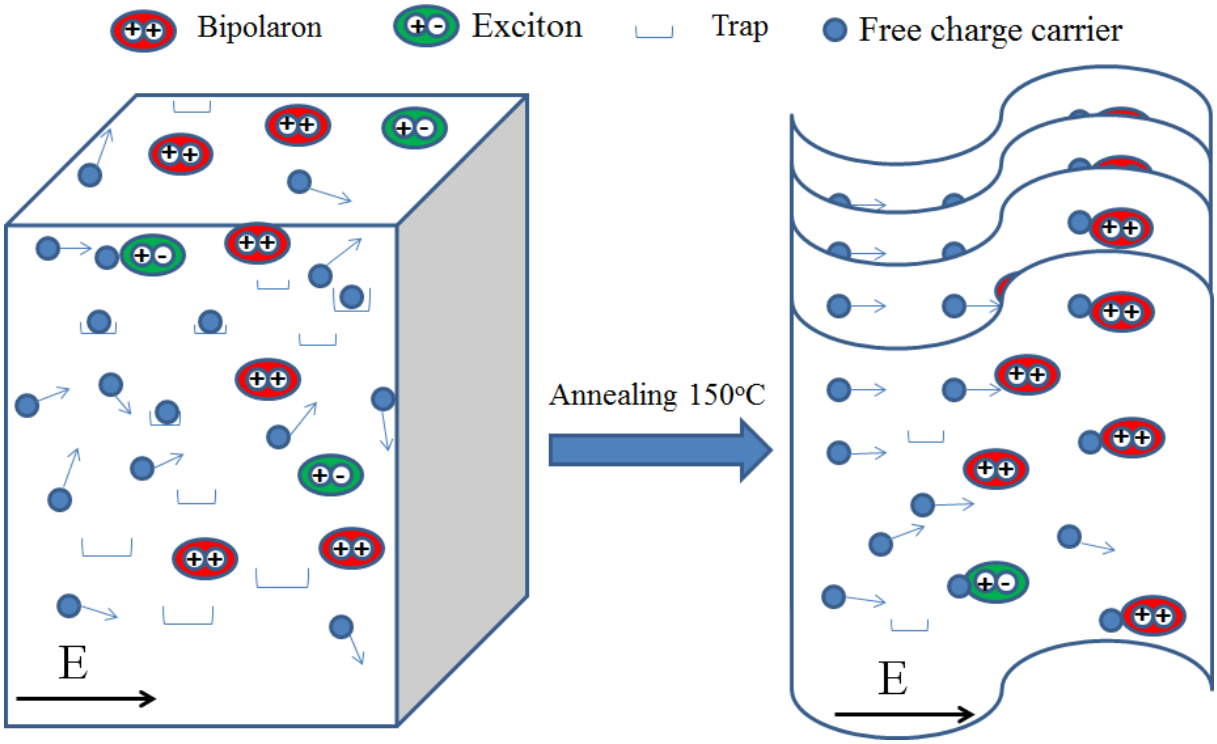

Figure 91: The prediction of dimensionality decrease effect on free charge carrier diffusion, charge-bipolaron interaction, charge-exiction interaction and deep trap states density due to annealing.

Both positive and negative contributions to the MC are found to increase after annealing, and this suggests an increase in probability of charge carriers interacting with both bipolarons and excitons. This is probably due to the irreversible change in crystallinity that the device undergoes after annealing and may result from a decrease in the dimensionality of carrier motion. Such a decrease in dimensionality as shown in figure 91 has been shown to greatly enhance MC in the literature. [147][185]

Even though it is possible to use a sum of only two functions in equation 48 to carry out the empirical fitting of the MC response (after annealing and re-doping) , there are in fact many microscopic mechanisms that could occur within the samples. Under relatively high bias drive conditions (>2V) both signs of charge carrier are expected to be present within the samples (albeit with different relative concentrations). This leads to a large number of possible interactions such as: hole-bipolaron blocking, [138] electron-bipolaron blocking, [138] triplet-polaron interaction, [139] exciton dissociation, [139] hole electron-bipolaron interaction and electron hole-bipolaron interaction.

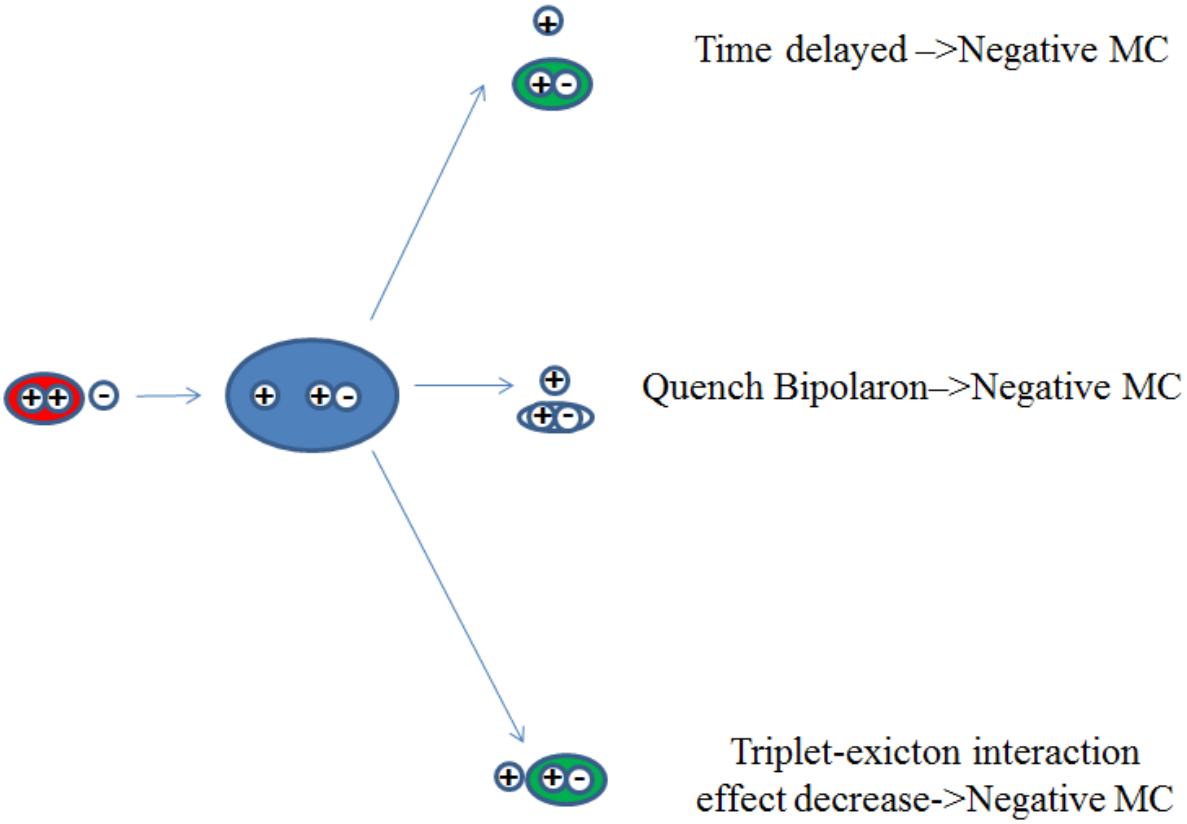

Figure 92: Three ways of electron interaction with hole-bipolaron.

The last two effects will require some explanation. As shown in figure 92, if a hole encounters an electron-bipolaron ultimately this should result in recombination and the formation of a single free electron. This will not change the total charge carrier density as the electron will also drift under the electric field. It is not obvious what overall effect this type of interaction ought to have on the MC. At the same time, the interaction reduces the total number of bipolarons which may cause positive MC. These effects should also occur when an electron encounters a hole bipolaron. Thus the microscopic situation within the samples when ambipolar injection is possible will be highly complicated.

For this reason the MC fitting carried out in this work has to be viewed as purely empirical.

It worth noting that although ambipolar injection is possible at high bias for both the annealed and re-doped samples, the transport is expected to be hole dominated and thus for the hole bipolaron based mechanism to be the main contributor to the overall MC. This is consistent with the negative sign of the saturation MC for these samples in figure 85.

In conclusion, the J-V and MC response have been analysed in an Au/P3HT(350 nm)/Al device before and after annealing above the glass transition temperature. A ~3 order of magnitude decrease in current density can be attributed to the large increase of the charge injection barriers at both electrodes, supported by the DI results. The ~1 order of magnitude increase of the negative MC response can be explained by a shift in the Fermi level ($|E_F|$ decrease) and deep trap DoS broadening (σ increase) after annealing, as predicted by the bipolaron mechanism. After re-doping the MC response shows a transition from a unipolar to an ambipolar behaviour as the bias voltage increases. A single non-Lorentzian function is chosen to fit the MC data in the unipolar cases (under low bias) and a sum of one non-Lorentzian function and one Lorentzian function is carried out to empirically fit the MC response in the ambipolar cases (under high bias). Many effects are expected to contribute to the MC under ambipolar drive conditions, as evidenced in the positive "spike" in the MC plots. The hole-bipolaron blocking effect, however, remains the dominant mechanism (leading to negative saturation MC) under such conditions.

3.3 Pentacene doping effects on P3HT

3.3.1 Overview:

Charge transport and magnetoconductance (MC) response in organic semiconductor diodes can be affected by introducing trap states through different routes, both in small molecule and polymer based devices.[112][186-189] Pentacene, due to its elevated highest occupied molecular orbital (HOMO), can act as a hole trap centre in P3HT. [190-192] In this section, current density, hole mobility, magnetoconductance (MC) and luminescence have been measured in poly(3-hexyl-thiophene) (P3HT) based diodes including pentacene as an impurity. The presence of pentacene will both improve hole injection and

reduce hole mobility. The pentacene doping is also found to increase the negative MC under low bias and enhance electroluminescence (EL) efficiency under high bias compared to an undoped diode. The enhancement of MC is attributed to the pentacene doping effect which will broaden the distribution of the density of states (DoS) in P3HT based on bipolaron theory. The enhancement of EL efficiency after pentacene doping is attributed to the balanced hole and electron mobility leading to a more balanced electron-hole combination in P3HT. The work in this section presents a controllable way of chemical doping to engineer the increase or decrease in an absolute current at a given bias depending on the choice of anodes and tune the magnitude of negative MC response and EL efficiency under different driving conditions.

Three device architectures are fabricated, as shown in figure 93. All devices are fabricated using a combination of vacuum deposition (for metals and LiF) and spin-coating (for organics). In general, all P3HT samples are dissolved in 1,2-dicholobenzene with different pentacene content (0%, 2%, 5% and 10%).

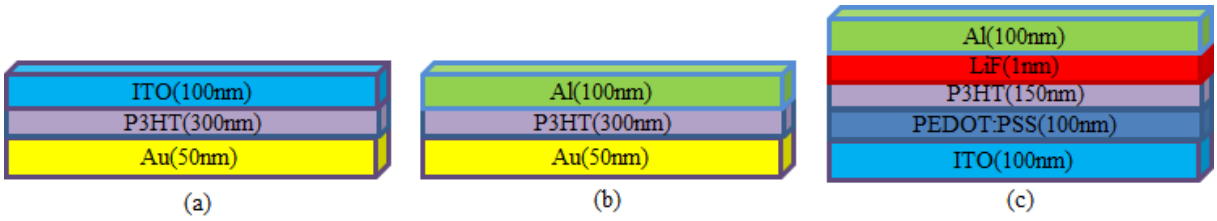

Figure 93: Schematic of three kinds of P3HT-based investigated devices.

3.3.2 Results:

Figure 94 shows the measured current density versus the nominal electric field for a number of Au/P3HT/ITO devices, as shown in figure 94(a), with different pentacene content in reverse and forward bias. In forward bias, Au acts as the anode, whereas in reverse bias ITO acts as the anode. As the pentacene concentration increases, the forward bias current is initially reduced (at a given bias), whereas the reverse bias current increases. The decrease in current density in forward bias can be attributed to the hole trapping effect of pentacene and subsequently reduced mobility. Any improved hole injection from the Au, due to the presence of pentacene, is more than offset by the trapping effect. When the pentacene concentration reaches 10%, there is a measured increase in current density. This may be due to holes hopping through the HOMO levels of

the pentacene at such high concentrations and/or significantly increases hole injection from Au to the pentacene HOMO. Both these effects will lead to an increase in current density.

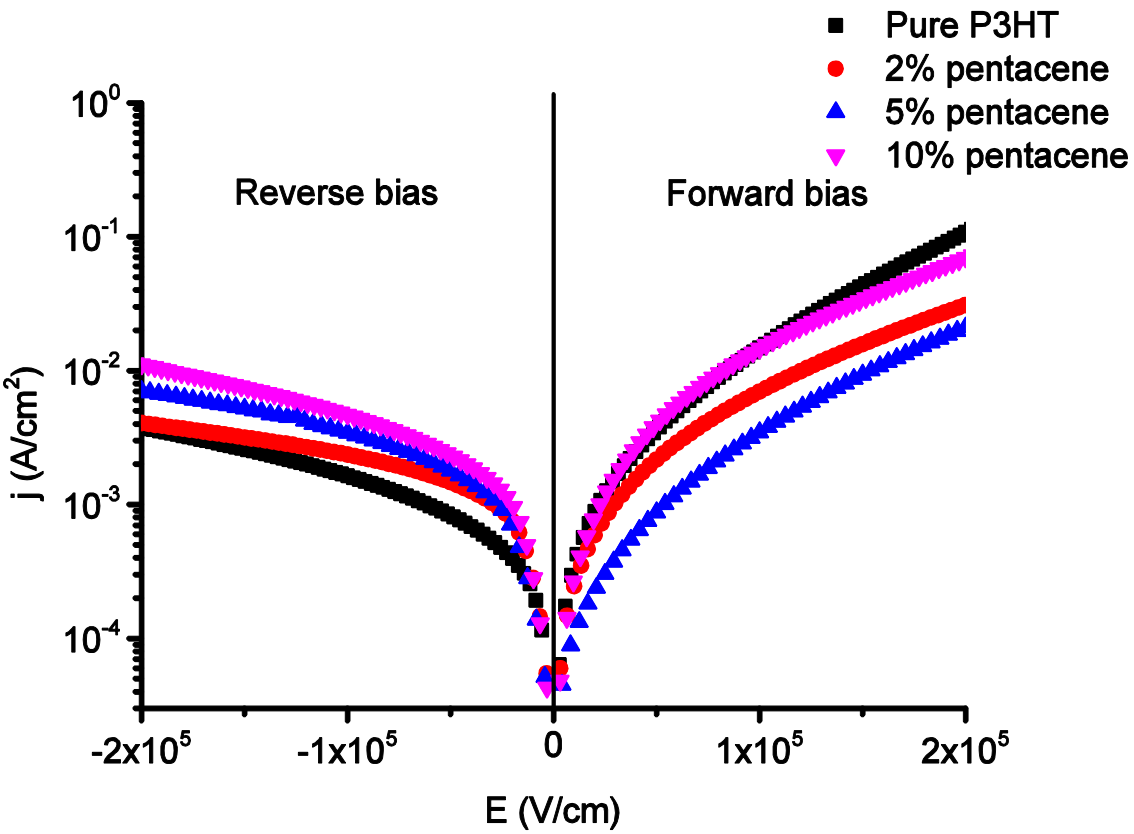

Figure 94: Current density as a function of the nominal electric field for Au/P3HT/ITO based devices with different pentacene content.

In order to investigate the hole trapping effect on charge transport due to pentacene doping, the hole mobility is measured through the dark injection (DI) transient current technique with a differential amplifier. Figure 95 shows comparison of the typical DI current transient results with and without a differential amplifier. Due to the limit of the pulse generator (TTi TG1010A), the largest output bias is 10V, which limits the electric field applied across the sample.

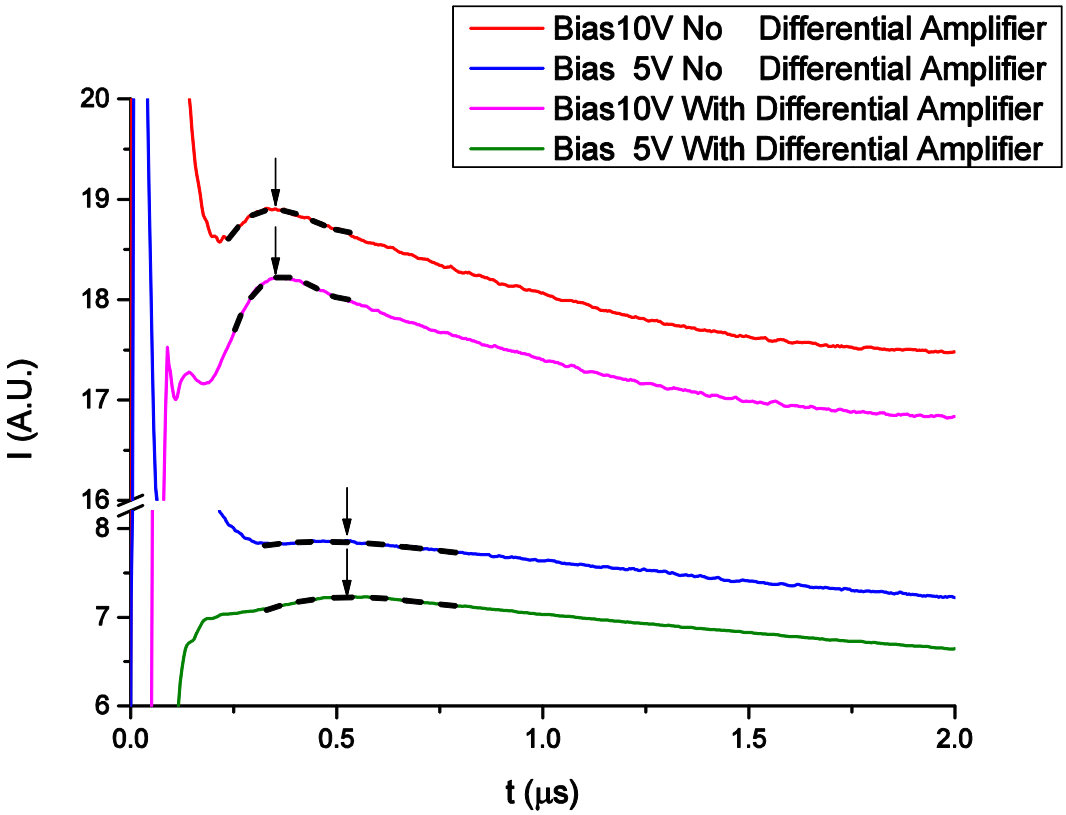

Figure 95: Typical DI current transients obtained in a 2% pentacene doped Au/P3HT/ITO device with and without, the differential amplifier circuit. The sample is biased in the forward direction (Au positive).

Figure 95 shows all the typical DI current transient results in Au/P3HT/ITO with a differential amplifier under different pentacene doping content. The difference of the work function between Au and plasma treated ITO is as small as 0.2 eV. The formation of a "flat band" condition due to oxygen doping in pristine P3HT (pre-doped) will also decrease the hole injection barrier. So the built-in voltage can be ignored and the electric field applied across the sample can be calculated using bias voltage divided by the sample thickness, *V/d*. The hole mobility, μ, is commonly calculated at a given field based on equation 40 and 41 in section 2:

$$\mu = \frac{v_d}{E} = 0.786 \times \frac{d^2}{Vt_{DI}} \tag{51}$$

Where, v_d is the drift velocity of the carriers, E is the electric field, V is the effective voltage, d is the thickness and t_{DI} is the DI transient time.

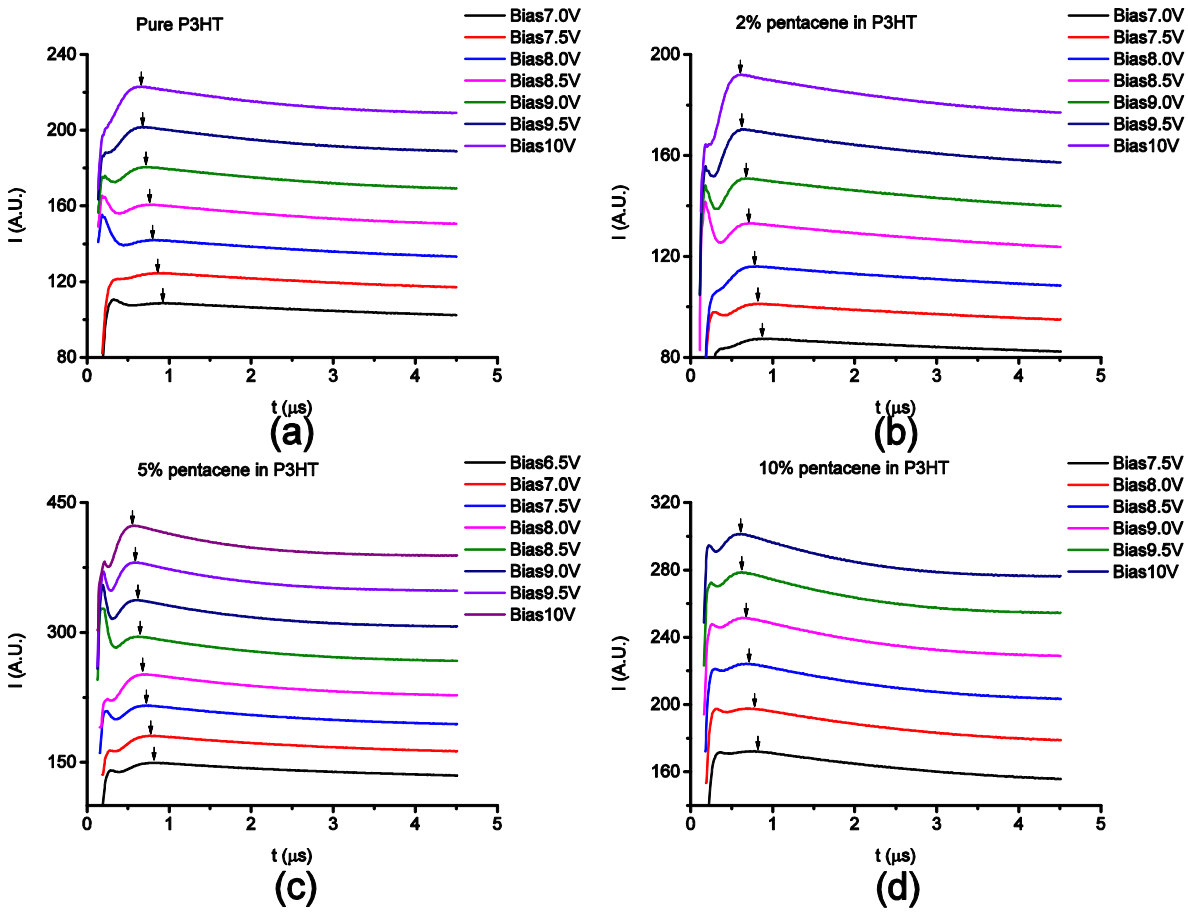

Figure 96: DI responses summary: (a) Pure P3HT, (b) 2% pentacene in P3HT, (c) 5% pentacene in P3HT and (d) 10% petancene in P3HT.

When pentacene is introduced into the system, however, the trapping effect cannot be ignored. There is evidence of a noticeable intercept in all doped results shown in figure 97. Using equation 51 to calculate the hole mobility at a given field will lead to an incorrect conclusion that the mobility will decrease with the electric field.

The parameter t_{trap} is introduced to describe the trapping effect. The life time of a charge carrier is defined to be terminated if it has been trapped by an introduced state. Thus, the lifetime (t_{trap}) will decrease as the concentration of the trap states increases.

$$\frac{1}{t_{trans}} = \frac{1}{t_{extraction}} + \frac{1}{t_{trap}} = \frac{0.786}{t_{DI}} + \frac{1}{t_{trap}} = \frac{\mu}{d}E + \frac{1}{t_{trap}} \tag{52}$$

Where $t_{\text{extraction}}$ is the charge extraction time without the trapping effect, t_{trap} is the life time due to trapping effect, μ is the mobility, E is the electric field and d is the device thickness.

In figure 97, the reciprocal of the transit time is plotted against the nominal electric field *E*. The gradient of such a plot is equal to the charge mobility divided by the thickness (μ/d), and the plot also highlights any trapping effects which may be present due to the presence of a noticeable y-axis intercept. In the absence of any trapping effect, such as in pure P3HT sample (figure 96), the mobility can be obtained by equation 52.

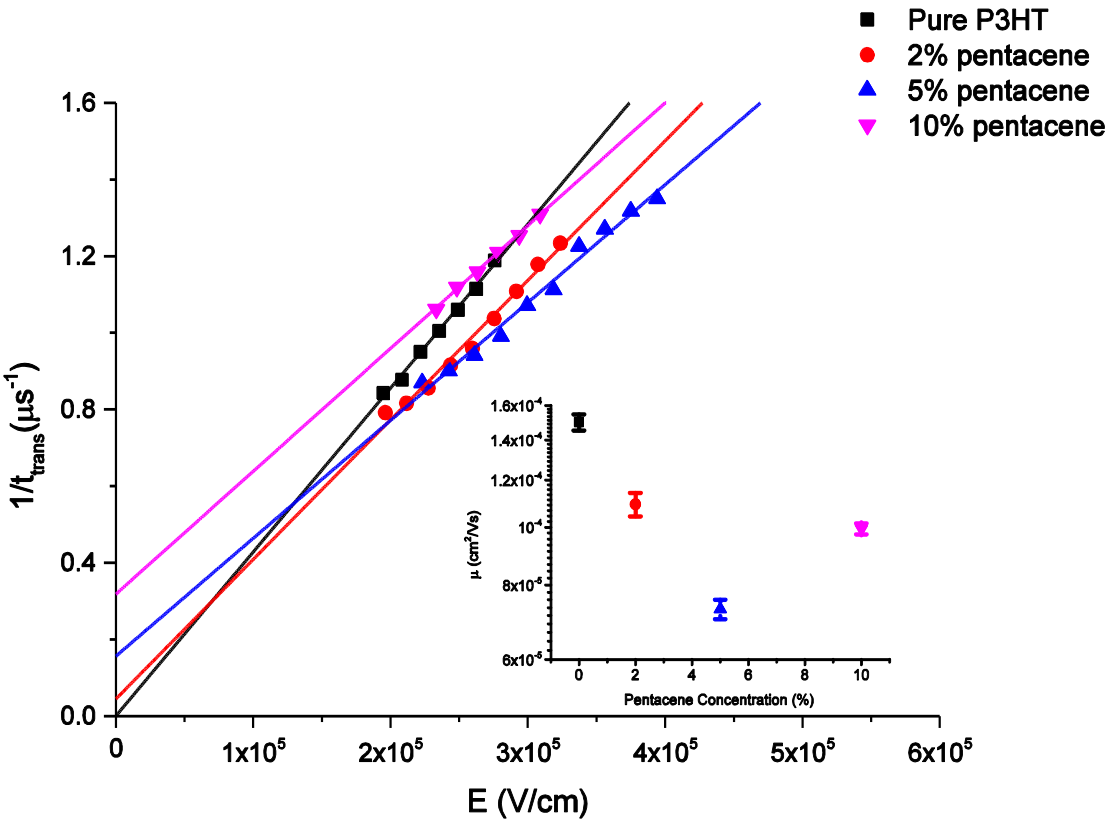

Figure 97: $1/t_{trans}$ versus *E* for unipolar devices (Au/P3HT/ITO) with different pentacene content.

The inset in figure 97 shows an average hole mobility (with error bar), calculated from the gradient multiplied by the thickness *d*, versus the pentacene content. The hole mobility first decreases and then increases when the concentration reaches 10%. The mobility decrease is attributed to the hole trapping effect, and the recovery at high pentacene content, to charge transport through the pentacene electronic states (HOMOs). At the same time, the intercept, which corresponds to the trapping rate, keeps increasing as the pentacene content increases.

Above all, the results in unipolar devices (Au/P3HT/ITO) prove that pentacene can both act as a hole trap centre and improve the hole injection. When using ITO as the anode, the injection enhancement will dominate the

process. However, no light emission can be detected in these unipolar devices, suggesting a low exciton population due to poor electron injection. Thus another type of device Au/P3HT/Al, as shown in figure 93(b), is fabricated to investigate the hole trapping effect in the ambipolar transport system.

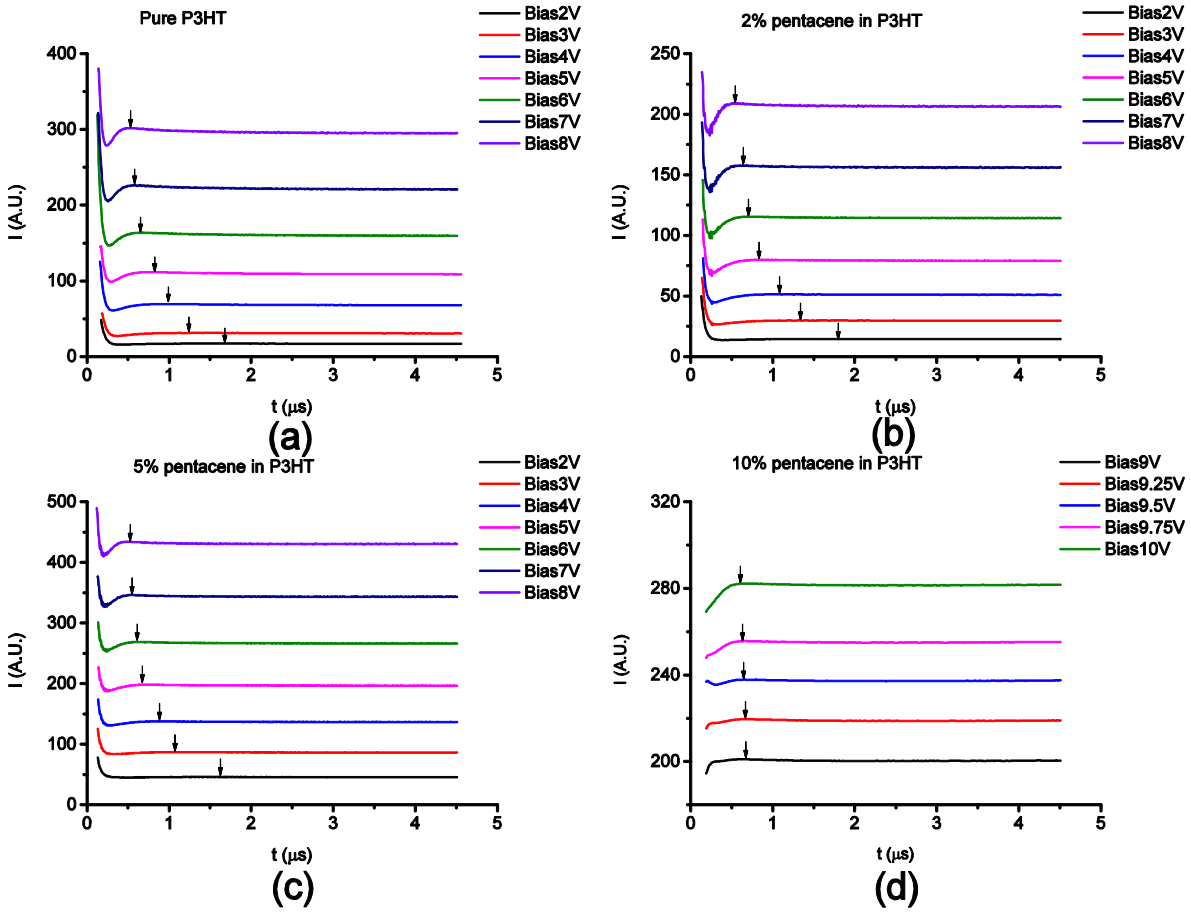

Figure 98: DI response in the Au/P3HT/Al device, (a) Pure P3HT, (b) 2% pentacene in P3HT, (c) 5% pentacene in P3HT, (d) 10% petancene in P3HT with differential amplifier.

Due to ambipolar transport in the system, the electron injection enhancement compared to that in unipolar devices (Au/P3HT/ITO) will slightly affect the DI measurement. As shown in figure 98, the differential amplifier is not used, as the RC decay did not affect the DI peak at low pentacene content. When the pentacene content is as high as 10%, the DI peak is impossible to detect under low bias (< 9 V). Under bias from 9 V to 10 V, the differential amplifier is chosen to remove the RC effect. Due to the limit of the pulse generator (TTi TG1010A), it can only extend the bias to 10V. Another amplifier is chosen to supply a large output voltage; however, the noise caused by the circuit affected the DI peak measurement.

In figure 99, $1/t_{trans}$ is plotted versus E the same way as that in figure 97.

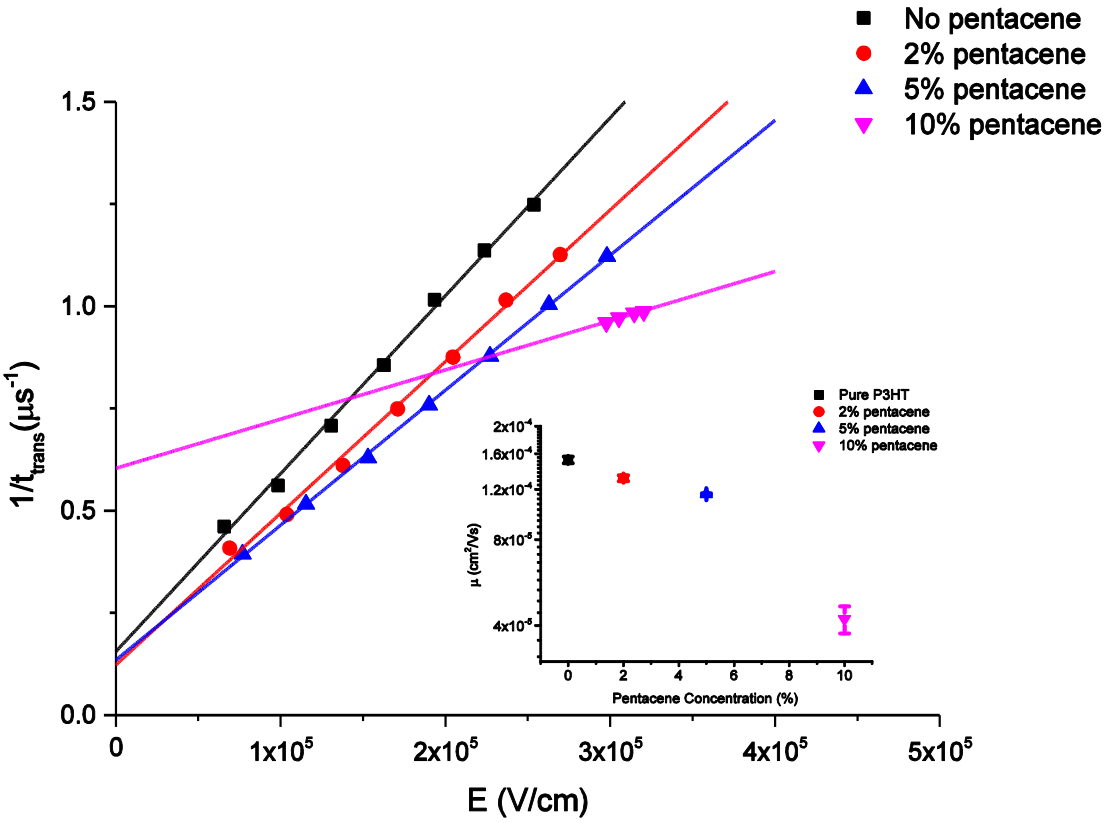

Figure 99: $1/t_{trans}$ versus E for the ambipolar devices (Au/P3HT/Al) with different pentacene content.

The mobility drops when the pentacene content increases. However, the mobility with 10% content shows a different result from that in the unipolar system, due to a big error bar in the small bias region from 9 V to 10 V. Pentacene doping not only affects the hole transport in P3HT, but also affects the electron injection, due to the change of the interface between P3HT and Al. However, here, the focus is on the hole trapping effect in P3HT. If the 10% pentacene doping will form a dual transport system, it will be difficult to explain any response related to the hole trapping effect in P3HT. Thus, in the following discussion, the research only focusses on pure P3HT, 2% pentacene content, and 5% pentacene content for further analysis.

For the MC measurement on unipolar devices (Au/P3HT/ITO), bias of between -5 V and 5 V is chosen, and the measurement is carried out in an Au/P3HT/ITO device with different pentacene content. The summary of saturation MC is plotted versus the magnetic field in figure 100.

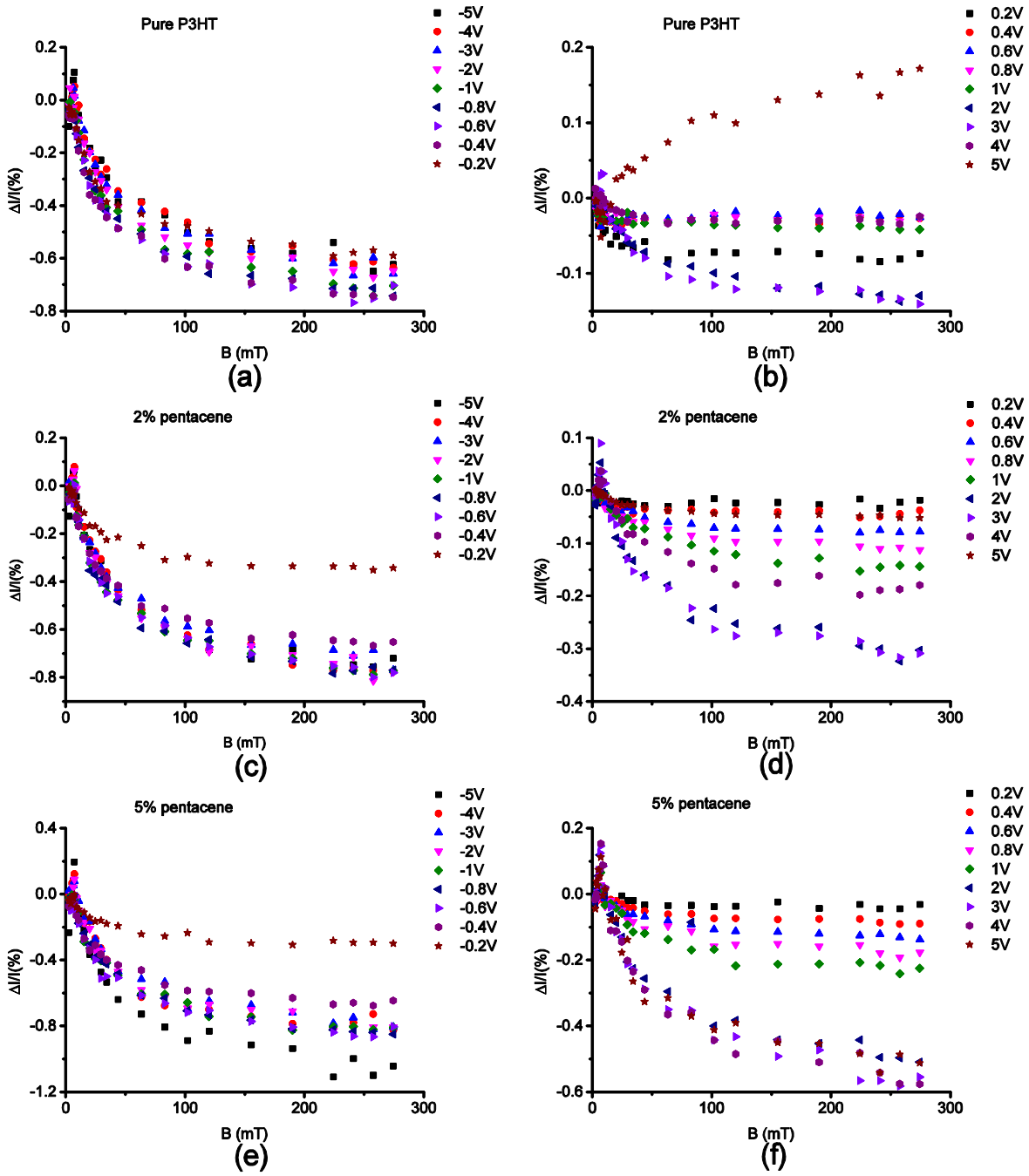

Figure 100: Summary of variation in current versus magnetic field in an Au/P3HT/ITO device. (a) Pure P3HT in reverse bias; (b) Pure P3HT in forward bias; (c) 2% pentacene in reverse bias; (d) 2% pentacene in forward bias; (e) 5% pentacene in reverse bias; (f) 5% pentacene in forward bias.

The saturation MC is always negative except in a pure P3HT device at the voltage of 5 V. The transition from negative MC to positive MC can be attributed to the dominating mechanism transition from bipolaron to triplet-polaron interaction, as discussed in Chapter 3.1. The formation of oxygen doping will decrease the barrier for electron injection from ITO leading to the triplet-polaron interaction dominating the MC response at high bias. At the same time, as reported in the literature, [186] the ITO/P3HT contact will cause

the electron leakage, which will also change the interface due to dipole formation or band bending, leading to an electron injection enhancement.

In figure 100, there is a slightly positive "spike" under low magnetic field (<10 mT), as that in the Au/P3HT/Al device in section 3.2. It can be attributed to the contribution from the triplet-polaron interaction mechanism. However, most of the MC responses under high magnetic field in the Au/P3HT/ITO device are negative. Thus it still can be concluded that the bipolaron mechanism is dominant in the system.

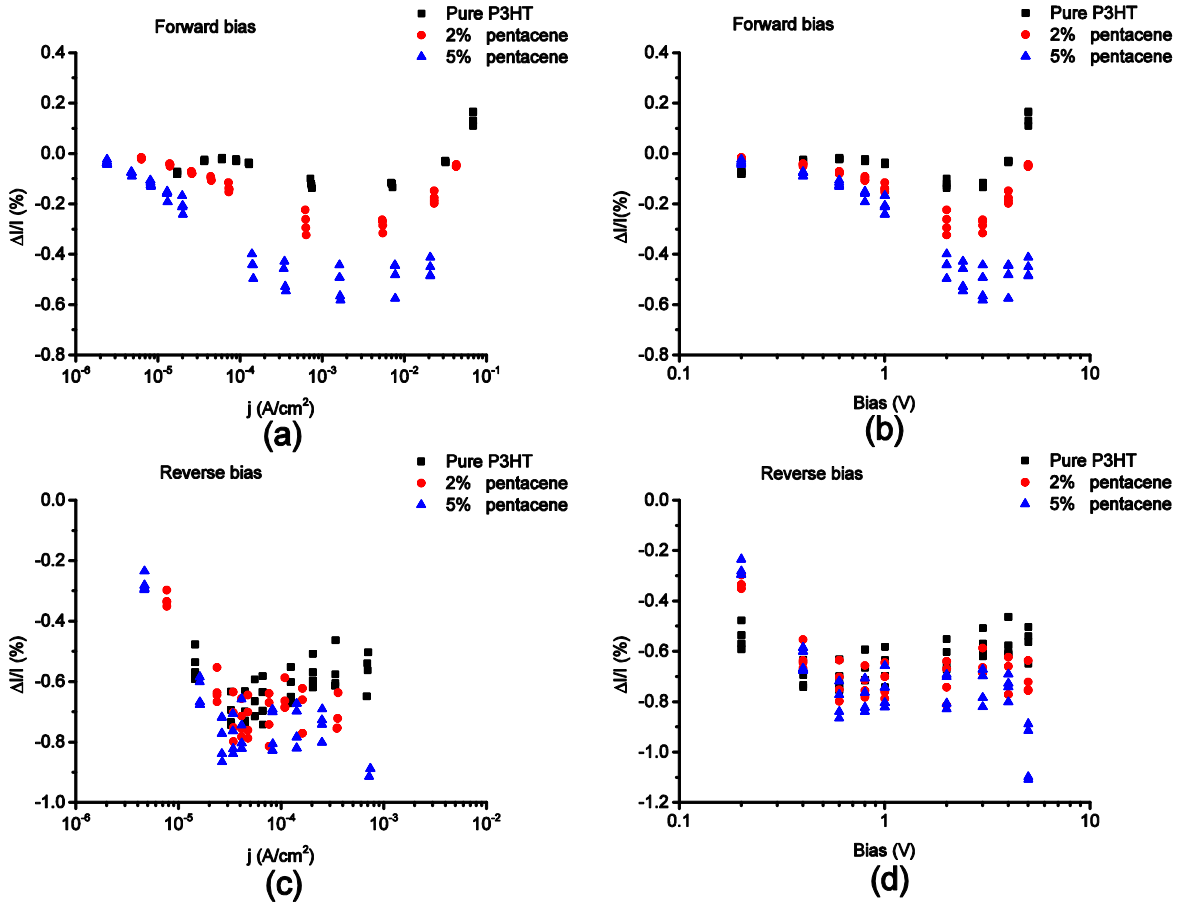

Figure 101: Saturation magnetoconductance (MC) response under high magnetic field (102 mT, 155 mT, 224 mT and 258 mT), plotted in forward and reverse bias: (a) In forward bias MC versus *j*. (b) In forward bias MC versus bias voltage. (c) In reverse bias MC versus *j*. (d) In reverse bias MC versus bias voltage.

In the Au/P3HT/ITO device, there is always a positive "spike" under low magnetic field (<10 mT), but it is impossible to use a single function to fit the MC. Thus the same way of analysing the MC response in section 3.2 is chosen, plotting a number of relatively high magnetic fields (102 mT, 155 mT, 224 mT and 258 mT) separately versus current density and bias voltage, as shown in figure 101.

There is a clear difference in MC response in forward bias with different pentacene content. In reverse bias, due to the ITO and P3HT contact, the change of the MC response is not as obvious as that in forward bias, suggesting the perturbation of the hole and bipolaron is suppressed by the dipole formation or band bending effect, leading to electron leakage and other effects.

Before the MC measurement in Au/P3HT/Al device, it is necessary to check the current density versus nominal electric field with different pentacene content. As shown in figure 102, the current density versus electric field results with different pentacene content suggest that in forward bias when Au acting as the anode, the current density decreases as the pentacene content increases at a fixed field. In reverse bias, Al acts as the anode the current density increases as the pentacene content increases at a fixed electric field. The trend is similar as that in Au/P3HT/ITO devices.

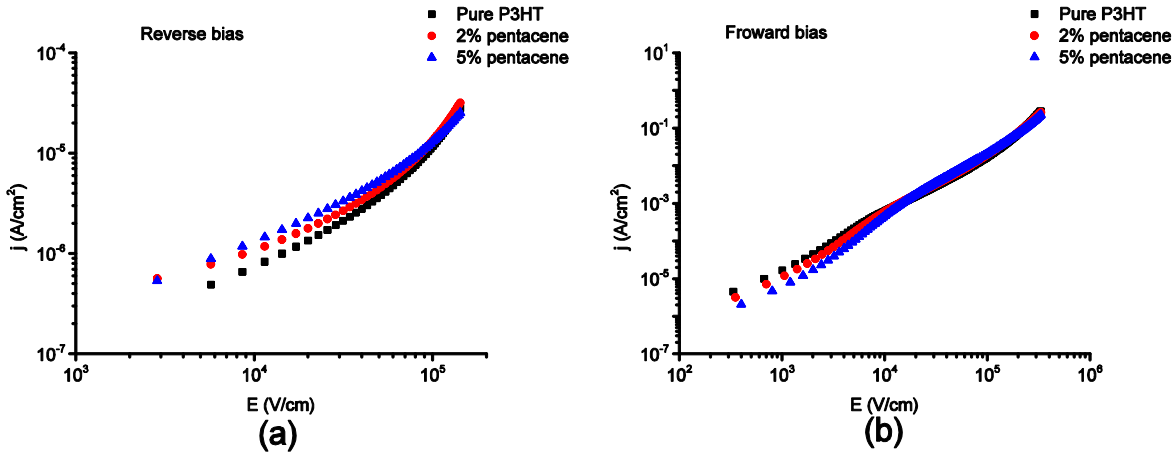

Figure 102: Current density plotted versus nominal electric field using logarithmic axis for Au/P3HT/Al based devices with different pentacene content. (a) Reverse bias; (b) Forward bias.

The MC measurement within Au/P3HT/Al is carried out from -5 V to 10 V with different pentacene content and the current deviation versus magnetic field is plotted in figure 103.

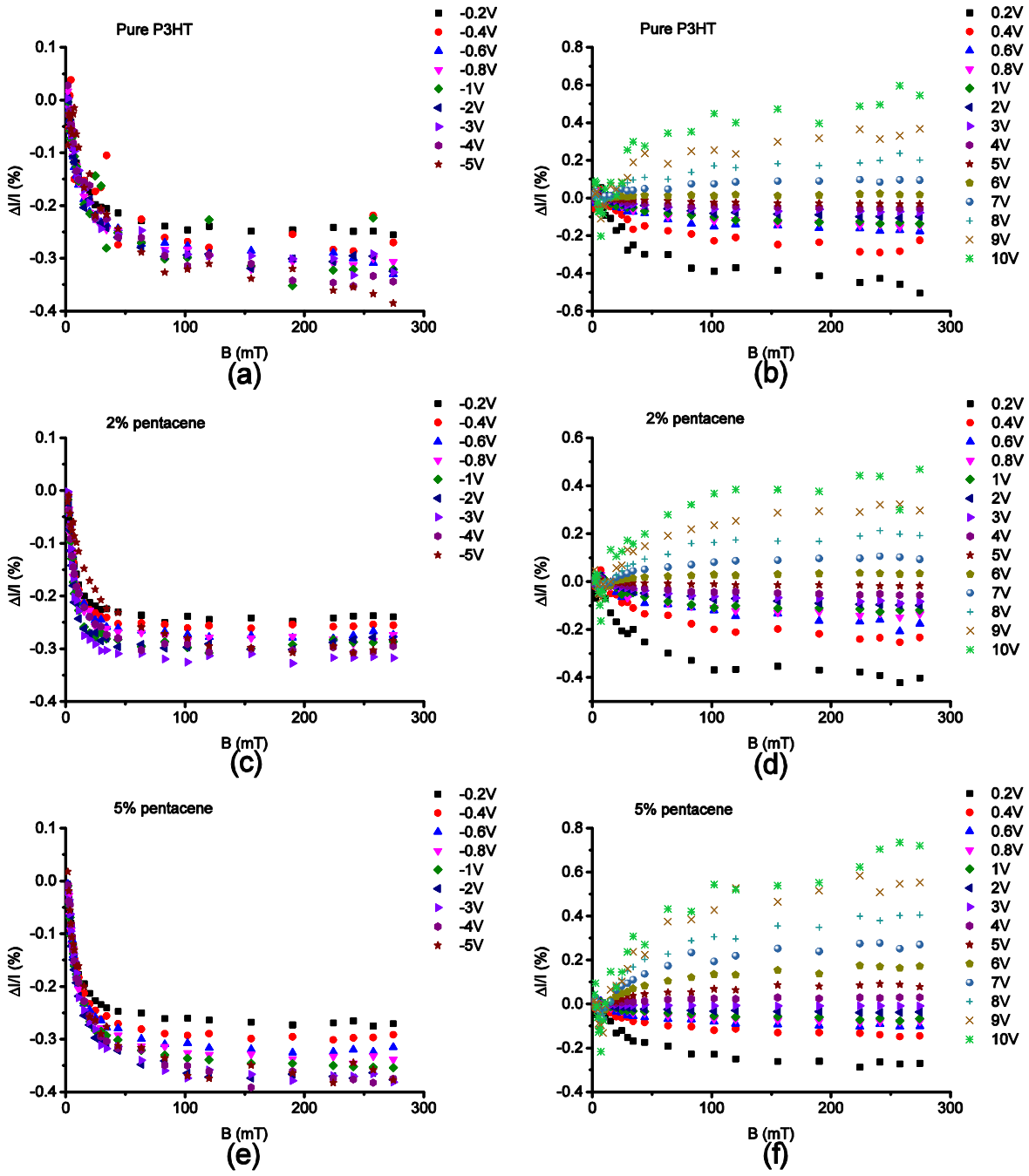

Figure 103: Summary of variation in current versus magnetic field in the Au P3HT/Al device. (a) Pure P3HT in reverse bias; (b) Pure P3HT in forward bias; (c) 2% pentacene in reverse bias; (d) 2% pentacene in forward bias; (e) 5% pentacene in reverse bias; (f) 5% pentacene in forward bias.

In reverse bias there is a negative MC without the positive "spike" under low bias. In forward bias, there is an obvious sign change from negative to positive as the driving voltage increases. A number of relatively high magnetic fields (102 mT, 155 mT, 224 mT and 258 mT) MC is plotted separately versus current density and bias voltage, as shown in figure 104.

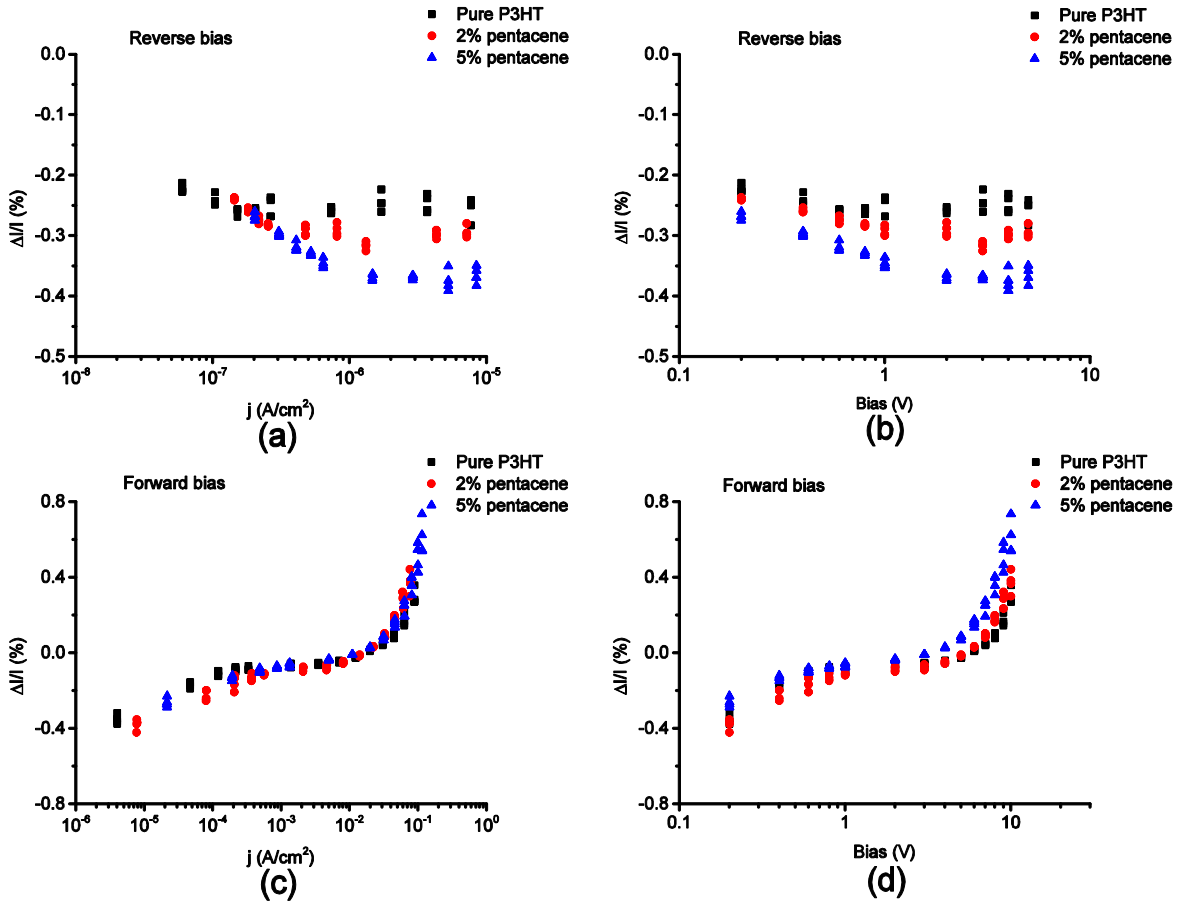

Figure 104: Saturation magnetoconductance (MC) response under high magnetic field (102 mT, 155 mT, 224 mT and 258 mT) of Au/P3HT Al plotted in forward and reverse bias: (a) In forward bias MC versus *j*; (b) In forward bias MC versus bias voltage; (c) In reverse bias MC versus *j*; (d) In reverse bias MC versus bias voltage.

There is no electroluminescence (EL) from the unipolar devices (Au/P3HT/ITO) due to poor electron injection from either ITO in forward bias or Au in reverse bias. Meanwhile, in the ambipolar device (Au/P3HT/Al) the optical transmission of Au is worse than that of ITO. It is hard to confirm the light emission as some of the electroluminescence is blocked by Au.

In order to investigate the pentacene doping effect on the MC and EL of P3HT, ITO/PEDOT:PSS/P3HT/LiF/Al as shown in figure 93(c), another type of ambipolar diode is chosen to carry out the measurement. As shown in figure 105, there is an enhancement in current density, as well as the light output, as the pentacene content increases. The EL initiates when the bias voltage is larger than 1.5 V as shown in the inset of figure 105.

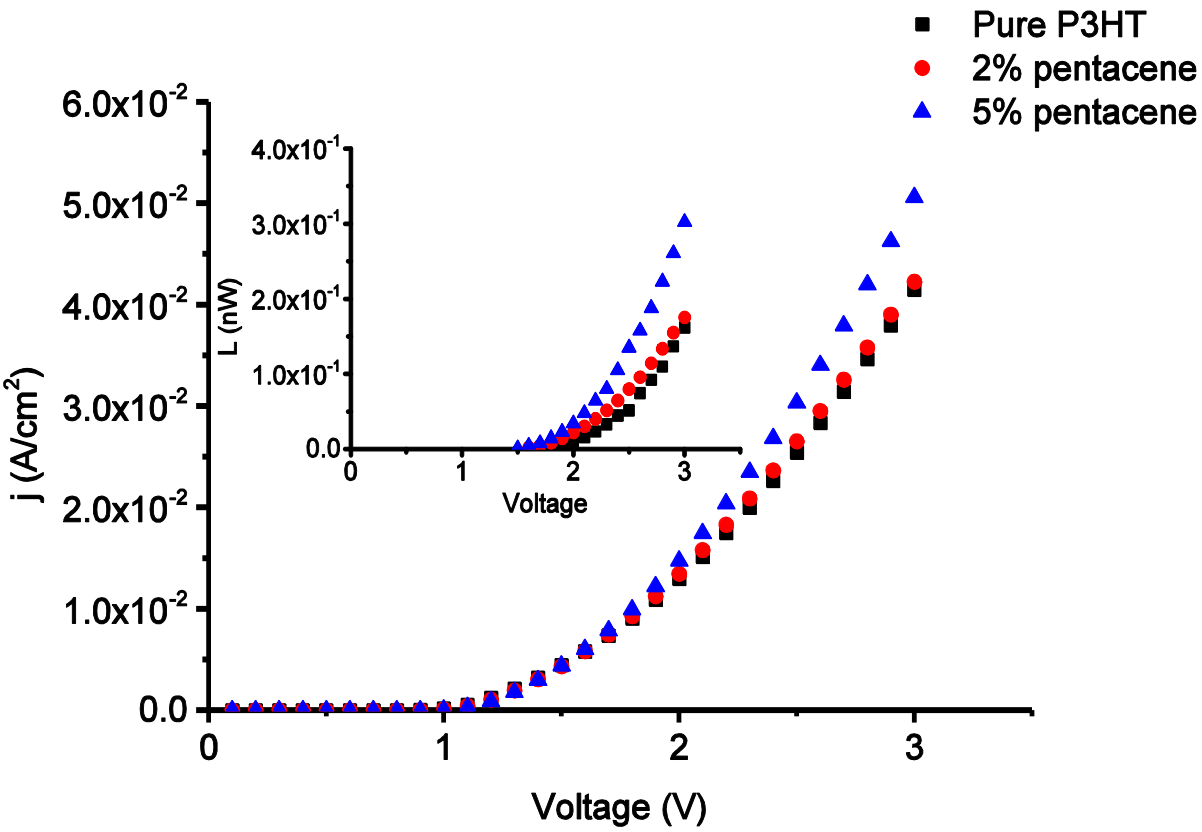

Figure 105: Current density as a function of bias voltage for ITO/PEDOT:PSS/P3HT/LiF/Al devices with different pentacene content. The inset shows the light emission versus bias voltage.

When the MC response above the onset of the light emission region (bias>1.5 V) is considered in an ITO/PEDOT:PSS/P3HT/LiF/Al diode, the system is quite complicated to understand due to pentacene doping effect. The excitons can both form in pentacene and P3HT through electrical excitation. Also, the possible luminescence of pentacene will be absorbed by P3HT resulting in energy loss, leading to a more complicated response which is difficult to discuss based on the hole trapping effect.

Thus the MC under low bias (from 0.8 V to 1.5 V) is measured with different pentacene content. The MC response is plotted versus the magnetic field in figure 106. The negative MC can be attributed to the bipolaron mechanism. [138] The MC responses show positive trend when the bias is larger than 1.1 V under higher magnetic field (>100 mT).

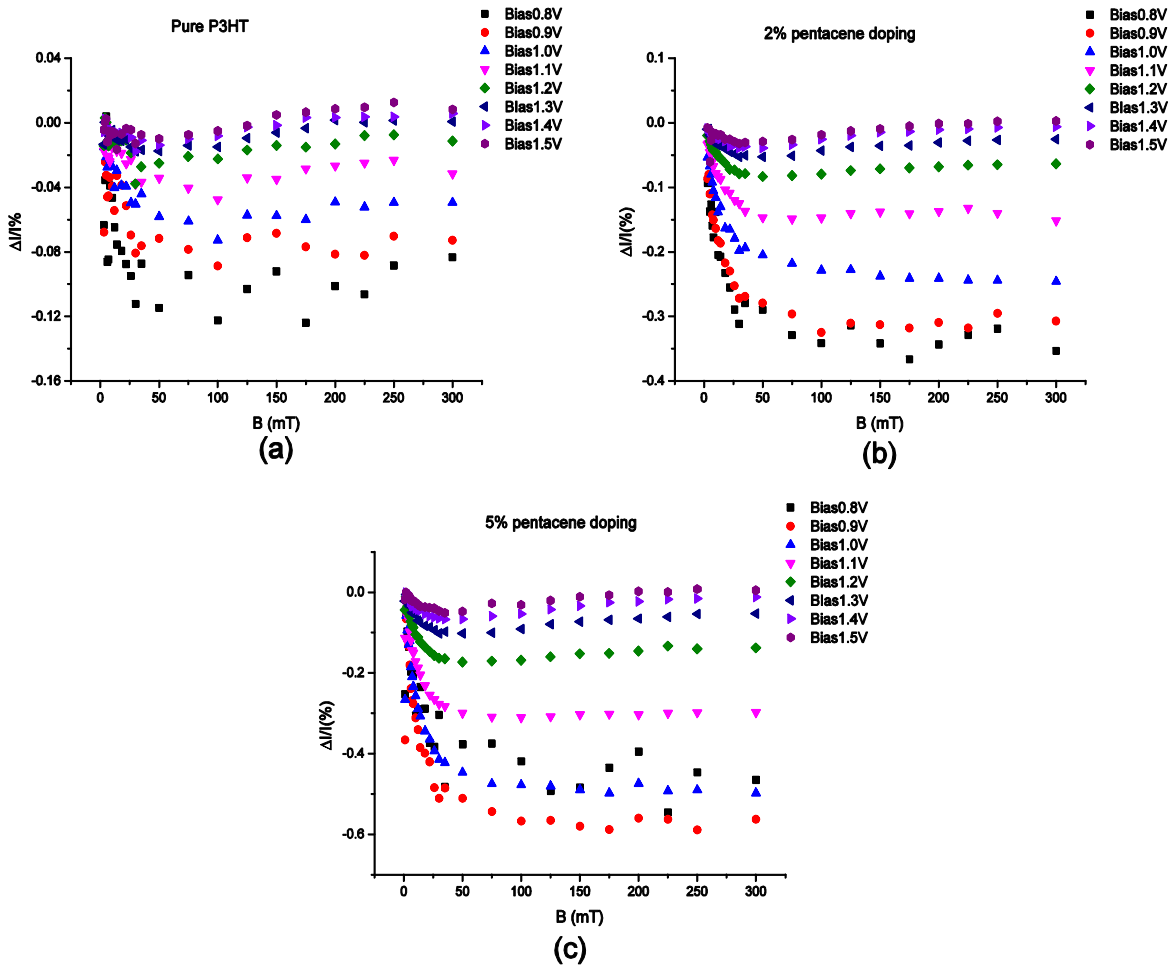

Figure 106: MC data at low bias from 0.8 V to 1.5 V with different pentacene doping concentration.

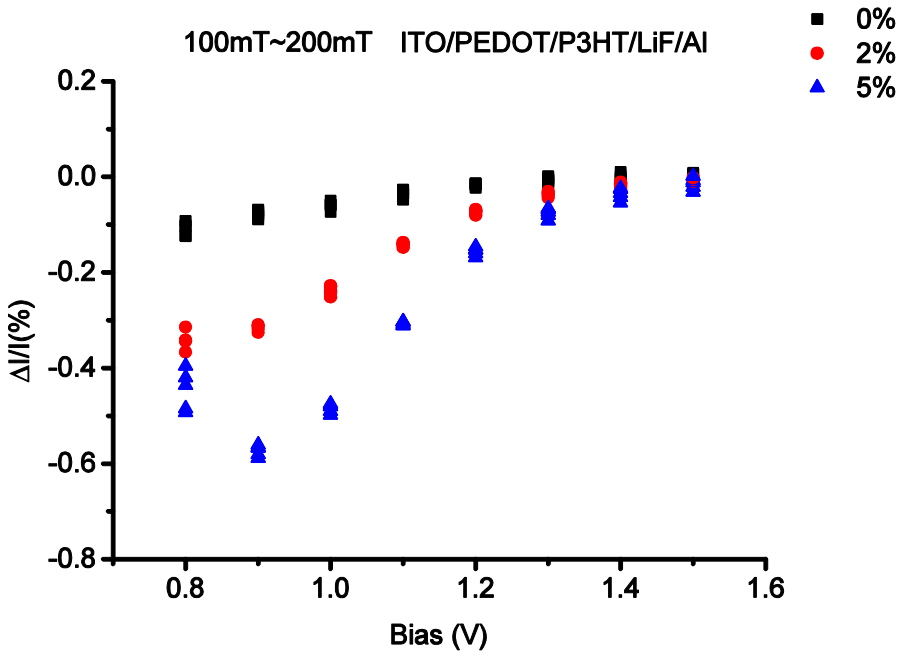

Figure 107: Saturation magnetoconductance (MC) response under high magnetic field (102 mT, 155 mT, 224 mT and 258 mT) versus bias voltage (0.8 V to 1.5 V) with different pentacene content.

The saturation MC (from 100 mT to 200 mT) is plotted versus different bias voltages from 0.8V to 1.5 V with different pentacene content, as shown in figure 107. The MC response is similar as that in forward bias of Au/P3HT/ITO and that in revere bias of Au/P3HT/Al.

The enhancement of the EL in figure 105 can be probably also due to the contribution from the electroluminescence of the pentacene. To investigate this effect, the luminescence experiment for pure P3HT and pentacene doped P3HT samples is carried out. The electroluminescence (EL) spectra of P3HT and the photoluminescence (PL) spectra of both P3HT and pentacene are measured. Before the PL spectra measurement, the visible light absorbance is measured separately for P3HT and pentacene to confirm the wavelength of laser for the PL spectra measurement.

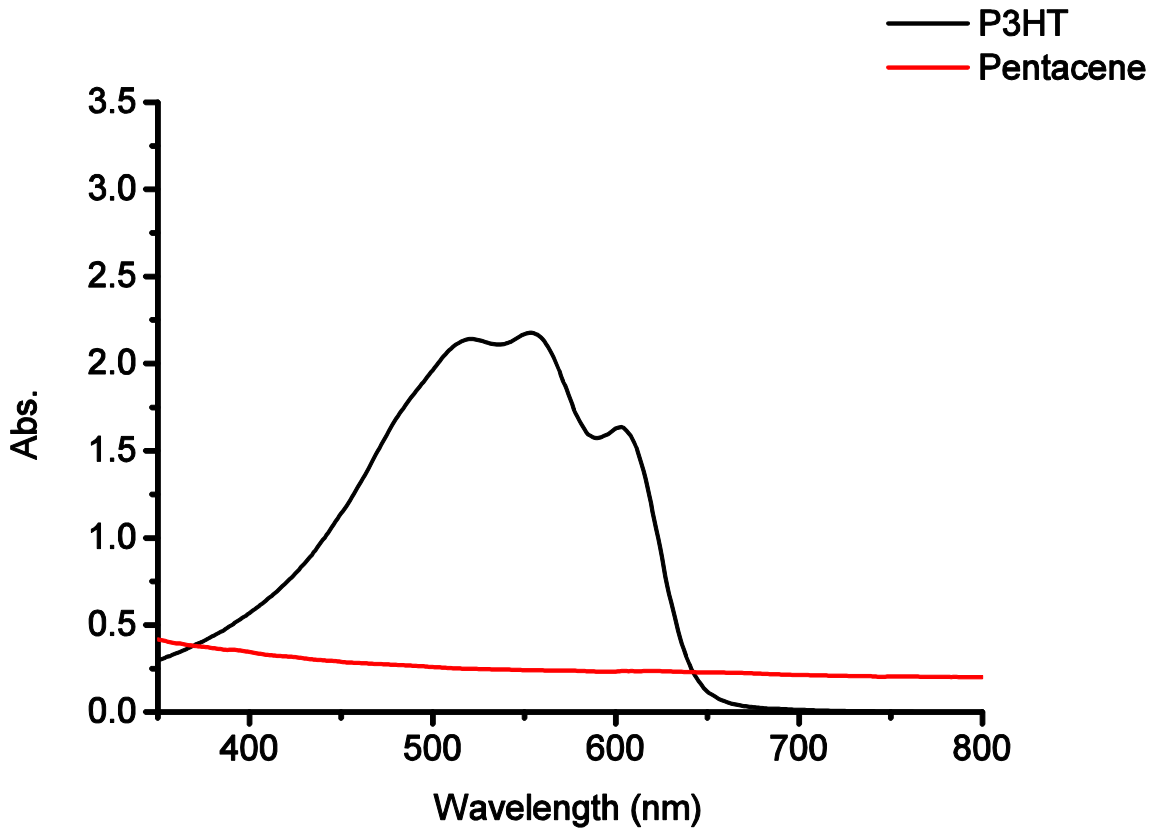

Figure 108: Visible light absorbance for P3HT (black) and pentacene (red).

As shown in figure 108, the obvious absorbance of P3HT is around 500 nm to 600 nm, and is consistent with the results in the literature. [25] The absorbance of visible light from pentacene is weak due to its conjugated structure, while ultraviolet absorbance should be stronger, as reported in the literature. [187]

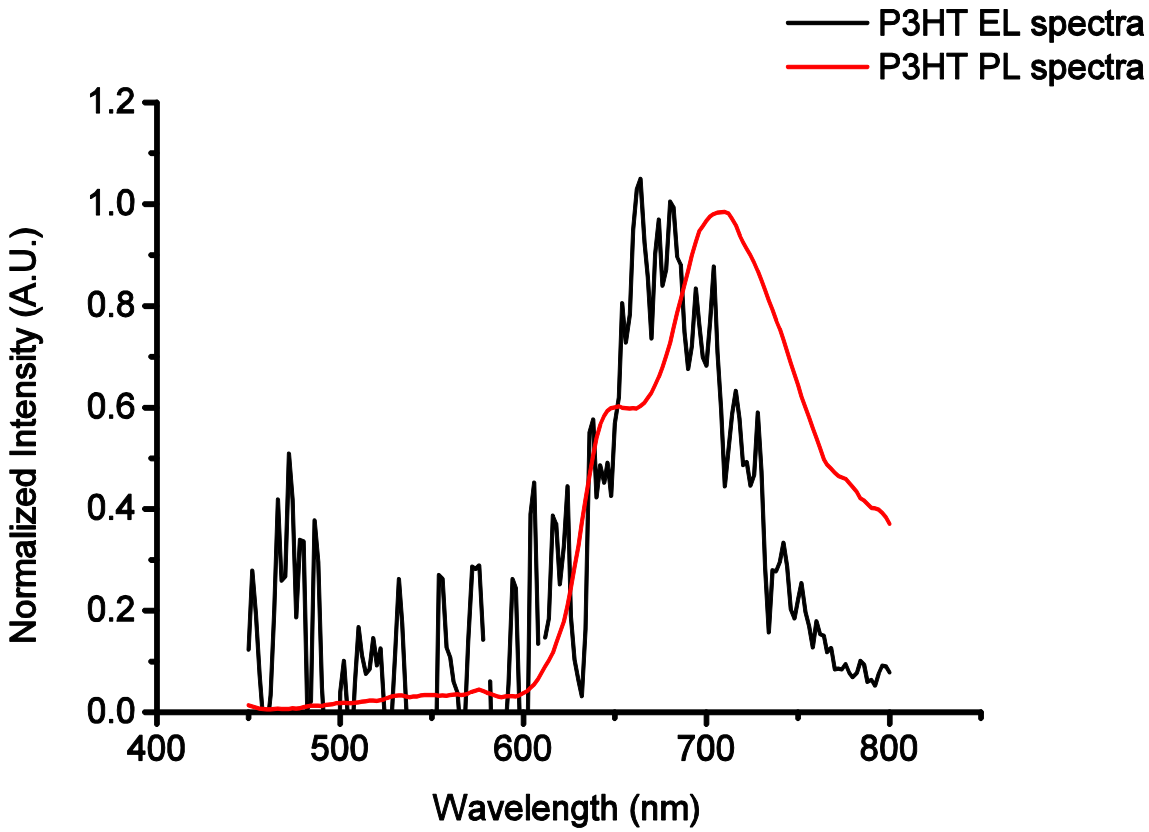

Figure 109: Comparison of the EL spectra and PL spectra for P3HT.

The laser with a wavelength of 375 nm is chosen for PL excitation, in which the absorbance of P3HT and pentacene are comparable. The comparison of the EL and PL spectra for P3HT is shown in figure 109. There is a strong EL peak with a wavelength of ~670 nm, but the measurement result is quite noisy. There is a strong PL peak with a wavelength of ~700 nm. The difference between the positions of the strongest peak may be due to the oxygen doping or different crystallinity in P3HT.

However, the oxygen doping in P3HT will quench the exciton. At the same time, the EL of a single layer P3HT diode is weak, which will decrease the signal and noise ratio for the EL spectra measurement. The PL spectra are chosen to analyse the pentacene doping effect on luminescence.

As shown in figure 110, the PL measurement is carried out between 450 nm to 900 nm in P3HT with different pentacene content. The PL spectra for pure P3HT are smoother and clearer than that in the EL spectra shown in figure 109. The strongest luminescence peak is around 710 nm, with a shoulder peak of 652 nm. For the PL spectra of pentacene, there are three peaks with the wavelengths of 592 nm, 648 nm and 816 nm.

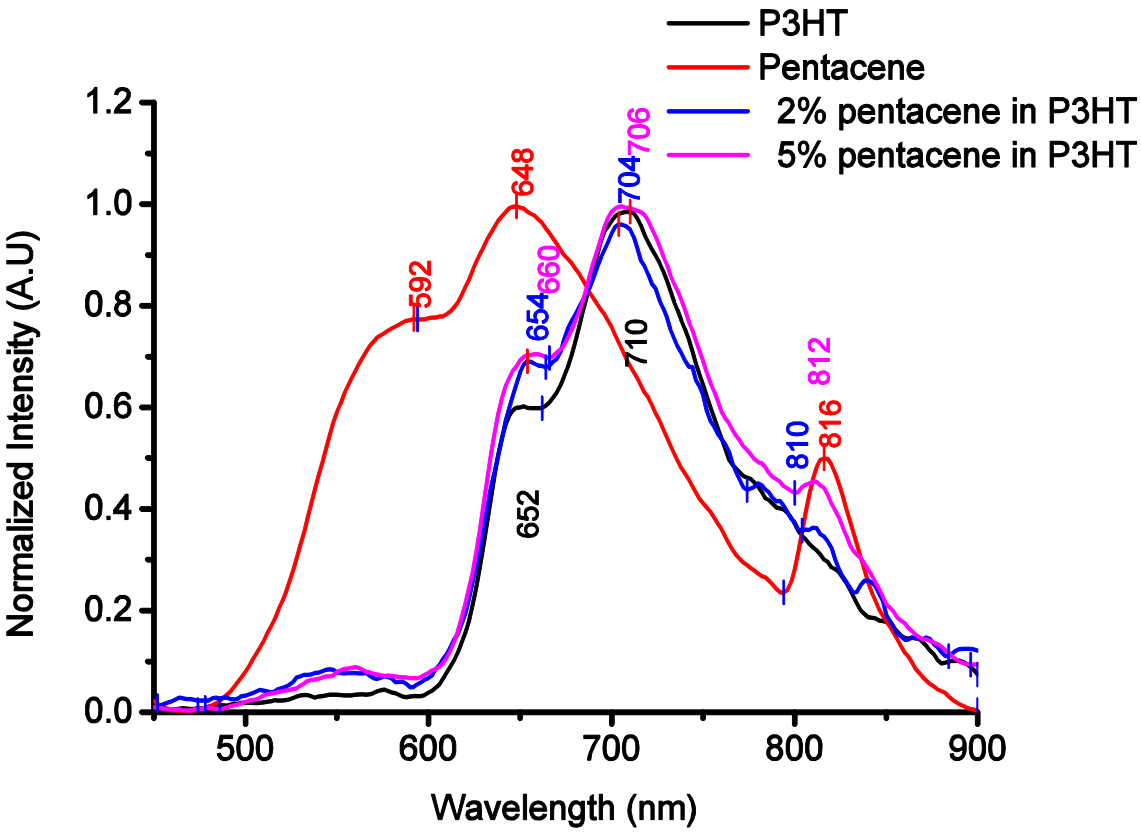

Figure 110: Summary of photoluminescence spectra for P3HT (black), pentacene (red), 2% pentacene doped P3HT (blue) and 5% pentacene doped P3HT (magenta).

There is an obvious shift of the strongest luminescence peak and the shoulder peak in pentacene doped P3HT. Meanwhile there is an appearance of the third peak at ~810 nm in pentacene doped P3HT which can be only due to the contribution from pentacene. The quantitatively analysis of the spectra due to doping will be carried out in the following section.

3.3.3 Discussion:

To explain the current density change with different pentacene content in figure 94, the electronic structure of the unipolar device Au/P3HT/ITO is analysed in figure 111. Large injection barriers exist between the electrodes (ITO and Au) and the LUMOs of both P3HT and pentacene, leading to poor electron injection. In forward bias, Au acts as the anode, whereas in reverse bias ITO acts as the anode. Pure P3HT unipolar devices show very different current densities in forward and reverse bias, consistent with the difference of the work functions (Au 5.1 eV and ITO 4.9 eV) [170][188] resulting in hole injection enhancement. The decrease in current density in forward bias can be explained

by the hole trapping effect of pentacene and subsequent reduction in mobility, leading to the conductance decrease as shown in figure 94.

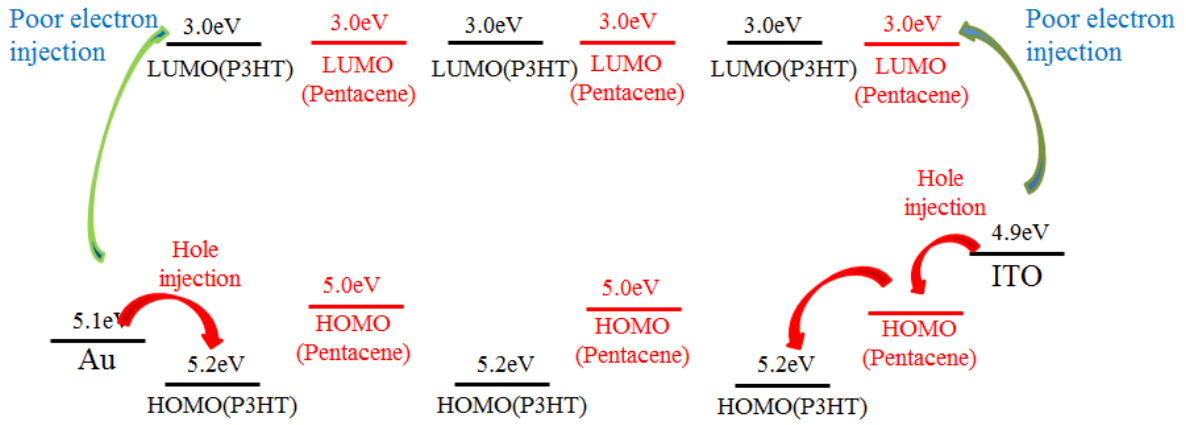

Figure 111: Schematic of the electronic level and charge injection in a pentacene doped Au/P3HT/Al device.

Any hole injection enhancement from ITO, due to the presence of pentacene, is more than offset by the trapping effect. When the pentacene concentration reaches 10%, there is a measured recovery in current density. This is due to the hole transport through the HOMO levels of pentacene at such high concentrations and/or significantly increases hole injection from Au. At the same time, the pentacene conductance will also make a contribution to the current density in P3HT. Both these effects will lead to an increase in current density. In reverse bias, holes can be injected from ITO into the HOMO of pentacene, with a reduced barrier compared to P3HT. The increase in pentacene content can lead to an increase of current density based on this method. In this case, it is the injection enhancement that dominates the hole trapping effect.

The MC in ITO/PEDOT:PSS/P3HT/LiF/Al (figure 107) can be explained by the bipolaron mechanism. [138] As shown in figure 111, pentacene acts as a hole trap centre which blocks the charge transport in P3HT. At the same time, it also broadens the distribution of the density of states (DoS) (standard deviation σ increase), as shown in figure 112(a), and shifts the Fermi level ($|E_F|$ decrease) from pure P3HT to the P3HT/pentacene system as shown in figure 112(b).

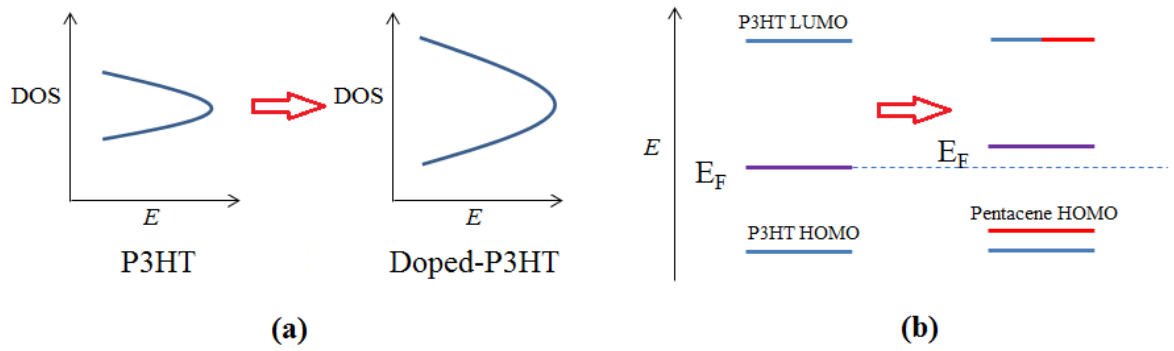

Figure 112: Pentacene doping effect for (a) DoS broadening and (b) Fermi level shift.

This will result in a decrease of the value $|-E_F/\sigma|$. As simulated by Peter Bobbert et al. [138] in figure 113, the MC response increases as $|-E_F/\sigma|$ decreases.

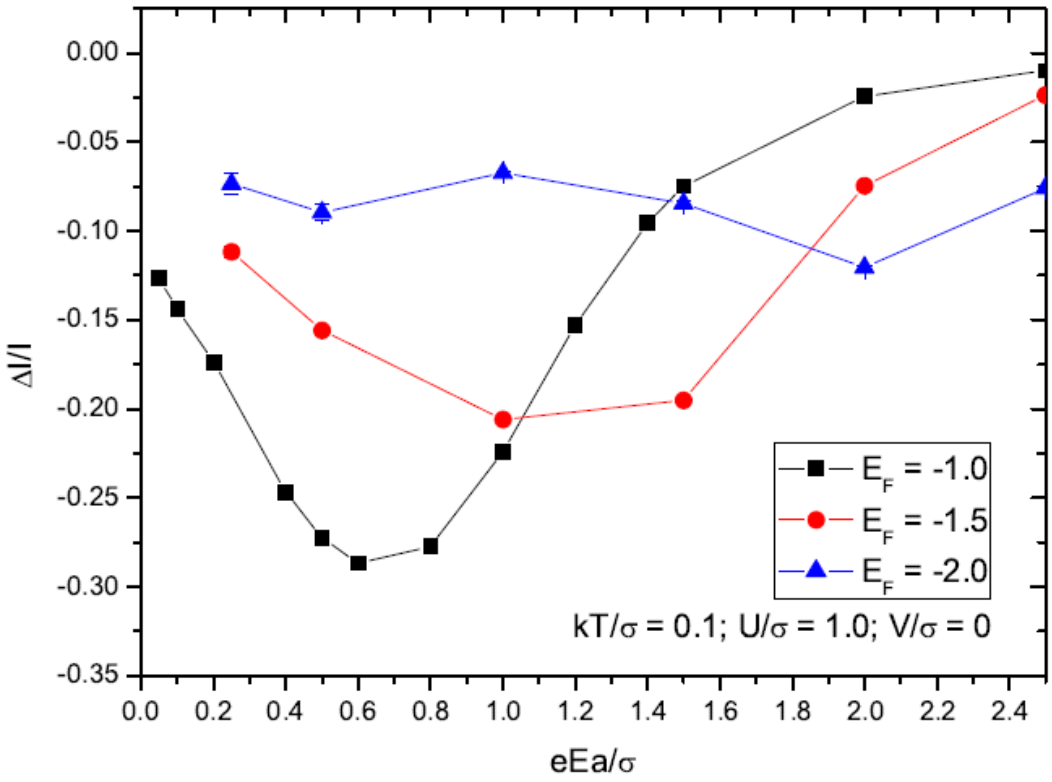

Figure 113: Simulation of magnetoconductance versus electric field strength eEa/σ. Reproduced from ref. [138]

The mechanism is that the effect of the electric field is to drive the charge carriers down field using a tilted energy landscape, and to provide energy to overcome the energy penalty for bipolaron formation. As shown in figure 113, their modelling results indicate that under low electric fields the MC does not extrapolate to zero in a linear fashion. For downfield hopping, the energy part of

Miller-Abraham hopping approaches 1. Under high electric fields, it will suppress energetic disorder in the field direction. Less disorder means that the average energy of charge carriers shifts to higher values, and where, due to the Gaussian density of states, more states become available. This makes the blocking effect of bipolaron states less pronounced, because charge carriers can easily take a detour around bipolaron blocking sites.

The decrease of MC as bias increases can be well explained using bipolaron theory. [138] At a higher bias (higher electric field), the charge carriers can easily take a detour around the bipolaron blocking sites, which will suppress the negative MC response. The experimental results in figure 107 coincide with the simulation results by Peter Bobbert et al. in figure 113. [138]

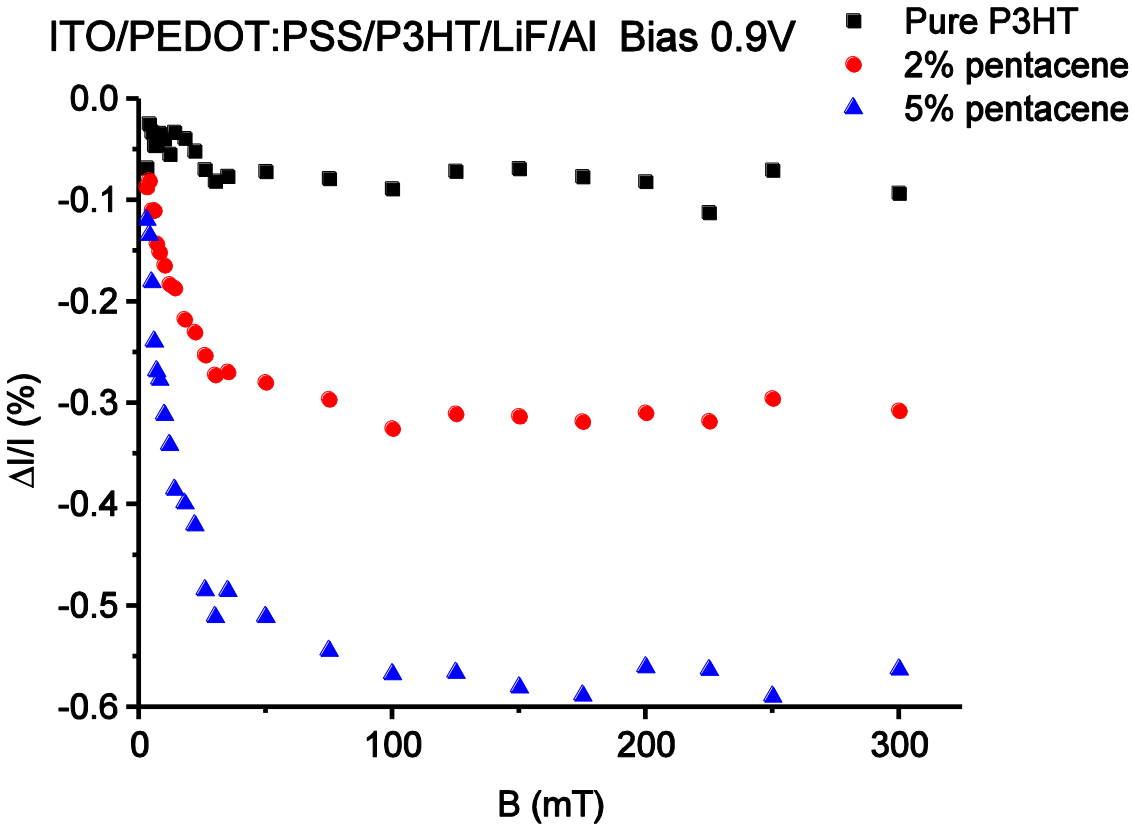

Figure 114: Magnetoresistance data as a function of magnetic field for ITO/PEDOT:PSS/P3HT/LiF/Al devices with different pentacene content. All MC data measured 0.9V.

The MC at 0.9 V is plotted with different pentacene content in figure 114. As reported in the literature, [131] pentacene showed a negative MC as large as -0.3% at room temperature. The increase in negative MC is due to the presence of pentacene, but far exceeds the MC mechanism in pure pentacene. The pentacene content is less than 10%, while the enhancement of negative MC response is larger than 100%. So it can be concluded that the increase of

negative MC under low bias is mainly due to the pentacene doping, leading to a broadening of the DoS (σ increase) and Fermi level shift corresponding to the bipolaron theory.

As discussed in previous sections, the pentacene doping effect can both block hole transport and increase hole injection in P3HT. When measuring MC in Au/P3HT/ITO devices, hole transport can dominate current density both in forward (Au as anode) and reverse (ITO as anode) bias.

Thus, before the MC measurement, two effects need to be considered: hole trapping effect and charge injection enhancement. As discussed above, the introduced hole trap states will broaden the DoS of P3HT and shift the Fermi level, leading to a decrease of $|-E_F/\sigma|$. According to bipolaron theory, the negative MC response will increase due to the value of $|-E_F/\sigma|$ decrease under the same electric field. As shown in figure 101 the MC in forward bias coincides well with the bipolaron mechanism in figure 113. In reverse bias, due to poor hole injection from ITO into P3HT, the pentacene doping will improve the hole injection from ITO which may affect the bipolaron mechanism based MC response as shown in figure 101(c) and (d)

Thus it can be expected that DoS broadening and a Fermi level shift in reverse bias, while in forward bias, due to the better electron injection from Au compared to ITO, the triplet-polaron interaction mechanism will appear to dominate MC under high bias as shown in section 3.1. This will make it hard to explain the MC change due to the complicated system with bipolarons, trap states, excitons and so on.

However, in forward bias, when the MC is plotted versus bias voltage, as shown in figure 104(d), the positive MC increases as the pentacene content increases under high bias. If the MC is plotted versus current density as shown in figure 104(c), the MC responses are nearly the same in the same current density. The traps can only block hole transport and broaden the DoS. The electron injection from Al leading to the exciton formation also makes a contribution to positive MC. The variation of the MC response under the same bias may be caused by the difference in thickness, leading to different electric fields. The MC plotted versus current density suggests that doping will not affect the transition of MC, and a dominant mechanism transition from bipolaron to triplet-polaron interaction also appears in the doped samples. As discussed in Chapter 3.1, the transition from negative MC to positive MC is due

to the competition between the bipolaron mechanism and triplet-polaron interaction mechanism. Thus individual pentacene doping effects in such a complicated system are difficult to distinguish.

As shown in figure 115, the MC in reverse bias is chosen for empirical analysis. The single non-Lorentzian function in equation 47 is chosen to analyse the data.

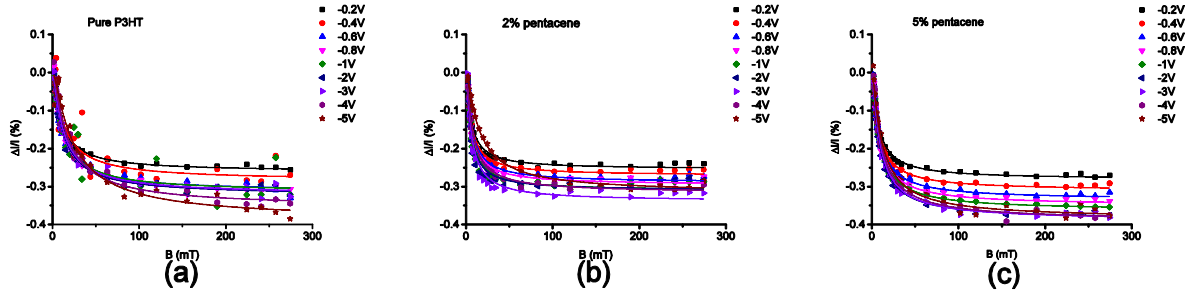

Figure 115: Non-Lorentzian fitting results in reverse bias with different pentacene content.

The summary of fitting parameters is shown in Tables X, XI and XII. The characteristic field B_0 changes as the pentacene content increases. In pure P3HT, the fitting results show that B_0 is ~5mT, which is in agreement with the literature. [130] However, after doping, the characteristic field B_0 decreases under 2% pentacene content and recovers under 5% pentacene content.

Table X. Summary of MC fitting parameters in a pure P3HT device

Bias(V)	a_0	error a_0	B_0 (mT)	error B_0 (mT)
-0.2	-0.26	0.004	4.4	0.24
-0.4	-0.28	0.016	5.7	0.19
-0.6	-0.31	0.004	4.7	0.22
-0.8	-0.32	0.004	5.2	0.25
-1	-0.32	0.013	5.3	0.83
-2	-0.32	0.005	5.3	0.31
-3	-0.32	0.005	5.6	0.33
-4	-0.35	0.008	7.7	0.57
-5	-0.39	0.012	10.8	1.13

Table XI. Summary of MC fitting parameters in a 2% pentacene device

Bias(V)	a_0	error a_0	B_0 (mT)	error B_0 (mT)
-0.2	-0.25	0.003	2.5	0.14
-0.4	-0.27	0.004	2.6	0.17
-0.6	-0.29	0.004	2.7	0.17
-0.8	-0.30	0.005	2.6	0.18
-1	-0.31	0.006	2.4	0.22
-2	-0.31	0.008	2.3	0.25
-3	-0.34	0.007	2.7	0.23
-4	-0.32	0.003	3.2	0.15
-5	-0.32	0.004	6.8	0.29

Table XII. Summary of MC fitting parameters in a 5% pentacene device

Bias(V)	a_0	error a_0	B_0 (mT)	error B_0 (mT)
-0.2	-0.28	0.003	3.3	0.14
-0.4	-0.31	0.003	3.4	0.13
-0.6	-0.33	0.003	3.6	0.15
-0.8	-0.35	0.003	3.7	0.14
-1	-0.36	0.002	3.8	0.10
-2	-0.39	0.003	3.9	0.13
-3	-0.39	0.003	4.2	0.14
-4	-0.39	0.004	4.7	0.18
-5	-0.39	0.006	5.2	0.29

For the MC in forward bias from 0.2 V to 10 V in figure 103, it has already been proved there are more than six mechanisms in the system. Thus, it is too complicated to attribute the empirical fitting results to any mechanisms directly. The MC response with different pentacene content can only be explained based on the bipolaron theory.

Above all, pentacene is introduced into P3HT devices and the MC is measured in different devices: ITO/PEDOT:PSS/P3HT/LiF/Al, Au/P3HT/ITO and Au/P3HT/Al. Petancene can act as a hole trap centre that both blocks hole transport and improves hole injection, depending on the choice of electrodes with different work functions. For Ohmic contact between Au and P3HT, the blocking effect dominates the conductance, leading to a decrease of current density under the same electric field. For Schottky contact at the interface of

ITO/P3HT and Al/P3HT, the charge injection enhancement dominates the conductance, leading to an increase of current density. At the same time, the introduced hole trap centre broadens the DoS and shifts the Fermi level. This change will decrease the value of $|-E_F/\sigma|$, leading to an increase of negative MC as per bipolaron theory.

The results in all the devices prove this effect in a unipolar system. However, when the electron injection improves under high bias in an ambipolar system, it is difficult to analyse the MC response due to the competition of bipolaron and triplet-polaron interaction. The hole trapping effect perturbs the formation of both the bipolaron and exciton, through blocking the hole transport and improving hole injection. The MC response in an ambipolar system suggests there is no change in MC response under the same current density, which is due to the competition of different mechanisms. Thus, the MC under low bias in a unipolar system can be explained quantitatively according to bipolaron theory.

For the j-V and EL results with different pentacene content in figure 105, there is an enhancement in current density, as well as the EL, as the pentacene content increases. Pentacene doping effect can both reduce hole mobility and improve the hole injection from ITO/PEDOT:PSS into P3HT. As reported in the literature, the work function of PEDOT:PSS is ~5.0 eV. The hole injection from PEDOT:PSS into the HOMO of pentacene will be improved compared to that of P3HT. Pentacene doping may also improve the electron conductance in P3HT, as the LUMOs of P3HT and pentacene are comparable. However, the pentacene doping is proved to block the hole transport in P3HT. Thus, the current density increase under the same bias is attributed to the competition of different mechanisms.

Meanwhile, in ambipolar devices the excitons will be formed due to a combination of holes and electrons. As discussed in Chapter 1, 25% of the excitons are singlets, and 75% are triplets. The electroluminescence is due to singlet exciton decay. Figure 116 is the schematic of calculated efficiency (η) according to equation 53, and corresponds to a given singlet concentration in the steady state versus bias.

$$\eta = \frac{L}{I \times V} \times 100\% \tag{53}$$

In equation 53, L is the light output power detected by the Newport photo-detector, including all the light under different wavelengths emitted from the diode. I is the detected current and V is the applied bias voltage.

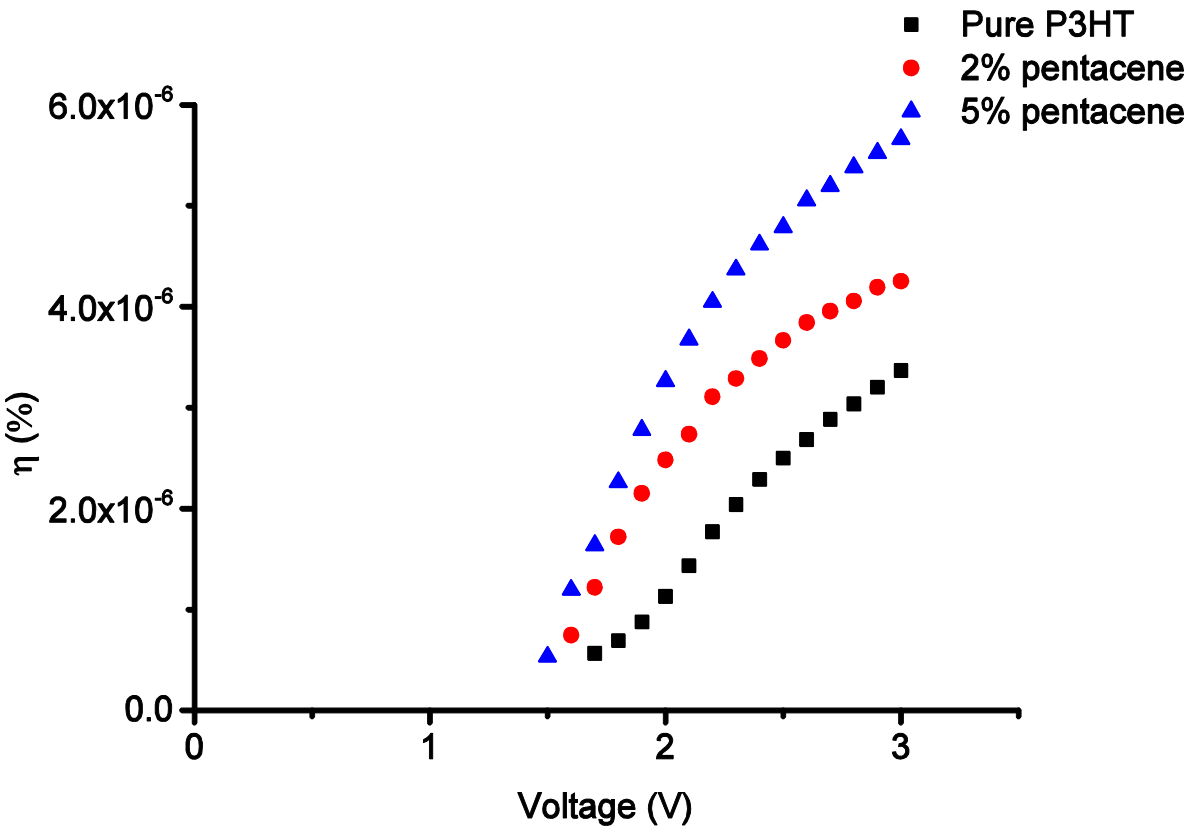

Figure 116: Light output efficiency as a function of bias voltage with different pentacene content for an ITO/PEDOT:PSS/P3HT/LiF/Al devices.

A given steady state singlet concentration will correspond to a given triplet concentration. In figure 116, the efficiency increases as the pentacene content increases, suggesting an increase in population of both singlets and triplets.

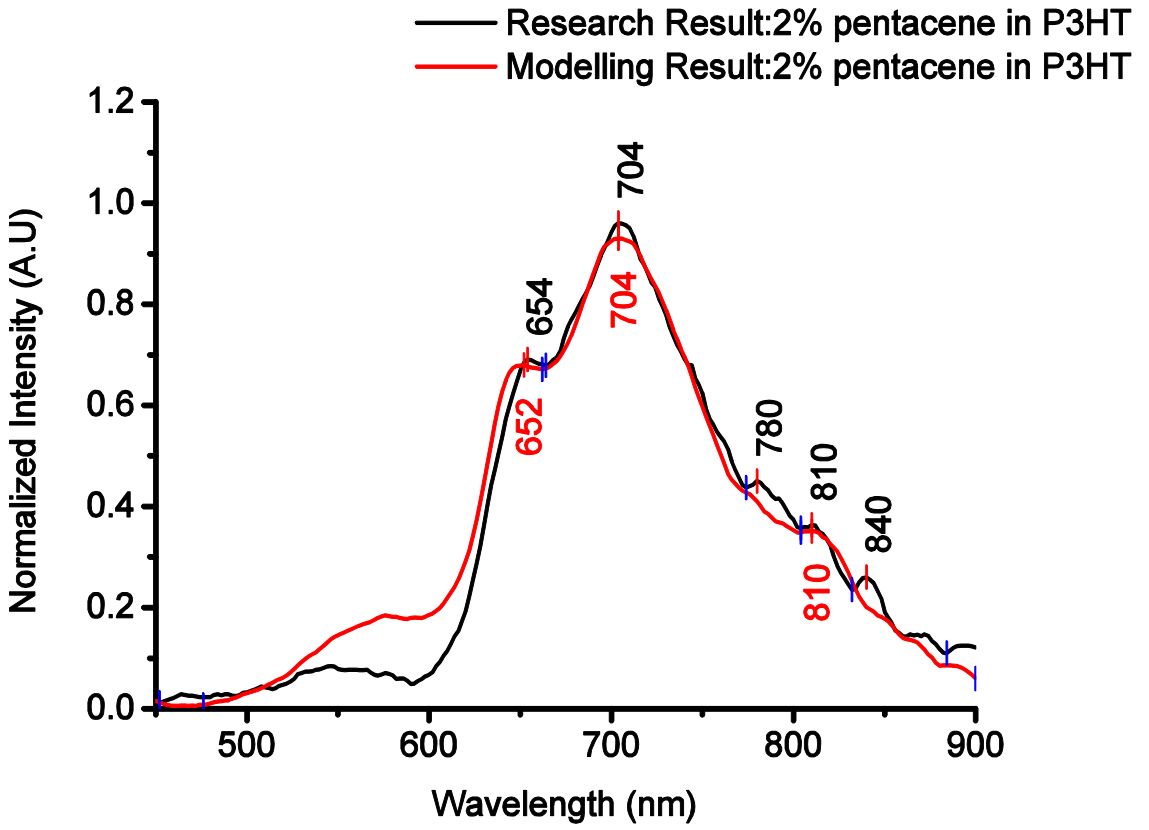

Figure 117: Photoluminescence spectra comparison of 2% pentacene doped content: measured PL spectra (black line) and modelled PL spectra (red line).

Before analysing the PL results for 2% and 5% doped samples, it can figure out that it is possible for P3HT to absorb the luminescence from pentacene between 500 nm and 650 nm. Thus the PL spectra of the doped device cannot be analysed using only the integration of the P3HT PL spectra and the pentacene PL spectra. However, the peak around 816 nm is only from pentacene, which cannot be absorbed by P3HT as per figure 117. It is possible to fit the position of the peak between 810 nm and 820 nm to analyse the luminescence of the doped device, through combining the spectra of P3HT and pentacene.

A combination of P3HT and pentacene spectra are chosen to model the 2% doped sample as per equation 54:

$$PL(doped\ ) = a_1 \times PL(P3HT\ ) + a_2 \times PL(\ pentacene\ \ ) \tag{54}$$

Where a_1 is the effective contribution ratio of PL from P3HT and a_2 is the effective contribution ratio of PL from pentacene. $a_1 = \frac{PL(P3HT)}{PL(doped\ sample)}$ and $a_2 = \frac{PL(pentacene)}{PL(doped\ sample)}$. The sum of a_1 and a_2 should be 100%.

As shown in figure 117, the modelling result for 2% pentacene content (red line) suggests the effective ratio a_1 of PL from P3HT is 80% and the effective ratio a_2 for pentacene is 20%. The highest peak is adjusted, which confirms that the peak around 810 nm is due to a sum of PL from P3HT and pentacene.

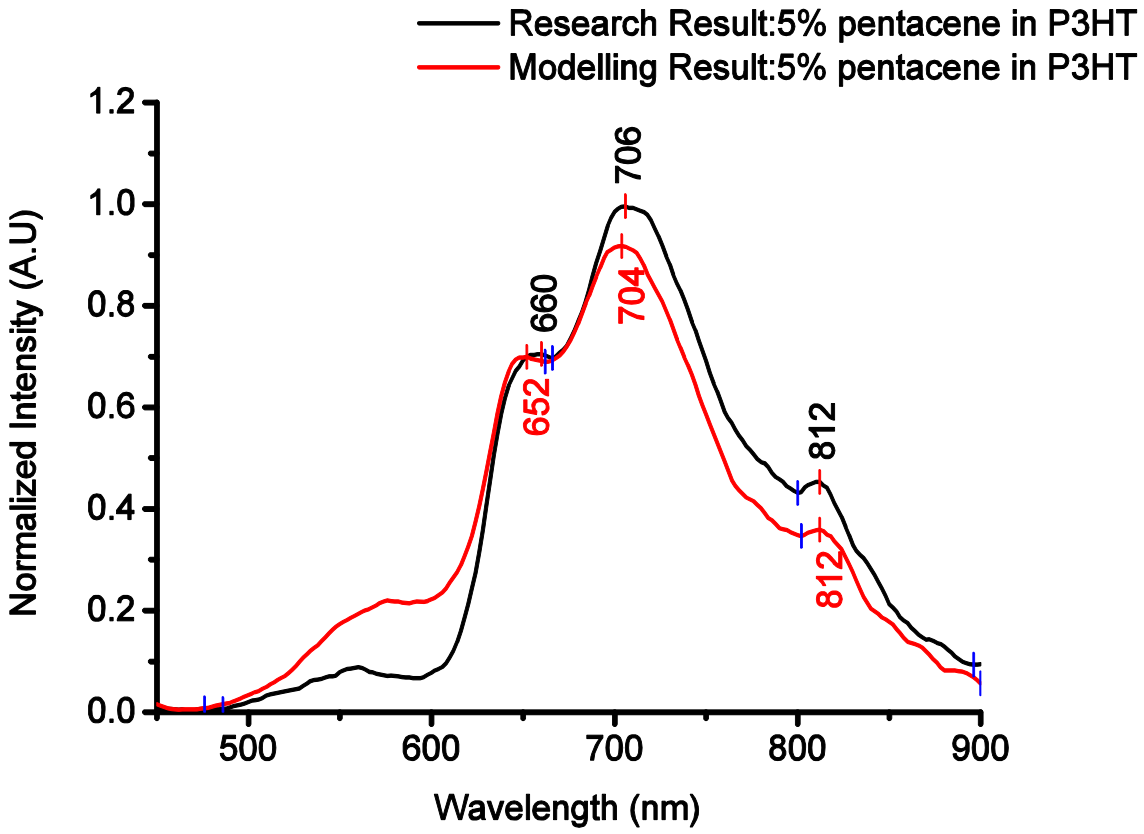

Figure 118: Photoluminescence spectra comparison of 5% pentacene doped content: measured PL spectra (black line) and modelled PL spectra (red line).

The results, for 5% and using the same modelling technique, are shown in figure 118. The red shift of the peak from 810 nm to 812 nm is due to the component of PL from pentacene. The modelling result for 5% pentacene content shows that the effective ratio a_1 of luminescence from P3HT is 75%, thus the effective ratio a_2 is 25%.

The effective ratio of luminescence from pentacene is always higher than the actual doping content. This suggests more PL component from pentacene is detected than expected.

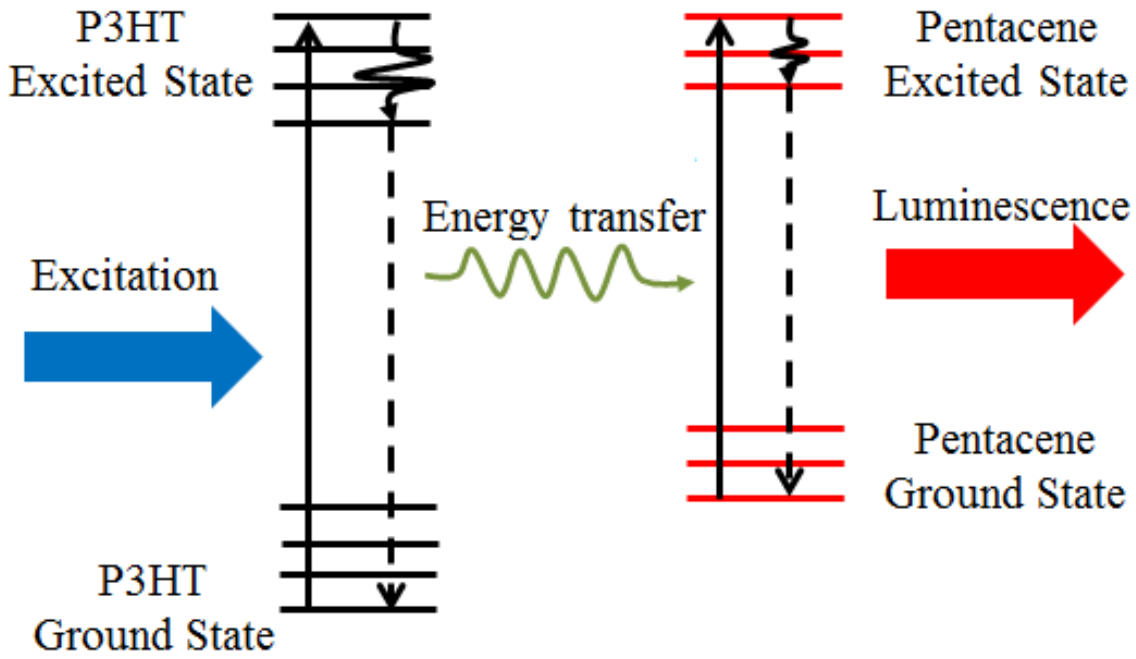

Figure 119: Intersystem energy transference between P3HT and pentacene.

According to the literature, [189-190] the quantum efficiencies of P3HT and pentacene (excitation wavelength = 375 nm) are comparable ~15%. Thus the high effective ratio is probably due to intersystem energy transference between P3HT and pentacene. As shown in figure 119, due to photo-excitation, the electron is excited from ground state to the excited state of P3HT. The transition from P3HT singlets (excited states) to pentacene singlets appears due to the intersystem energy transference. Finally, the pentacene singlets radiative decay leads to luminescence. This can explain the higher effective PL ratio (compared to the doping content) of pentacene in the P3HT/pentacene system.

By integrating the normalized pure P3HT and pentacene PL spectra in figure 110 and get the following effective areas: 140 (nm) for P3HT and 206 (nm) for pentacene. The area can quantitatively describe the effective luminescence contribution from P3HT and pentacene.

Thus the improvement of PL can be calculated in the doped sample compared to pure P3HT as per equation 55:

$$\theta = \frac{(a_1 \times 140 + a_2 \times 206) - 100\% \times 140}{140 \times 100\%} \times 100\% \qquad (55)$$

Where θ is the PL improvement ratio due to pentacene doping, a_1 is the effective ratio for PL from P3HT, and a_2 is the effective ratio for PL from pentacene as in equation 54.

The modelling results suggest the PL improvement for 2% pentacene content is 9.4%, and for 5% pentacene content is 11.7%. This assumption is based on the co-emission of P3HT and pentacene. However, P3HT can also absorb the light emission from pentacene, which results in the non-radiative energy loss. Thus measured increase of PL due to co-emission must be lower than the calculated improvement: 9.4% in 2% pentacene content, and lower than 11.7% in 5% pentacene content. It can be concluded that pentacene doping makes a contribution to luminescence enhancement in P3HT, leading to efficiency enhancement.

The electroluminescence efficiency improvement is calculated in figure 116, according to equation 56, under the bias from 2.1 V to 3.0 V. The summary is shown in Table XIII.

$$\frac{\Delta\eta}{\eta} = \frac{\eta(doped) - \eta(P3HT)}{\eta(P3HT)} \times 100\% \tag{56}$$

Table XIII. Efficiency summary comparison

Bias(V)	η(P3HT)	η(2% doped)	Δη/η (%)	η(5% doped)	Δη/η (%)
2.1	1.44E-06	2.74E-06	90.7	3.68E-06	156.1
2.2	1.77E-06	3.11E-06	75.4	4.05E-06	128.5
2.3	2.04E-06	3.29E-06	61.1	4.37E-06	114.0
2.4	2.29E-06	3.49E-06	52.3	4.62E-06	101.6
2.5	2.50E-06	3.67E-06	46.7	4.79E-06	91.5
2.6	2.68E-06	3.84E-06	43.2	5.06E-06	88.4
2.7	2.88E-06	3.96E-06	37.2	5.20E-06	80.2
2.8	3.04E-06	4.06E-06	33.6	5.38E-06	77.2
2.9	3.20E-06	4.19E-06	30.9	5.52E-06	72.4
3.0	3.37E-06	4.25E-06	26.3	5.66E-06	68.0

The enhancement in efficiency is always larger than 25%. At a bias above 2 V, the light emission suggests the onset of exciton formation. If assuming the

same probability of electro-excitation for pentacene and P3HT, the pentacene doping will also make a contribution to the EL, as that in the PL measurement.

However, as discussed above, the enhancement of PL due to co-emission must be less than 9.4% in 2% pentacene content and less than 11.7% in 5% pentacene content. So it can be concluded that the efficiency enhancement in doped P3HT cannot be attributed to the co-emission of pentacene and P3HT. Meanwhile, the improvement of charge injection, leading to the current density enhancement under the same bias, will make a negative contribution to the efficiency improvement, as per equation 53. So there must be other mechanisms contributing to the enhanced efficiency in Table XIII.

The EL is due to singlet decay. So the improvement of EL relates to the improvement of the population of exciton increase in the pentacene doped P3HT system. Pentacene will act as hole trap centres in P3HT. Thus hole concentration in pentacene will be higher than that in P3HT due to the trapping effect. Thus it increases the probability for the trapped holes with higher concentration to form excitons.

At the same time, the LUMO of pentacene is comparable to that of P3HT, so pentacene doping may also improve the electron transport in P3HT. This will both improve the conductance and luminescence in P3HT. Thus, the efficiency improvement can be attributed to a competition of different mechanisms. Pentacene doping blocks the hole transport, and improves the current density as well as the EL efficiency in P3HT.

4. Conclusions and Future work

The measurements are carried out on both unipolar and ambipolar systerms within P3HT based diodes. Two kinds of doping methods, photo-oxidation doping and pentacene doping are chosen to introduce trap states in P3HT and explained the MC change using different mechanisms.

The MC response is based on bipolaron mechanism in unipolar system. However, in ambipolar system the mechanisms are more complicated including triplet-polaron interaction, bipolaron, exciton dissociation and so on. An empirical fitting for the MC can be carried out both in unipolar and ambipolar systems. However, the fitting results cannot be easily distinguished in ambipolar system due to the complicated mechanism. There is a transition from bipolaron dominant (unipolar) to triplet-polaron interaction dominant (ambipolar) as the driving condition changes. Doping and de-doping will have an effect on the charge injection and transport in P3HT based diodes. Meanwhile, they will shift the Fermi level (E_F) and broaden the DoS (σ increases) leading to the MC change based on the simulation results of bipolaron mechanism.

In the device of Au/P3HT/Al, the single non-Lorentzian MC fitting results in reverse bias indicate a bipolaron mechanism in a unipolar transport system. In forward bias, there is a sign change of MC as the driving voltage increases due to the dominant mechanism transition from bipolaron to triplet-polaron interaction. When annealing above the glass transition temperature of P3HT, the current density will drop by ~3 orders of magnitude and the negative MC response will increase by ~1 order of magnitude. The drop of the conductance can be attributed to the charge injection barrier increase between P3HT and electrode for both holes and electrons due to the removal of p-doping effect. The DI measurement confirms that the injection barrier increase after annealing leading to a disappearance of the transient peak. The ~1 order of magnitude increase in negative MC is attributed to the Fermi level shift and the DoS broadening leading to an increase of the value $|-E_F/\sigma|$ according to bipolaron theory. [138]

After re-doping through photo-oxidation, the recovery of conductance and MC response confirms the explanation of doping effect on charge injection barrier and MC response based on bipolaron mechanism. Meanwhile, after re-doping there is a transition from bipolaron mechanism to a combination of bipolaron and triplet-polaron interaction mechanisms as the driving voltage

increase due to the transport system change from unipolar (hole only) to ambipolar (hole and electron). The barriers around interfaces will be enhanced after annealing and the hole injection from Au into P3HT will recover after re-doping leading to a unipolar transport system under low bias. Thus, the barrier of P3HT and electrode in Au/P3HT/Al diode is successfully tuned through annealing and re-doping which will make it possible to separately analyse the MC in unipolar and ambipolar system.

Pentacene is also chosen as a hole trap centre to carry out a chemical doping experiment in P3HT in three different kinds of devices. The DI measurement results prove that pentacene will block the hole transport which will decrease the hole mobility in P3HT. At the same time, pentacene will also improve the conductance when choosing Al or ITO as the anode for hole injection. All the MC responses based on bipolaron mechanism [138] can be explained by the Fermi energy shift and DoS broadening due to a pentacene doping effect. However in ambipolar system, the co-emission of P3HT and pentacene will make the system more complicated and the luminescence results prove the possibility of intersystem energy transference and non-radiative absorbance with energy loss which will make the efficiency lower than expected. It is difficult to correlate the hole trapping effect of pentacene to the MC response in ambipolar system, because the trapping effect will both perturb the formation of bipolaron and exciton. Thus it is only possible to qualitatively describe the pentacene doping effect.

The future work will focus both on the explanation of the doping effect in both unipolar and ambipolar systems. The MC in P3HT based diode after annealing will be discussed with different pentacene doping concentration. This will detect the hole trap effect in unipolar system based on bipolaron mechanism. It is also possible to improve the thickness of P3HT in the diode of ITO/PEDOT:PSS/P3HT/LiF/Al to improve light emission intensity under high bias. This will make it possible for us to detect the EL efficiency upon application of a magnetic field. The EL response is due to the perturbation of exciton population by the magnetic field which can offer us more information to analyse the complicated MC mechanisms in ambipolar transport system.

References

[1] J.D. Fan, Y.M. Malozovsky, International Journal of Modern Physics B 27 (2013) 1362024.

[2] I.G. Hill, A. Kahn, Z.G. Soos, J.R.A. Pascal, Chemical Physics Letters 327 (2000) 181.

[3] A. Bernanose, M. Comte, P. Vouaux, J. Chim. Phys. 50 (1953) 64.

[4] A. Bernanose, P. Vouaux, J. Chim. Phys. 50 (1953) 261.

[5] A. Bernanose, J. Chim. Phys. 52 (1955) 396.

[6] A. Bernanose, P. Vouaux, J. Chim. Phys. 52 (1955) 509.

[7] W. Helfrich, W.G. Schneider, Physical Review Letters 14 (1965) 229.

[8] C.W. Tang, S.A. VanSlyke, Applied Physics Letters 51 (1987) 913.

[9] J. Burroughes, D. Bradley, A. Brown, R. Marks, K. Mackay, R. Friend, P. Burns, A. Holmes, nature 347 (1990) 539.

[10] T.R. Hebner, C.C. Wu, D. Marcy, M.H. Lu, J.C. Sturm, Applied Physics Letters 72 (1998) 519.

[11] A. MacDiarmid, W. Salaneck, I. Lundstrom, B. Ranby, by WR Salaneck, I. Lundstrom, and B. Ranby, Oxford University Press, New York (1993).

[12] W.J.M. Naber, S. Faez, W.G.v.d. Wiel, Journal of Physics D: Applied Physics 40 (2007) R205.

[13] S. Günes, H. Neugebauer, N.S. Sariciftci, Chemical Reviews 107 (2007) 1324

[14] D.M. Chapin, C.S. Fuller, G.L. Pearson, Journal of Applied Physics 25 (1954) 676.

[15] C.W. Tang, Applied Physics Letters 48 (1986) 183.

[16] B.R. Saunders, M.L. Turner, Advances in Colloid and Interface Science 138 (2008) 1.

[17] S.C.J. Meskers, J. Hübner, M. Oestreich, H. Bässler, The Journal of Physical Chemistry B 105 (2001) 9139.

[18] J.D. Myers, J. Xue, Polymer Reviews 52 (2012) 1.

[19] W.A. Luhman, R.J. Holmes, Advanced Functional Materials 21 (2011) 764.

[20] P.E. Shaw, A. Ruseckas, I.D.W. Samuel, Advanced Materials 20 (2008) 3516.

[21] P. Peumans, S. Uchida, S.R. Forrest, Nature 425 (2003) 158.

[22] G. Yu, J. Gao, J.C. Hummelen, F. Wudl, A.J. Heeger, Science 270 (1995) 1789.

[23] J.J.M. Halls, C.A. Walsh, N.C. Greenham, E.A. Marseglia, R.H. Friend, S.C. Moratti, A.B. Holmes, Nature 376 (1995) 498.

[24] Z.D. Popovic, M.I. Khan, S.J. Atherton, A.-M. Hor, J.L. Goodman, The Journal of Physical Chemistry B 102 (1998) 657.

[25] Y. Xin, Z. Wang, L. Xu, X. Xu, Y. Liu, F. Zhang, Journal of Nanomaterials 2013 (2013) 6.

[26] P.J. Brown, D.S. Thomas, A. Köhler, J.S. Wilson, J.-S. Kim, C.M. Ramsdale, H. Sirringhaus, R.H. Friend, Physical Review B 67 (2003) 064203.
[27] C.H. Woo, P.M. Beaujuge, T.W. Holcombe, O.P. Lee, J.M.J. Fréchet, Journal of the American Chemical Society 132 (2010) 15547.
[28] A. Zen, J. Pflaum, S. Hirschmann, W. Zhuang, F. Jaiser, U. Asawapirom, J.P. Rabe, U. Scherf, D. Neher, Advanced Functional Materials 14 (2004) 757.
[29] B.C. Thompson, J.M.J. Fréchet, Angewandte Chemie International Edition 47 (2008) 58.
[30] S.E. Shaheen, C.J. Brabec, N.S. Sariciftci, F. Padinger, T. Fromherz, J.C. Hummelen, Applied Physics Letters 78 (2001) 841.
[31] G. Li, V. Shrotriya, J. Huang, Y. Yao, T. Moriarty, K. Emery, Y. Yang, Nat Mater 4 (2005) 864.
[32] W. Ma, C. Yang, X. Gong, K. Lee, A.J. Heeger, Advanced Functional Materials 15 (2005) 1617.
[33] M. Reyes-Reyes, K. Kim, D.L. Carroll, Applied Physics Letters 87 (2005) 083506.
[34] J.I. Nakamura, K. Murata, K. Takahashi, Applied Physics Letters 87 (2005) 132105.
[35] M. Reyes-Reyes, K. Kim, D.L. Carroll, Applied Physics Letters 87 (2005) 083506.
[36] L.J. Edgar, Method and apparatus for controlling electric currents. Google Patents, (1930).
[37] H. Koezuka, A. Tsumura, T. Ando, Synthetic Metals 18 (1987) 699.
[38] Y. Sun, Y. Liu, D. Zhu, Journal of Materials Chemistry 15 (2005) 53.
[39] A.R. Murphy, J.M.J. Fréchet, Chemical Reviews 107 (2007) 1066.
[40] J.E. Anthony, Angewandte Chemie International Edition 47 (2008) 452.
[41] S. Allard, M. Forster, B. Souharce, H. Thiem, U. Scherf, Angewandte Chemie International Edition 47 (2008) 4070.
[42] H. Naarmann, Ullmann's Encyclopedia of Industrial Chemistry, Wiley-VCH Verlag GmbH & Co. KGaA, (2000).
[43] A.J. Ben-Sasson, M. Greenman, Y. Roichman, N. Tessler, Israel Journal of Chemistry 54 (2014) 568.
[44] P. Aigrain, Journal of Physics and Chemistry of Solids 5 (1958) 237.
[45] V.I. Arkhipov, H. von Seggern, E.V. Emelianova, Applied Physics Letters 83 (2003) 5074.
[46] J.G. Simmons, Journal of Physics and Chemistry of Solids 32 (1971) 1987.
[47] T. van Woudenbergh, Charge Injection Into Organic Semiconductors, University Library Groningen] [Host], 2005.
[48] S.M. Sze, K.K. Ng, Physics of Semiconductor Devices (1981).
[49] W. Schottky, Naturwissenschaften 26 (1938) 843.

[50] J.G. Simmons, Physical Review Letters 15 (1965) 967.
[51] P.R. Emtage, J.J. O'Dwyer, Physical Review Letters 16 (1966) 356.
[52] P.W.M. Blom, M.C.J.M. Vissenberg, Materials Science and Engineering: R: Reports 27 (2000) 53.
[53] A.M. Ballantyne, J.S. Wilson, J. Nelson, D.D.C. Bradley, J.R. Durrant, M. Heeney, W. Duffy, I. McCulloch, TOF mobility measurements in pristine films of P3HT: control of hole injection and influence of film thickness, (2006) 633408.
[54] R.G. Forbes, Applied Physics Letters 89 (2006) 113122.
[55] A.K. Thakur, A.K. Mukherjee, D.M.G. Preethichandra, W. Takashima, K. Kaneto, Journal of Applied Physics 101 (2007) 104508
[56] R.N. Marks, D.D.C. Bradley, R.W. Jackson, P.L. Burn, A.B. Holmes, Synthetic Metals 57 (1993) 4128.
[57] L. Bozano, S.A. Carter, J.C. Scott, G.G. Malliaras, P.J. Brock, Applied Physics Letters 74 (1999) 1132.
[58] P.W.M. Blom, M.J.M. de Jong, M.G. van Munster, Physical Review B 55 (1997) R656.
[59] R.M. Hill, Philosophical Magazine 23 (1971) 59.
[60] M. Giulianini, E.R. Waclawik, J.M. Bell, N. Motta, Journal of Applied Physics 108 (2010) 014512.
[61] W.D. Gill, Journal of Applied Physics 43 (1972) 5033.
[62] L.B. Schein, A. Peled, D. Glatz, Journal of Applied Physics 66 (1989) 686.
[63] P.M. Borsenberger, Journal of Applied Physics 68 (1990) 6263.
[64] M.A. Abkowitz, Philosophical Magazine Part B 65 (1992) 817.
[65] H. Bässler, physica status solidi (b) 175 (1993) 15.
[66] A. Miller, E. Abrahams, Physical Review 120 (1960) 745.
[67] S.D. Baranovskii, P. Thomas, G.J. Adriaenssens, Journal of Non-Crystalline Solids 190 (1995) 283.
[68] V.I. Arkhipov, U. Wolf, H. Bässler, Physical Review B 59 (1999) 7514.
[69] D. Monroe, Physical Review Letters 54 (1985) 146.
[70] V.I. Arkhipov, E.V. Emelianova, H. Bässler, Philosophical Magazine Part B 81 (2001) 985.
[71] R.A. Marcus, The Journal of Chemical Physics 81 (1984) 4494.
[72] K. Seki, M. Tachiya, Physical Review B 65 (2001) 014305.
[73] G.L. Closs, J.R. Miller, Science 240 (1988) 440.
[74] V.I. Arkhipov, E.V. Emelianova, Y.H. Tak, H. Bässler, Journal of Applied Physics 84 (1998) 848.
[75] M.A. Abkowitz, H.A. Mizes, J.S. Facci, Applied Physics Letters 66 (1995) 1288.
[76] Y.N. Gartstein, E.M. Conwell, Chemical Physics Letters 255 (1996) 93.
[77] E.M. Conwell, M.W. Wu, Applied Physics Letters 70 (1997) 1867.
[78] D.F. Blossey, Physical Review B 9 (1974) 5183.

[79] D.R. Kearns, G. Tollin, M. Calvin, The Journal of Chemical Physics 32 (1960) 1020.
[80] M. Maitrot, G. Guillaud, B. Boudjema, J.J. Andr é, J. Simon, Journal of Applied Physics 60 (1986) 2396.
[81] J.J. Andre, J. Simon, R. Even, B. Boudjema, G. Guillaud, M. Maitrot, Synthetic Metals 18 (1987) 683.
[82] B. V. Zeghbroeck, Principles of Semiconductor Devices. Web-based book, University of Colorado at Boulder, 2004
[83] I. Salzmann, G. Heimel, S. Duhm, M. Oehzelt, P. Pingel, B.M. George, A. Schnegg, K. Lips, R.-P. Blum, A. Vollmer, N. Koch, Physical Review Letters 108 (2012) 035502.
[84] K. Walzer, B. Maennig, M. Pfeiffer, K. Leo, Chemical Reviews 107 (2007) 1233.
[85] S. Olthof, W. Tress, R. Meerheim, B. L üssem, K. Leo, Journal of Applied Physics 106 (2009) 103711.
[86] M. Pfeiffer, A. Beyer, T. Fritz, K. Leo, Applied Physics Letters 73 (1998) 3202.
[87] B. Maennig, M. Pfeiffer, A. Nollau, X. Zhou, K. Leo, P. Simon, Physical Review B 64 (2001) 195208.
[88] M. Pfeiffer, K. Leo, X. Zhou, J.S. Huang, M. Hofmann, A. Werner, J. Blochwitz-Nimoth, Organic Electronics 4 (2003) 89.
[89] A. Sperlich, H. Kraus, C. Deibel, H. Blok, J. Schmidt, V. Dyakonov, The Journal of Physical Chemistry B 115 (2011) 13513.
[90] H. Hintz, H. Peisert, H.J. Egelhaaf, T. Chassé, The Journal of Physical Chemistry C 115 (2011) 13373.
[91] C.-K. Lu, H.-F. Meng, Physical Review B 75 (2007) 235206.
[92] D.B.A. Rep, A.F. Morpurgo, T.M. Klapwijk, Organic Electronics 4 (2003) 201.
[93] B.H. Hamadani, H. Ding, Y. Gao, D. Natelson, Physical Review B 72 (2005) 235302.
[94] L. An, Y. Duan, Y. Yuan, L. Zhou, J. Zhang, Vibrational Spectroscopy 68 (2013) 40.
[95] L. Bonoldi, C. Carati, L. Montanari, R. Po', The Journal of Physical Chemistry C 118 (2014) 7751.
[96] D.M. Ivory, G.G. Miller, J.M. Sowa, L.W. Shacklette, R.R. Chance, R.H. Baughman, The Journal of Chemical Physics 71 (1979) 1506.
[97] T. Yoshikazu, A. Soichiro, T. Masayoshi, N. Susumu, S. Akio, Japanese Journal of Applied Physics 29 (1990) L1040.
[98] J. Kido, K. Nagai, Y. Okamoto, Electron Devices, IEEE Transactions on 40 (1993) 1342.
[99] T. Mori, H. Fujikawa, S. Tokito, Y. Taga, Applied Physics Letters 73 (1998) 2763.

[100] G. Parthasarathy, C. Shen, A. Kahn, S.R. Forrest, Journal of Applied Physics 89 (2001) 4986.
[101] B.W. Dandrade, S.R. Forrest, A.B. Chwang, Applied Physics Letters 83 (2003) 3858.
[102] S. Reineke, F. Lindner, G. Schwartz, N. Seidler, K. Walzer, B. Lussem, K. Leo, Nature 459 (2009) 234.
[103] A. Nollau, M. Pfeiffer, T. Fritz, K. Leo, Journal of Applied Physics 87 (2000) 4340.
[104] T. Senku, K. Kaname, K. Eiji, I. Takashi, N. Toshio, O. Yukio, S. Kazuhiko, Japanese Journal of Applied Physics 44 (2005) 3760.
[105] C.K. Chan, F. Amy, Q. Zhang, S. Barlow, S. Marder, A. Kahn, Chemical Physics Letters 431 (2006) 67.
[106] C.J. Bloom, C.M. Elliott, P.G. Schroeder, C.B. France, B.A. Parkinson, The Journal of Physical Chemistry B 107 (2003) 2933.
[107] K. Harada, M. Riede, K. Leo, O.R. Hild, C.M. Elliott, Physical Review B 77 (2008) 195212.
[108] A. Werner, F. Li, K. Harada, M. Pfeiffer, T. Fritz, K. Leo, S. Machill, Advanced Functional Materials 14 (2004) 255.
[109] A.G. Werner, F. Li, K. Harada, M. Pfeiffer, T. Fritz, K. Leo, Applied Physics Letters 82 (2003) 4495.
[110] P. Wei, J.H. Oh, G. Dong, Z. Bao, Journal of the American Chemical Society 132 (2010) 8852.
[111] P. Wei, T. Menke, B.D. Naab, K. Leo, M. Riede, Z. Bao, Journal of the American Chemical Society 134 (2012) 3999.
[112] H. Ahn, A. Ohno, J.-i. Hanna, Journal of Applied Physics 102 (2007) 093718.
[113] U. Niedermeier, M. Vieth, R. Pätzold, W. Sarfert, H. von Seggern, Applied Physics Letters 92 (2008) 193309.
[114] S.A. Bagnich, U. Niedermeier, C. Melzer, W. Sarfert, H. von Seggern, Journal of Applied Physics 106 (2009) 113702.
[115] J. Rybicki, R. Lin, F. Wang, M. Wohlgenannt, C. He, T. Sanders, Y. Suzuki, Physical Review Letters 109 (2012) 076603.
[116] M. Cox, E.H.M. van der Heijden, P. Janssen, B. Koopmans, Physical Review B 89 (2014) 085201.
[117] V.A. Dediu, L.E. Hueso, I. Bergenti, C. Taliani, Nat Mater 8 (2009) 707.
[118] W. Zhao, Y. Qi, T. Sajoto, S. Barlow, S.R. Marder, A. Kahn, Applied Physics Letters 97 (2010).
[119] J.Y. Kim, I.J. Chung, C. Lee, Y.C. Kim, J.K. Kim, J.-W. Yu, Current Applied Physics 5 (2005) 615.
[120] R.C. Johnson, R.E. Merrifield, P. Avakian, R.B. Flippen, Physical Review Letters 19 (1967) 285.
[121] R.C. Johnson, R.E. Merrifield, Physical Review B 1 (1970) 896.
[122] V. Ern, R.E. Merrifield, Physical Review Letters 21 (1968) 609.

[123] G.J. Sloan, Molecular Crystals 1 (1966) 161.
[124] R.P. Groff, R.E. Merrifield, A. Suna, P. Avakian, Physical Review Letters 29 (1972) 429.
[125] R.P. Groff, A. Suna, P. Avakian, R.E. Merrifield, Physical Review B 9 (1974) 2655.
[126] M. Wittmer, I. Zschokke - Gränacher, The Journal of Chemical Physics 63 (1975) 4187.
[127] J. Kalinowski, M. Cocchi, D. Virgili, P. Di Marco, V. Fattori, Chemical Physics Letters 380 (2003) 710.
[128] J. Kalinowski, M. Cocchi, D. Virgili, V. Fattori, P. Di Marco, Physical Review B 70 (2004) 205303.
[129] T.L. Francis, M. Ö, G. Veeraraghavan, M. Wohlgenannt, New Journal of Physics 6 (2004) 185.
[130] Ö. Mermer, G. Veeraraghavan, T.L. Francis, M. Wohlgenannt, Solid State Communications 134 (2005) 631.
[131] Ö. Mermer, G. Veeraraghavan, T.L. Francis, Y. Sheng, D.T. Nguyen, M. Wohlgenannt, A. Köhler, M.K. Al-Suti, M.S. Khan, Physical Review B 72 (2005) 205202.
[132] J.M. Ziman, Principles of the Theory of Solids, Cambridge university press, (1972).
[133] V.N. Prigodin, J.D. Bergeson, D.M. Lincoln, A.J. Epstein, Synthetic Metals 156 (2006) 757.
[134] M.A. Baldo, S.R. Forrest, Physical Review B 62 (2000) 10958.
[135] R.D. Johnson, L.C. Chapon, D.D. Khalyavin, P. Manuel, P.G. Radaelli, C. Martin, Physical Review Letters 108 (2012) 067201.
[136] Y. Wu, B. Hu, Applied Physics Letters 89 (2006).
[137] B. Hu, Y. Wu, Nat Mater 6 (2007) 985.
[138] P.A. Bobbert, T.D. Nguyen, F.W.A. van Oost, B. Koopmans, M. Wohlgenannt, Physical Review Letters 99 (2007) 216801.
[139] P. Desai, P. Shakya, T. Kreouzis, W.P. Gillin, N.A. Morley, M.R.J. Gibbs, Physical Review B 75 (2007) 094423.
[140] P. Desai, P. Shakya, T. Kreouzis, W.P. Gillin, Journal of Applied Physics 102 (2007) 073710.
[141] W.P. Gillin, S. Zhang, N.J. Rolfe, P. Desai, P. Shakya, A.J. Drew, T. Kreouzis, Physical Review B 82 (2010) 195208.
[142] S. Zhang, J. Song, T. Kreouzis, W.P. Gillin, Journal of Applied Physics 106 (2009) 043511.
[143] S. Zhang, A.J. Drew, T. Kreouzis, W.P. Gillin, Synthetic Metals 161 (2011) 628.
[144] P. Desai, P. Shakya, T. Kreouzis, W.P. Gillin, Physical Review B 76 (2007) 235202
[145] J.Y. Song, N. Stingelin, A.J. Drew, T. Kreouzis, W.P. Gillin, Physical Review B 82 (2010) 085205.

[146] H. Gu, T. Kreouzis, W.P. Gillin, Organic Electronics 15 (2014) 1711.
[147] R.N. Mahato, H. Lülf, M.H. Siekman, S.P. Kersten, P.A. Bobbert, M.P. de Jong, L. De Cola, W.G. van der Wiel, Science 341 (2013) 257.
[148] P. Desai, PhD Thesis (2008).
[149] D. Poplavskyy, PhD Thesis (2003).
[150] A. Many, G. Rakavy, Physical Review 126 (1962) 1980.
[151] W. Helfrich, W.G. Schneider, The Journal of Chemical Physics 44 (1966) 2902.
[152] J. Scott, S. Ramos, G. Malliaras, Journal of Imaging Science and Technology 43 (1999) 233.
[153] C.A. Gedelian, K.C. Rajanna, B. Premerlani, T.-M. Lu, Journal of Luminescence 145 (2014) 473.
[154] J.F. James, Spectrograph design fundamentals, Cambridge University Press Cambridge, MA, (2007).
[155] W.A.Jeffers, American Journal of Physics 39 (1971) 1210.
[156] F.L. Bloom, W. Wagemans, M. Kemerink, B. Koopmans, Physical Review Letters 99 (2007) 257201.
[157] T.-H. Lee, T.-F. Guo, J.C.A. Huang, T.-C. Wen, Applied Physics Letters 92 (2008).
[158] F.L. Bloom, W. Wagemans, M. Kemerink, B. Koopmans, Applied Physics Letters 93 (2008) 263302.
[159] J.D. Bergeson, V.N. Prigodin, D.M. Lincoln, A.J. Epstein, Physical Review Letters 100 (2008) 067201.
[160] T.D. Nguyen, Y. Sheng, J. Rybicki, G. Veeraraghavan, M. Wohlgenannt, Journal of Materials Chemistry 17 (2007) 1995.
[161] P. Janssen, M. Cox, S.H.W. Wouters, M. Kemerink, M.M. Wienk, B. Koopmans, Nat Commun 4 (2013).
[162] H. Kang, I.-J. Lee, C. Sup Yoon, Applied Physics Letters 100 (2012) 073302.
[163] H. Gu, J. Guo, R. Sadu, Y. Huang, N. Haldolaarachchige, D. Chen, D.P. Young, S. Wei, Z. Guo, Applied Physics Letters 102 (2013) 212403.
[164] A. Assadi, C. Svensson, M. Willander, O. Inganas, Journal of Applied Physics 72 (1992) 2900.
[165] G. Dennler, C. Lungenschmied, N.S. Sariciftci, R. Schwodiauer, S. Bauer, H. Reiss, Applied Physics Letters 87 (2005) 163501.
[166] G. Garcia-Belmonte, A. Munar, E.M. Barea, J. Bisquert, I. Ugarte, R. Pacios, Organic Electronics 9 (2008) 847.
[167] E. Itoh, K. Terashima, H. Nagai, K. Miyairi, Thin Solid Films 518 (2009) 810.
[168] M.S.A. Abdou, F.P. Orfino, Y. Son, S. Holdcroft, Journal of the American Chemical Society 119 (1997) 4518.
[169] S. Hoshino, M. Yoshida, S. Uemura, T. Kodzasa, N. Takada, T. Kamata, K. Yase, Journal of Applied Physics 95 (2004) 5088.

[170] S. Zhang, N.J. Rolfe, P. Desai, P. Shakya, A.J. Drew, T. Kreouzis, W.P. Gillin, Physical Review B 86 (2012) 075206.
[171] Y. Shi, S.-C. Luo, W. Fang, K. Zhang, E.M. Ali, F.Y.C. Boey, J.Y. Ying, J. Wang, H.-h. Yu, L.-J. Li, Organic Electronics 9 (2008) 859.
[172] S.-W. Oh, H. Woo Rhee, C. Lee, Y. Chul Kim, J. Kyeong Kim, J.-W. Yu, Current Applied Physics 5 (2005) 55.
[173] Y. Sheng, T.D. Nguyen, G. Veeraraghavan, Ö. Mermer, M. Wohlgenannt, S. Qiu, U. Scherf, Physical Review B 74 (2006) 045213.
[174] N. Tho Duc, S. Yugang, E.R. James, W. Markus, Science and Technology of Advanced Materials 9 (2008) 024206.
[175] J.Y. Song, N. Stingelin, W.P. Gillin, T. Kreouzis, Applied Physics Letters 93 (2008) 233306.
[176] N. Rolfe, P. Desai, P. Shakya, T. Kreouzis, W.P. Gillin, Journal of Applied Physics 104 (2008) 083703.
[177] N.J. Rolfe, M. Heeney, P.B. Wyatt, A.J. Drew, T. Kreouzis, W.P. Gillin, Synthetic Metals 161 (2011) 608.
[178] M. Cox, P. Janssen, F. Zhu, B. Koopmans, Physical Review B 88 (2013) 035202.
[179] B. Xu, S. Holdcroft, Thin Solid Films 242 (1994) 174.
[180] M.A. Baklar, F. Koch, A. Kumar, E.B. Domingo, M. Campoy-Quiles, K. Feldman, L. Yu, P. Wobkenberg, J. Ball, R.M. Wilson, I. McCulloch, T. Kreouzis, M. Heeney, T. Anthopoulos, P. Smith, N. Stingelin, Advanced Materials 22 (2010) 3942.
[181] O.V. Kozlov, S.A. Zapunidi, Synthetic Metals 169 (2013) 48.
[182] D. Alberga, G.F. Mangiatordi, L. Torsi, G. Lattanzi, The Journal of Physical Chemistry C 118 (2014) 8641
[183] S. Cho, K. Lee, J. Yuen, G. Wang, D. Moses, A.J. Heeger, M. Surin, R. Lazzaroni, Journal of Applied Physics 100 (2006) 114503.
[184] V.D. Mihailetchi, H.X. Xie, B. de Boer, L.J.A. Koster, P.W.M. Blom, Advanced Functional Materials 16 (2006) 699.
[185] F.J. Yang, W. Qin, S.J. Xie, The Journal of Chemical Physics 140 (2014) 144110.
[186] B.-F. Ding, W.C.H. Choy, W.-M. Kwok, Y. Yao, K.Y.F. Ho, C.-Q. Wu, Organic Electronics 14 (2013) 457.
[187] S. Ochiai, K. Palanisamy, S. Kannappan, P.-K. Shin, ISRN Condensed Matter Physics 2012 (2012) 7.
[188] S. Hamwi, J. Meyer, T. Winkler, T. Riedl, W. Kowalsky, Applied Physics Letters 94 (2009) 253307.
[189] R.A. Cruz, T. Catunda, W.M. Facchinatto, D.T. Balogh, R.M. Faria, Synthetic Metals 163 (2013) 38.
[190] J.H. Schön, C. Kloc, E. Bucher, B. Batlogg, Synthetic Metals 115 (2000) 177.